

The Pennsylvania State University  
The Graduate School

LOW-ENERGY IONIZATION YIELD IN LIQUID ARGON FOR A  
COHERENT NEUTRINO-NUCLEUS SCATTER DETECTOR

A Dissertation in  
Nuclear Engineering  
by  
Michael P. Foxe

© 2013 Michael P. Foxe

Submitted in Partial Fulfillment  
of the Requirements  
for the Degree of

Doctor of Philosophy

May 2013

The dissertation of Michael P. Foxe was reviewed and approved\* by the following:

Igor Jovanovic  
Associate Professor of Nuclear Engineering / Bashore Career Development  
Professor  
Dissertation Advisor, Chair of Committee

Kenan Ünlü  
Professor of Nuclear Engineering

Jack Brenizer  
J. Lee Everett Professor of Mechanical and Nuclear Engineering

Tyce DeYoung  
Associate Professor of Physics

Kareem Kazkaz  
Physicist, Lawrence Livermore National Laboratory  
Special Member

Arthur Motta  
Chair of Nuclear Engineering

\*Signatures are on file in the Graduate School.

# Abstract

In recent years, antineutrinos have been used to track the power output and isotopic content of nuclear reactors, as the flux of emitted antineutrinos normalized to reactor thermal power varies over the course of the fuel cycle with the change of fuel composition. Since antineutrinos interact weakly with matter, they cannot be shielded and their flux is not appreciably attenuated as they leave the reactor core and structure. As a result, antineutrino detectors can be placed outside of containment and used to track the reactor power and isotopic content within the core. The current generation of antineutrino detectors used for nuclear reactor monitoring utilize the inverse  $\beta$ -decay detection mechanism, in which the antineutrino interacts with a proton, producing a neutron and a positron, which are subsequently detected in coincidence.

Another mode of interaction predicted by the Standard Model of particle physics, but not yet observed, is coherent neutrino-nucleus scattering (CNNS). CNNS results from the neutrino (or antineutrino) scattering coherently with the entire nucleus rather than a single nucleon. When the wavelength of the neutrino is on the order of the size of the target nucleus or greater ( $E_\nu \lesssim 50$  MeV), the neutrino can scatter coherently off of the entire nucleus. CNNS is of significant scientific interest because its observation would represent another confirmation of the Standard Model. Additionally, the cross section for CNNS scales with the square of the number of neutrons within the nucleus, resulting in a  $\sim 100\times$  greater per-atom interaction probability when compared to inverse  $\beta$ -decay. This offers a prospect for CNNS-based nuclear reactor monitoring using detectors with considerably lower active masses.

The leading challenge in detecting CNNS is the resulting sub-keV nuclear recoil energies, producing little ionization in the detector medium. In order to detect the CNNS interaction, it is beneficial to first measure the nuclear ionization yield for the chosen detector medium. The ionization yield represents the expected

number of electrons produced by a nuclear recoil, and it depends both on the recoil energy and on the detector medium in which the recoil occurs. Additionally, the ionization yield depends on the applied electron drift electric field, and for this reason it should be measured directly in the detector type anticipated for future CNNS measurements. This dissertation is focused on making the prediction and measurement of the ionization yield in LAr using a dual-phase Ar detector.

Due to the complexity of measuring the ionization yield at various energies, it is beneficial to also construct a predictive model for the ionization yield. In this dissertation, the prediction of the ionization yield is made on the basis of a simulation of a two-stage process. The number of ionizations generated from Ar recoil of a given energy is simulated using a Monte Carlo atomic collision model, along with the cross sections for ionization and excitation in Ar + Ar collisions. After the electrons are generated, a fraction of them recombine with the initially generated ion cloud. The electron recombination fraction is simulated by assigning the emitted electrons either 1 or 10 eV of initial kinetic energy and transporting the electrons under the influence of Coulomb forces of the ion cloud and an applied external electric field. The simulation predicts the energy dependent ionization yield, with a value of  $\sim 4e^-$  per keVr at 8 keVr. For gaseous Ar, the nuclear ionization quench factor is predicted to be  $\sim 0.13$  at 10 keVr, which is the upper limit on this quantity obtained from the atomic collision model.

In order to confidently apply the predictions of the ionization yield model, several experiments have been carried out for its validation. A single-phase Ar detector is used to both understand the processes occurring in the amplification region of a dual-phase Ar detector and to measure the nuclear ionization quench factor (ratio of the ionization signal produced in a nuclear recoil compared to that produced in an electron recoil of equal energy) in gaseous Ar. Using a portable neutron generator based on the  ${}^7\text{Li}(p,n){}^7\text{Be}$  reaction, the nuclear ionization quench factor at 13 keVr was measured in gaseous Ar to be  $0.138 \pm 0.012$ , which is in good agreement with the predictions of the ionization yield model. The absolute ionization yield was not measurable in gaseous Ar, because single ionization electron sensitivity has not been achieved in the single-phase Ar detector.

The Gamma or Neutron Argon Recoils Resulting in Liquid Ionization (G/NARRLI) detector is a dual-phase Ar detector, which was developed to measure the ionization yield at energies below 10 keVr. While operating the G/NARRLI detector, high purity was achieved, extending the electron lifetime to  $\approx 100 - 200 \mu\text{s}$ . The ultimate sensitivity was achieved by detecting the single ionization electron peak. Detection of the single electron peak allowed absolutely calibrated spectroscopy to be performed using  ${}^{55}\text{Fe}$  to produce a 6 keV peak and  ${}^{37}\text{Ar}$  to produce a peak at 2.822 keV and a low-energy peak at 270 eV. Spectroscopic detection of the 270 eV peak represents the lowest energy measured to date



in a dual-phase Ar detector. The electron yields for the  $^{55}\text{Fe}$  and  $^{37}\text{Ar}$  sources were used for the validation of the electron transport code, which was in good agreement with the modeling results. An effort was made to measure the ionization yield at energies below  $\sim 8$  keVr, using neutrons generated from the  $^7\text{Li}(p,n)^7\text{Be}$  reaction in a similar manner as that performed with the gaseous Ar detector. Unfortunately, the Li target had degraded due to the diffusion of Ag into the Li, and the neutron production rates were  $\sim 10\times$  lower than expected, which resulted in a low signal-to-background ratio for this measurement. Therefore, the ionization yield model was used alone to predict the detector response to elastic neutron scatters.

Using the ionization yield model, the expected signal from the CNNS interaction with an Ar detector 25 m from a nuclear reactor was calculated. It is expected that 70% of all Ar recoils produced by CNNS result in no electrons generated, 14% of the events are predicted to generate a single electron, and 16% of the events are expected to produce two or more electrons. With the addition of 1% Xe to facilitate the Penning ionization mechanism, these values change to 63%, 17%, and 20%, respectively. CNNS is thus predicted to be a viable detection technique for close proximity monitoring of nuclear reactors, but due to its sensitivity to the solar neutrino background, it is not suitable for long range ( $\gtrsim 1$  km) detection.

# Table of Contents

<b>List of Figures</b>	<b>x</b>
<b>List of Tables</b>	<b>xv</b>
<b>List of Symbols</b>	<b>xvi</b>
<b>List of Acronyms</b>	<b>xxii</b>
<b>Acknowledgments</b>	<b>xxiv</b>
<b>Chapter 1</b>	
<b>Introduction</b>	<b>1</b>
1.1 Antineutrinos . . . . .	1
1.1.1 Oscillation Between Flavors . . . . .	1
1.1.2 Neutrino Production . . . . .	2
1.2 Nuclear Non-Proliferation . . . . .	5
1.3 Detection of Antineutrinos Produced in Nuclear Reactors . . . . .	6
1.4 Coherent Neutrino-Nucleus Scatter (CNNS) . . . . .	9
1.4.1 Physics of the CNNS Interaction . . . . .	10
1.4.1.1 Weak Neutral Current . . . . .	10
1.4.1.2 Cross Section . . . . .	10
1.4.1.3 Recoil Energy . . . . .	11
1.4.2 CNNS Detection Challenges . . . . .	12
1.4.3 CNNS Detector Candidates . . . . .	12
1.5 Noble Element Detector Introduction . . . . .	17
1.5.1 Wavelength Shifting of Argon Scintillation Light . . . . .	18
1.5.1.1 Nitrogen Doping . . . . .	19
1.5.1.2 Tetraphenyl butadiene (TPB) Coatings . . . . .	21

1.5.2	Xenon Doping for Wavelength Shifting . . . . .	22
1.5.3	Penning Mechanism in Liquid Argon . . . . .	23
1.5.4	Electron-Nuclear Recoil Discrimination . . . . .	24
1.5.4.1	Singlet-Triplet Population Ratios . . . . .	25
1.5.4.2	S2/S1 Ratios . . . . .	25

## Chapter 2

<b>Monte Carlo Simulation of Ionization Yield</b>	<b>28</b>
2.1 Ionization Yield . . . . .	28
2.2 Current Ionization Yield Models . . . . .	30
2.3 Atomic Collision Model . . . . .	34
2.3.1 Impact Parameter . . . . .	36
2.3.2 Elastic Energy Transfer . . . . .	37
2.3.3 Distance of Closest Approach . . . . .	37
2.3.4 Radii of Curvature . . . . .	40
2.3.5 The Correction Term . . . . .	40
2.3.6 Inelastic Collision Probability . . . . .	42
2.3.7 Sum Ionizations and Excitations . . . . .	43
2.3.8 Intrinsic Ionization Yields . . . . .	45
2.3.9 Quench Factor Value . . . . .	46
2.4 Electron Transport Model . . . . .	48
2.4.1 Forces on Electrons and Ions . . . . .	49
2.4.2 Electron Capture . . . . .	51
2.4.3 Electron Positions . . . . .	51
2.4.4 Ion Velocities . . . . .	52
2.4.5 Ion Positions . . . . .	52
2.4.6 Electron-Atom Collision . . . . .	52
2.4.7 Electron Drift Velocity . . . . .	54
2.4.8 Electron Collection Efficiency . . . . .	55
2.5 Detectable Ionization Yield . . . . .	57

## Chapter 3

<b>Single-Phase Argon Detector</b>	<b>59</b>
3.1 Single-Phase Detector . . . . .	59
3.2 Event Characteristics . . . . .	61
3.3 Detector Calibration . . . . .	63
3.4 Detector Optimization . . . . .	66
3.5 Pre-Filtering of Data . . . . .	67
3.6 Signal Pathologies . . . . .	69
3.7 Radial Dependence . . . . .	73

3.8	Geant4 Simulation . . . . .	75
<b>Chapter 4</b>		
	<b>Single-Phase Argon Nuclear Ionization Quench Factor Measurement</b>	<b>77</b>
4.1	Experimental Setup . . . . .	78
4.2	Neutron Generation . . . . .	78
4.3	Nuclear Ionization Quench Factor Results . . . . .	81
4.4	Comparison with Model . . . . .	85
<b>Chapter 5</b>		
	<b>Gamma or Neutron Argon Recoils Resulting in Liquid Ionization (G/NARRLI) Detector</b>	<b>87</b>
5.1	Design of the G/NARRLI Detector . . . . .	87
5.2	Electrostatic Model . . . . .	90
5.2.1	COMSOL Model Setup for the G/NARRLI Detector . . . . .	90
5.2.2	Study of the Current G/NARRLI Design . . . . .	91
5.3	Wavelength Shifting . . . . .	94
5.3.1	Vacuum Evaporation of TPB . . . . .	95
5.3.2	TPB Window Coating . . . . .	98
5.3.3	TPB Reflector Coating . . . . .	100
5.4	G/NARRLI Detector Operation . . . . .	101
5.5	Photomultiplier Tube Characteristics . . . . .	107
5.6	Event Characteristics . . . . .	108
5.7	Event Position Reconstruction . . . . .	110
5.8	Measuring Detector Purity Through the Electron Lifetime . . . . .	113
5.9	Single Ionization Electron Detection . . . . .	116
<b>Chapter 6</b>		
	<b>Electron Transport Model Validation</b>	<b>118</b>
6.1	Validation Using $^{55}\text{Fe}$ . . . . .	118
6.1.1	Experimental Procedure for $^{55}\text{Fe}$ Measurements . . . . .	119
6.1.2	$^{55}\text{Fe}$ Spectra and Source Localization . . . . .	120
6.2	Validation Using $^{37}\text{Ar}$ . . . . .	120
6.2.1	Experimental Procedure for $^{37}\text{Ar}$ Measurements . . . . .	121
6.2.2	$^{37}\text{Ar}$ Spectra and Localization . . . . .	122
6.3	Event Integrals with Varying Drift Field . . . . .	125
6.4	Ionization Profile Source Terms . . . . .	131
6.5	Electron Transport Model Results . . . . .	132

6.6	Comparison between the Measurements and the Electron Transport Model . . . . .	136
<b>Chapter 7</b>		
	<b>G/NARRLI Detector Nuclear Ionization Quench Factor Measurements</b>	<b>139</b>
7.1	Detector Transport and Setup . . . . .	139
7.2	Neutron Generation and Optimization . . . . .	140
7.3	LUXSim Simulations . . . . .	145
7.4	Measurements at the Center for Accelerator Mass Spectrometry (CAMS) Facility . . . . .	147
7.5	Prediction of the Neutron Signal . . . . .	155
7.6	Extraction of the Ionization Yield . . . . .	157
<b>Chapter 8</b>		
	<b>Prospects for Detection of CNNS and Conclusions</b>	<b>162</b>
8.1	Detection of Coherent Neutrino-Nucleus Scatter (CNNS) . . . . .	162
8.1.1	CNNS Signal from Nuclear Reactors . . . . .	162
8.1.2	CNNS Backgrounds . . . . .	165
8.1.2.1	Close Proximity Reactor Monitoring . . . . .	166
8.1.2.2	Long Range Detection Limit . . . . .	167
8.2	Reactor Monitoring . . . . .	170
8.2.1	Inverse Beta Decay vs CNNS for Neutrino Detection . . . . .	170
8.2.2	Detection of CNNS using Neutrino Beams . . . . .	173
8.3	CNNS Detection for Neutrino Physics . . . . .	174
8.4	Conclusions . . . . .	175
8.5	Future Work . . . . .	177
	<b>Bibliography</b>	<b>179</b>

# List of Figures

1.1	Standard Model table of elementary particles . . . . .	2
1.2	Antineutrino spectra coming out of a nuclear reactor . . . . .	4
1.3	Isotopic content within a light water reactor over the course of a fuel cycle . . . . .	5
1.4	Nuclear fuel cycle diagram . . . . .	6
1.5	Inverse Beta Decay cross section for interaction . . . . .	7
1.6	Current inverse $\beta$ -decay nuclear reactor monitoring detector . . . . .	8
1.7	Tracking the power output of a nuclear reactor . . . . .	8
1.8	Tracking the isotopic content of a nuclear reactor . . . . .	9
1.9	Comparison of CNNS cross section and the average recoil energy . .	13
1.10	Comparison of antineutrino interaction cross section for CNNS and inverse $\beta$ decay . . . . .	16
1.11	CNNS recoil spectra for nuclear reactor antineutrinos on natural argon . . . . .	16
1.12	Principle of operation for a dual-phase detector . . . . .	18
1.13	Emission spectrum for nitrogen wavelength shifted scintillation light	20
1.14	Emission spectrum for TPB wavelength shifted scintillation light . .	22
1.15	Emission spectrum for xenon wavelength shifted scintillation light .	23
1.16	Electronic recoil event created from a $\gamma$ -ray interaction . . . . .	26
1.17	Nuclear recoil event created from a neutron interaction . . . . .	26
2.1	Schematic for electron and nuclear recoils . . . . .	29
2.2	Measured quench factors in Ge . . . . .	31
2.3	Lindhard theory predicted ionization yields in LAr . . . . .	33
2.4	Algorithm for the Atomic Collision Model . . . . .	35
2.5	Schematic for a two atom elastic scatter event . . . . .	38
2.6	Molière and Coulomb Potentials . . . . .	39
2.7	Inelastic cross sections for neutral-neutral Ar collision . . . . .	43
2.8	Inelastic cross sections for ion-neutral Ar collision . . . . .	44
2.9	Sample schematic for an Ar collision cascade . . . . .	44
2.10	Predicted intrinsic ionization and scintillation yields for LAr . . . .	46

2.11	Calculated nuclear quench factors for LAr . . . . .	48
2.12	Cross section for electron-atom collisions . . . . .	54
2.13	Comparison of the predicted electron mobility with previous experiments and models . . . . .	55
2.14	Measured electron emission spectrum from Ar-Ar collisions . . . . .	56
2.15	Calculated electron collection efficiencies dependent on the number of initial electrons and electric field. . . . .	57
2.16	Expected ionization and scintillation yields for LAr . . . . .	58
3.1	Single-phase Ar detector used for studying the amplification properties of a dual-phase Ar detector . . . . .	60
3.2	Sample trace from the single-phase Ar detector showing $^{55}\text{Fe}$ and single photoelectrons . . . . .	64
3.3	Characteristic $^{55}\text{Fe}$ event from the single-phase Ar detector with $\text{N}_2$ wavelength shifting . . . . .	64
3.4	Energy deposition spectrum from the $^{55}\text{Fe}$ calibration source in the single-phase Ar detector . . . . .	65
3.5	Detector <i>F.O.M.</i> as a function of $\text{N}_2$ content . . . . .	66
3.6	Spectra comparison with and without a data pre-filter . . . . .	68
3.7	Event width and the event energy in the single phase Ar detector . . . . .	68
3.8	Single-phase Ar pathological traces . . . . .	69
3.9	Total trace integral for the signal pathologies algorithm . . . . .	70
3.10	Number of threshold crossings per trace for the signal pathologies algorithm . . . . .	71
3.11	The event integral spectrum for good and spurious traces . . . . .	72
3.12	Schematic of optical response model geometry . . . . .	73
3.13	Comparison of the optical model and detector radial dependence . . . . .	75
3.14	Single-phase Ar detector as coded into the Geant4 simulation . . . . .	76
3.15	Comparison of $^{55}\text{Fe}$ data with simulation . . . . .	76
4.1	Cart for the single-phase Ar detector . . . . .	79
4.2	Experiment schematic for measuring the nuclear ionization quench factor with the single-phase Ar detector . . . . .	80
4.3	Neutron distribution from the $^7\text{Li}(p,n)^7\text{Be}$ reaction for 1.93 MeV protons . . . . .	80
4.4	$^{40}\text{Ar}(n,\text{el})$ Cross Section . . . . .	81
4.5	Predicted neutron spectrum incident on the single-phase Ar detector . . . . .	82
4.6	Predicted recoil spectrum in the single-phase Ar detector . . . . .	83
4.7	Portable neutron generator . . . . .	84
4.8	Portable neutron generator internals . . . . .	84

4.9	Calibrated neutron recoil spectrum in gaseous Ar . . . . .	85
5.1	Schematic and picture of the G/NARRLI detector . . . . .	89
5.2	Picture of the G/NARRLI detector experimental setup . . . . .	90
5.3	Geometry used in the electrostatic model . . . . .	91
5.4	Meshing of the electrostatic model geometry . . . . .	92
5.5	Voltage potential surface plot for the current G/NARRLI detector .	93
5.6	Calculated local electric field near the extraction grid wires . . . . .	94
5.7	Calculated radial component of the electric field within the G/NARRLI detector . . . . .	95
5.8	Calculated z component of the electric field within the G/NARRLI detector . . . . .	96
5.9	Calculated electron drift tracks for the G/NARRLI detector . . . . .	97
5.10	TPB coating pictures for vacuum evaporation and spraying appli- caiton . . . . .	97
5.11	Vacuum evaporator chamber used for TPB coating . . . . .	98
5.12	Crucible holding the TPB for vacuum evaporation coating . . . . .	99
5.13	Vacuum evaporator pressure during the TPB coating procedure . . .	99
5.14	Optimal TPB coating thicknesses for PMT windows . . . . .	100
5.15	Window coated with $\sim 0.06\text{mg}/\text{cm}^2$ of TPB for wavelength shifting	101
5.16	Comparison of the effectiveness of different light reflectors . . . . .	102
5.17	Optimal TPB coating thicknesses for the reflectors . . . . .	103
5.18	TPB coated 3M foil with and without UV light . . . . .	103
5.19	Plumbing schematic for the G/NARRLI detector . . . . .	104
5.20	Pulse tube cryocooler used with the G/NARRLI detector . . . . .	105
5.21	Cryocooler condenser where the argon is liquified . . . . .	105
5.22	Slow control monitoring of the G/NARRLI detector as Ar is liquified	106
5.23	Argon liquid-gas vapor pressure curve . . . . .	107
5.24	Single photoelectron peaks for the PMTs used in the G/NARRLI detector . . . . .	108
5.25	Characteristic $^{241}\text{Am}$ event in the G/NARRLI detector . . . . .	109
5.26	Threshold crossings versus the calculated integral in photoelectrons	110
5.27	Top view schematic of the fiducialization setup in purity measure- ments . . . . .	112
5.28	Reconstructed fiducialization plot for the G/NARRLI detector with an $^{241}\text{Am}$ source . . . . .	112
5.29	$^{241}\text{Am}$ spectra before and after a fiducialization cut . . . . .	113
5.30	Calculation of the detector purity using $^{241}\text{Am}$ . . . . .	114
5.31	Measured electron lifetimes versus time into the detector run . . . .	115
5.32	Single ionization electron event trace . . . . .	115



5.33	Single ionization electron peak in the light collection histogram . . .	116
5.34	Fiducialization plot of the single ionization electron events . . . . .	117
6.1	The $^{55}\text{Fe}$ source within the dual-phase Ar detector active volume . .	119
6.2	$^{55}\text{Fe}$ spectra in terms of photoelectrons . . . . .	121
6.3	Fiducial plot of the $^{55}\text{Fe}$ events with the source approximately centered	122
6.4	Isotopic activities after the irradiation of natural Ar . . . . .	123
6.5	$^{37}\text{Ar}$ injection setup . . . . .	124
6.6	Fiducial plot of the $^{37}\text{Ar}$ with uniform event position reconstruction	125
6.7	$^{37}\text{Ar}$ spectra in terms of photoelectrons . . . . .	126
6.8	Spectra for $^{55}\text{Fe}$ and $^{37}\text{Ar}$ used in the drift field study . . . . .	127
6.9	Single electron light yield as a function of gain field . . . . .	127
6.10	Electron yield from $^{241}\text{Am}$ as a function of drift electric field . . . .	128
6.11	Electron yield from $^{55}\text{Fe}$ as a function of drift electric field . . . . .	128
6.12	Electron yield from $^{37}\text{Ar}$ K-shell peak as a function of drift electric field . . . . .	129
6.13	Electron yield from $^{37}\text{Ar}$ L-shell peak as a function of drift electric field . . . . .	130
6.14	Calculated electron yield from $^{37}\text{Ar}$ L-shell as a function of drift electric field . . . . .	135
6.15	Calculated electron yield from $^{37}\text{Ar}$ K-shell as a function of drift electric field . . . . .	136
6.16	Calculated electron yield from $^{55}\text{Fe}$ as a function of drift electric field	137
6.17	Electron yield comparison between simulation and experiment . . .	138
7.1	Schematic for measuring the ionization yield at 7 keVr . . . . .	140
7.2	Transporting the dual-phase argon detector to CAMS . . . . .	141
7.3	Setting the dual-phase argon detector up at CAMS . . . . .	141
7.4	Theoretical Neutron spectrum at $45^\circ$ and the $^{40}\text{Ar}(\text{n},\text{el})$ cross section	143
7.5	Alignment of the collimator to $45^\circ$ . . . . .	143
7.6	Predicted neutron spectrum exiting collimator with no filter . . . .	144
7.7	(n,el) cross sections for $^{56}\text{Fe}$ , $^{48}\text{Ti}$ , and $^{40}\text{Ar}$ . . . . .	145
7.8	Predicted neutron spectrum exiting the collimator with Fe/Ti filter	146
7.9	Geant4 model of the G/NARRLI detector . . . . .	147
7.10	Predicted neutron energy deposition spectra with and without Fe/Ti filter . . . . .	148
7.11	CAMS accelerator used for neutron generation . . . . .	149
7.12	Silicon detector and $^{226}\text{Ra}$ source for calibrating the proton beam .	149
7.13	Li target holder used with the proton beam . . . . .	150
7.14	Installation of the Li target at the end of the proton accelerator . .	150

7.15	View of the Li target placed inside the proton accelerator . . . . .	151
7.16	View of the Li target with protons bombarding the target . . . . .	152
7.17	Proton energy versus the (neutron yield) <sup>2/3</sup> . . . . .	152
7.18	Neutron yields versus angle as a function of proton energy . . . . .	153
7.19	Reduction of neutron yields from Li versus AgLi <sub>x</sub> . . . . .	154
7.20	Measured gamma background with the neutrons being generated below 45° . . . . .	155
7.21	Prediction of neutron signal within the LAr detector . . . . .	156
7.22	Comparison of single and multiple scatter neutron energy deposi- tions within the Ar detector . . . . .	157
7.23	Prediction of background subtracted neutron signal . . . . .	158
7.24	Exercise prediction of the ionization yield . . . . .	161
7.25	Exercise predicted signal and background subtracted signal prediction	161
8.1	Reactor $\bar{\nu}$ spectrum for 61.9% <sup>235</sup> U, 27.2% <sup>239</sup> Pu, 6.7% <sup>238</sup> U, and 4.2% <sup>241</sup> Pu . . . . .	163
8.2	Argon recoil spectrum from CNNS with reactor $\bar{\nu}$ . . . . .	164
8.3	Predicted CNNS electron yields for a pure Ar detector . . . . .	165
8.4	Predicted CNNS electron yields for an Ar detector with and without a 1% Xe dopant . . . . .	166
8.5	Predicted CNNS signal and backgrounds for CNNS detection . . . .	168
8.6	Neutrino interaction spectrum for CNNS and inverse $\beta$ -decay . . . .	171
8.7	Interactions per kg per day for CNNS and inverse $\beta$ -decay . . . . .	172
8.8	Stopped-pion source neutrino energies . . . . .	173

# List of Tables

1.1	Average number of antineutrinos emitted per fission . . . . .	4
1.2	Predicted event rates for a Ge CNNS detector . . . . .	14
1.3	Characteristic decay times for the scintillation processes in Ar and Xe . . . . .	17
1.4	Antoine’s Equation parameters for Ar, N <sub>2</sub> , and Xe . . . . .	20
1.5	Relative population ratios of the singlet and triplet states in LAr . .	25
2.1	Possible interactions throughout the Ar cascade in the atomic col- lision model . . . . .	36
2.2	Liquid Argon quench model properties . . . . .	36
2.3	Fit parameters for the Molière Potential . . . . .	42
2.4	Ar Cascade Meta-Data Summary . . . . .	45
2.5	Electron recombination criteria in LAr . . . . .	51
3.1	X-ray emission energies for the <sup>55</sup> Fe source . . . . .	62
3.2	Electron transition energies resulting in X-ray escape peaks . . . . .	62
3.3	Single-phase Ar signal pathologies cut criteria . . . . .	72
4.1	Portable neutron generator specifications . . . . .	82
6.1	Electron capture decay branching ratios for <sup>37</sup> Ar. . . . .	120
6.2	Isotopic data for Argon . . . . .	123
6.3	Measured infinite field W-Values for LAr . . . . .	130
6.4	EADL transition table for the K-shell decay of <sup>37</sup> Ar . . . . .	132
6.5	EADL transition table for the L-shell decay of <sup>37</sup> Ar . . . . .	133
6.6	Secondary electron energy distributions for primary electron ener- gies energies of 100-600 eV . . . . .	134
6.7	Average number of electrons and photons generated . . . . .	135
6.8	Calculated infinite field W-Values for LAr . . . . .	136
8.1	Solar neutrino properties . . . . .	169
8.2	Spallation Neutron Source parameters . . . . .	174

# List of Symbols

$\nu_e$	Electron neutrino, p. 1
$\nu_\mu$	Muon neutrino, p. 1
$\nu_\tau$	Tau neutrino, p. 1
$p$	Proton, p. 1
$n$	Neutron, p. 1
$e^+$	Positron, p. 1
$\pi^\pm$	Pion, p. 1
$\mu^\pm$	Muon, p. 3
$\beta^+$	Beta-plus, p. 3
$\beta^-$	Beta-minus, p. 3
$Z$	Atomic number, p. 3
$A$	Atomic mass number, p. 3
$\lambda_{\bar{\nu}}$	Antineutrino wavelength, p. 9
$R_{\text{nuc}}$	Nucleus radius, p. 9
$E_\nu$	Neutrino energy, p. 10
$G$	Conventional Fermi constant, p. 10
$q_m$	Momentum transfer, p. 10

$N$	Atomic neutron number, p. 10
$\theta_W$	Weinberg weak-mixing angle, p. 10
$\Delta^2$	Three-momentum transfer, p. 10
$q_{ion}$	Nuclear ionization quench factor, p. 12
$N_{ion}^{nucl}$	Number of ionizations from nuclear recoils, p. 12
$N_{ion}^{elec}$	Number of ionizations from electron recoils, p. 12
$y_i$	Elemental mole fraction in gas, p. 19
$x_i$	Elemental mole fraction in liquid, p. 34
$P^o$	Vapor pressure, p. 19
$p_{Penning}$	Probability of the Penning mechanism occurring, p. 24
$f_{Xe}$	Fraction of Xe in LAr in %, p. 24
$\tau_{fast}$	Decay lifetime of Ar excitation singlet state in LAr, p. 25
$\tau_{slow}$	Decay lifetime of Ar excitation triplet state in LAr, p. 25
$I_{fast}$	Intensity of Ar excitation singlet state in LAr, p. 25
$I_{slow}$	Intensity of Ar excitation triplet state in LAr, p. 25
$Q_y$	Ionization yield, p. 29
$N_{e-}$	Number of electrons, p. 29
$E$	Energy, p. 29
$keVr$	keV of recoil energy, p. 29
$\eta$	Lindhard theory: energy given to electrons, p. 30
$\zeta$	Lindhard theory: energy given to atoms, p. 30
$k$	Lindhard theory: $dE/dx$ proportionality constant, p. 30
$\varepsilon$	Lindhard theory: reduced energy, p. 30
$a_0$	Bohr's radius, p. 30

$M$	Atomic mass, p. 30
$e$	Electron charge, p. 30
$g$	Lindhard theory: energy dependent function, p. 30
$N_{\text{exc}}$	Number of excitations, p. 31
$N_{\text{ion}}$	Number of ionizations, p. 31
$W_{ph}$	Energy required to generate an ionization or excitation, p. 32
$\frac{\partial N_+}{\partial t}$	Thomas-Imel: ion diffusion equation, p. 33
$\frac{\partial N_-}{\partial t}$	Thomas-Imel: electron diffusion equation, p. 33
$\frac{Q}{Q_0}$	Thomas-Imel: fraction of electrons collected, p. 34
$\xi$	Thomas-Imel: dependent parameter, p. 34
$\alpha$	Thomas-Imel: coefficient of recombination, p. 33
$a$	Thomas-Imel: dimension of the box containing the charge, p. 34
$u_-$	Thomas-Imel: electron mobility, p. 34
$E_f$	Electric field, p. 34
$E_{\text{elec}}$	Atomic Collision: energy of ionization, p. 35
$E_{\text{exc}}$	Atomic Collision: energy of excitation, p. 35
$I_p$	Atomic Collision: ionization potential, p. 35
$\rho_{\text{atom}}$	Atomic Collision: atom density, p. 36
$L$	Atomic Collision: collisional path length, p. 36
$\sigma_{\text{geo}}$	Atomic Collision: geometric cross section, p. 36
$P$	Atomic Collision: impact parameter, p. 36
$R_n$	Atomic Collision: random number, p. 36
$T$	Energy transferred to the target atom, p. 37
$\theta$	Atomic Collision: atom scattering angle, p. 37

$r_0$	Atomic Collision: distance of closest approach, p. 37
$\rho$	Atomic Collision: atom trajectory radius of curvature, p. 37
$\delta$	Atomic Collision: scatter triangle correction term, p. 37
$V$	electric potential, p. 37
$E_c$	Center-of-mass energy, p. 37
$\epsilon_0$	Permittivity of free space, p. 38
$\Phi$	Atomic Collision: Moliere's screening function, p. 39
$a_{sc}$	Interatomic screening length, p. 39
$\omega$	Atomic Collision: reduced energy, p. 40
$p_{\text{Penning}}$	Probability of the Penning mechanism occurring, p. 24
$Q_{ie}$	Atomic Collision: intrinsic ionization yield, p. 45
$E_{init}$	Initial kinetic energy, p. 45
$q_{\text{tot}}$	Total nuclear quench factor, p. 47
$q_{\text{ion}}$	Nuclear ionization quench factor, p. 47
$q_{\text{ion-Penn}}$	Nuclear ionization quench factor with the Penning mechanism, p. 47
$W$	W-value, average energy required to make an electron-ion pair, p. 47
$r_{\text{max}}$	Electron Transport: maximum collision rate, p. 49
$v$	Electron Transport: electron velocity, p. 49
$\sigma_{\text{tot}}$	Electron Transport: total electron-atom collision cross section, p. 49
$\langle \Delta t \rangle$	Electron Transport: mean collision time, p. 49
$\Delta t$	Electron Transport: time step, p. 49
$R_t$	Electron Transport: random number, p. 49
$r$	Electron Transport: distance between charges, p. 50
$x$	Electron Transport: charge location on the x-axis, p. 50

$y$	Electron Transport: charge location on the y-axis, p. 50
$z$	Electron Transport: charge location on the z-axis, p. 50
$a_x$	Electron Transport: x component of the acceleration, p. 50
$a_y$	Electron Transport: y component of the acceleration, p. 50
$a_z$	Electron Transport: z component of the acceleration, p. 50
$a$	Electron Transport: acceleration due to Coulomb forces, p. 50
$q_{el}$	Electron Transport: charge of the electron, p. 50
$q_{ion}$	Electron Transport: charge of the ion, p. 50
$\epsilon_r$	Relative permittivity of LAr, p. 50
$m_{el}$	Mass of the electron, p. 50
$m_{ion}$	Mass of the ion, p. 51
$E_{crit}$	Electron Transport: critical energy for electron-ion recombination, p. 51
$r_{crit}$	Electron Transport: critical radius for electron-ion recombination, p. 51
$\mu_{ion}$	Electron Transport: ion mobility, p. 52
$\sigma_{et}$	Electron Transport: electron-atom energy transfer cross section, p. 52
$\sigma_{pt}$	Electron Transport: electron-atom momentum transfer cross section, p. 52
$\sigma_{exc}$	Electron Transport: electron-atom excitation cross section, p. 53
$\sigma_{ion}$	Electron Transport: electron-atom ionization cross section, p. 53
$Prob$	Electron Transport: randomly sampled probability, p. 53
$\sigma_{elas}$	Electron Transport: electron-atom elastic collision cross section, p. 53
$\sigma_{inelas}$	Electron Transport: electron-atom inelastic collision cross section, p. 53
$F.O.M.$	Figure of merit, p. 66
$C_{Fe}$	Centroid of $^{55}\text{Fe}$ peak, p. 66



$\sigma_{Fe}$	Sigma of $^{55}\text{Fe}$ peak, p. 66
$C_{spe}$	Centroid of single photoelectron peak, p. 66
$C_{spe}$	Sigma of single photoelectron peak, p. 66
$D$	Normal vector from event to PMT window, p. 74
$t$	PMT and Viewport window thickness, p. 74
$T_{ArMax}$	Maximum recoil energy for Ar, p. 78
$E_n$	Neutron energy, p. 78
$keVee$	keV of electron recoil equivalent energy, p. 83
$CE$	Electron collection efficiency, p. 85
$t_{TPB}$	TPB coating thickness, p. 96
$M_{TPB}$	Mass of TPB, p. 96
$d_W$	Distance from evaporator crucible to reflector, p. 96
$MCA$	MCA channel number, p. 148
$E_p$	Proton energy, p. 151
$Y$	Neutron yield, p. 151
$L_{Ag \rightarrow Li}$	Diffusion length for Ag into Li, p. 153
$D_{Ag}$	Diffusion constant for Ag into Li, p. 153
$\lambda(\theta)$	Maximum likelihood ratio, p. 159
$\chi^2$	Chi-squared value, p. 159
$L_\nu$	Neutrino luminosity, p. 169
$H$	Heating power, p. 169
$R_\oplus$	Radius of the earth, p. 169
$\mu_\nu$	Neutrino magnetic moment, p. 175
$\mu_B$	Bohr magneton, p. 175

# List of Acronyms

IAEA	International Atomic Energy Agency, p. 5
SNM	Special Nuclear Material, p. 5
SONGS	San Onofre Nuclear Generating Station, p. 7
CNNS	Coherent Neutrino-Nucleus Scatter, p. 9
CDMS	Cryogenic Dark Matter Search, p. 12
TES	Transition Edge Sensor, p. 13
ULGeN	Ultra-Low Germanium Neutrino detection system, p. 13
FWHM	Full Width Half Max, p. 14
CONNIE	Coherent Neutrino Nuclear Interaction Experiment, p. 14
CCD	Charge-Coupled Device, p. 14
RED	Russian Emission Detector, p. 14
PMT	Photomultiplier Tube, p. 17
TPB	Tetraphenyl Butadiene, p. 19
VUV	Very Ultra-Violet, p. 21
LAr	Liquid Argon, p. 32
TRIM	TRansport of Ions in Matter, p. 35
DAQ	Data Acquisition Software, p. 61

TTL	Transistor-Transistor Logic , p. 61
UV	Ultra-Violet, p. 63
F.O.M.	Figure of Merit, p. 66
LLNL	Lawrence Livermore National Laboratory, p. 77
MCNP	Monte Carlo N-Particle, p. 78
ECR	Electron Cyclotron Resonance, p. 81
RFQ	Radiofrequency Quadrupole, p. 81
G/NARRLI	Gamma or Neutron Argon Recoils Resulting in Liquid Ionization, p. 87
UHV	Ultra-High Vacuum, p. 88
PEEK	Polyether Ether Ketone, p. 88
BNC	Bayonet Neill-Concelman, p. 88
HV	High Voltage, p. 88
SHV	Safe High Voltage, p. 88
PTFE	Polytetrafluoroethylene, p. 100
TTX	Tetratex, p. 100
RTD	Resistance Temperature Detectors, p. 104
PID	Proportional-Integral-Derivative, p. 105
EADL	Evaluated Atomic Data Library, p. 131
CAMS	Center for Accelerator Mass Spectrometry, p. 139
MCNPX	Monte Carlo N-Particle eXtended, p. 142
MCA	Multi-Channel Analyzer, p. 148
SNS	Spallation Neutron Source, p. 173

# Acknowledgments

I would like to thank the G/NARRLI collaboration, as I owe a great deal of gratitude to the collaboration for the knowledge and experience I have gained through the course of this project.

I thank my advisor Igor Jovanovic for his guidance through my pursuit of a Ph.D. I have gained a great amount of knowledge through his leadership. He always pointed in the right direction and taught me when to expand the work I was doing and when to focus on obtaining data first chance available.

I thank Chris Hagmann for his support in the development of the ionization yield model while I was at LLNL. I am indebted to Chris for the assistance he gave me in understanding the physical processes included in the simulation. I look forward to the detection of coherent neutrino-nucleus scattering to validate the predictions made with the ionization yield simulation.

I thank Adam Bernstein for his leadership of the Advanced Detector Group at LLNL, and push to always keep the project moving. He continually sought necessary funding which allowed for the development of the single-phase and dual-phase Ar detectors which have provided me with the knowledge and information needed for this dissertation. I also thank Adam for his collaborative efforts which have allowed me to meet experts in the CNNS field from all over the world.

I thank Kareem Kazkaz for his guidance as we worked on the single-phase Ar detector together. I learned to have patience with experimental physics as we spent weeks looking for phantom leaks in the gaseous Ar detector only to have them vanish later. I am also thankful Kareem and his coding knowledge which stopped me from running in circles while trying to debug analysis code and LUXSim simulations.

I thank Samuele Sangiorgio for his effort in developing the dual-phase Ar detector together. I thank him for his work that he put into the analysis routines which allowed for the measurement of the data used to set the world class performance of the G/NARRLI detector.

I am grateful to Peter Sorensen for sharing his knowledge in dual-phase noble

element detectors which aided in the success of the project thus far and for his talks about the extraction of the ionization yield values from a continuum of data.

I thank Sergey Pereverzev as he shared his immense knowledge of the lab work and kept me always learning about how the machines worked. His single handed effort to fix the leak detector allowed for a confidence in the detector purity fittings and achievement of high purity.

I thank Vladimir Mozin for his help with the MCNP models and studies of the neutron emission spectra from the Li target.

I thank Tenzing Joshi for his company in this project as we pursued our Ph.D.s and shared in the joy and frustration of the G/NARRLI detector along side each other.

I thank Jon Coleman and Kostas Mavrokoridis for their support from the University of Liverpool. I thank them for the fabrication of the vacuum evaporator chamber used in the TPB coatings. I thank Kostas for his aid in the development of the vacuum evaporation setup at Penn State University.

I also thank my reading committee of Igor, Kareem, Samuele, and Chris who helped me to ensure that this dissertation was of the highest quality obtainable.

Lastly, I thank my family, Jenni, my friends, and everyone else not specifically mentioned here who has provided me with support and inspiration as I pursued the long road to my Ph.D.

# Dedication

I dedicate this dissertation to my grandparents  
Tom and Mary Jane Skillicorn  
and  
Russell and Dorothy Foxe

# Introduction

## 1.1 Antineutrinos

The Standard Model is consistent with the existence [1] of a set of elementary particles which make up the matter in the universe. The particles contained in the Standard Model (Figure 1.1) can be categorized into quarks, leptons, and force carriers (bosons). The quarks and leptons are divided into three generations, of which the first generation makes up the matter in ordinary conditions. The Standard Model contains three flavors of neutrinos and antineutrinos: the electron flavor ( $\bar{\nu}_e$ ), the muon flavor ( $\bar{\nu}_\mu$ ), and the tau flavor ( $\bar{\nu}_\tau$ ). Neutrinos and antineutrinos are ubiquitous in nature, with the term neutrino often referring to both neutrinos and antineutrinos.

### 1.1.1 Oscillation Between Flavors

Neutrinos change from one flavor to another as they travel, an effect referred to as *neutrino oscillation* [4] [5]. In the current nuclear reactor monitoring detectors, the mechanism for detection is the *inverse  $\beta$ -decay* [6, 7, 8, 9, 10, 11]:

$$\bar{\nu}_e + p \rightarrow n + e^+, \tag{1.1}$$

where  $\bar{\nu}_e$  represents the incoming antineutrino,  $p$  is a target proton,  $n$  is an outgoing neutron, and  $e^+$  is an outgoing positron. Inverse  $\beta$ -decay is possible only

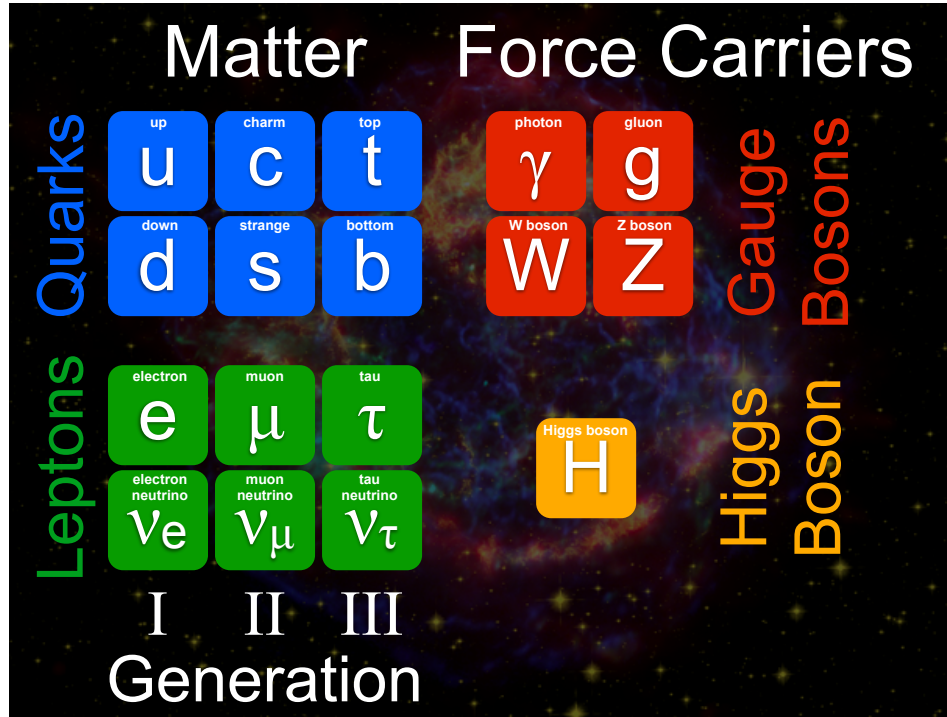


**Figure 1.1.** The Standard Model of particle physics predicts three generations of leptons: electron, muon, and tau, with their corresponding neutrinos [2]. The Higgs Boson discovered in 2012, at the time this research was conducted, is also shown [3].

for electron flavor antineutrinos. This requirement, combined with neutrino oscillation, can contribute to the reduction of the signal as the distance between the detector and the reactor increases [12, 13, 14] (in addition to the usual reduction of the solid angle subtended by the detector with distance from the source). This effect is well-known from solar neutrino measurement and the observation of the solar neutrino deficit [15, 16].

### 1.1.2 Neutrino Production

Neutrinos can be produced at various energies in particle accelerator facilities [17, 18]. Stopped-pion sources are used to produce neutrinos at energies of order 10-50 MeV by the decay of the  $\pi$  meson:

$$\pi^+ \rightarrow \mu^+ + \nu_\mu \quad (1.2)$$



and the muon:

$$\mu^+ \rightarrow e^+ + \bar{\nu}_\mu + \nu_e, \quad (1.3)$$

where  $\pi^+$  is the pion that decays,  $\mu^+$  is a muon,  $\bar{\nu}_\mu$  is a muon antineutrino,  $\nu_\mu$  is a muon neutrino, and  $\nu_e$  is an electron neutrino. Neutrinos and antineutrinos are also produced in  $\beta$ -decay processes. Neutrinos are generated through  $\beta^+$ -decay:

$${}^A_Z X \rightarrow {}^A_{Z-1} Y + \beta^+ + \nu_e, \quad (1.4)$$

and antineutrinos are produced via  $\beta^-$ -decay:

$${}^A_Z X \rightarrow {}^A_{Z+1} Y + \beta^- + \bar{\nu}_e, \quad (1.5)$$

where  $A$  is the mass number,  $Z$  is the atomic number,  $X$  is the radioactive isotope,  $Y$  is the daughter isotope,  $\beta^+$  is a positron, and  $\beta^-$  is an electron. Similar to  $\beta^+$ -decay, neutrinos can also be produced through electron capture:

$${}^A_Z X + e^- \rightarrow {}^A_{Z-1} Y + \nu_e. \quad (1.6)$$

Natural neutrino and antineutrino sources exist which produce a continuous neutrino background. Fusion reactions in the sun (pp chain) produce a large number of  $\nu_e$ , which provide a *solar neutrino* background on the earth. As the neutrinos travel the distance from the sun to the earth, a fraction of the initial  $\nu_e$  oscillate to the muon and tau flavors [19, 20, 21, 22]. High energy *atmospheric neutrinos* are produced from cosmic rays through the decays of secondary pions and muons, Equations (1.2) and (1.3), respectively [23]. Neutrinos are also produced in the decay of radioactive nuclides within earth's interior and referred to as *geo-neutrinos*. Geo-neutrinos consist primarily of antineutrinos from the decay of  $^{238}\text{U}$  and  $^{232}\text{Th}$ , with an additional neutrino component originating from the decay of  $^{40}\text{K}$  [24].

In nuclear reactors, large quantities of electron antineutrinos ( $\bar{\nu}_e$ ) are produced via  $\beta^-$ -decay of fission products. The reactor antineutrino energy spectrum depends on the composition of the fuel, and it has an energy range of 0-10 MeV [25, 26], shown in Figure 1.2. The average number of antineutrinos per fission is  $\sim 5$ , with the values for  $^{235}\text{U}$ ,  $^{238}\text{U}$ ,  $^{239}\text{Pu}$  and  $^{241}\text{Pu}$  shown in Table 1.1.

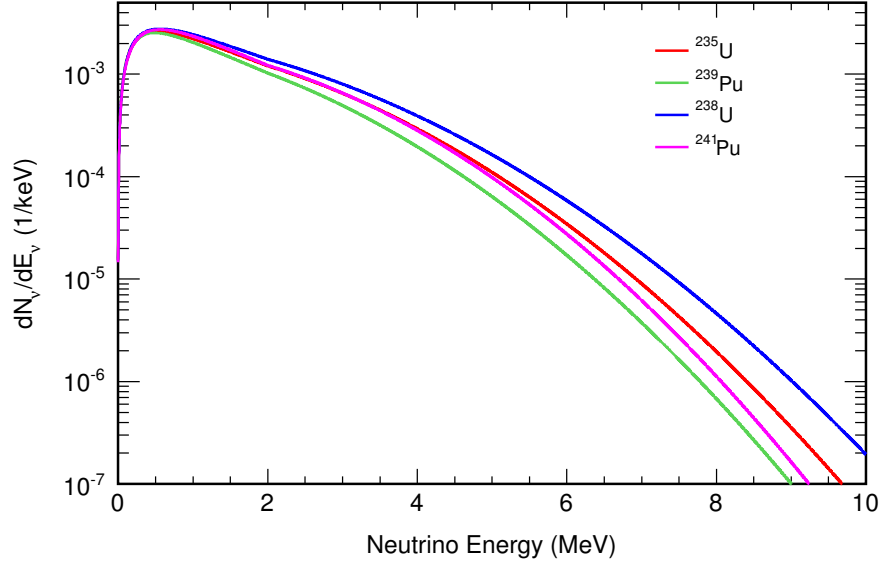


**Figure 1.2.** The antineutrino energy spectrum emitted from a nuclear reactor varies depending on the nuclide that was fissioned. This feature enables monitoring of nuclear reactor isotopic composition.[25].

**Table 1.1.** Average number of antineutrinos emitted per fission of  $^{235}\text{U}$ ,  $^{238}\text{U}$ ,  $^{239}\text{Pu}$  and  $^{241}\text{Pu}$ , as calculated by [25]

Isotope	Average # of $\bar{\nu}_e$
$^{235}\text{U}$	5.51
$^{238}\text{U}$	6.28
$^{239}\text{Pu}$	4.83
$^{241}\text{Pu}$	5.63

Over the course of the fuel cycle the amount of uranium and plutonium within the core changes, causing the relative rate of fissions from different nuclides to change as well [10]. A drop in the rate of  $^{235}\text{U}$  fissions and an increase in the rate of  $^{239}\text{Pu}$  fissions occurs as the reactor progresses through its normal fuel cycle, Figure 1.3. The change in isotopic content within the reactor, combined with the fact that fission of different nuclides produces different average antineutrino emission rates, Figure 1.2 results in the ability to track the composition of the reactor fissile inventory by antineutrino detection.

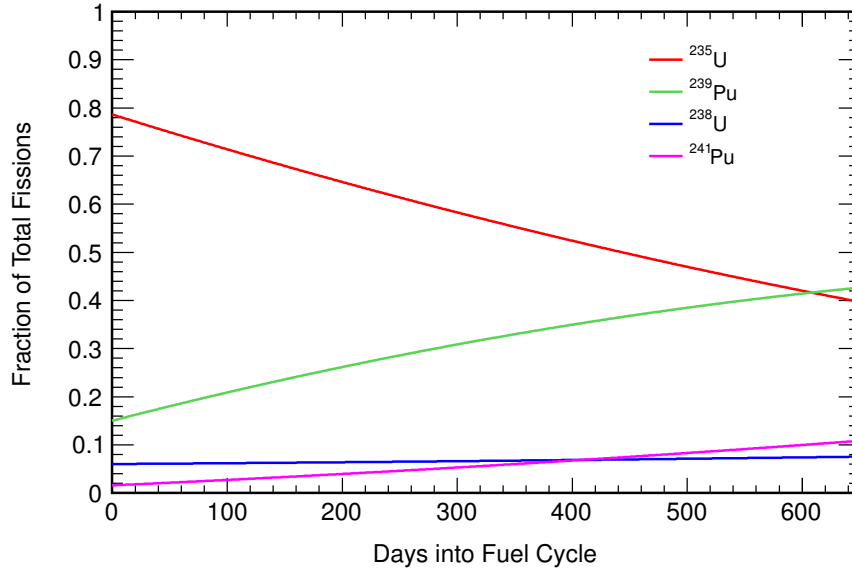


**Figure 1.3.** As the fuel cycle progresses,  $^{235}\text{U}$  is burnt up, while  $^{239}\text{Pu}$  is produced, which alters the relative rate of fissions from these two nuclides [27].

## 1.2 Nuclear Non-Proliferation

Throughout the course of the nuclear fuel cycle (Figure 1.4 [28]), the International Atomic Energy Agency (IAEA) monitors the amount and location of the uranium and plutonium present. At this time, the IAEA can not directly monitor the amount of plutonium being produced once the nuclear fuel is placed in the reactor. Thus when the fuel is removed from the nuclear reactor either for storage or reprocessing, a significant uncertainty exists in the amount of uranium and plutonium removed, both of which need to be tracked throughout the rest of the fuel cycle. Antineutrino detection near a nuclear reactor can provide information on the operation of a nuclear reactor and the uranium and plutonium content, aiding the IAEA in the complete tracking of the special nuclear material (SNM).

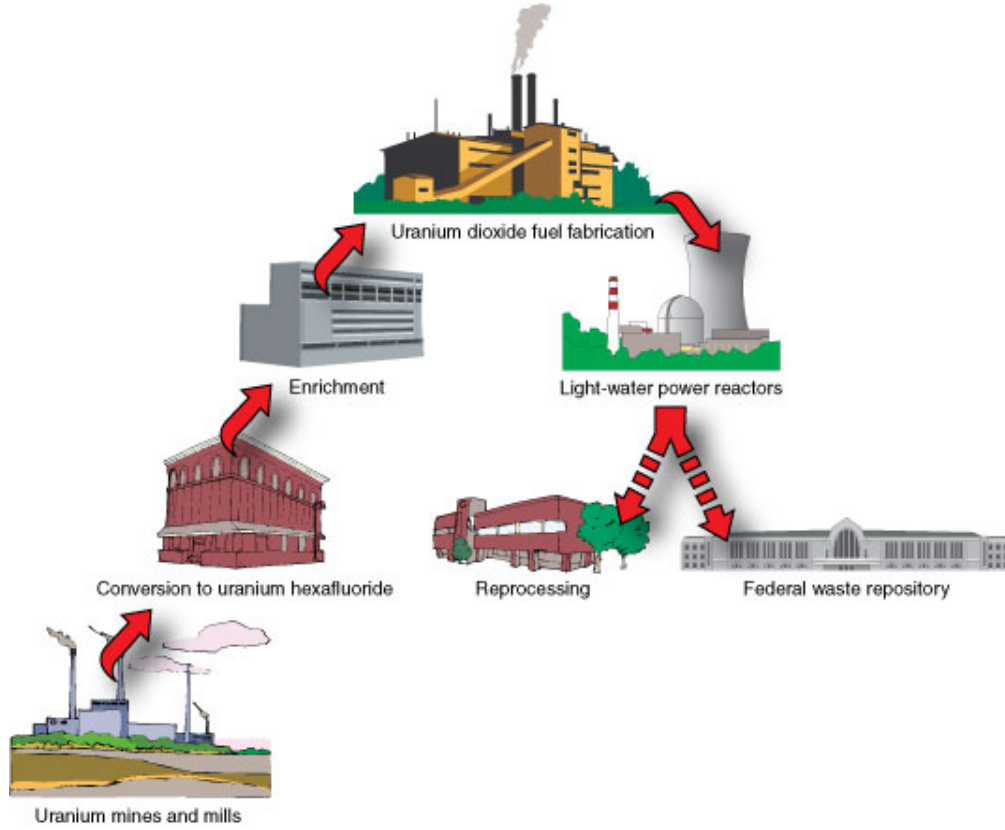


**Figure 1.4.** A significant effort is expended by the IAEA to monitor the uranium and plutonium inventory throughout the fuel cycle. The time when this inventory is in the reactor is exceedingly difficult to monitor for fissile material content directly [28].

### 1.3 Detection of Antineutrinos Produced in Nuclear Reactors

The current generation of antineutrino detectors for monitoring nuclear reactors are based on inverse  $\beta$ -decay for detection, Equation (1.1). A liquid scintillator detector is used as both the detection medium as well as the interaction medium. The antineutrino interacts with a proton within the liquid scintillator,  $(\text{CH}_2)_n$ . The interaction results in a positron and neutron being emitted. The positron annihilates with an electron, and the neutron is moderated and subsequently captured on either hydrogen  $\sim 200 \mu\text{s}$  or gadolinium  $\sim 28 \mu\text{s}$  after the positron annihilation [6, 7, 8, 9, 10, 11]. Two important limitations of inverse  $\beta$ -decay detectors are the existence of the 1.804 MeV threshold [29] on the antineutrino energy for

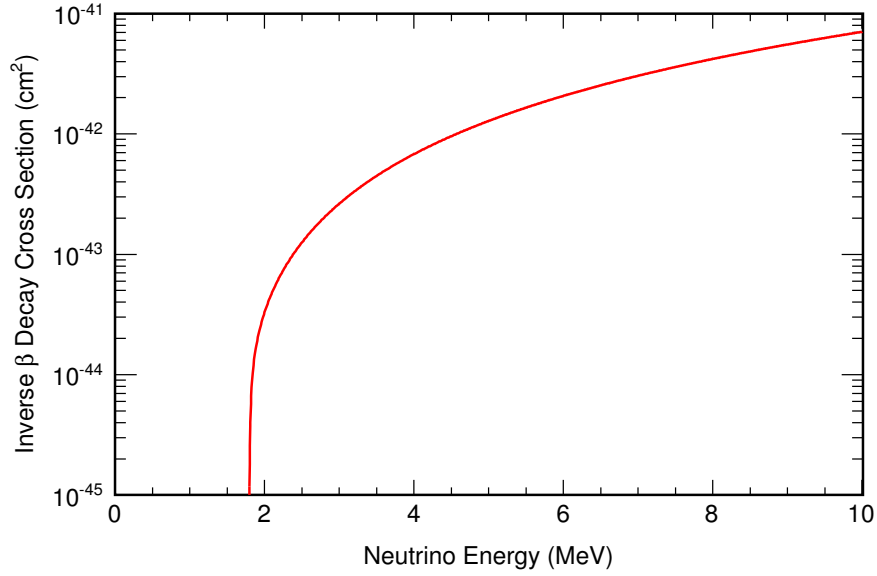


**Figure 1.5.** The cross section for the inverse  $\beta$ -decay interaction to occur with an incoming antineutrino of a given energy onto a hydrogen, calculated from [29]

the interaction to take place, Figure 1.5, and the sensitivity limited to electron flavor antineutrinos. An example inverse  $\beta$ -decay detector, the San Onofre Nuclear Generating Station (SONGS) detector, is shown in Figure 1.6. The SONGS detector is capable of measuring a change in reactor power based on the number of antineutrino interactions within hours of the power change, as shown in Figure 1.7. Over the course of the fuel cycle, the number of antineutrinos emitted from the nuclear reactor decreases as the isotopic composition changes, Figure 1.3. The SONGS detector has shown the ability to track the consumption of  $^{235}\text{U}$  and the production of  $^{239}\text{Pu}$  over the course of the fuel cycle, Figure 1.8.

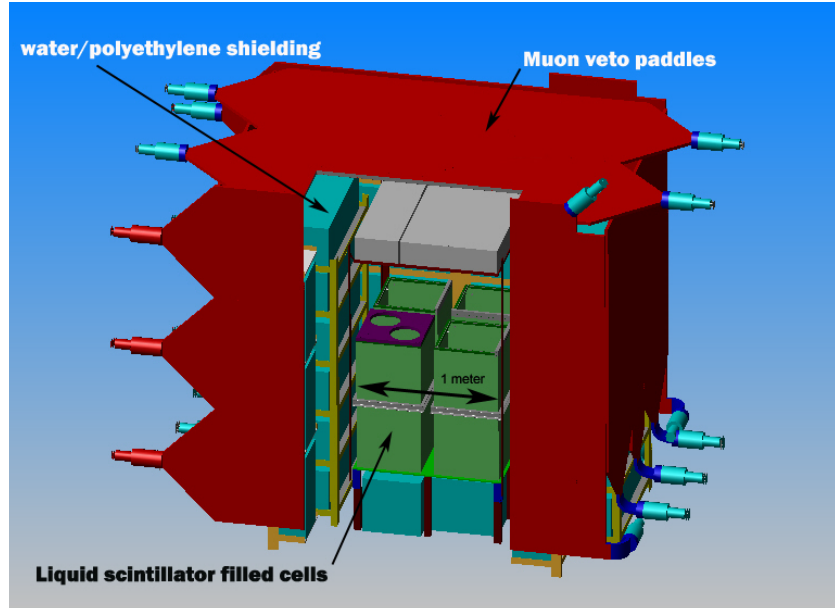


**Figure 1.6.** The current generation of antineutrino reactor monitoring detectors is based on inverse  $\beta$ -decay and utilizes liquid scintillator to detect the antineutrinos and monitor the nuclear reactor [8].

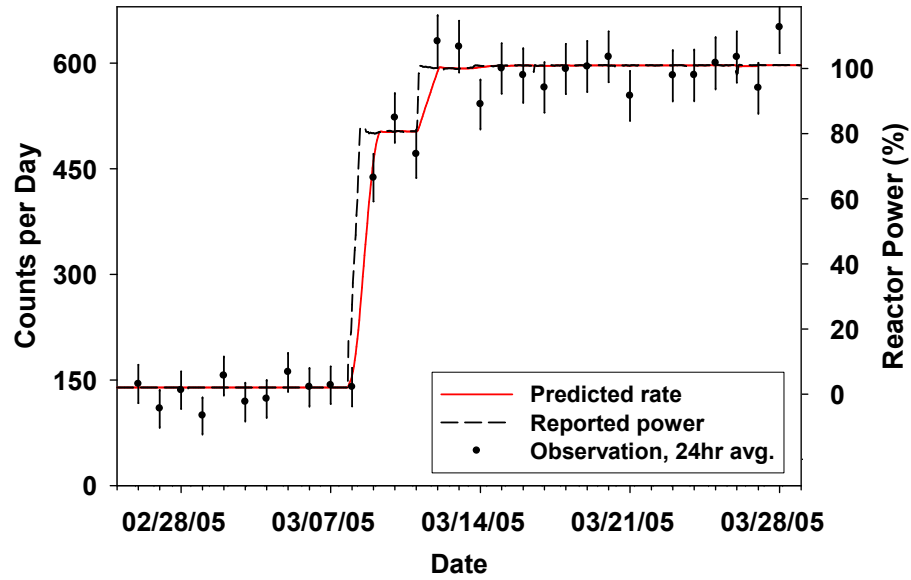


**Figure 1.7.** Since the number of antineutrinos emitted per fission of each isotope is known, the number of detected antineutrinos can be correlated to the total number of fissions within the nuclear reactor [9].

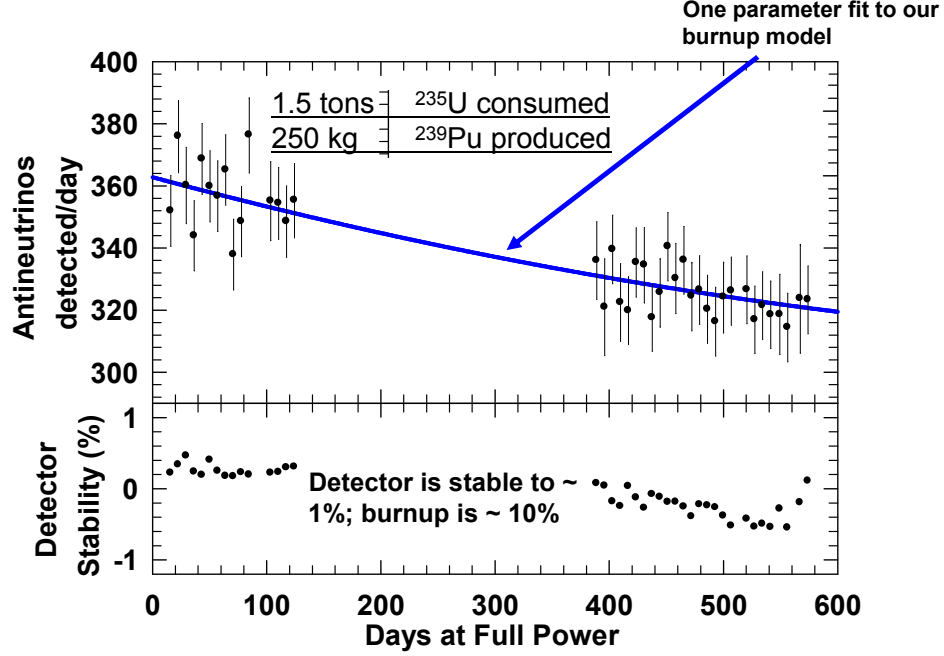


**Figure 1.8.** By correlating the number of detected antineutrinos over time with the expected output of each isotope, the relative isotopic fractions can be tracked with time [11].

## 1.4 Coherent Neutrino-Nucleus Scatter (CNNS)

Coherent neutrino-nucleus scatter (CNNS) is a flavor-blind interaction predicted by the Standard Model [30], which has yet to be observed. If a neutrino has a wavelength on the order of the size of the nucleus with which it interacts or greater, the neutrino can scatter coherently with the entire nucleus:[31]:

$$\lambda_{\bar{\nu}} \gtrsim R_{\text{nuc}} = 1.25A^{1/3} \text{ fm}, \quad (1.7)$$

where  $\lambda_{\bar{\nu}}$  is the wavelength of the neutrino,  $R_{\text{nuc}}$  is the radius of the nucleus, and  $A$  is the atomic mass number. Thus the criterion for CNNS to occur is that the energy of the neutrino be less than  $\sim 50$  MeV for typical detector candidate nuclei, such as Ar, Xe, Si, and Ge.

## 1.4.1 Physics of the CNNS Interaction

### 1.4.1.1 Weak Neutral Current

The Standard Model predicts a weak neutral current interaction between the neutrino ( $\nu$ ) and a nucleus for neutrinos of sufficiently low energy, Equation (1.7). From this prediction, elastic scattering between an antineutrino and a nucleus should occur. As discussed by Freedman in 1974 [30], the neutrino should also interact coherently.

From the electron-nucleus scattering calculations, it is shown that  $b = \frac{1}{6}R_{\text{nuc}}^2$  [30]. The differential cross section for the coherent neutrino-nucleus scatter (CNNS) interaction ( $\nu + A \rightarrow \nu + A$ ) is then given as

$$\frac{d\sigma}{dq_m^2} = \frac{G^2}{2\pi} a_0^2 A^2 e^{-2bq_m^2} \left( 1 - q_m^2 \frac{2ME_\nu + M^2}{4M^2 E_\nu^2} \right), \quad (1.8)$$

where  $E_\nu$  is the neutrino energy in the lab frame,  $q_m^2$  is the momentum transfer,  $M$  is the target mass, and  $G$  is the conventional Fermi constant defined as  $G = 1.01 \times 10^{-5} (M_{\text{proton}})^{-2}$ , where  $M_{\text{proton}}$  is the mass of the proton [30]. For the CNNS interaction, there is an intrinsic trade-off between the cross section and the observability of the recoil signals.

### 1.4.1.2 Cross Section

For low momentum transfer and lower neutrino energies (of order a few MeV), the nucleus is considered point-like and the differential cross section, Equation (1.8) can be rewritten in terms of  $\cos\theta$  [32] to obtain:

$$\frac{d\sigma}{d(\cos\theta)} = \frac{G^2}{8\pi} [Z(4\sin^2\theta_W - 1) - N]^2 E_\nu^2 (1 + \cos\theta), \quad (1.9)$$

where  $\theta$  is the neutrino scattering angle,  $Z$  is proton number of the target nucleus,  $N$  is the neutron number of the target nucleus, and  $\theta_W$  is the Weinberg weak-mixing angle with a value of  $\sin^2\theta_W = 0.23116$ . Since  $\sin^2\theta_W \approx 0.25$ , the cross section does not depend appreciably on  $Z$ . If the three-momentum transfer is defined as:

$$\Delta^2 = 2E_\nu^2(1 - \cos\theta), \quad (1.10)$$



then the differential cross section, Equation (1.9) can be expressed as

$$\frac{d\sigma}{d\Delta^2} = \frac{G^2}{8\pi} [Z(4\sin^2\theta_W - 1) - N]^2 \left[ 1 - \frac{\Delta^2}{\Delta_{\max}^2} \right], \quad (1.11)$$

where  $\Delta_{\max}^2$  is the maximum momentum transfer. The total cross section for interaction is calculated by integrating over  $\Delta$  to obtain

$$\sigma = \frac{G^2}{16\pi} [Z(4\sin^2\theta_W - 1) - N]^2 \Delta_{\max}^2. \quad (1.12)$$

With a maximum momentum transfer of  $4E^2$ , the total cross section becomes

$$\sigma = \frac{G^2 [Z(4\sin^2\theta_W - 1) - N]^2}{4\pi} E_\nu^2. \quad (1.13)$$

Under the assumption of zero proton number dependence, the cross section can be approximated as

$$\sigma \sim 0.4 \times 10^{-44} N^2 \left( \frac{E_\nu}{\text{MeV}} \right)^2 \text{ cm}^2. \quad (1.14)$$

#### 1.4.1.3 Recoil Energy

The recoil energy for a given CNNS interaction is given by

$$E_r = \frac{\Delta^2}{2MA} [32], \quad (1.15)$$

where  $M$  is the nucleon mass and  $A$  is the atomic mass number. By convolving the differential cross section, Equation (1.11), with the recoil energy per scattering angle, Equation (1.15), the average recoil energy for a target material is calculated to be

$$\langle E_r \rangle = \frac{1}{3} \frac{\Delta_{\max}^2}{2MA}. \quad (1.16)$$

Substituting  $\Delta_{\max}^2$  gives the recoil energy of

$$\langle E_r \rangle = \frac{2}{3} \left[ \frac{\left( \frac{E}{\text{MeV}} \right)^2}{A} \right] \text{ keV} [32]. \quad (1.17)$$

### 1.4.2 CNNS Detection Challenges

While CNNS results in a  $> 100\times$  increase in cross section over inverse  $\beta$  decay, detection of the very low recoil energy ( $< \sim 10$  keV) is a significant obstacle that must be overcome to detect CNNS [33, 34, 35]. In addition to this low recoil energy, nuclear recoils result in a reduced ionization signal compared to that produced by electron recoils of equal energy. This phenomenon is termed nuclear ionization quenching [36, 37], and the ratio of ionization from a nuclear recoil to an electronic recoil is referred to as the *nuclear ionization quench factor* [38, 39, 40, 41, 42]:

$$q_{\text{ion}}(E) = \frac{N_{\text{ion}}^{\text{nuc}}(E)}{N_{\text{ion}}^{\text{elc}}(E)}, \quad (1.18)$$

where  $N_{\text{ion}}^{\text{nuc}}$  is the number of ionizations that occur in a nuclear recoil of a given energy and  $N_{\text{ion}}^{\text{elc}}$  is the number of ionizations that occur in an electron recoil of equal energy. The quantity of primary interest is the number of electrons detected per nuclear collision producing a recoil of a given energy (typically measured in units of keVr) - a quantity termed the *ionization yield*. A prerequisite for detection of CNNS is the measurement of the nuclear ionization quench factor in the chosen medium at typical expected CNNS-induced nuclear recoil energies.

### 1.4.3 CNNS Detector Candidates

Four primary candidates for the detection of CNNS via nuclear recoil have been identified [18, 33, 34, 35]. Two of those candidates are based on previously developed Dark Matter detectors, which utilize a noble liquid target region and a noble gas as the amplification region [18, 34, 35]. These detectors are referred to as dual-phase noble element detectors. A third candidate for detecting CNNS is a HPGe detector used both as the interaction medium and the detection medium [33, 39]. Other candidates for the detection of CNNS are Si or Ge detectors based on phonon detection, an example of which is the Cryogenic Dark Matter Search (CDMS) detector. In order to assist with the selection of the technology for CNNS detection, the predicted interaction rates and average recoil energies for three ionization-based detector media are shown in Figure 1.9.

The CDMS detector in phonon detection mode operates as a transition edge

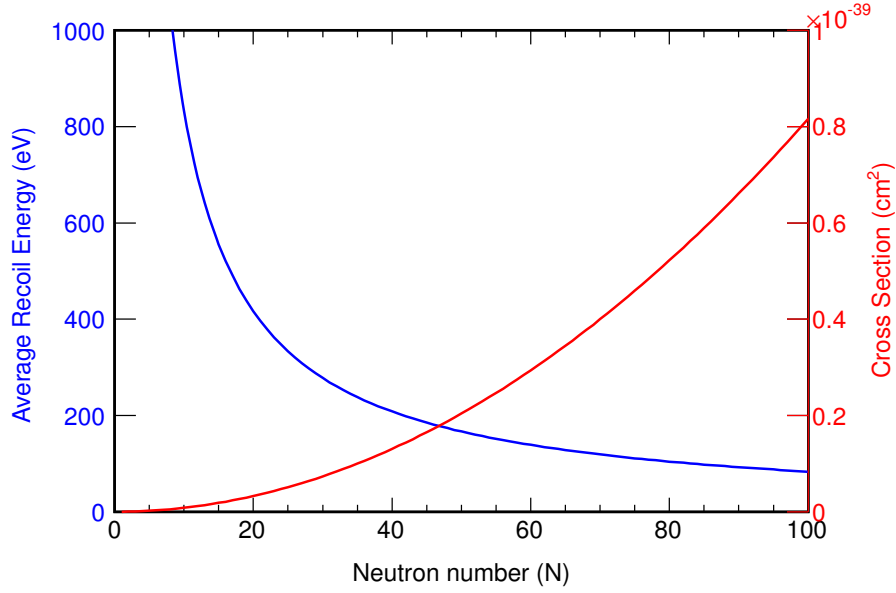


**Figure 1.9.** The cross section for CNNS (red) scales with the square of the number of neutrons, while the average recoil energy (blue) scales inversely with the atomic mass number of the target nucleus. Selection of the detection medium requires that this trade-off be made. Values shown here assume that the proton number  $Z$  is equal to the neutron number  $N$ , and that the neutrino energy is 5 MeV.

sensor (TES), in which the resistance of a superconductor exhibits a sharp increase based on the amount of heat deposited into the crystal. CDMS utilizes Ge crystals with a total mass of  $\sim 1$  kg and an additional  $\sim 500$  g Si detector mass. Based on the demonstrated performance of CDMS, it is predicted that the current CDMS detectors could observe CNNS at a nuclear reactor, with an expected Ge detection threshold of  $\sim 40$  eVr [43, 44]. However, to do so would require a dedicated experiment and significant resources to move the experimental setup near a nuclear reactor, where the backgrounds for this type of detector have not been previously measured. Additionally, due to the nature of the CDMS detector design, the detector volume is limited and not easily scalable.

Solid state ionization detectors are attractive candidates for detecting CNNS due to the ease of operation, good energy resolution, and sensitivity to low energy signals. One potential detector is the Ultra-Low Germanium Neutrino detection system (ULGeN), a collaboration between Sandia National Lab, Lawrence Berkeley National Lab, and UC Berkeley. The ULGeN detector is a point-contact BEGe

**Table 1.2.** Predicted CNNS event rates per kg of Ge per day for a Ge detector placed 25 m from a 3 GWth core with the specified detection thresholds.

Energy Threshold (eV)	Events Rate (counts $\cdot$ kg $^{-1}$ $\cdot$ day $^{-1}$ )
300	$\sim 0.08$
200	$\sim 0.60$
100	$\sim 5.01$

detector made by Canberra, Inc., with a detector mass up to  $\sim 1$  kg [45]. Electronic noise full width half max (FWHM) of  $\sim 150$  eV has been measured in this detector, and the predicted FWHM required for CNNS detection is  $\sim 100$  eV. The electronic noise results from the capacitance effects within the detector and in the electronics used to read out the detector. Setting the detector threshold to approximately three times the electronic noise threshold, the threshold energy of  $\sim 350$ -450 eV can be detected [45, 46]. Table 1.2 shows the predicted event rates for various detector thresholds, given for a detector placed 25 meters from a reactor core [45].

The Coherent Neutrino Nuclear Interaction Experiment (CONNIE) is a Si ionization detector which utilizes thick charge-coupled devices (CCDs) as the target material and records the ionization produced within each CCD [47]. Each CCD is 250  $\mu$ m thick, with a detector mass of  $\sim 1$  g per CCD. An energy threshold of 40 eV electron equivalent (eVee) has been reported, which corresponds to  $\sim 350$  eVr. A total detector mass of 10 g is currently being deployed at a nuclear power plant in Angra, Brazil, with an expected event rate of  $\sim 0.3$   $\nu$  events per day [47]. The background rate has not been measured yet, so it is unclear what signal-to-background ratios will be ultimately achievable.

With a neutron number of  $\sim 80$ , xenon provides an increase in cross section of  $\sim 1500$  over inverse  $\beta$  decay. However, the average recoil energy from CNNS on xenon is only 70 eV. LXe detectors have demonstrated the ability to detect single ionization electrons, which suggests their ability to also detect CNNS. With the ability to detect single ionization electrons, the single electron background becomes a dominant background for CNNS and must be minimized in an effort to keep a high signal-to-noise ratio. The Russian Emission Detector (RED) [48], a proposed dual-phase Xe detector, would involve deploying a large 100 kg detector near a reactor. The single electron background rate measured in this sort of small

prototype detector has been  $\sim 100$  Hz. The expected CNNS rates with a 2 electron threshold for detection are  $\sim 400$  events per 100 kg Xe per day [49]. One issue encountered by the RED project is the limited Xe purity, which results in ionization electrons capture on electro negative impurities and a relatively short electron lifetime of  $\sim 2$   $\mu$ s.

Due to the large number of antineutrinos emitted by a nuclear reactor [25, 50], selection of the medium with the highest cross section is not imperative for detection of CNNS. In argon the cross section for CNNS [32] is  $\sim 100\times$  that of inverse  $\beta$  decay on hydrogen [29], Figure 1.10. Thus the interaction rate is predicted to be significantly higher than in the current antineutrino monitoring detectors. Also, Ar produces a higher recoil energy than Ge and Xe, resulting in an increase in *observable* event rate [34]. For this project, dual-phase noble element detectors were also chosen for their comparative advantage of easy scalability to large volumes compared to Ge or Si detectors. The operation of a 10-100 kg detector should be nearly identical to that of a 1 kg detector. In summary, Ar was selected for this study instead of Xe due to the potentially greater ionization signal than that produced in Xe and due to its lower cost. Additionally, it is expected that the single electron background will be lower in Ar than in Xe as a result of the electron varying work functions at the liquid-gas interface [51].

With Ar chosen as the detector medium, the expected recoil spectra must be calculated based on the incident antineutrino spectra shown in Figure 1.2. For this calculation to be carried out, the incident antineutrino spectra are used in Equation (1.9) to calculate the interaction rate and Equation (1.15) to calculate the recoil energies. This results in the recoil spectra for natural Ar shown in Figure 1.11, in which the shoulder is due to the presence of  $^{36}\text{Ar}$  in natural Ar (the majority of the Ar being  $^{40}\text{Ar}$ ).

Given that these recoil energies are so small,  $< 6$  keV [34, 35], it is vital that the ionization yield be known at the energies of a few keV. Predicting and measuring this ionization yield in LAr is the focus of this dissertation.

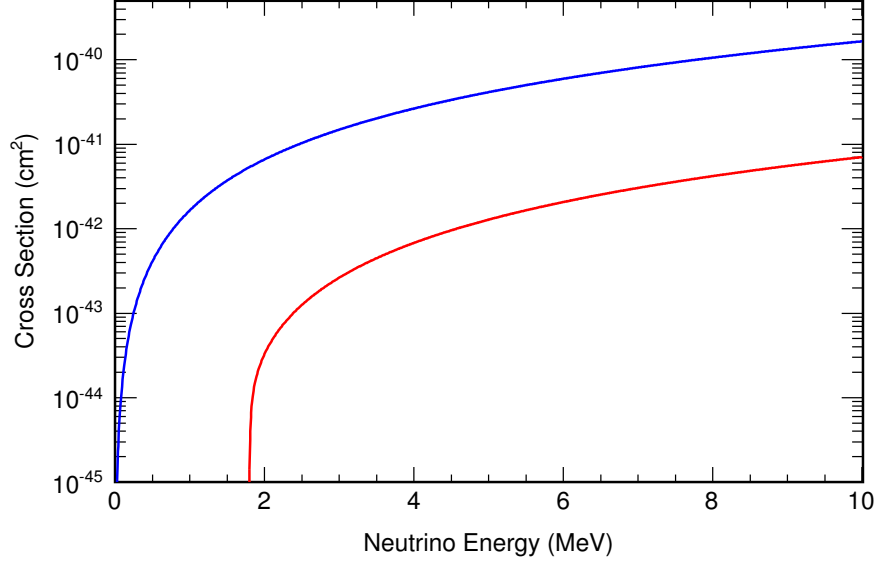


**Figure 1.10.** The cross section for an antineutrino interacting by CNNS on argon (blue) is  $\sim 100\times$  that of an antineutrino undergoing inverse  $\beta$  decay on hydrogen (red).

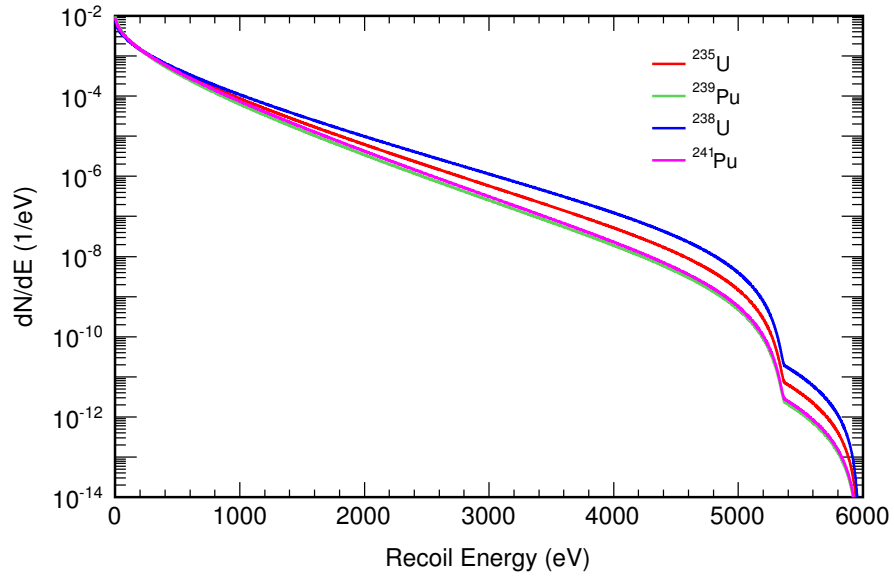


**Figure 1.11.** Calculated nuclear recoil energy for antineutrinos emitted from a nuclear reactor. The peak at  $\sim 5$  keV is due to the small fraction of  $^{36}\text{Ar}$ .

**Table 1.3.** The triplet decay time is much longer than that of the singlet state in both Xe and Ar. If a quench particle is present, it decreases the amount of scintillation light produced, but also greatly decreases the decay time constant. The triplet state is referred to as the slow component of the scintillation light, while the singlet state is the fast component.

	Singlet (ns)	Triplet (ns)	Reference
LXe	$2.2 \pm 0.3$	$27 \pm 1$	[67]
GXe	$5.5 \pm 1.0$	$96 \pm 5$	[68]
LAr	$6 \pm 2$	$1590 \pm 100$	[64]
GAr	$4.2 \pm 0.13$	$3200 \pm 300$	[68]

## 1.5 Noble Element Detector Introduction

Dual-phase noble element detectors are extensively used in the search for Dark Matter [52, 53, 54, 55, 56, 57], and therefore are of great interest in the quest to detect CNNS [34, 35]. The reason for their extensive use is the scalability, high sensitivity [58, 59], electron drift properties [60, 61], and relatively low cost of a dual-phase xenon (Xe) or argon (Ar) detector. The principle of operation for a dual-phase noble element detector, Figure 1.12, can be summarized as follows. The incoming neutral particle interacts with the liquid phase detector component, creating ionization and primary scintillation (S1) light. The scintillation is detected by photomultiplier tubes (PMTs), and the ionization electrons drift toward the gas phase. Once in the gas phase, the electrons are accelerated, resulting in excited Ar or Xe atoms which then emit electroluminescence or proportional scintillation (S2) light. The S2 scintillation light is detected by the PMTs and because it is directly proportional to the number of electrons created, it gives the energy deposited within the detector.

During the process of electroluminescence, there are two different excitation states populated, the singlet and the triplet [62]. The importance of the two populated states is that each state has a different characteristic decay time for the scintillation process. The characteristic decay times depend on whether the process occurs in the liquid or gas phase [63, 64], as well as if there are any process quenching atoms present [65, 66]. A summary of these different decay times is shown in Table 1.3.

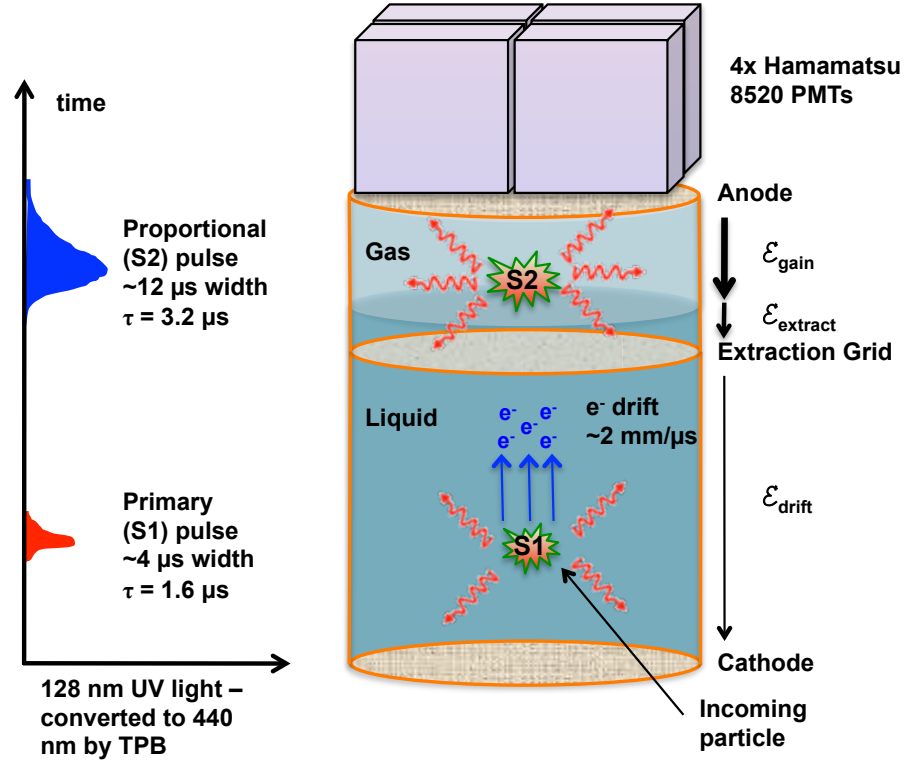


**Figure 1.12.** As the particle interacts within the liquid region, it produces primary scintillation (S1) light and ionization. The resulting ionization is then drifted to the gaseous amplification region where electroluminescence occurs and the secondary proportional scintillation (S2) light is detected by the PMTs, thereby providing an energy deposition within the detector.

An important property of the scintillation light produced is the wavelength at which the light is emitted. The scintillation light in Xe is produced at a wavelength of 178 nm [62], while in Ar it is produced at 128 nm [62]. This means that it is possible for the Xe scintillation light to be detected directly by the PMTs [69, 70], while the Ar scintillation light must be shifted to a higher wavelength for detection [71].

### 1.5.1 Wavelength Shifting of Argon Scintillation Light

There are two standard methods for wavelength shifting of the scintillation light from Ar. The first method consists of adding a dopant to the argon in order to quench the scintillation process and emit a different wavelength scintillation light [65]. The primary dopant used is nitrogen ( $\text{N}_2$ ) [66, 72], Section 1.5.1.1. While



other dopants such as Xe can be used in single phase systems [73], Xe does not work in a dual-phase system, Section 1.5.3. The second method consists of absorption and re-emission of a different wavelength photon, which can then be detected by the PMTs. There are a variety of different organics usable as a wavelength shifting film [74, 75, 76], but the one commonly used is tetraphenyl butadiene (TPB) [77, 78, 79, 80], Section 1.5.1.2.

#### 1.5.1.1 Nitrogen Doping

For the process of wavelength shifting with nitrogen, a small fraction of  $N_2$ ,  $\sim 1 - 2\%$ , is added to the Ar. A portion of the energy of the excited Ar atoms is transferred to the  $N_2$  molecules, resulting in an excited  $N_2$  molecule:



where  $Ar^m$  is metastable Ar and  $N_2^*$  is an excited nitrogen molecule. The  $N_2^*$  subsequently emits scintillation light with a peak wavelength of 337 nm [72], as shown in Figure 1.13.

In order to utilize nitrogen as a wavelength shifter in a dual-phase Ar detector, the vapor pressures need to be balanced. This helps determine the total amount of nitrogen to be added for 1.5% of the gas to be  $N_2$ . To find the amount of nitrogen that needs to be added to 100 kg of argon in the dual phase detector Raoult's Law [81] is used:

$$y_i P = x_i P_i^o, \quad (1.20)$$

where  $y_i$  is the fraction of the gas which is element  $i$ ,  $P$  is the total pressure,  $x_i$  is the fraction of the liquid which is element  $i$ , and  $P_i^o$  is the vapor pressure of element  $i$ . The calculation starts by specifying the operating temperature, which is assumed to be  $T_{\text{Dual}} = 87$  K. Since the desired gas fraction of  $N_2$  is 1.5% for wavelength shifting,  $y_{N_2} = 0.01$  and  $y_{Ar} = 0.985$ .

The vapor pressures of both argon and nitrogen at this temperature can be calculated using Antoine's Equation:

$$P_i^o = \text{Exp} \left[ A - \left( \frac{B}{T + C} \right) \right] \quad (1.21)$$

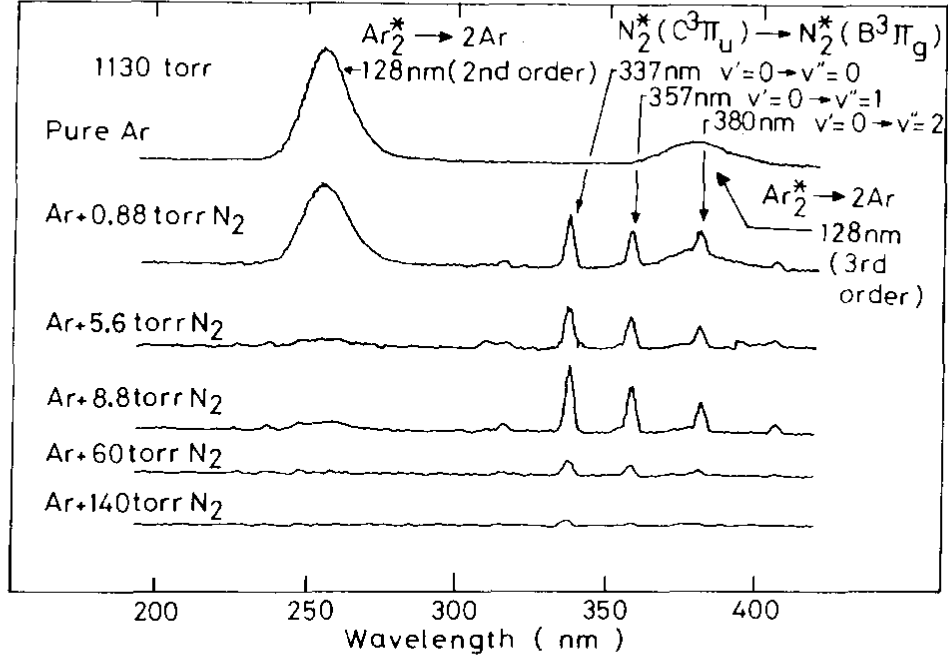


**Figure 1.13.** As the  $N_2$  is added to the Ar, it shifts the emission spectra from 128 nm up to 337 nm, while losing a fraction of the deposited energy [65].

**Table 1.4.** Antoine's Equation parameters given for Ar,  $N_2$  and Xe, with the data taken from [82], where it is interpolated from the paper given.

	A	B [K]	C [K]	Reference
Ar	3.29555	215.240	-22.233	[83]
$N_2$	3.63792	257.887	-6.344	[84]
Xe	3.80675	577.661	-13.0	[85]

where  $P_i^o$  is the vapor pressure of component  $i$  given in bar,  $T$  is the operational temperature, and  $A$ ,  $B$ , and  $C$  are element specific parameters. Antoine's Equations parameters for argon, nitrogen and xenon are given in Table 1.4.

Plugging the constants from Table 1.4 into Equation (1.21), the vapor pressures for argon and nitrogen are calculated to be 0.973 and 1.554 bar, respectively.

Using Raoult's Law, Equation (1.20), for both argon and nitrogen, along with the sum of the liquid mole fractions having to be equal to one, the mole fractions and total pressure are solved for. For 1.5% of  $N_2$  in the gas phase of Ar, the liquid will consist of 0.94%  $N_2$  and 99.06% Ar, and the total pressure of the system will

be 0.978 bar.

To calculate the amount of nitrogen needed to produce a mole fraction of 1.5% in the gas phase, assume that all of the argon and nitrogen is in the liquid phase. This is a good assumption because of the larger liquid volume along with the increased density in the liquid phase. Taking into account the atomic weight of both nitrogen and argon, the mass of the nitrogen needed for 100 kg of Ar is calculated with:

$$m_{\text{N}_2} = 100 \left( \frac{M_{\text{N}_2}}{M_{\text{Ar}}} \right) \left( \frac{x_{\text{N}_2}}{x_{\text{Ar}}} \right), \quad (1.22)$$

where  $m_{\text{N}_2}$  is the required mass of nitrogen in kg,  $M_{\text{N}_2}$  is the atomic mass of nitrogen,  $M_{\text{Ar}}$  is the atomic mass of argon,  $x_{\text{N}_2}$  is the liquid fraction of nitrogen, and  $x_{\text{Ar}}$  is the liquid fraction of Ar. The required nitrogen mass is calculated to be 640.8 g per 100 kg of Ar.

It could be useful to simulate similar conditions with a single-phase detector to study the wavelength shifting efficiency. To do tests at room temperature, the pressures should be increased using the ideal gas law, to 2.884 bar of Ar and 0.044 bar of  $\text{N}_2$ .

#### 1.5.1.2 Tetraphenyl butadiene (TPB) Coatings

While it is possible to use nitrogen as a wavelength shifter in dual-phase Ar detectors, it is more common to use TPB. TPB is an organic chemical which absorbs the VUV (very ultra-violet) light from the Ar, and reemits the light at a higher wavelength. TPB has two benefits over the use of nitrogen. With a TPB coating, the wavelength shifter does not have to be re-calibrated and injected with each detector run, and TPB is easily combined with light reflectors for  $\sim 4\pi$  light collection [79]. The emission spectrum of the light converted using TPB is shown in Figure 1.14. It has a peak at  $\sim 440$  nm, which is efficiently reflected with materials such as teflon. By coating reflectors with TPB, the light that is emitted in directions other than towards the PMTs can be collected after it is wavelength shifted and reflected back towards the PMTs, increasing the geometric efficiency. This method provides a higher light collection efficiency than using a dopant and reflectors by  $\sim 2\times$ [76].

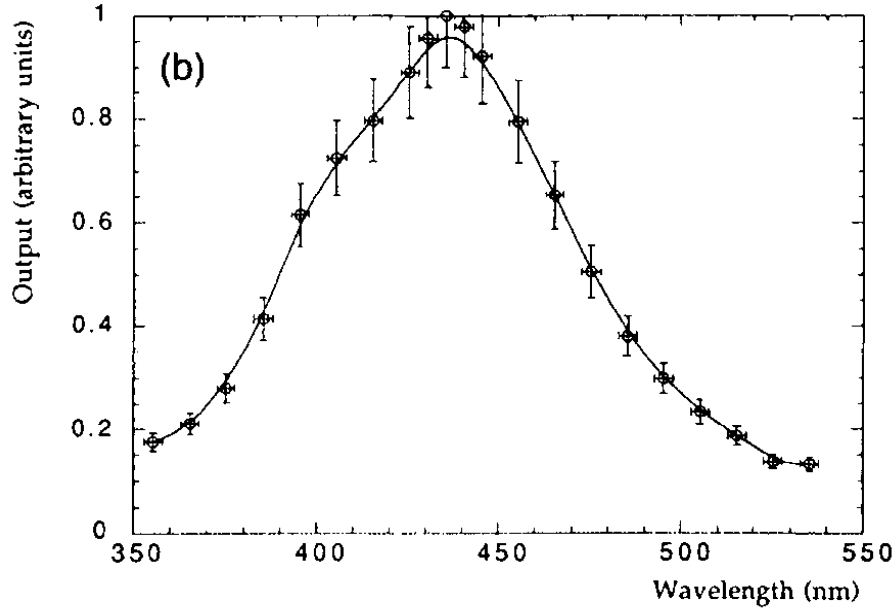


**Figure 1.14.** The 128 nm scintillation light from the Ar is absorbed by the TPB molecules and subsequently emitted at a higher wavelength, centered  $\sim 440$  nm [74].

### 1.5.2 Xenon Doping for Wavelength Shifting

Xe works for wavelength shifting in a single-phase system [73], such as a gaseous argon detector, Figure 1.15. Xenon works in a similar manner as the nitrogen doping, but it wavelength shifts the light up to 180 nm instead of 337 nm [65]. Xe doping for wavelength shifting does not work in a two-phase system due to the large difference in vapor pressures.

Using the same techniques used in Section 1.5.1.1 to calculate the nitrogen content in a dual-phase Ar detector, the Xe fraction is calculated. In this instance, instead of specifying the operating temperature, the operating pressure is specified to be 1 atm (1.01325 bar). As with the nitrogen, a 1.5% mole fraction in the gas of Xe is desired. Using Antoine's Equation, Equation (1.21) and Raoult's Law, Equation (1.20), the mole fractions in the liquid are calculated to be 33.74% Xe and 66.26% Ar, with an operating temperature of 96.5 K. The mass of Xe required to produce 1.5% in the gas phase as a wavelength shifter is 167.14 kg of Xe per 100 kg of Ar.

Two important points stand out from this calculation: the temperature at 96

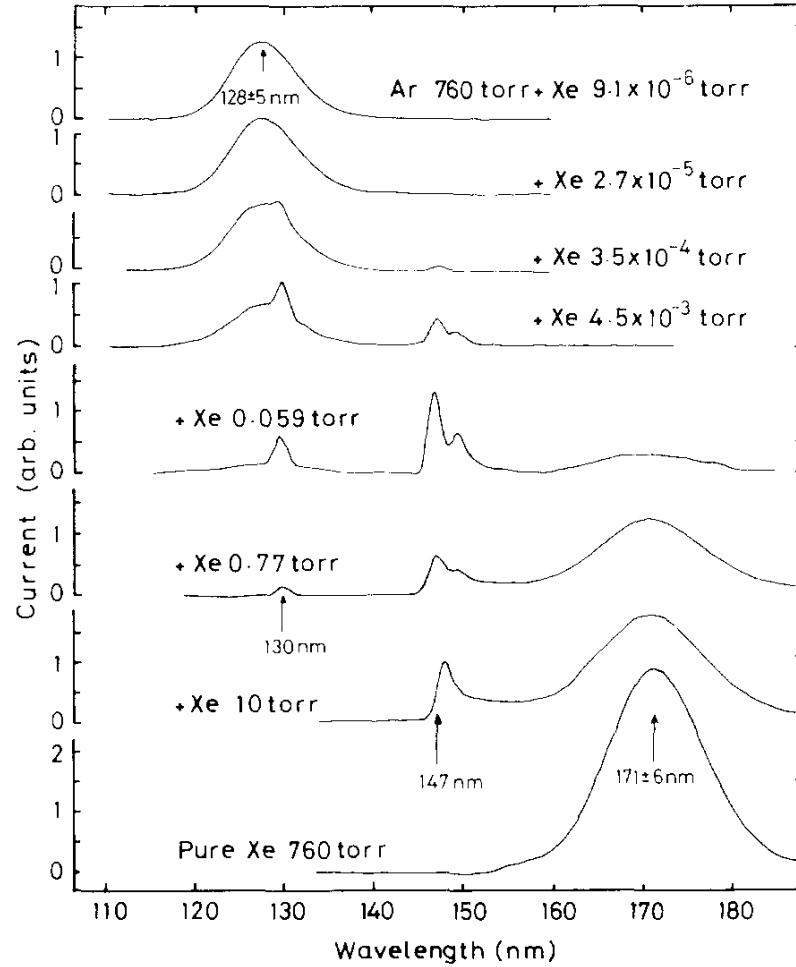


**Figure 1.15.** As the Xe is added to the Ar, it shifts the emission spectra from 128 nm up to 180 nm, while losing some of the energy deposited [65].

K is outside the limit of having Ar as a liquid given a pressure of 1 atm, and the detector has more Xe mass than it does Ar. It can thus be concluded that this would be a Xe based detector, with Ar dissolved in the liquid phase instead of an Ar based detector. Therefore, wavelength shifting with Xe is not a feasible option.

### 1.5.3 Penning Mechanism in Liquid Argon

By doping the Ar with an atom that has a lower ionization potential, in this case Xe, a given fraction of the excited Ar atoms interact with the Xe atoms, subsequently ionizing the Xe atom and increasing the ionization signal within the

detector:



where  $Ar^*$  is excited argon, and  $Xe^+$  is ionized xenon. The reason for the effectiveness of this process is that the excitation energy for Ar is 12 eV, while the ionization energy for Xe is 10.6 eV, compared to 14.3 eV for Ar [86]. With the excitation energy of Ar above the ionization energy of Xe, an excited Ar is able to ionize a neutral Xe atom and generate an electron instead of a photon through the process.

For an electronic recoil, there are 0.19 excitons per electron-ion pair created [87]. When the pure Ar is doped with 1.6% Xe, a relative increase in ionization yield of 13% is observed [87], with a maximum increase of 19% based on the number of excitons created. Calculating the probability for the Penning effect to occur can be done using:

$$p_{\text{Penning}} = \frac{1.44f_{\text{Xe}}}{1 + 1.44f_{\text{Xe}}} \quad (1.24)$$

where  $f_{\text{Xe}}$  is the fraction of Xe within the Ar liquid in percent. For 1.6% Xe the Penning probability is calculated to be  $\sim 70\%$ , for an increase in ionization yield of 14.5% which is within the error of the measured value.

For 1% Xe in the liquid phase and a total pressure of 1 atm, the gas phase is calculated to be 0.02% Xe with an operating temperature of 87.7 K. Thus for the Penning mechanism, all of the Xe added is contained within the LAr, requiring 3.32 kg of Xe per 100 kg of Ar.

#### 1.5.4 Electron-Nuclear Recoil Discrimination

With the observation of signals within a dual-phase noble element detector, it becomes important to distinguish between electron and nuclear recoils. To discriminate between electron and nuclear recoils, one can consider:

- Ratio of singlet and triplet populations [64, 67]
- Ratio of S1 to S2 light [52, 53, 54, 57, 88, 89, 90, 91]

**Table 1.5.** The ratio light emitted from the singlet and triplet states is very different for an electronic and nuclear recoil and is used to discriminate different events [64].

Particle	$\tau_{\text{fast}}(ns)$ (Singlet)	$\tau_{\text{slow}}(ns)$ (Triplet)	$I_{\text{fast}}/I_{\text{slow}}$
Electron	$6 \pm 2.0$	$1590 \pm 100$	0.3
Alpha	$7.1 \pm 1.0$	$1660 \pm 100$	1.3
Fission Fragment	$6.8 \pm 1.0$	$1550 \pm 100$	3

#### 1.5.4.1 Singlet-Triplet Population Ratios

As can be concluded by inspecting the S1 pulse, some of the light is emitted promptly from the singlet state, while some is emitted with a longer time constant from the triplet state. The fraction of light emitted with each time constant depends strongly on the ionization density, and is a powerful method that allows discrimination between electronic and nuclear recoils. The ratios of fast to slow light component intensity for different ionization densities are summarized in Table 1.5.

#### 1.5.4.2 S2/S1 Ratios

Another difference that arises from the difference in ionization density is the ratio of S1 to S2 light. This ratio can be used to help distinguish whether a recoil was a nuclear or electronic recoil. For the higher ionization densities of nuclear recoils, electron recombination within the initial ion cloud is higher. When the electron and ion recombine, the atom is in an excited state emitting a scintillation photon. Due to this fact, as the electron-ion recombination increases, the S1 signal increases, and the S2 signal decreases. Example  $\gamma$ -ray and neutron events are shown in Figure 1.16 and Figure 1.17, respectively. The ratio of S2/S1 light is approximately 210 for electronic recoils and 70 for nuclear recoils [88].

Distinguishing an electron recoil from a nuclear recoil becomes more difficult due to the nuclear ionization quenching [36, 37]. Nuclear recoils result in less observable signal than an electronic recoil of equal energy.

A detailed description of the ionization yield simulation used to predict the expected ionization yields and CNNS signals is given in Chapter 2. Chapter 3 provides a description of the single-phase Ar detector used to study the amplification

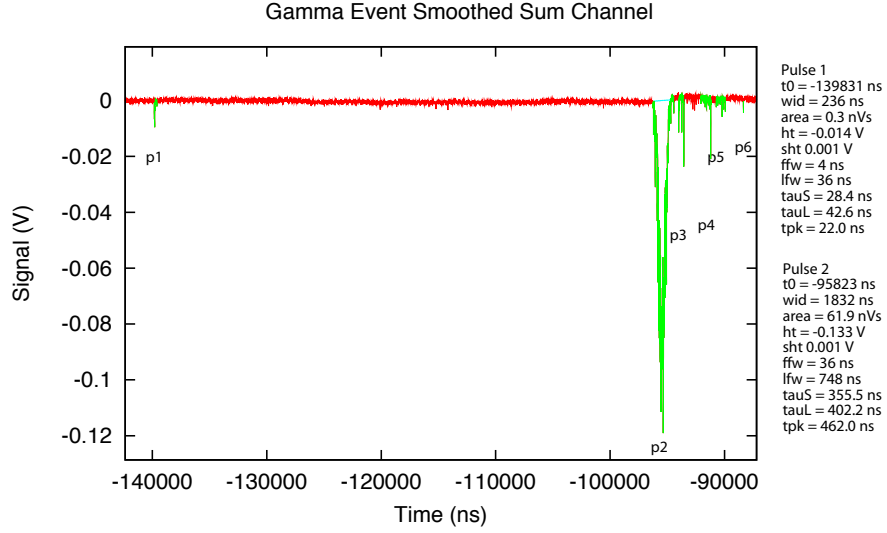


**Figure 1.16.** Interaction of a  $\gamma$ -ray with the LAr creates the initial S1 pulse, and the ionization electrons are then drifted to the gas phase to create an S2 pulse. The S2/S1 ratio is  $\sim 210$  for an electronic recoil [54, 88].

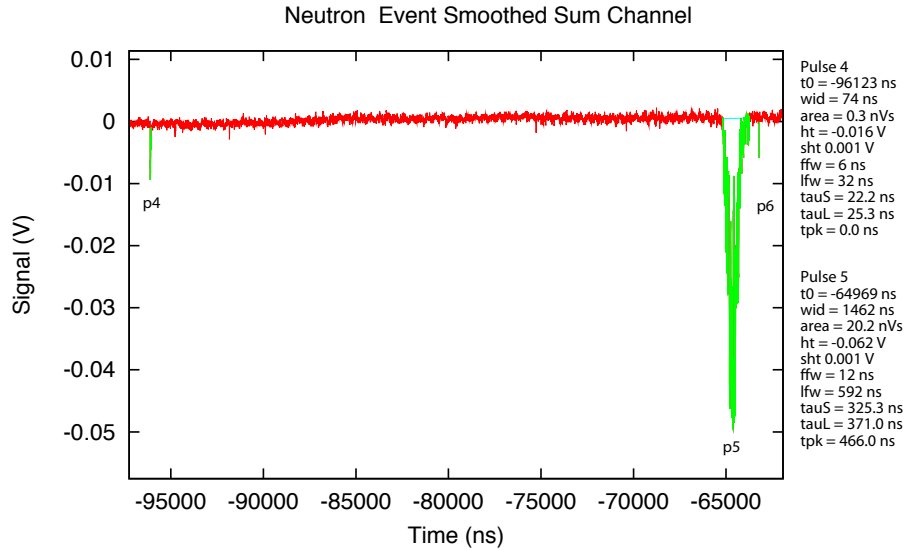


**Figure 1.17.** Interaction of a neutron with the LAr creates the initial S1 pulse, and the ionization electrons are then drifted to the gas phase to create an S2 pulse. The S2/S1 ratio is  $\sim 70$  for a nuclear recoil [54, 88].



of the electron signals through electroluminescence. The first ever measurement of the nuclear ionization quench factor with the gaseous Ar detector using elastic neutron scatter is presented in Chapter 4. The progress in the development of a dual-phase Ar detector is presented in Chapter 5, including the state-of-the-art results obtained with this detector. Chapter 6 includes a validation of the electron transport code used in predicting the ionization yield by comparison with the electron recoil experimental data. The experimental setup for measuring the ionization yield using a dual-phase Ar detector is described in Chapter 7. Finally, the predictions for detection of the CNNS interaction with an Ar detector at a nuclear reactor and the expected backgrounds are provided in Chapter 8.

# Monte Carlo Simulation of Ionization Yield

## 2.1 Ionization Yield

Interaction of neutrons or neutrinos with matter proceeds through different mechanisms than that of electromagnetic radiation, Figure 2.1. Electromagnetic radiation interacts primarily with atomic electrons and produces *electron recoils* (for example, in Compton scattering), while neutrons interact with the atomic nucleus or individual nucleons. Interactions with the nucleus can produce *nuclear recoils*. In both the electron and nuclear recoils, the resulting charged particle loses its energy in the target volume via Coulomb collisions (and bremsstrahlung, which is significant only for high-energy electron recoils). Coulomb collisions can induce ionization (electron emission) and excitation (photon emission) of the atoms present in the target volume, and can also produce delta-electrons. In the excitation of an atom, the potential energy of a shell electron is increased resulting in an excited state of the atom. The atom subsequently relaxes into a ground state giving off the excess potential energy in the form of a photon.

While both electron and nuclear recoils deposit their energy by Coulomb collisions, the partition of energy deposited to electrons (ionization), photons (excitation), and phonons is different for those two types of recoils. This partition also

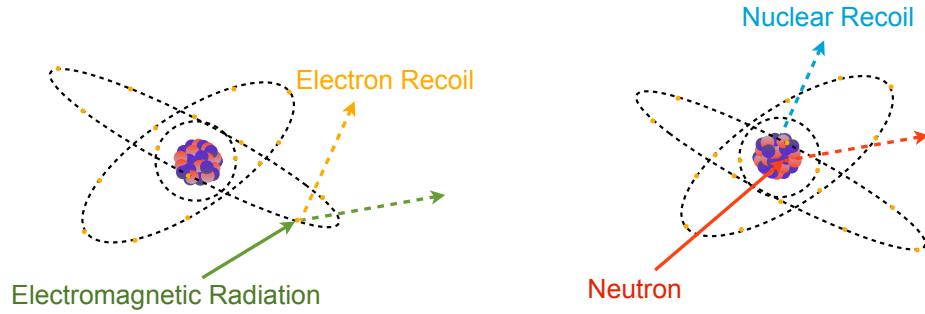


**Figure 2.1.** Electromagnetic radiation primarily interacts with atomic electrons resulting in an electron recoil. Neutrons and neutrinos interact with the nucleus, resulting in a nuclear recoil.

depends on the target medium and the energy of the recoiling electron or nucleus, and is ideally experimentally measured. Dual-phase argon detectors can be instrumented to measure both the primary scintillation photons or the secondary scintillation, which is proportional to the number of ionization electrons produced. Because the detection sensitivity is significantly greater for electrons, the quantity of central interest is the ionization yield,  $Q_y$ , or the number of electrons,  $N_{e-}$ , generated per keV of recoil energy,  $keVr$ ,

$$Q_y = \frac{N_{e-}(E)}{E(keVr)}. \quad (2.1)$$

Unfortunately, it is not always feasible or practical to experimentally measure the ionization yield for a given energy deposition. In liquid argon, for example, no measurements of the ionization yield below 25 keVr have been reported, and very few measurements have been made above this energy [92]. For this reason, theoretical models have been constructed to predict the amount of energy deposited to electrons, which are specific for a given detector medium and for a characteristic recoil energy. The remainder of this Chapter discusses the methods for calculating the ionization yield. Section 2.3 and Section 2.4 present a discussion of the two-stage model that has been developed from first principles to predict the ionization yield and local electron recombination for low-energy nuclear recoils.

## 2.2 Current Ionization Yield Models

While there are models available to predict the ionization yield from nuclear recoils, there are various deficiencies which require one to use caution when utilizing the models. In this Section, the prominent models currently used to predict the ionization yield in noble element detectors and their shortcomings are described.

The Lindhard theory [36] was developed in 1963 to calculate the energy deposited to electrons and that given to atoms. In the Lindhard theory, the energy given to electrons through both by ionization and excitation is represented by the symbol  $\eta$ . The energy given to atomic motion is represented by symbol  $\zeta$  and  $\eta + \zeta = E$ . From the detection perspective,  $\eta$  is the energy available for producing electrons and photons, while  $\zeta$  is the initial energy available for phonon production.

In cases where the target medium is the same as that of the recoiling atom, the fraction of energy transferred through atomic motion is given as

$$\bar{\zeta} = \frac{\varepsilon}{1 + kg(\varepsilon)}, \quad (2.2)$$

where  $k = 0.133Z^{2/3}A^{-1/2}$ ,  $Z$  being the atomic number, and  $A$  being the atomic mass number. The reduced energy,  $\varepsilon$ , is given as

$$\varepsilon = E \frac{0.8853a_0Z^{-1/3}M_2}{Z_1Z_2e^2(M_1 + M_2)} \approx 11.5EZ^{-7/3}, \quad (2.3)$$

with  $a_0$  being Bohr's radius,  $Z_1$ ,  $Z_2$ ,  $M_1$ , and  $M_2$  are the atomic number and atomic mass of the projectile and target, respectively,  $e$  is the charge of the electron, and

$$g(\varepsilon) = 3\varepsilon^{0.15} + 0.7\varepsilon^{0.6} + \varepsilon. \quad (2.4)$$

The energy deposited to the electrons is then defined as

$$\bar{\eta} = \frac{\varepsilon kg(\varepsilon)}{1 + kg(\varepsilon)}. \quad (2.5)$$

As the recoil energy is reduced,  $\varepsilon \rightarrow 0$ , both  $g \rightarrow 0$  and  $\eta \rightarrow 0$ . This can be interpreted as follows: when the recoil energy is sufficiently reduced, the recoiling particle is below the ionization threshold and no free electrons can be created.

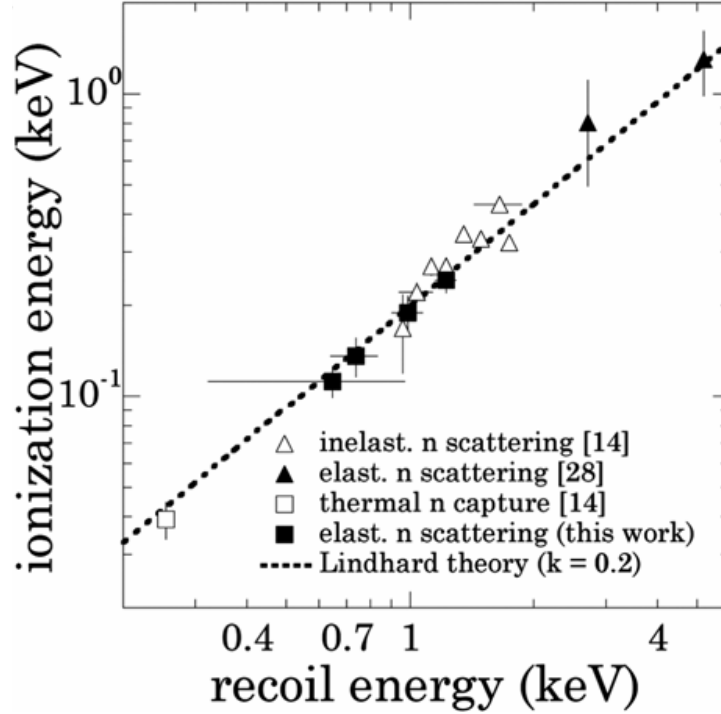


**Figure 2.2.** Barbeau et al. [39] compiled the quench factor measurements,  $N_{\text{ion}}^{\text{nucl}}/N_{\text{ion}}^{\text{elec}}$ , in germanium. The Lindhard theory fits the experimental data very well, suggesting the accuracy and applicability of the Lindhard theory for low-energy nuclear recoils in semiconductor detectors.

While the Lindhard theory represents a successful general model for predicting the amount of energy deposited to electrons, there are still questions regarding its applicability to all detector media and energies. Two important quantities needed to accurately predict the ionization yield cannot be obtained by calculations from the Lindhard theory. First, the fraction of energy deposited to electrons that produce ionization rather than excitation needs to be known. The ratio of excitation and ionization rates  $N_{\text{exc}}/N_{\text{ion}}$  can be obtained through experimental measurement. However, as is the case in argon, if there has not been a measurement of the ionization yield, there is also no measure of the  $N_{\text{exc}}/N_{\text{ion}}$  ratio. In argon, the  $N_{\text{exc}}/N_{\text{ion}}$  ratio has been measured for electron recoils [87], but not for nuclear recoils. In addition to the unknown  $N_{\text{exc}}/N_{\text{ion}}$  ratio, to correctly determine the number of  $N_{\text{ion}}$  events, it is imperative that one knows the average energy required to generate an electron-ion pair for the given detector medium,  $W$ -value, and recoil type. With knowledge of the  $N_{\text{exc}}/N_{\text{ion}}$  ratio and the  $W$ -value, the Lindhard

theory has been previously shown to accurately predict the ionization yield. This is exemplified in germanium, Figure 2.2, in which all of the electron energy loss is expended on creating electron-hole pairs. In dual-phase noble element detectors, the energy lost to electrons is partitioned between ionization and excitation, a property that enables the localization of the interaction event, Section 1.5.4.2. Measurements of the  $N_{\text{exc}}/N_{\text{ion}}$  ratio in xenon have been reported, which have allowed for the application of the Lindhard theory to xenon [93].

In argon, however, there have been no such measurements, and thus two parameters needed to make predictions via the Lindhard theory are unknown:  $N_{\text{exc}}/N_{\text{ion}}$  ratio and the  $W$ -value. As a result, caution must be taken when applying the Lindhard theory to liquid argon (LAr). A model that would not rely on these assumptions would be better suited for predicting the ionization yield. For reference, Figure 2.3 shows the predicted ionization yield in LAr calculated from the Lindhard theory assuming  $N_{\text{exc}}/N_{\text{ion}} = 1$ , and  $W_{ph} = 19.5\text{eV}$ , where  $W_{ph}$  is the energy required to induce either an ionization or excitation event, based on the measurements made for electron recoils [94]. Another shortcoming of the Lindhard theory is that it is a continuum theory, which does not take into account atomic excitation levels or electron shell structure. This means that the Lindhard theory is likely to break down at low energies, when the atomic excitation levels and electron shell structure have a significant effect on the ionization yield. The point where the Lindhard theory becomes inaccurate is not currently known for LAr.

While the Lindhard theory may be used estimate the initial number of electrons created in a nuclear recoil, it is also important to understand what fraction of those electrons can be drifted and measured. Some fraction of the generated electrons undergoes geminate recombination prior to being drifted away from the ion cloud. In 1987, J. Thomas and D. A. Imel developed the Thomas-Imel Box Model to predict electron-ion recombination in LAr and LXe [95]. The Thomas-Imel Box Model was initially developed to describe recombination in LAr and LXe with better accuracy than the Onsager theory of geminate recombination [96].

The Thomas-Imel Box Model uses a diffusion equation with no Coulomb force terms, instead assuming that the recombination rate separately depends on the

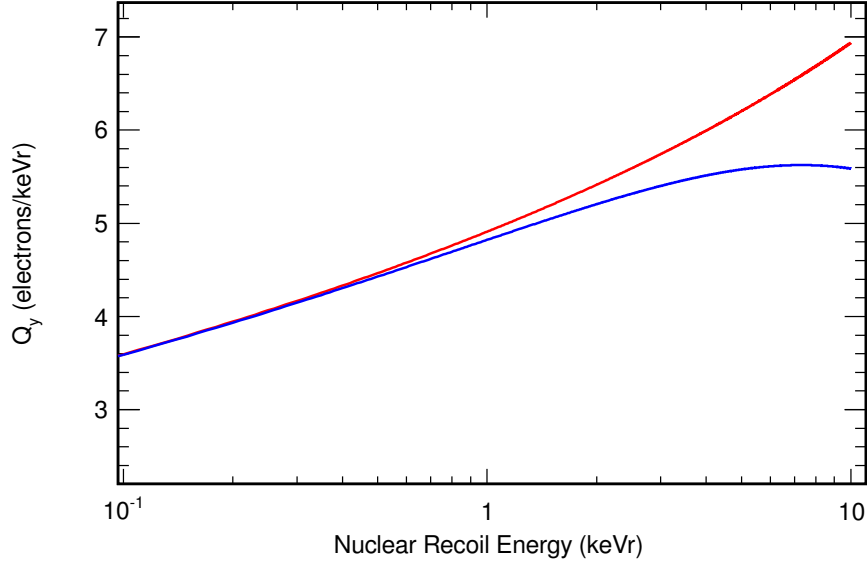


**Figure 2.3.** Prediction of the ionization yield in LAr using the Lindhard theory (blue), with  $k = 0.144$ ,  $N_{\text{exc}}/N_{\text{ion}} = 1$ , and  $W_{ph} = 19.5$  eV. After applying the Thomas-Imel Box recombination model to the Lindhard theory predictions, the ionization yield after local electron recombination is obtained (red). In the Thomas-Imel model, a value of 0.03 is assumed for  $\alpha/(a^2 u_-)$ .

density of ions and density of electrons:

$$\frac{\partial N_+}{\partial t} = -u_+ \mathbf{E} \nabla N_+ + d_+ \nabla^2 N_+ - \alpha N_- N_+, \quad (2.6)$$

$$\frac{\partial N_-}{\partial t} = u_+ \mathbf{E} \nabla N_- + d_- \nabla^2 N_- - \alpha N_+ N_-, \quad (2.7)$$

where  $N_+$  is the number of ions,  $N_-$  is the number of electrons,  $u_+$  is the ion mobility,  $u_-$  is the electron mobility,  $d_+$  is the ion diffusion coefficient,  $d_-$  is the electron diffusion coefficient, and  $\alpha$  is the coefficient of recombination. In LAr and LXe, the ions are assumed to be stationary and the diffusion term is assumed to be small with respect to the recombination and drift terms. With a constant electric field acting along the z-axis, Equations (2.6) and (2.7) can then be simplified to obtain:

$$\frac{\partial N_+}{\partial t} = -\alpha N_- N_+, \quad (2.8)$$

$$\frac{\partial N_-}{\partial t} = u_+ E \frac{\partial N_-}{\partial z} - \alpha N_+ N_- . \quad (2.9)$$

The differential equations are solved and the box model boundary conditions are applied. The fraction of electrons that recombine can then be calculated as

$$\frac{Q}{Q_0} = \frac{1}{\xi} \ln(1 + \xi), \text{ where } \xi = \frac{N_{\text{ion}} \alpha}{4a^4 u_- E f}, \quad (2.10)$$

where  $Q/Q_0$  is the fraction of electrons collected, and  $\xi$  is the independent parameter of the model. As  $\xi \rightarrow 0$ , all of the electrons are collected, and when  $\xi \rightarrow \infty$  all of the electrons recombine.  $N_{\text{ion}}$  is the initial number of electron-ion pairs created,  $a$  is the dimension of the box containing the charge,  $u_-$  is the electron mobility, and  $Ef$  is the electric field.

While the Thomas-Imel Box Model has been shown to be accurate for both electron recoil events and for an ionization track produced by  $\alpha$ -particles, it can not be applied universally for two reasons: it is not thought to apply to low-energy recoils when  $N_{\text{ion}} \rightarrow 0$ , and the value of  $\alpha/(a^2 u_-)$  needs to be measured experimentally prior to extrapolating the model results.

In order to accurately predict the ionization yield for low-energy nuclear recoils, a model needs to be generated from first principles, which does not rely on previous measurements of the  $N_{\text{exc}}/N_{\text{ion}}$  ratio, the  $W$ -value, and  $\alpha/(a^2 u_-)$ . A two-stage Monte Carlo simulation for the purpose of predicting the low-energy ionization yields in LAr has been developed as part of this Dissertation. The first stage of the simulation models the initial nuclear recoil. A cascade of Ar ions is produced as the primary Ar atom loses its kinetic energy produced by the initial recoil. The second stage of the simulation takes the produced ionization profile as an input and transports the electrons under an external electric drift field. The electron transport is applicable to both nuclear and electronic recoils.

## 2.3 Atomic Collision Model

To predict the amount of initial ionization produced in Ar recoil, a Monte Carlo atomic collision model has been developed. In the simulation, the cascade of Ar atoms and ions are tracked from the initial creation until their energies fall below



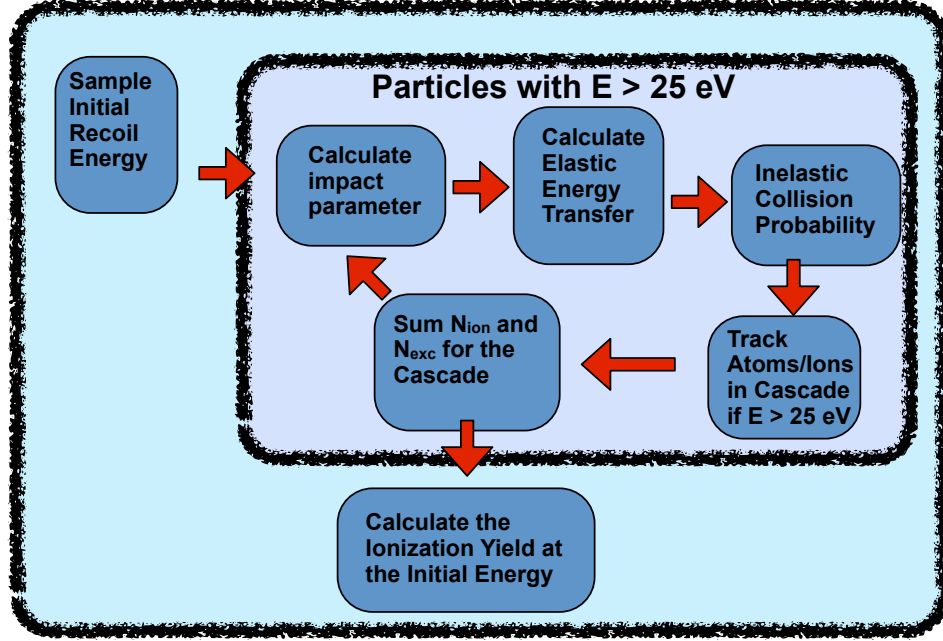


**Figure 2.4.** Diagram of the atomic collision algorithm used for the intrinsic ionization yield in Ar due to the Ar recoil cascade.

the threshold for excitation or ionization [86, 97, 98], which is 25 eV in the lab frame. Once all Ar atoms and ions are below the inelastic collision threshold, the total number of electron-ion pairs created and their final positions are logged. A diagram of the algorithm used for calculating the intrinsic ionization yield is given in Figure 2.4. The TRansport of Ions in Matter (TRIM) [99] algorithm is utilized to predict the elastic energy transfer between atoms at each collision. A previous version of the atomic collision model was published by C. Hagmann, [34]. The newly developed atomic collision model expands the work of C. Hagmann to track the Ar atoms above threshold and record the final ionization profile, which is then input into the electron transport model. Additionally, to better predict the number of ionizations and excitations that occur, an  $\text{Ar}^+$  ion is tracked from the time it is generated until it is below the excitation threshold.

In a given collision elastic scattering, ionization, excitation, or charge transfer can occur [100]. A summary of these interactions and resulting energy loss is given in Table 2.1, where  $E_{\text{elec}}$  is the energy of ionization,  $E_{\text{exc}}$  is the excitation energy, and  $I_p$  is the ionization potential. A variety of material specific input parameters accounted for in the simulation are stated in Table 2.2.

**Table 2.1.** A summary of the possible interactions between both neutral and ionized Ar atoms as they slow down within the TRIM-based Monte Carlo simulation.  $E_{\text{elec}}$  is the energy of ionization,  $E_{\text{exc}}$  is the excitation energy, and  $I_p$  is the ionization potential.

Particle	Target	Collision Type	Inelastic Energy Loss
Neutral	Neutral	Elastic Scatter	0
Neutral	Neutral	Ionization	$E_{\text{elec}}$
Neutral	Neutral	Excitation	$E_{\text{exc}}$
Ion	Neutral	Charge Transfer	$I_p$
Ion	Neutral	Ionization	$E_{\text{elec}}$
Ion	Neutral	Excitation	$E_{\text{exc}}$

**Table 2.2.** Properties of LAr required as inputs in the atomic collision model.

Property	Variable	Value	Units
Atom Density	$\rho_{\text{atom}}$	$2.108 \times 10^{22}$	$\text{cm}^{-3}$
Collisional Path Length	$L = \rho_{\text{atom}}^{-1/3}$	3.62	$\text{\AA}$
Geometric Cross Section	$\sigma_{\text{geo}} = \rho_{\text{atom}}^{-2/3}$	$1.31 \times 10^{-15}$	$\text{cm}^2$

### 2.3.1 Impact Parameter

The first step in tracking a recoiling Ar atom through the collision cascade is to calculate the impact parameter ( $P$ ) for the collision between the Ar atoms. The impact parameter is used to determine the scattering angle of the incident atom, and thus the energy transferred to the target atom. The impact parameter is selected by randomly sampling a radius from within the geometrical cross section ( $\sigma_{\text{geo}}$ ):

$$P = \sqrt{\frac{R_n}{\pi \rho_{\text{atom}}^{2/3}}}, \quad (2.11)$$

where  $R_n$  is a random number with the bounds  $[0,1]$  and  $\rho_{\text{atom}}$  is the atom density in the LAr.

### 2.3.2 Elastic Energy Transfer

With a known impact parameter, the elastic energy transferred to the target atom,  $T$ , is calculated as

$$T = \frac{4M_1M_2}{(M_1 + M_2)^2} E \sin^2(\theta/2), \quad (2.12)$$

where  $M_1$  is the mass of the projectile atom,  $M_2$  is the mass of the target atom,  $E$  is the kinetic energy of the projectile atom, and  $\theta$  is the scattering angle for the collision. In modeling nuclear recoils in LAr, both the projectile and target atoms are Ar, resulting in

$$\frac{4M_1M_2}{(M_1 + M_2)^2} = 1 \quad (2.13)$$

and

$$T = E \sin^2(\theta/2) \Rightarrow T = E(1 - \cos^2(\theta/2)). \quad (2.14)$$

The schematic for an elastic collision is shown in Figure 2.5, which is used to calculate the scattering angle:

$$\cos(\theta/2) = \frac{P + \rho_1 + \rho_2 + \delta_1 + \delta_2}{r_0 + \rho_1 + \rho_2}, \quad (2.15)$$

where  $P$  is the impact parameter,  $r_0$  is the distance of closest approach,  $\rho_1$  and  $\rho_2$  are the radius of curvature for the trajectory of the projectile and target atoms respectively, and  $\delta_1$  and  $\delta_2$  are correction terms to the contribution of the scattering angle due to the radius of curvature of the trajectory for the projectile and target atoms respectively [99].

### 2.3.3 Distance of Closest Approach

Following the approach given in Reference [99], the distance of closest approach can be calculated by solving

$$1 - \frac{V(r_0)}{E_c} - \left(\frac{P}{r_0}\right)^2 = 0 \quad (2.16)$$

in an iterative fashion, where  $V$  is the electric potential,  $P$  is the sampled impact parameter,  $r_0$  is the current distance of closest approach, and  $E_c$  is the center of

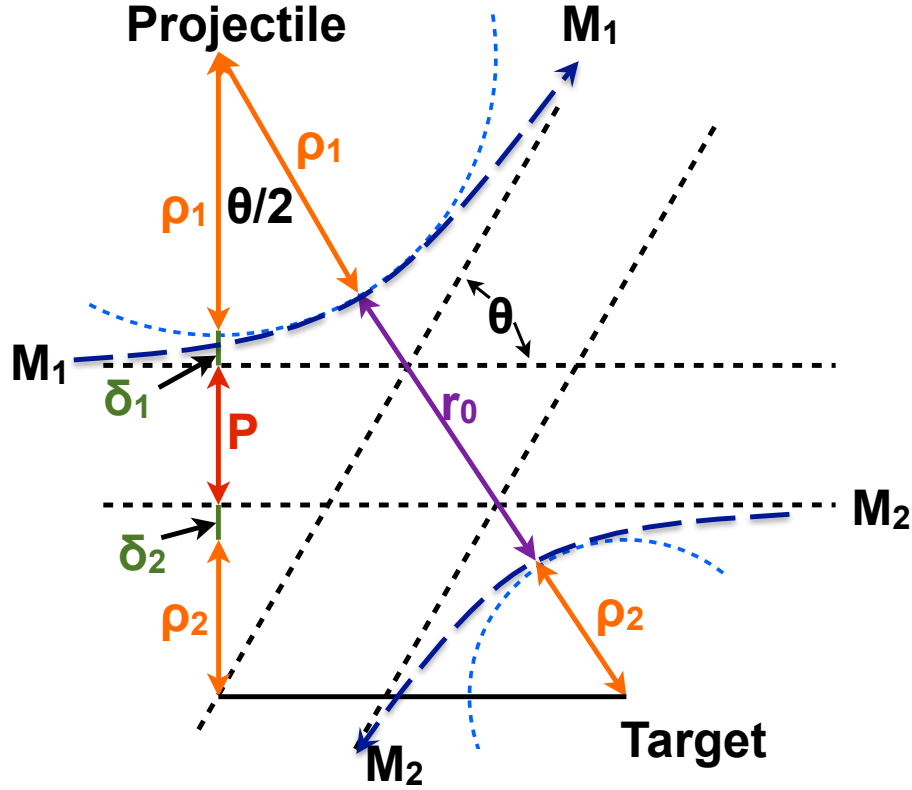


**Figure 2.5.** Particle trajectories for the collision of two atoms in the center-of-mass frame, with the “scattering triangle” super-imposed. As the incoming particle approaches with an impact parameter  $P$ , the distance of closest approach,  $r_0$ , is calculated, along with the radius of curvature ( $\rho = \rho_1 + \rho_2$ ) and correction term ( $\delta = \delta_1 + \delta_2$ ) to then determine the scattering angle ( $\theta/2$ ) [99].

mass energy:

$$E_c = \frac{E}{1 + M_1/M_2} = E/2. \quad (2.17)$$

For the electric potential, the Molière potential shown in Figure 2.6 [101, 102] is used. The Molière potential is shown to be a better fit for low-energy nuclear stopping than the Coulomb/Bohr potential [102].

$$V(r) = \frac{1}{4\pi\epsilon_0} \frac{Z_1 Z_2 e}{r} \Phi(R)(eV), \quad (2.18)$$

where  $\epsilon_0$  is the permittivity of free space,  $Z_1$  is the proton number for the projectile atom,  $Z_2$  is the proton number for the target atom,  $e$  is the charge of the electron,

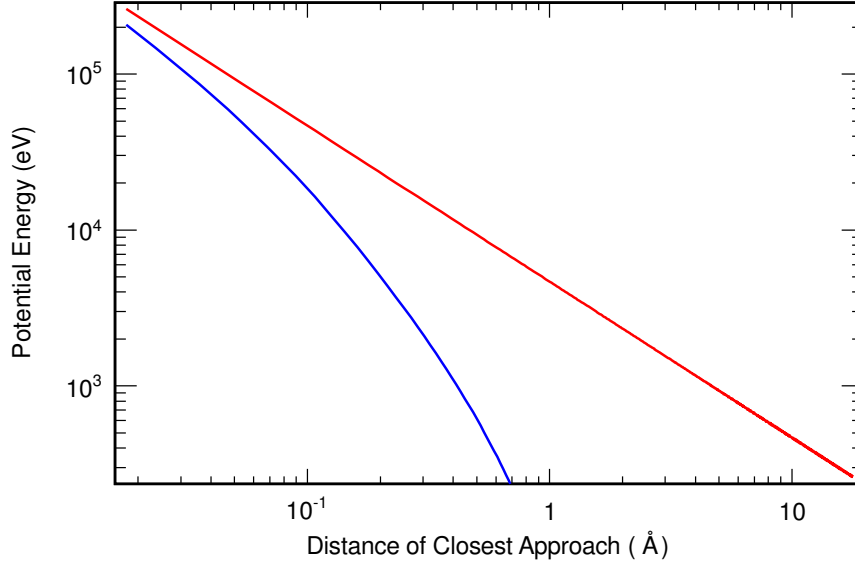


**Figure 2.6.** Comparison of the Coulomb potential (red) and the Molière potential (blue). The Molière potential is plotted from Equation (2.18) [101]. The Molière potential drops off more quickly than the Coulomb potential, and was shown to be a better fit than the Coulomb potential for the low-energy atomic collision model [102].

and  $\Phi(R)$  is Molière's screening function, defined as:

$$\Phi(R) = 0.35\exp(-0.3R) + 0.55\exp(-1.2R) + 0.1\exp(-6R), \quad (2.19)$$

where  $R = r/a_{sc}$  and  $a_{sc}$  is the interatomic screening length. The interatomic screening length [103, 104] is given by:

$$a_{sc} = \frac{0.8853a_0}{(Z_1^{1/2} + Z_2^{1/2})^{2/3}}, \quad (2.20)$$

where  $a_0$  is Bohr's radius. The following results are obtained when the collision parameters are input into Equation (2.20):

$$a_{sc} = \frac{0.8853 \times 0.53\text{\AA}}{(Z_1^{1/2} + 18^{1/2})^{2/3}} = 0.112573\text{\AA} \text{ for Ar + Ar} \\ 0.113643\text{\AA} \text{ for Ar}^+ + \text{Ar}. \quad (2.21)$$

The distance of closest approach for a given collision is solved for using the bisection method with an error value of  $10^{-6}$ . With a known distance of closest approach, the radius of curvature for the two particle trajectories can be calculated for any given energy and impact parameter.

### 2.3.4 Radii of Curvature

The radii of curvature for particle trajectories in a given collision are solved for based on the Molière potential at the distance of closest approach, Equation (2.22), by applying the elementary rule for centrifugal force:

$$\rho_1 + \rho_2 = \rho = \frac{2[E_c - V(r_0)]}{-V'(r_0)}, \quad (2.22)$$

where  $E_c$  is the center of mass energy,  $V(r_0)$  is the Molière potential, Equation (2.18) is solved at the distance of closest approach, and  $V'(r_0)$  is the derivative of the Molière potential. Equation (2.23) is also solved at the distance of closest approach:

$$V'(r) = \frac{V(r)}{r} - \frac{Z_1 Z_2 e}{4\pi\epsilon_0 r \cdot a_{sc}} \cdot (0.105\exp[-0.3R] + 0.66\exp[-1.2R] + 0.6\exp[-6R]). \quad (2.23)$$

The distance of closest approach ( $r_0$ ) is then entered into Equations (2.18) and (2.23) to solve for the radius of curvature ( $\rho$ ). Lastly, the correction term ( $\delta$ ) must be calculated.

### 2.3.5 The Correction Term

A correction term is needed to complete the “scatter triangle” for a given collision energy, Figure 2.5, and has been previously measured [99, 105] for a range of reduced energies ( $\omega$ ) between  $10^{-5}$  and 10, where

$$\omega = \frac{a_{sc} E_c}{Z_1 Z_2 e^2}. \quad (2.24)$$

The correction term is calculated from the product of the screening length for the detector medium ( $a_{sc}$ ) and an energy-dependent variable ( $\Delta$ ), based on previously

measured fit parameters for the Molière potential [102]:

$$\delta = a_{sc} \cdot \Delta, \quad (2.25)$$

where  $\Delta$  is given by:

$$\Delta = A \frac{R_0 - B}{1 + G}, \quad (2.26)$$

where  $R_0$ ,  $B$ ,  $A$ , and  $G$  are defined by:

$$R_0 = \frac{r_0}{a_{sc}}, \quad (2.27)$$

$$B = \frac{P}{a_{sc}}, \quad (2.28)$$

$$A = 2\alpha\omega B^\beta, \quad (2.29)$$

and

$$G = \gamma[(1 + A^2)^{1/2} - A]^{-1}. \quad (2.30)$$

Where  $\alpha$ ,  $\beta$ , and  $\gamma$  are based on fit parameters of the Molière potential ( $C_1$  -  $C_5$ ) [99], reference Table 2.3.

$$\alpha = 1 + C_1\omega^{-1/2}, \quad (2.31)$$

$$\beta = \frac{C_2 + \omega^{1/2}}{C_3 + \omega^{1/2}}, \quad (2.32)$$

and

$$\gamma = \frac{C_4 + \omega}{C_5 + \omega}. \quad (2.33)$$

With the impact parameter  $P$ , distance of closest approach  $r_0$ , radius of curvature  $\rho$  and correction factor  $\delta$ , the elastic scattering angle, Equation (2.15) and, subsequently, the energy transfer, Equation (2.14) can be calculated. If more than 25 eV (the threshold for excitation in the lab frame) is transferred to the target atom in the collision, the energy, position, and trajectory of the secondary argon atom are added to the particle bank for future cascade analysis.

**Table 2.3.** Pre-determined fit parameters for the Molière potential [99].

Parameter	Pre-determined Value [99]
$C_1$	0.6743
$C_2$	0.009611
$C_3$	0.005175
$C_4$	10.00
$C_5$	6.314

### 2.3.6 Inelastic Collision Probability

For a given interaction, there is a finite probability of an inelastic collision occurring in addition to elastic energy transfer. The probability of an inelastic collision is calculated from previously measured cross section data, Figure 2.7 and Figure 2.8 [100]. In a neutral-neutral collision, either elastic or inelastic interactions can occur, with inelastic collisions subdivided into ionization, Equation (2.34) and excitation, Equation (2.35). In an ion-neutral collision, charge transfer, Equation (2.36), ionization, Equation (2.37) or excitation, Equation (2.38) can occur.



In neutral Ar conditions, the probability of each interaction occurring is calculated by taking the ratio of the inelastic cross section (Figure 2.7) to the geometric cross section (Table 2.2). In the case of an ionized Ar atom, the cross section for charge transfer is sufficiently large that it is assumed to always occur in the absence of excitation or ionization. For this reason, the probability is obtained from the ratio of the inelastic cross section, Figure 2.8, to the sum of the cross sections for the three possible interactions.

At each collision, a random number is sampled to determine which inelastic



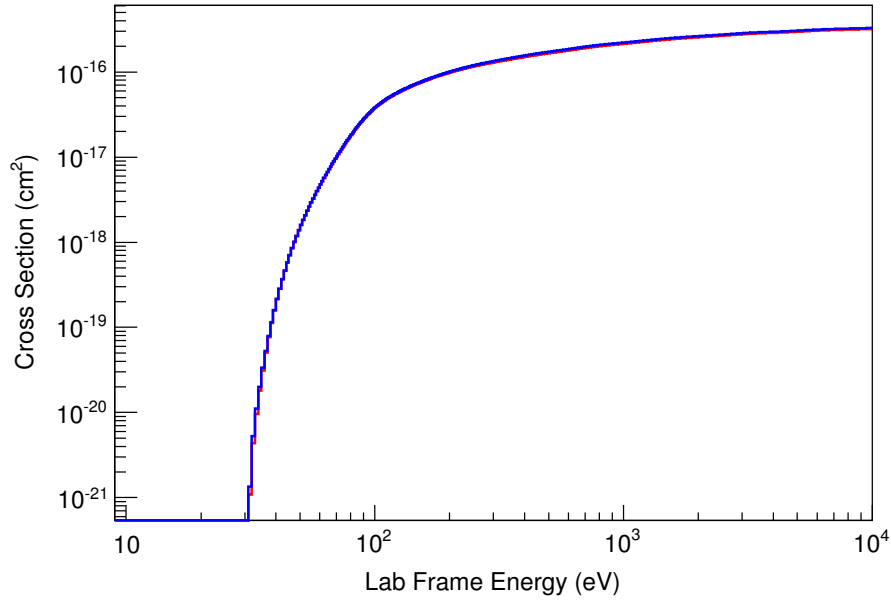


**Figure 2.7.** In a given neutral-neutral ( $Ar + Ar$ ) collision, either elastic scattering, ionization, or excitation can occur. Shown here are the cross sections for ionization (red),  $Ar + Ar \rightarrow Ar + Ar^+$ , and excitation (blue),  $Ar + Ar \rightarrow Ar + Ar^*$ , based on tabulated values in Reference [100]. Note that the cross sections are nearly equal, with excitation cross section being slightly higher than ionization cross section, which results in similar rates of excitation and ionization.

interaction takes place. The energy balance is then updated to reflect the energy transfer and the energy used in an inelastic collision. The initial Ar atom and all of the cascading Ar atoms are tracked until all of the Ar atoms are below the inelastic interaction threshold of 25 eV in the lab frame. A sample of the atom tracking throughout the collision cascade is shown in Figure 2.9.

### 2.3.7 Sum Ionizations and Excitations

Once all of the Ar atoms in the cascade have been tracked, all ionization and excitation events are tallied and the positions of the electron-ion pairs are stored for use with the electron transport model. A meta-data summary for a sample cascade is shown in Table 2.4.

It is possible to give a boost to the ionization branch of the signal through the Penning mechanism, Equation (1.23). Through the Penning mechanism, a fraction of the excitations result in a subsequent ionization of Xe. The potential boost in

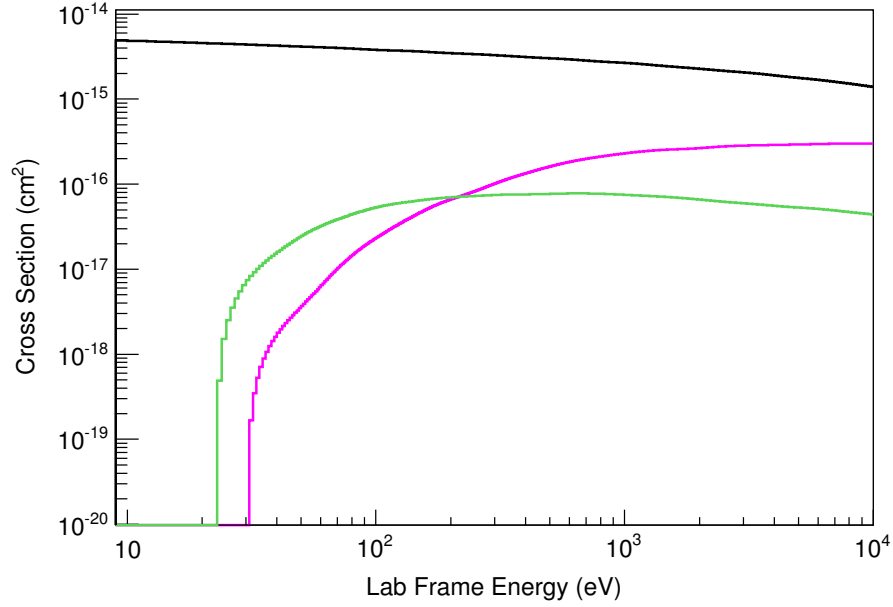


**Figure 2.8.** In an ion-neutral ( $Ar^+ + Ar$ ) collision, the cross section for charge transfer is so large that if ionization or excitation do not occur, it is assumed that charge transfer will occur. Shown here are the cross sections for charge transfer (black),  $Ar^+ + Ar \rightarrow Ar + Ar^+$ , ionization (magenta),  $Ar^+ + Ar \rightarrow Ar^+ + Ar^+$ , and excitation (green),  $Ar^+ + Ar \rightarrow Ar^+ + Ar^*$ , based on tabulated values in Reference [100].

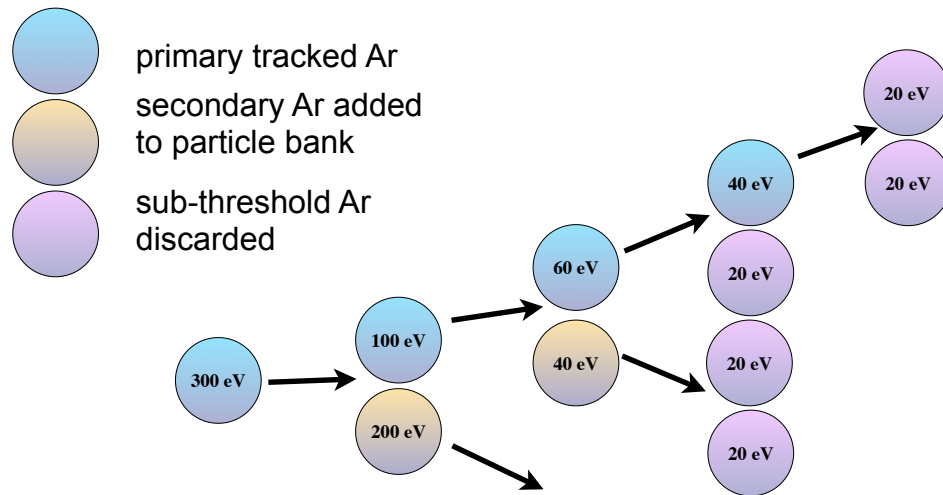


**Figure 2.9.** Example of an Ar collision cascade, as all Ar atoms are tracked until their energies drop below the 25 eV threshold.

**Table 2.4.** Example summary of the meta-data from a collision cascade obtained using the atomic collision model.

Particle Type	Initial Energy	Collisions	$N_{\text{ion}}$	$N_{\text{exc}}$
Primary	500 eV	8	2	3
Secondary	100 eV	1	0	0
Tertiary	80 eV	3	1	0
Secondary	60 eV	3	0	0
Secondary	200 eV	4	2	2
Tertiary	120 eV	5	1	2
Totals		24	6	7

ionization signal can be calculated as:

$$N_{e^-} = N_{\text{ion}} + p_{\text{Penning}} N_{\text{exc}}, \quad (2.39)$$

where  $p_{\text{Penning}}$  is assumed to be 0.6 for a Xe doping in the LAr of 1%. With the total number of ionization and excitation events tallied, the intrinsic ionization yield and nuclear quench factors can be calculated directly.

### 2.3.8 Intrinsic Ionization Yields

The intrinsic ionization yield

$$Q_{ie} = N_{\text{ion}}/E_{\text{init}} \quad (2.40)$$

is defined as the number of electrons generated per keV of initial energy, where  $E_{\text{init}}$  is given in keV. Figure 2.10 shows the calculated intrinsic ionization yields between 25 eV and 10 keV for LAr.

As seen in similar excitation and ionization cross sections, Figure 2.7, before any electron recombination occurs, the ionization and scintillation yields are approximately equal between 25 eV and 10 keV. While the cross sections for excitation and ionization are not as similar for ion-neutral collisions (Figure 2.8), the majority of ion-neutral collisions result in charge transfer and the additional contribution to the number of ionizations and excitations is negligible. As electron recombination occurs, an excited Ar atom,  $\text{Ar}^*$ , is produced which subsequently scintillates re-

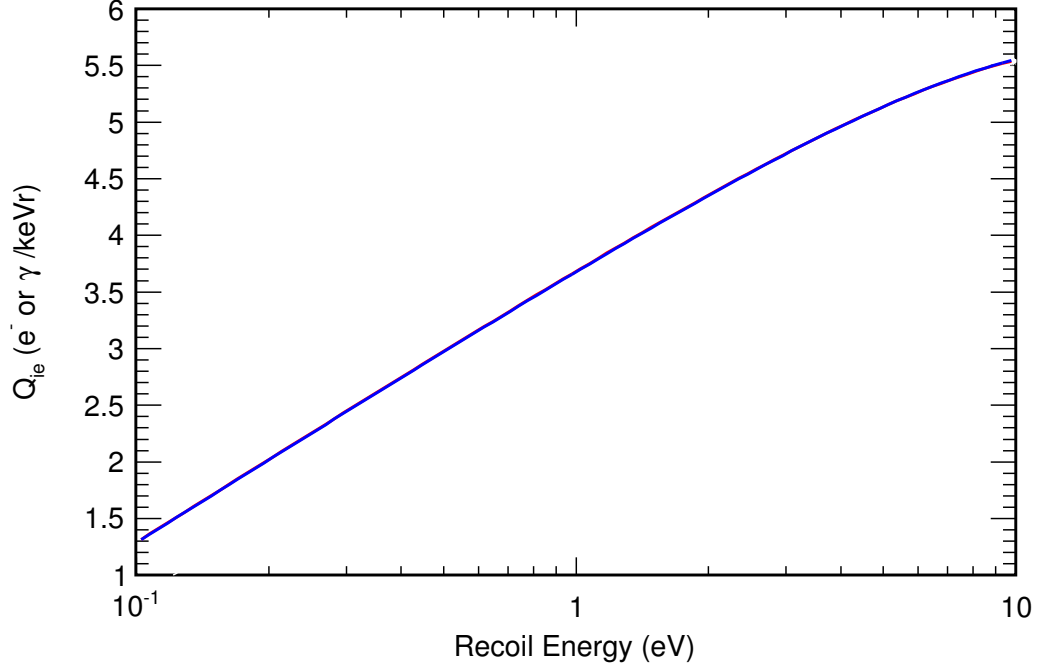


**Figure 2.10.** Intrinsic ionization (red) and scintillation (blue) yields for LAr before electron recombination, calculated by the atomic collision model. Note that the intrinsic ionization and scintillation yields are nearly equal.

sulting in an increase in scintillation yield and a decrease in ionization yield. The full extent of the increase and decrease depends on the number of total electron-ion pairs generated and is calculated in Section 2.5.

### 2.3.9 Quench Factor Value

In addition to the ionization yield, the nuclear quench factor is used to describe the efficiency of the nuclear recoil in producing ionization as compared to an electronic recoil of equal energy. Three nuclear quench factors can be defined from the amount of ionization and excitation produced by the collision cascade:

1. total quench factor – ionization and excitation:

$$q_{\text{tot}} = \frac{N_{\text{ion}}^{\text{nucl}}(E) + N_{\text{exc}}^{\text{nucl}}(E)}{N_{\text{ion}}^{\text{elec}}(E) + N_{\text{exc}}^{\text{elec}}(E)}, \quad (2.41)$$

2. ionization quench factor – ionization:

$$q_{\text{ion}} = \frac{N_{\text{ion}}^{\text{nucl}}(E)}{N_{\text{ion}}^{\text{elec}}(E)}, \quad (2.42)$$

and

3. Penning ionization quench factor – ionization and a fraction of excitations:

$$q_{\text{ion-Penn}} = \frac{N_e^{\text{nucl}}(E)}{N_{\text{ion}}^{\text{elec}}(E)}. \quad (2.43)$$

It has been previously measured that the  $W$ -value ( $W$ ) for LAr is 23.6 eV [58] and that

$$N_{\text{exc}}^{\text{elec}} \approx 0.19 \pm 0.02 N_{\text{ion}}^{\text{elec}} [87]. \quad (2.44)$$

With the assumption that  $N_{\text{ion}}^{\text{elec}} = E/W$ , Equations (2.41–2.43) become:

$$q_{\text{tot}} = \frac{N_{\text{ion}}^{\text{nucl}}(E) + N_{\text{exc}}^{\text{nucl}}(E)}{1.21E/W}, \quad (2.45)$$

$$q_{\text{ion}} = \frac{N_{\text{ion}}^{\text{nucl}}(E)}{E/W}, \quad (2.46)$$

and

$$q_{\text{ion-Penn}} = \frac{N_e^{\text{nucl}}(E)}{E/W}. \quad (2.47)$$

The predicted intrinsic total quench factor, the ionization quench factor and Penning ionization quench factor before electron recombination are shown in Figure 2.11. The ion positions are then saved to file, to use as an input when calculating the electron collection efficiency, Section 2.4.8. For  $N_{\text{ion}} \leq 10$  the initial Ar energies are sampled from the CNNS recoil spectra. For  $N_{\text{ion}} > 10$ , the atomic collision model is run for a single energy which has an average ionization yield corresponding to the number of electrons being run (i.e. 20, 30, 40, or 50).

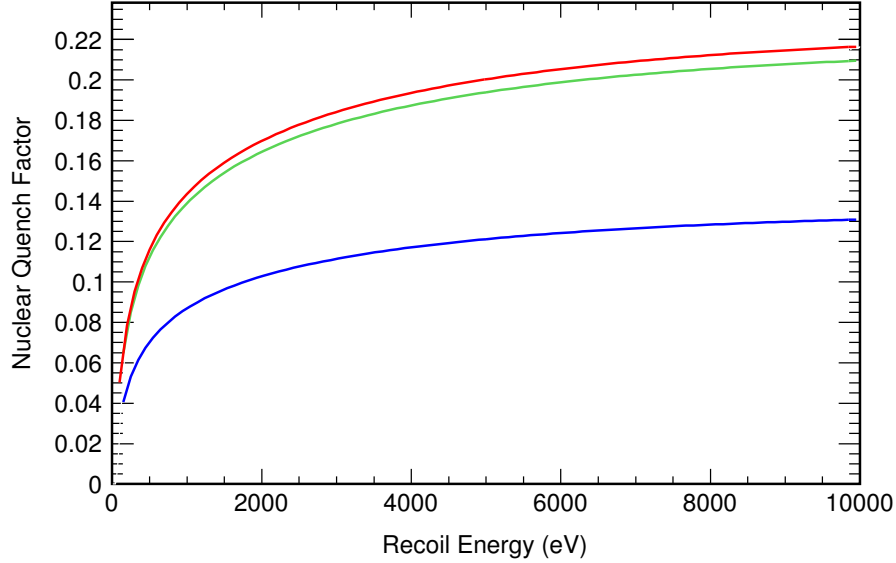


**Figure 2.11.** The total nuclear quench factor (red) as calculated from Equation (2.45), nuclear ionization quench factor (blue), Equation (2.46), and the Penning nuclear ionization quench factor (green), Equation (2.47), as calculated from the atomic collision simulation. A  $W$ -value of 23.6 eV was assumed in each case, with an exciton fraction of 0.19 assumed in the total quench factor. For the Penning nuclear ionization quench factor, a fraction of xenon of 1% was assumed, for a Penning probability of 0.6.

## 2.4 Electron Transport Model

In addition to the number of electrons created in a given recoil, the fraction of electrons that escape from the initial ion cloud without recombining needs to be calculated. This is done with the simulation based on the Cohen-Lekner theory [106, 107]. The electrons are initially emitted in a random direction with a given kinetic energy. There are then two sets of forces acting on the electron as it slows down, the Coulomb forces from the other electron-ion pairs created, and the external electric field applied within the detector. Once the electron is thermalized, it is possible that it recombines with one of the ionized Ar atoms. Otherwise, the electron escapes the ion cloud with the external electric field as the dominant force.

Starting with the positions of the Ar ions from the nuclear quenching model, and emitting the electrons randomly into the entire  $4\pi$  solid angle, the initial momenta and positions of the electrons and ions were obtained. The forces on

the electrons created by the Coulomb forces exerted by the charge cloud, along with the external electric field were subsequently calculated. The recombination and escape criteria are then evaluated to determine the status of each electron in the system. After the system of electrons and ions is updated, the new electric forces are calculated. Simultaneously, the new positions and the velocities of each electron and ion within the system are calculated [108, 109]. At each electron collision, there is a probability of either energy loss or a momentum change due to the collision [107]. For large numbers of electron-ion pairs, it is also possible to accelerate the electrons sufficiently to excite or ionize the Ar ions as the electrons fall into the Coulomb potential well.

The electron transport model performs the following calculations on a step by step basis. The maximum collision rate,  $r_{\max}$ , is chosen to be  $3.4 \times 10^9$  cm/s  $\text{\AA}^2$ , slightly greater than the product of electron velocity and the collisional cross section,  $v\sigma_{\text{tot}}$ , ensuring that at least 1 time step occurs between each collision. The mean collision time is determined by taking the inverse of the density times the maximum collision rate:

$$\langle \Delta t \rangle = \frac{1}{\rho r_{\max}}. \quad (2.48)$$

The step time is then calculated by sampling the mean collision time:

$$\Delta t = -\langle \Delta t \rangle \log(R_t), \quad (2.49)$$

where  $R_t$  is a random number with the bounds (0,1].

### 2.4.1 Forces on Electrons and Ions

With the initial positions of the ions and electrons and the momentum of the electrons known, the first step in transporting the electrons is to calculate the forces on each electron due to the remaining electrons and ions.

The forces between the electrons and the ions are calculated first by determining the distance between the current electron and each of the charges generated, Equation (2.50):

$$r = \sqrt{(x_i^{\text{el}} - x_j^{\text{ion/el}})^2 + (y_i^{\text{el}} - y_j^{\text{ion/el}})^2 + (z_i^{\text{el}} - z_j^{\text{ion/el}})^2}, \quad (2.50)$$

where  $(x_i^{\text{el}}, y_i^{\text{el}}, z_i^{\text{el}})$  is the position of the  $i$ -th electron and  $(x_j^{\text{ion/el}}, y_j^{\text{ion/el}}, z_j^{\text{ion/el}})$  is the position of the  $j$ -th ion or electron. The acceleration of the electron is then updated for the force of each ion acting upon it,

$$a_{x,i} = a_{x,i} \mp \sum_{j=0}^n \frac{a}{r^2} \frac{(x_i^{\text{el}} - x_j^{\text{ion/el}})}{r}, \quad (2.51)$$

$$a_{y,i} = a_{y,i} \mp \sum_{j=0}^n \frac{a}{r^2} \frac{(y_i^{\text{el}} - y_j^{\text{ion/el}})}{r}, \quad (2.52)$$

$$a_{z,i} = a_{z,i} \mp \sum_{j=0}^n \frac{a}{r^2} \frac{(z_i^{\text{el}} - z_j^{\text{ion/el}})}{r}. \quad (2.53)$$

$$a = 10^6 \frac{q_{\text{el}} q_{\text{ion}}}{2\pi\epsilon_0\epsilon_r m_{\text{el}}}, \quad (2.54)$$

where  $n$  is the number of ions present for a given time step,  $a$  is the acceleration in  $\text{cm/s}^2$ ,  $q_{\text{el}}$  is the charge of the electron,  $q_{\text{ion}}$  is the charge of the ion,  $\epsilon_0$  is the permittivity of free space,  $\epsilon_r$  is the relative permittivity of the LAr, and  $m_{\text{el}}$  is the mass of the electron in kg. The updated acceleration term is subtracted in the case of the electron-ion interaction (attraction), and added in the case of the electron-electron or ion-ion interaction (repulsion).

With all of the Coulomb forces for the charge cloud calculated, the external electric field is applied, Equation (2.55). The electric field is assumed to be a uniform 1-D electric field within the active volume and only acting on the  $x$  component of the acceleration. While this is not completely true in experiments, the uniformity is calculated to 1 part in  $10^6$  based on the electrostatic simulations of the dual-phase detector, Section 5.2.

$$a_{x,i} = a_{x,i} + \frac{q_{\text{el}} E f}{m_{\text{el}}}, \quad (2.55)$$

$$a_{y,i} = a_{y,i}, \quad (2.56)$$

$$a_{z,i} = a_{z,i}, \quad (2.57)$$

where  $Ef$  is the electric field in  $\text{V/m}$ .



**Table 2.5.** Criteria used to determine if an electron and ionized Ar atom recombine in the LAr.

Parameter	Variable	Value	Units	Reference
Critical Recombination Energy	$E_{\text{crit}}$	1	eV	[107, 110, 111, 109]
Critical Recombination Radius	$r_{\text{crit}}$	1.29	nm	[110, 111, 109]

The forces on the ions are calculated with the same procedure used to calculate the forces on the electrons, but with the acceleration of

$$a = 10^6 \frac{q_{\text{el}} q_{\text{ion}}}{2\pi\epsilon_0\epsilon_r m_{\text{ion}}}, \quad (2.58)$$

where  $m_{\text{ion}}$  is the mass of the ion. In contrast to the electrons, the ions accelerate in the direction of the applied electric field, which is towards the cathode potential:

$$a_{\text{x,i}} = a_{\text{x,i}} - \frac{q_{\text{ion}} E f}{m_{\text{ion}}}. \quad (2.59)$$

## 2.4.2 Electron Capture

At this point in the simulation, it is determined whether the electrons are still free, or if they have recombined with ions. If an electron has an energy below  $E_{\text{crit}}$  and is within  $r_{\text{crit}}$  of an ion, Table 2.5, then it recombines and the respective electron and ion are removed from the simulation [107, 110, 111, 109] and assumed to proceed directly into primary scintillation. For the electrons and ions which do not recombine, the positions and velocities are updated.

## 2.4.3 Electron Positions

With the electron velocity known from the previous time step, and the acceleration calculated when solving for the forces on the electron, the new position of each electron is determined using:

$$\mathbf{r}_i(t + \Delta t) = \mathbf{r}_i(t) + \mathbf{v}_i \Delta t + \frac{1}{2} \mathbf{a}_i(t) \Delta t^2, \quad (2.60)$$

where  $\Delta t$  is the time step, Equation (2.49),  $\mathbf{r}$  is the electron position,  $\mathbf{v}$  is the electron velocity, and  $\mathbf{a}$  is the electron acceleration.

#### 2.4.4 Ion Velocities

Because the ions stop over a short distance, the ion velocities are simply calculated from the acceleration due to the forces acting on the electrons:

$$\mathbf{v}_i(t + \Delta t) = \frac{\mu_{\text{ion}} m_{\text{ion}} \mathbf{a}_i(t)}{q_{\text{ion}}}, \quad (2.61)$$

where  $\mu_{\text{ion}}$  is the mobility of the argon ion,  $m_{\text{ion}}$  is the mass of the argon ion, and  $q_{\text{ion}}$  is the charge of the argon ion.

#### 2.4.5 Ion Positions

Using the previously determined ion velocity, the position after time step  $\Delta t$  is calculated:

$$\mathbf{r}_i(t + \Delta t) = \mathbf{r}_i(t) + \mathbf{v}_i \Delta t. \quad (2.62)$$

#### 2.4.6 Electron-Atom Collision

The forces on the electrons must be recalculated for the new charge profile, and then the velocities can be calculated:

$$\mathbf{v}_i(t + \Delta t) = \mathbf{v}_i + \frac{1}{2}[\mathbf{a}_i(t) + \mathbf{a}_i(t + \Delta t)]\Delta t. \quad (2.63)$$

Any electrons that do not recombine with an ion undergo a collision with an Ar atom. For the electron-atom collision, the atom velocities are randomly sampled assuming thermal motion of the atoms. When an electron and atom collide, there are four possible types of interactions, shown in Figure 2.12 up to an energy of 10 keV.

Elastic - Energy transfer,  $\sigma_{et}$  [107, 112, 113, 114, 115, 116]

Elastic - Momentum transfer,  $\sigma_{pt}$  [107, 112, 113, 114, 115, 116]

Inelastic - Excitation,  $\sigma_{exc}$  [112, 113, 114, 115, 117, 118]

Inelastic - Ionization,  $\sigma_{ion}$  [112, 113, 114, 115, 117, 118]

The cross section for an elastic collision is taken as the maximum of the energy transfer and momentum transfer cross sections. The inelastic cross section is the summation of the excitation and ionization cross sections. An interaction occurs if

$$Prob < \frac{v\sigma_{tot}}{r_{max}}, \quad (2.64)$$

where  $Prob$  is a randomly sampled probability,  $v$  is the electron velocity,  $\sigma_{tot}$  is the total cross section for interaction, and  $r_{max}$  is the maximum collision rate. If a collision occurs, another probability is sampled to determine if the resulting collision is elastic or inelastic. If the  $Prob < \sigma_{elas}/\sigma_{tot}$ , an elastic collision occurs; otherwise an inelastic collision occurs. For elastic collisions, if  $Prob < \sigma_{pt}/\sigma_{elas}$  then a momentum transfer collision occurs. Note that at energies above  $\sim 5$  eV, all elastic collisions are momentum transfer collisions, but below this energy it is assumed that collisions may occur with a loss in energy without a change in direction. For the inelastic collisions, excitation occurs if  $Prob < \sigma_{exc}/\sigma_{inelas}$ , with the remaining inelastic collisions resulting in ionization. If ionization occurs, the emission direction of the secondary electron is randomly sampled, and the energy of the primary electron is shared evenly between the two resulting electrons. The cross sections for each interaction are compiled from [119], and shown in Figure 2.12.

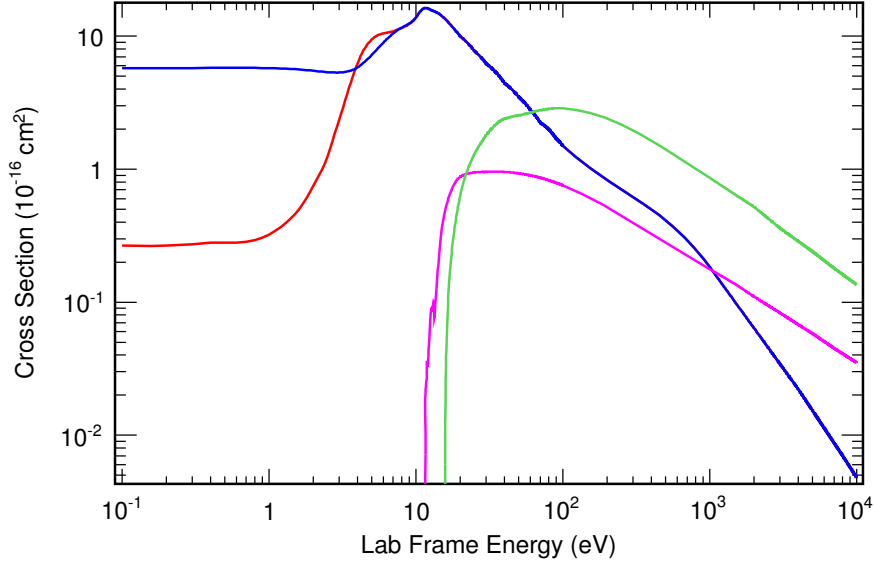


**Figure 2.12.** In a given elastic collision, either the energy loss without a direction change (blue)[107, 112, 113, 114, 115, 116], or a change of momentum (red)[107, 112, 113, 114, 115, 116] can occur. If the electron energy is large enough, either excitation (magenta)[112, 113, 114, 115, 117, 118] or ionization (green)[112, 113, 114, 115, 117, 118] can also occur. Below 1 keV, cross sections are compiled from [112]. Above 1 keV cross sections are compiled from [116] for elastic collisions and [117] for inelastic collisions.

### 2.4.7 Electron Drift Velocity

As a check of the electron transport algorithm, the electron transport code was run for 1 electron and 0 ions under the presence of an electric field. By tracking the position of the electron, the transport code is able to predict the known electron mobility for liquid argon. Subsequent comparisons with previously measured data and predictions were performed for the electron mobility, Figure 2.13.

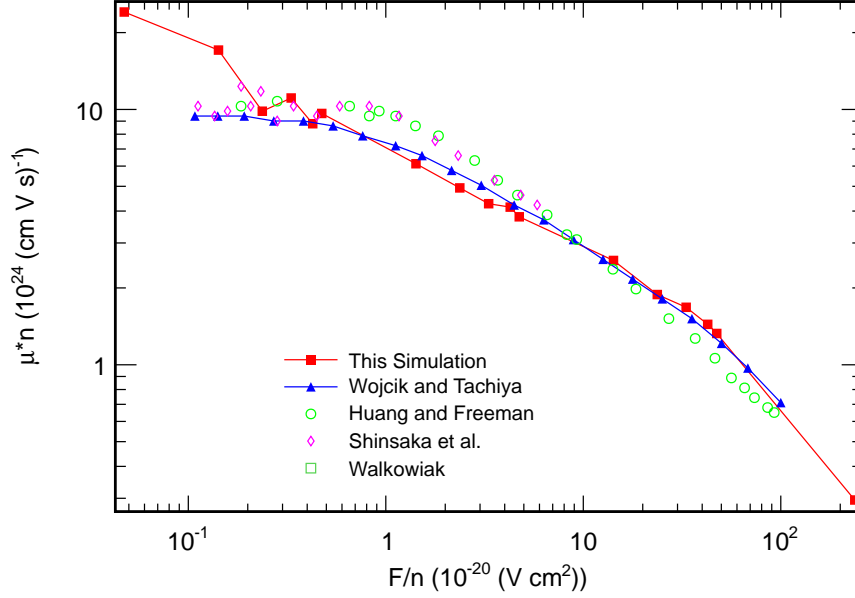


**Figure 2.13.** The electron transport code (red closed squares) is checked against previous data for calculating the electron mobility. The code matches well with both experiments (green open circles) [120], (magenta open diamonds) [121] and a previous simulation (blue closed triangles) [107].

## 2.4.8 Electron Collection Efficiency

After all of the electrons are either captured by an ion or escape to the gas phase, the electron collection efficiency is calculated. When an electron is emitted from the Ar atom, it is emitted with a given emission spectra, which asymptotically rises at the lowest measured energy (2 eV), and has a few auto-ionization peaks at 9.4, 11.1, and 11.3 eV, Figure 2.14. The electron collection efficiency is calculated for various electric fields and for two electron emission energies from the Ar atom, of 1 eV and 10 eV [98], Figure 2.15. As the number of ionization electrons created by the initial recoil increases, the probability of any electron escaping the initial ion cloud decreases.

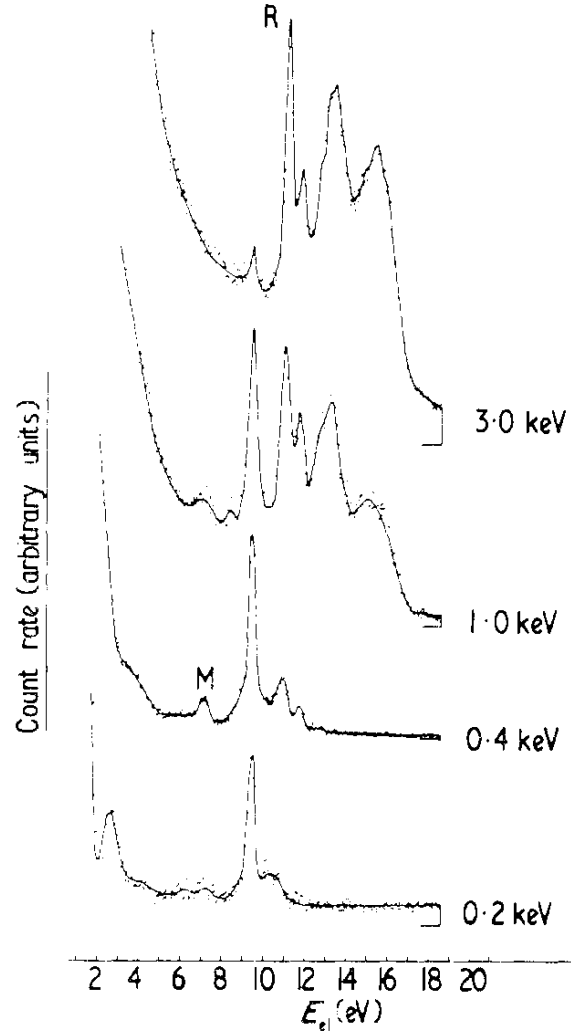


**Figure 2.14.** Previously measured electron emission spectrum from Ar-Ar collisions [98]. There is a continuum of possible emission energies, with auto-ionization energy peaks at 9.4, 11.1 and 11.3 eV. The peak marked with the M is due to molecular ionization, while the peaks marked with R are from the auto-ionization process. The simulation assumed two discrete energies of 1 eV and 10 eV. 1 eV is selected to correspond to the asymptotic energy, and 10 eV is chosen to correspond to the auto-ionization peaks.

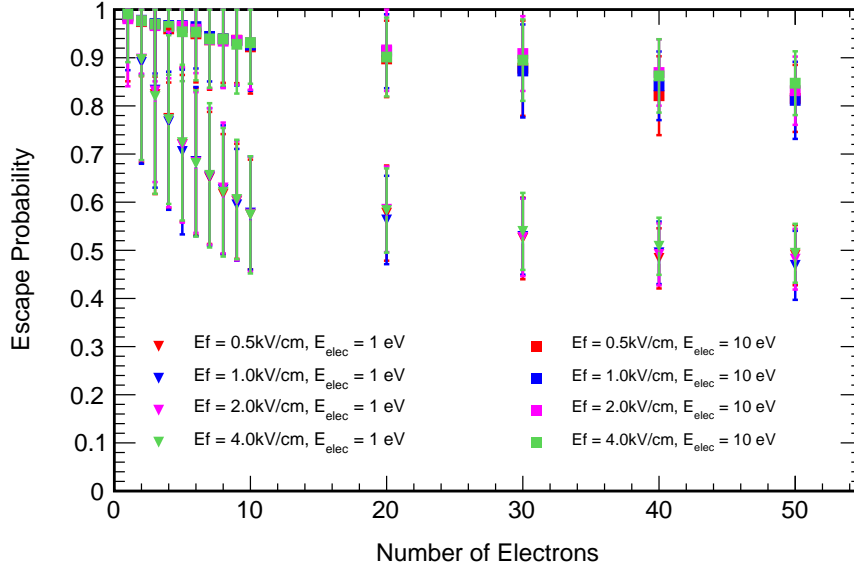


**Figure 2.15.** The electron extraction efficiency is calculated for various numbers of electrons created, along with different external electric fields. The error bars are  $1\text{-}\sigma$  based on the number of trials run.

## 2.5 Detectable Ionization Yield

In order to calculate a detectable ionization yield such as that measured in a detector, the intrinsic ionization yield, Figure 2.10 must be convolved with the electron collection efficiency, Figure 2.15. The atomic collision model is run and the number of ions and their positions are input to the electron recombination model. This produces the electron collection efficiency for that given energy. The ionization yield can then be calculated for the energy both before and after electron recombination, Figure 2.16.

This electron transport model takes into account the initial local geminate recombination, but there are additional effects which could lead to a loss in electron collection efficiency. Such additional loss mechanisms are non-uniform electric fields and impurities within the detector. Non-uniformity of the electric field can result in the drifting of the electrons on the edge of the active region into field rings or out of the active region. Electronegative impurities within the detector absorb electrons as they drift through the active region. The capture of electrons by electronegative impurities is what determines the electron lifetime within the detector,

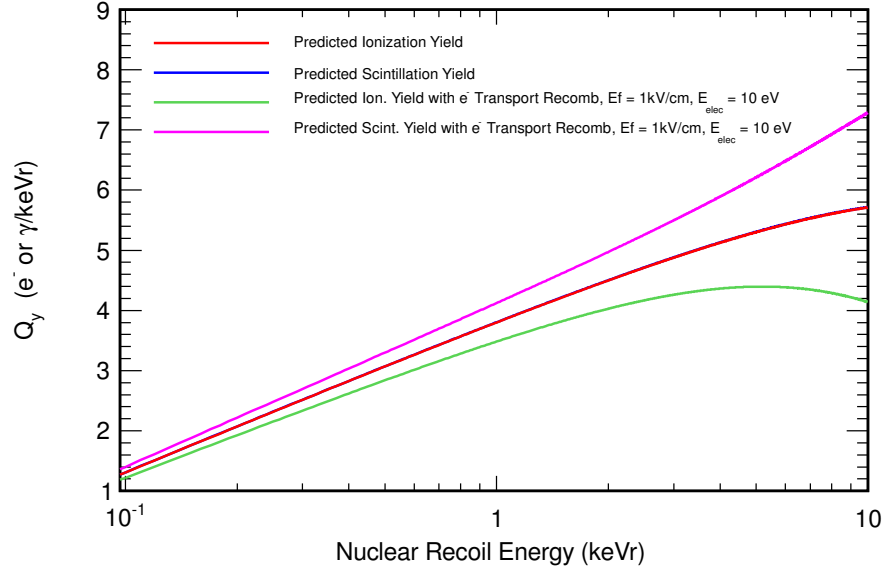


**Figure 2.16.** Ionization and scintillation yields for LAr at different energies before and after recombination as calculated by the Monte Carlo simulation. The red curve is the ionization yield before electron recombination and drops down to the green curve as the electrons recombine. The blue curve is the scintillation yield before electron recombination and increases to the magenta curve after electron recombination. Note that the initial ionization and scintillation yields are nearly equal.

Section 5.8. Low electron lifetimes result in a variation of electron collection efficiency with the z-position (drift time) of the event. The variation of collection efficiency results in a loss of energy resolution within the detector, limiting the maximum length of the active volume. For these reasons, the electron transport model sets an upper limit on the electron collection efficiency for a detector.



## Single-Phase Argon Detector

Direct comparison with the ionization yield model, Section 2.3-2.4, requires an ionization yield measurement in LAr, for which a detailed understanding of entire dual-phase detector operation is needed. To gain this detailed understanding, it is beneficial to study its gaseous amplification region. Operation of a single-phase argon detector allows for the study of the amplification process and detector systematics without the added complication of cryogenic conditions [122, 123]. In this Chapter, Section 3.1 provides a discussion of the operation of the single-phase argon detector developed for these studies. In Section 3.2 the event characteristics of the Ar electroluminescence process is presented. Section 3.6 is dedicated to the description of an analysis method for identifying and removing detector signal pathologies. A discussion of the detector response characteristics is provided in Section 3.7. Finally, a discussion of the Geant4 simulation of the detector and the results of the comparison with the measured data are provided in Section 3.8.

### 3.1 Single-Phase Detector

The single-phase Ar detector, Figure 3.1, has an active volume which is 10.2 cm in diameter and 12 cm in height. Above the active volume is a secondary gain volume, which has the same diameter and a height of 4 cm. 1-cm thick aluminum field cage rings with a 1-cm gap between each ring define the electric field within the active volume. At the bottom of the field cage, an aluminum hemisphere is attached to the cathode to prevent electrical breakdown to the walls of the 40.6-cm

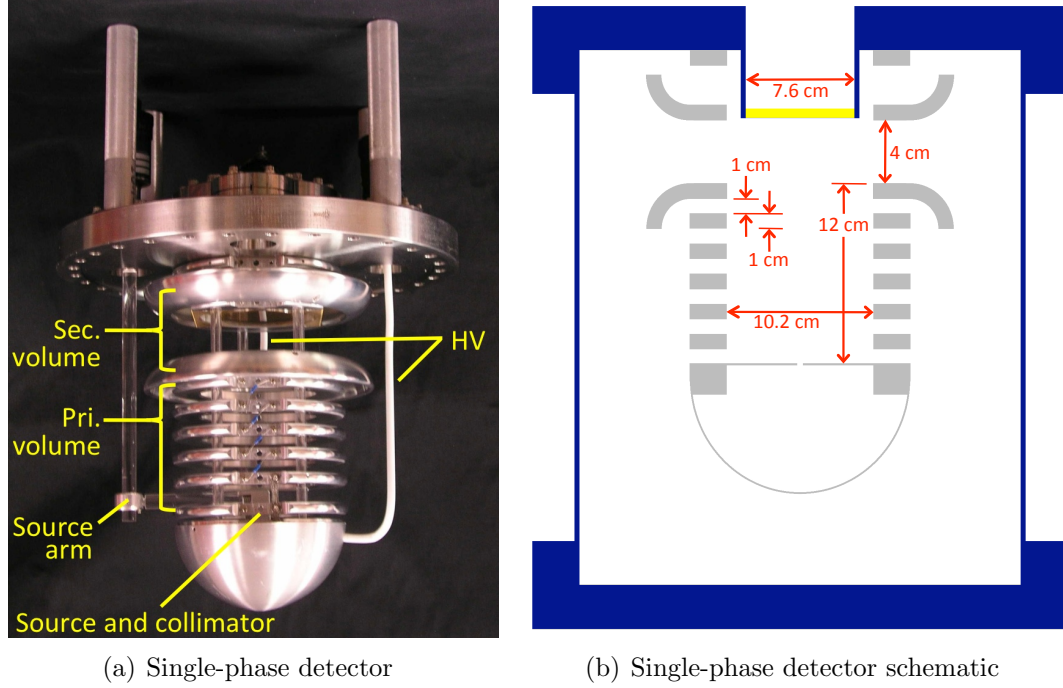


**Figure 3.1.** Interior of the single-phase Ar detector (a) used to characterize the amplification properties of a dual-phase Ar detector. Dimensions of the detector (b); the collimating plate is shown above the hemisphere [123]. The electrons are drifted through the primary volume to the secondary volume where amplification occurs.

diameter  $\times$  40.6-cm tall stainless steel pressure vessel which encloses the detector. The detector is supported by acrylic rods inserted through the field cage rings, with 1-cm thick acrylic spacers placed between the field rings. The gain region is bounded on its top and bottom by field shaping rings. A wire mesh spans the diameter of the active volume to provide a uniform electric field within the amplification region. Each wire mesh consists of 30  $\mu\text{m}$  gold-plated tungsten wires with a 1-mm pitch, which are held at tension to the field shaping rings using epoxy. The scintillation light produced within the amplification volume due to electroluminescence is wavelength-shifted using  $\text{N}_2$ , Section 1.5.1.1. As a result, it can be transmitted through a 7.6-cm diameter quartz viewport, where it is detected by a PMT. Calibration of the detector is performed by placing an  $^{55}\text{Fe}$  source under a fixed collimator at the bottom of the active volume.

When operating the detector, the chamber is first pumped down to a reference

pressure of  $\sim 10^{-6}$  Torr and sealed off with a gate-valve. The chamber is then filled with approximately 10 Torr of 99.998% Ar to exceed the threshold of the Baratron pressure gauge, followed by 6 Torr of 99.995% N<sub>2</sub> to act as the wavelength shifter, Section 1.5.1.1. The chamber is then filled with an additional 390 Torr of Ar to bring the total pressure to 406 Torr of the Ar-N<sub>2</sub> gas mixture. 6 Torr of N<sub>2</sub> was found to be the optimal fraction of N<sub>2</sub> for increased light collection, Section 3.4. All gases were obtained from the Lawrence Livermore National Laboratory gas facilities.

To set up the electric field, 75 M $\Omega$  resistors were used to link the field cage rings, while a 375 M $\Omega$  resistor was used between the upper field shaping ring (grounded) and the lower field shaping ring, held at potential with the primary volume. Primary and secondary potentials were increased independently until consistent electrostatic discharge was observed. The potentials were then lowered to reduce the rate of discharge to a maximum rate of approximately once per hour. In order to deal with the remaining high voltage sparking events, an algorithm was developed, Section 3.6, to exclude pathological events from the collected data. Using this method, the electric potentials were set to 8 kV in the secondary amplification volume ( $E = 2$  kV/cm) and 3 kV in the primary active volume ( $E = 0.250$  kV/cm). With these potentials, the reduced electric field ( $E/p$ ) in the primary volume was below the 1 V/cm/Torr scintillation threshold. This ensured that the observed events resulted from scintillation in the amplification volume and were not produced during drift through the active volume. In the secondary volume, the reduced electric field was held just below the ionization threshold of 5 V/cm/Torr, which was verified using the collected data.

## 3.2 Event Characteristics

A Hamamatsu 6522 PMT [124] biased at -2.6 kV was used for light collection. The PMT signal was digitized and acquired using a GaGe CompuScope 14200 digitizing PCI card installed in a Dell Optiplex GX270 computer. The GaGe card operated with a sampling rate of 200 MHz, with a 14-bit range, and a bandwidth of 100 MHz. The data acquisition software (DAQ) was developed using LabView, and was triggered externally with an uncorrelated Transistor-Transistor Logic (TTL)

**Table 3.1.** The most intense X-rays from  $^{55}\text{Fe}$ , reproduced from the Table of Isotopes [125]. The most intense X-ray not included in this Table has a relative intensity of 0.28%, approximately 100 times smaller than the intensity of the combined 5.888 and 5.899 keV X-rays.

Energy (keV)	Relative Intensity (%)
5.888	8.5
5.899	16.98
6.490	1.01
6.490	1.98

**Table 3.2.** Electron transitions in argon for a missing K-shell electron, obtained from the Evaluated Atomic Data Library [126, 127].

Transition	Energy (keV)	Frac. Prob. of Transition
K-L2	2.9282	$3.559 \times 10^{-2}$
K-L3	2.9305	$7.033 \times 10^{-2}$
K-M2	3.1630	$2.913 \times 10^{-3}$
K-M3	3.1632	$5.756 \times 10^{-3}$

signal from a Stanford Research Systems DG535 pulse generator operating at 4900 Hz. The uncorrelated trigger was used to eliminate any data bias from a data-triggered readout, and to prepare for a pulsed neutron beam experiment, Section 4.2. The acquisition speed was limited by the speed of writing the data to disk, which set a limit of 8 MB/s ( $\sim 50$  traces per second), for a live time of  $\sim 1\%$ .

A 30- $\mu\text{Ci}$   $^{55}\text{Fe}$  calibration source was located within the aluminum hemisphere, with a collimation hole limiting the X-rays to the vertical direction.  $^{55}\text{Fe}$  primarily emits X-rays of 4 energies near 6 keV, Table 3.1. The  $^{55}\text{Fe}$  X-rays interact within the primary volume 94.6% of the time, with events in the secondary volume making up  $\sim 2.0\%$  of the interactions. Events in the secondary volume produce partial energy deposition; because the generated electrons do not traverse the entire secondary volume, the number of photons generated per electron is reduced. Approximately 11% of the photoelectric events on Ar result in X-ray emission, Table 3.2. Ar X-rays can also escape the active volume to produce an X-ray escape peak within the energy spectrum.

Each photon detected by the PMT produces a 10-20 ns long electrical pulse,

which can be identified as a single photoelectron pulse. In the sample trace, Figure 3.2, a  $^{55}\text{Fe}$  event that includes several single photoelectron pulses is shown. A time-enlarged  $^{55}\text{Fe}$  event is shown in Figure 3.3. The observed event width is  $\sim 2.5\ \mu\text{s}$ , which is due to the drift time of the electrons through the secondary region and the scintillation relaxation time. Using *Magboltz*, a Monte Carlo-based simulation package for calculating electron transport speed in gaseous media [113], the event width is predicted to be  $1.77 \pm 0.03\ \mu\text{s}$ . The difference between the observed and predicted event duration is due to the relaxation time for the scintillation process. Ar scintillates in the deep ultra-violet (UV) region at 128 nm, which is not transmitted by the quartz PMT window. The scintillation light is thus wavelength-shifted to 337 nm [66, 72] by the addition of  $\text{N}_2$  to the detector. In order to attribute multiple photoelectrons to a single event, a gate time,  $T_g$ , was defined as the maximum time no pulse exceeding a given threshold is recorded by the PMT. If a threshold-exceeding PMT pulse occurs within  $T_g$  of the previously recorded pulse that exceeded the threshold, the two PMT pulses were considered to be related to the same event.  $T_g$  was optimized to  $2\ \mu\text{s}$ . This gate time was chosen to increase the sensitivity to the low-energy events. With a PMT dark rate of 1 kHz and an event rate of 230 Hz when acquired with the uncorrelated trigger, there is an accidental coincidence of  $\sim 0.5$  single photoelectrons within the  $T_g$  of  $2\ \mu\text{s}$ .

### 3.3 Detector Calibration

The detector was calibrated using both the primary X-rays from  $^{55}\text{Fe}$  and the X-ray escape peaks resulting from the atomic transitions within Ar. The primary X-rays from  $^{55}\text{Fe}$ , Table 3.1, are grouped into two X-ray peaks at 5.895 keV and 6.490 keV with the relative intensities of 25.4 and 2.99, respectively. The X-ray escape peaks are grouped into two weighted-average X-ray peaks for the transitions from the K-shell to the L-shell and from the K-shell to the M-shell. The Ar X-ray emission energies are 2.930 keV and 3.163 keV, with the fractional probabilities of 0.106 and 0.009, respectively.

The data is fit with a sum of 6 gaussian functions, accounting for a group of primary X-ray peaks and the two associated X-ray escape peaks. The background

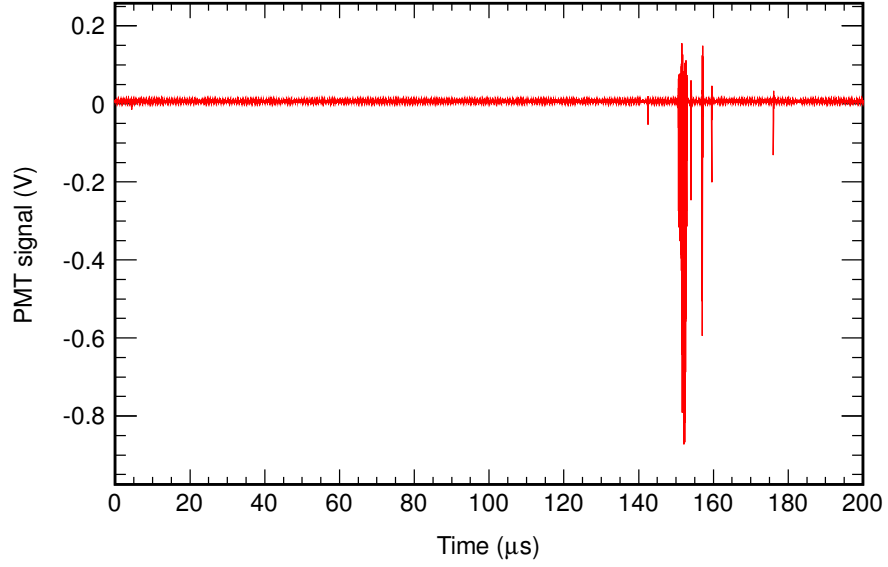


**Figure 3.2.** Representative trace acquired by the GaGe CompuScope 14200. An  $^{55}\text{Fe}$  event is visible at  $\sim 150 \mu\text{s}$ . Single photoelectron signals are also present in the trace.

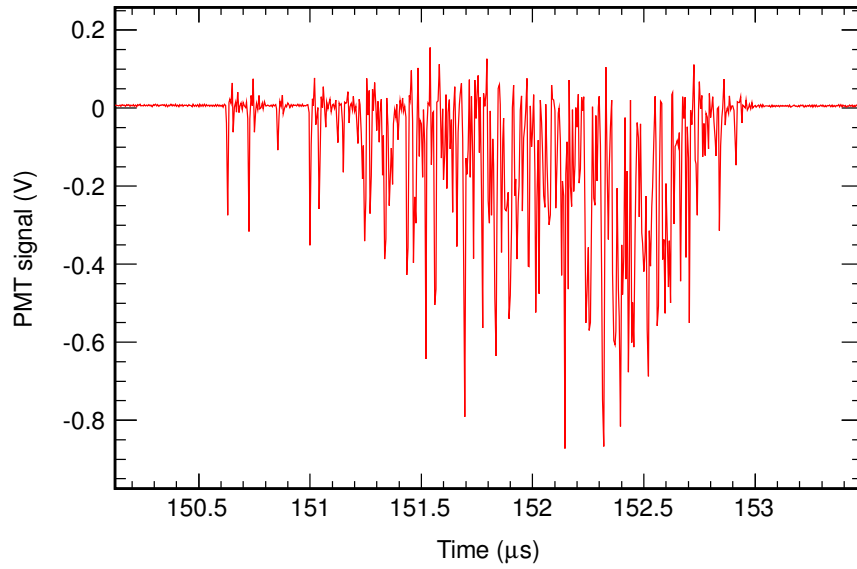


**Figure 3.3.** Characteristic  $^{55}\text{Fe}$  event when  $\text{N}_2$  is used as a wavelength shifter. The event width is  $\sim 2.5 \mu\text{s}$ , due to the time required for the electron cloud to drift through the secondary volume along with the scintillation decay time constant.

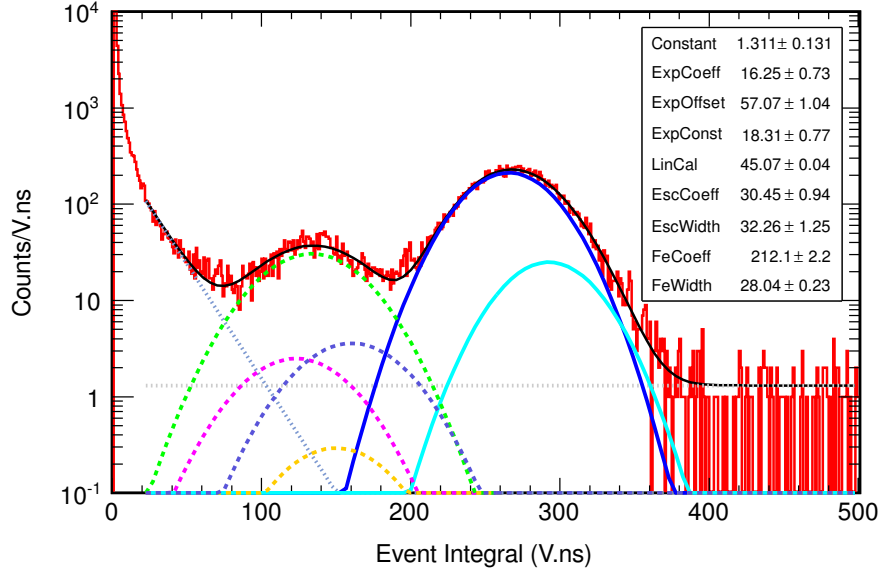


**Figure 3.4.** Energy deposition spectrum from the  $^{55}\text{Fe}$  calibration source, with the full energy deposition peak at approximately 300 V.ns, and the various X-ray escape peaks overlapping at approximately 150 V ns;  $\chi^2/\text{d.o.f.} = 451.5/416$ , with a p-value of 0.11. The two primary X-ray peaks are plotted as solid curves, the four X-ray escape peaks are plotted as dashed lines, while the background is plotted as a dotted line.

was assumed to have a shape of a constant plus an exponential background. The exponential fit had its own horizontal offset for the purpose of setting the initial values in the calibration fit. Initially, there were 22 free parameters in the fit for 6 gaussians, a constant, an exponential background, and the horizontal offset. The free variables decreased to nine parameters once the appropriate constraints for the X-ray peak intensities, energies, and widths were applied. With the applied calibration function, an energy calibration value of  $45.07 \pm 0.04$  V.ns/keV was obtained, Figure 3.4.

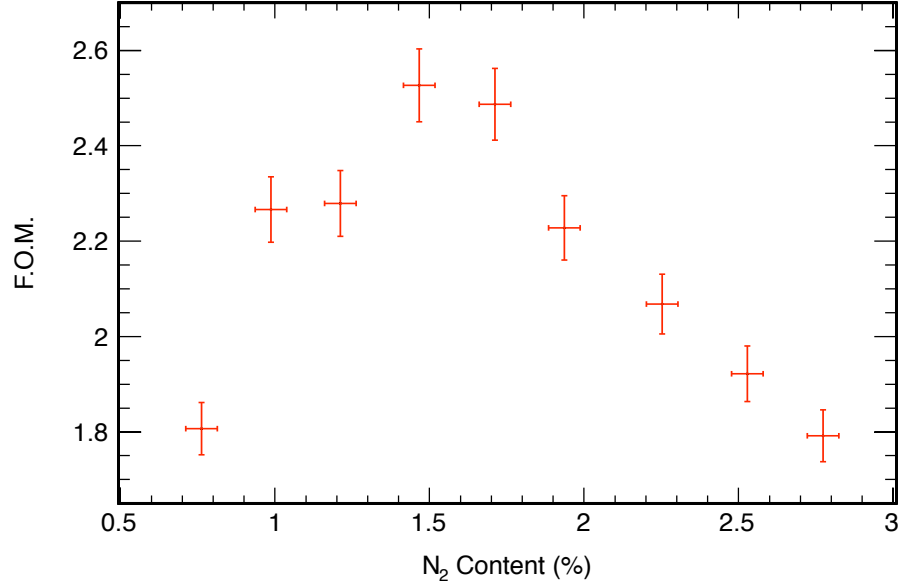


**Figure 3.5.** The *F.O.M.* was calculated for N<sub>2</sub> content between 0.75% and 2.75%. The optimal N<sub>2</sub> content was found to be  $\sim 1.5\%$ .

### 3.4 Detector Optimization

The gas mixture within the detector was optimized to obtain the greatest separation between the  $^{55}\text{Fe}$  peak and the single photoelectron peak. The degree of separation can be characterized by a figure of merit:

$$F.O.M. = \frac{(C_{Fe} - \sigma_{Fe}) - (C_{spe} + \sigma_{spe})}{\sigma_{Fe} + \sigma_{spe}}, \quad (3.1)$$

where  $C_{Fe}$  is the centroid of the  $^{55}\text{Fe}$  primary X-ray peak,  $\sigma_{Fe}$  is the sigma of the primary X-ray peak,  $C_{spe}$  is the centroid of the single photoelectron (s.p.e.) peak, and  $\sigma_{spe}$  is the sigma of the s.p.e. peak. The total pressure in the system was kept between 400 and 410 Torr, with the nitrogen content varied between 0.75% and 2.75% in 0.25% increments. The spectrum was recorded and the *F.O.M.* calculated for each gas mixture, Figure 3.5. The optimal N<sub>2</sub> content in the single-phase Ar detector was found to be 1.5%, consistent with prior work [72, 128]. For the rest of the data shown for the single-phase Ar detector, the N<sub>2</sub> concentration of 1.5% was used.



### 3.5 Pre-Filtering of Data

With the uncorrelated trigger, most of the data does not contain  $^{55}\text{Fe}$  events; rather, it typically includes only of a few single photoelectron (s.p.e.) events. Therefore, a software pre-filter was used to reduce the number of traces written to disk, both to conserve the hard drive space and reduce analysis time. The data was pre-filtered, requiring that any recorded trace contain an event longer than 100 ns. This event length was selected because the width of a s.p.e. peak was 30 ns, and an electronic signal reflection was observed, with approximately 1/5 the amplitude of the primary s.p.e. pulse occurring 40 ns later. The pre-filter did not affect the DAQ operation; it was only used as a criterion for saving the trace to disk. In order to verify that the pre-filter did not introduce any bias in the data, a comparison data collection and analysis was performed with and without the pre-filter. The data was collected for 2 hours (120 data files) and 9.5 hours (70 data files) for the unfiltered and pre-filtered cases, respectively. The unfiltered data contained 5470 X-ray peak counts, while the pre-filtered data contained 28300 counts in the same X-ray peak. For a comparison of the spectra, the data was normalized by the number of counts within the X-ray peak, Figure 3.6. The centroids, amplitudes, and widths of both the primary and escape X-ray peaks all varied within  $1\text{-}\sigma$ , concluding that there were no significant effects from the pre-filter.

When the event width is plotted against the event energy, two distinct areas corresponding to the primary X-ray peak and the X-ray escape peak appear, Figure 3.7. While the time for an electron to traverse the secondary region and for the  $\text{Ar}/\text{N}_2$  scintillation process to occur predicts an event width of  $\sim 2.3\text{ }\mu\text{s}$ , the observed event widths extend up to nearly  $10\text{ }\mu\text{s}$ . The ranges of the 6 keV and 3 keV electrons within the detector are approximately 1.94 mm and 0.59 mm [129], respectively. Using *Magboltz*, the finite range of the electrons adds a maximum of 0.09 and 0.03  $\mu\text{s}$ . The cause of the long event widths can be explained by the events being artificially extended due to s.p.e. events occurring within  $T_g$ . While the long gate time adds to the event width of some events, it is a small and acceptable tradeoff given the resulting increase of resolution in the low-energy region.

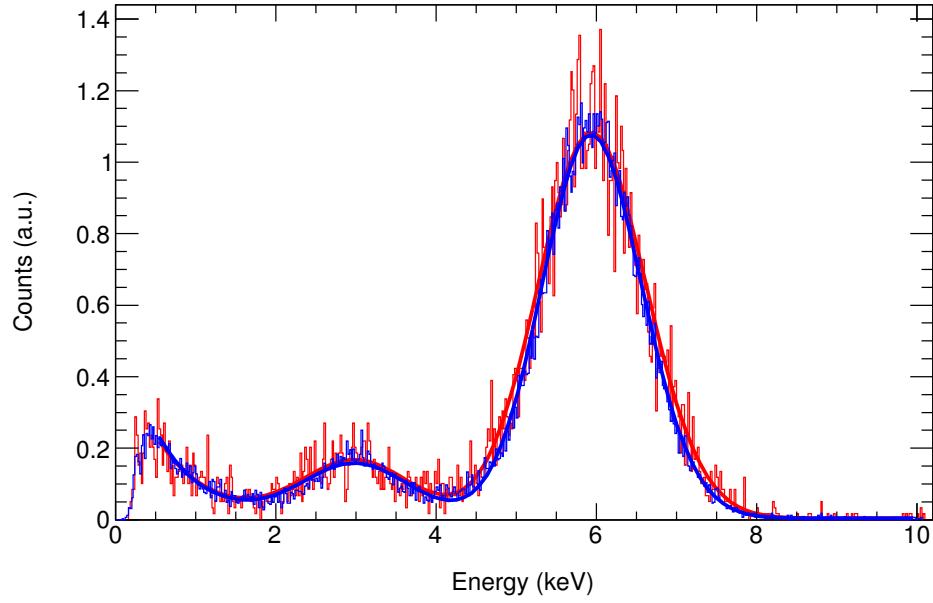


**Figure 3.6.** Pre-filtered data spectrum (blue) retains the features of the raw data spectrum (red). The pre-filter increases the efficiency of writing X-ray events to disk and improves the statistics of the pre-filtered data. This results in smaller statistical fluctuations in the data, as can be seen in the raw data without a pre-filter.

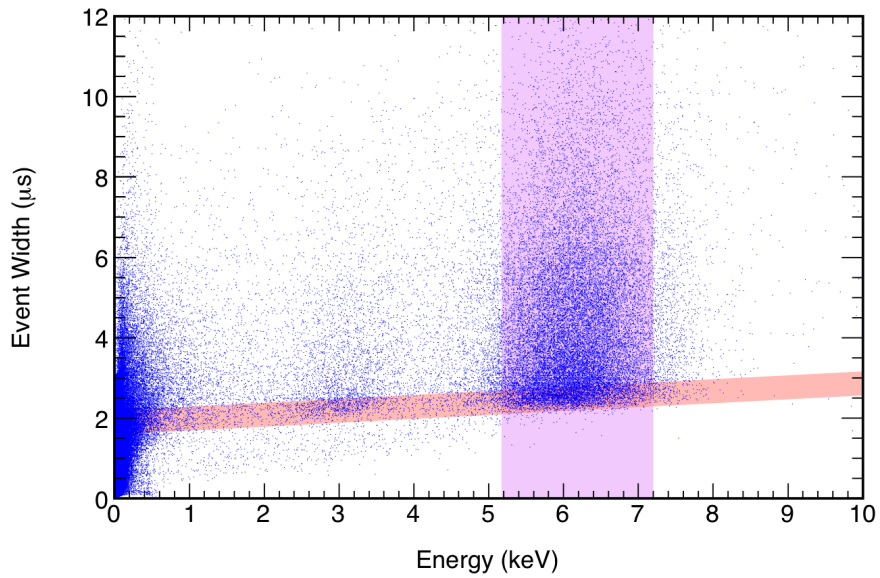


**Figure 3.7.** The event width is plotted against the event integral. By making an event cut on the vertical band, only the primary X-ray peak events are selected. Selecting the horizontal band selects events which have traversed the amplification region.

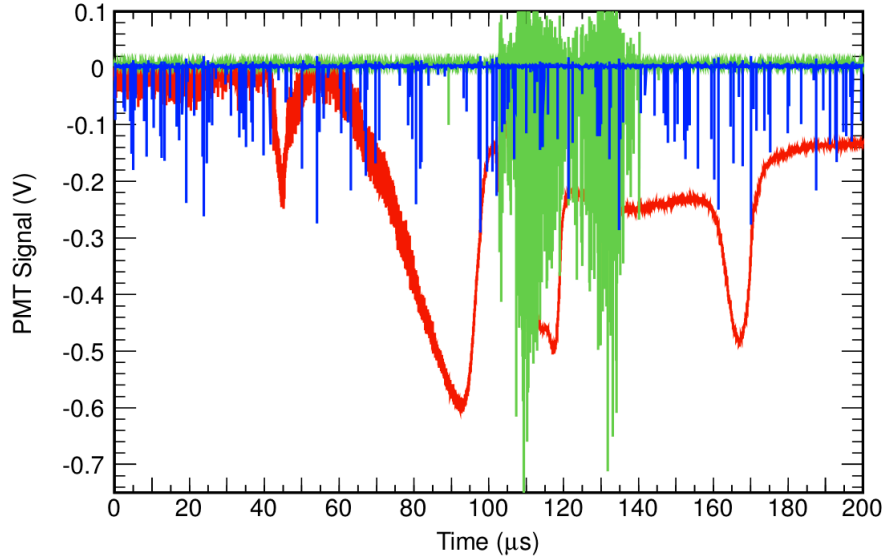


**Figure 3.8.** Examples of three types of pathological traces identified using the analysis algorithm. The pathological traces were referred to as wandering baseline (red), photon grass (blue) and pathological events (green). A trace demonstrating normal-operation is shown in Figure 3.2.

### 3.6 Signal Pathologies

Even during normal operation, the detector occasionally experiences a high-voltage spark or another spurious event. In order to adequately analyze the data, a signal pathologies detection algorithm was developed to identify pathological traces, such as high-voltage discharges and small discharges resulting in electron saturation within the detector. Instead of trying to characterize all of the spurious traces, the signal pathologies algorithm focused on identifying valid signal waveforms. Three examples of pathological signals rejected using this algorithm are shown in Figure 3.8.

The signal pathologies analysis starts by integrating over 200  $\mu\text{s}$  traces from the pre-filtered data set. A histogram is created of the trace integrals, with the results shown in Figure 3.9. In the trace integral histogram, the primary  $^{55}\text{Fe}$  X-ray peak is visible at  $\sim 280 \text{ V}\cdot\text{ns}$ , with the X-ray escape peak at  $\sim 140 \text{ V}\cdot\text{ns}$ . An additional peak is present at  $\sim 560 \text{ V}\cdot\text{ns}$ , corresponding to data traces containing two  $^{55}\text{Fe}$  events. The area of the double- $^{55}\text{Fe}$  peak area is approximately 0.6% of the area of

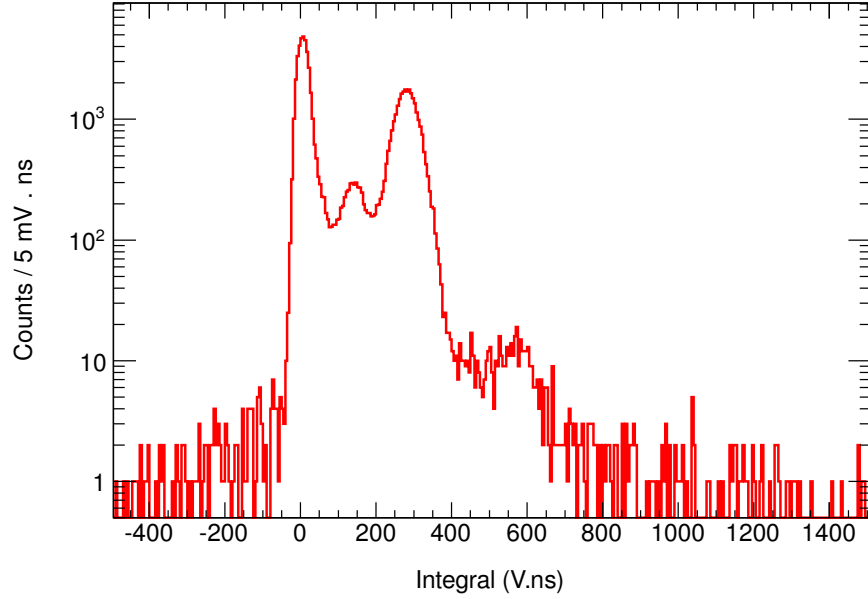


**Figure 3.9.** Trace integral for a data set containing known sparking events. The peak at  $\sim 280$  V $\cdot$ ns originates from the  $^{55}\text{Fe}$  calibration source. The X-ray escape peak is at  $\sim 140$  V $\cdot$ ns, and the double- $^{55}\text{Fe}$  peak is at  $\sim 560$  V $\cdot$ ns.

the single- $^{55}\text{Fe}$  peak, which agrees with the expected accidental coincidence rate of 1-2%. The signal pathologies analysis assumes that no more than two  $^{55}\text{Fe}$  events occur in a single trace, which eliminates approximately one out of 30000 acceptable traces.

The second criteria used in the analysis of signal pathologies relied on the number of PMT pulses observed in a single 200  $\mu\text{s}$  trace. It is possible that two PMT pulses occur close in time, such that the PMT voltage does not decrease all the way to the baseline before another photoelectron pulse occurs. It would be more ideal to fit each of the PMT pulses with a Gaussian in order to determine if there were two PMT pulses, but the computational cost of fitting every pulse does not warrant the implementation of the peak fitting analysis. The signal pathologies analysis instead counted the number of times that the PMT signal crossed the threshold for the trace. A histogram is generated from the number of threshold crossings per trace, Figure 3.10. For traces which included a single  $^{55}\text{Fe}$  X-ray event, the centroid for the number of threshold crossings was 116.3, with a  $\sigma$  of 14.4 counts. With the assumption that there were a maximum of two  $^{55}\text{Fe}$  events

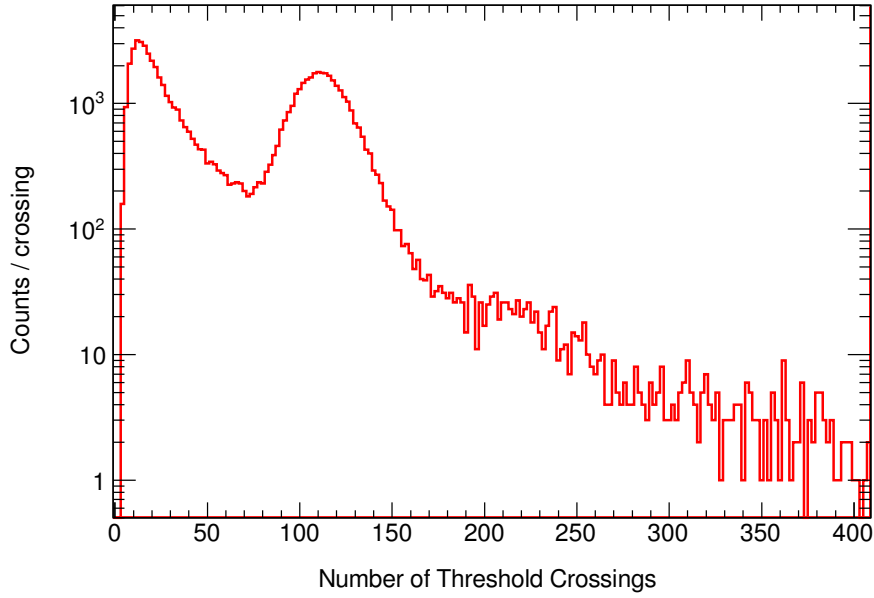


**Figure 3.10.** Total number of threshold crossings per trace (red). The centroid and  $\sigma$  for the  $^{55}\text{Fe}$  peak are 116.3 and 14.4 crossings per trace, respectively. The double- $^{55}\text{Fe}$  peak is visible at  $\sim 230$  threshold crossings, and the upper limit of the analysis is set at 276 crossings.

per trace, a cut can be placed at 276 threshold crossings per trace, corresponding to twice that of a single  $^{55}\text{Fe}$  peak plus three- $\sigma$ .

The third criteria was implemented to reject traces with a high multiplicity of events. An event refers to the event envelope which contains the PMT pulses from a single event as determined by the gate time,  $T_g$  of the analysis. For traces with a single  $^{55}\text{Fe}$  event, the average multiplicity was found to be 4.65, with a Poisson distribution. For an acceptance rate of 99% of all single  $^{55}\text{Fe}$  events, the multiplicity limit is 11 events per trace. The multiplicity limit is subsequently set at 12 events to allow for one additional  $^{55}\text{Fe}$  X-ray in the trace, eliminating 0.4% of traces from the data set.

The final criterion limited the total time spent beyond the trace threshold. This was designed to eliminate traces that had a wandering baseline throughout the trace, such as the red curve in Figure 3.8. Using the same methods as the previous three criteria, a limit of no more than 16.64  $\mu\text{s}$  beyond threshold was determined, with an efficiency of eliminating 0.1% of all traces from the data set.

**Table 3.3.** Using the analysis of spurious events from the single-phase Ar detector, criteria to accept non-spurious traces were determined.

Cut Description	Cut Criteria	Trace Rejection
$^{55}\text{Fe}$ Events per Trace	$\leq 2$	1 acceptable trace in 30,000
Threshold Crossings per Trace	$\leq 276$	0.5%
Event Multiplicity per Trace	$\leq 12$	0.4%
Time Beyond Threshold per Trace	$\leq 16.64 \mu\text{s}$	0.1%
Combined Cuts		0.73%

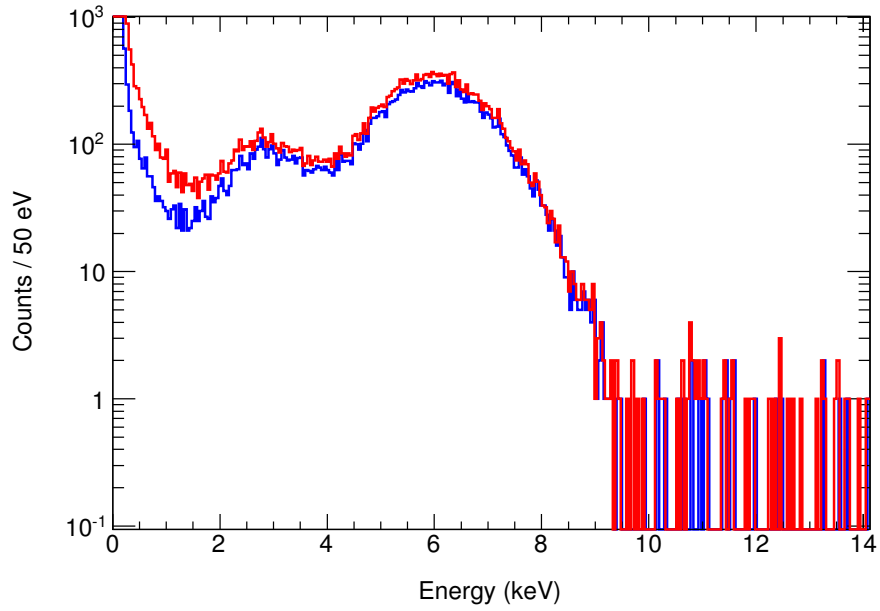


**Figure 3.11.** Event integrals for events occurring in all traces (red) and traces that pass the signal pathologies analysis (blue). There are some  $^{55}\text{Fe}$  events which are rejected, but the events mainly consist of spurious non-source correlated events.

The analysis criteria are summarized in Table 3.3, with the effects on the spectrum shown in Figure 3.11.

### 3.7 Radial Dependence

An alternative configuration for detector characterization utilizes a movable source arm with a collimated  $^{55}\text{Fe}$  source attached to it. This arm allows the  $^{55}\text{Fe}$  source to be translated radially. In this configuration, the height of the active volume was decreased from 12 cm to 9 cm in order to accommodate the additional components in the detector. The drift electric field increased from 0.25 kV/cm to 0.333 kV/cm, and the fraction of X-rays interacting in the primary and secondary region became 87% and 5.3%, respectively. The detector response function was experimentally determined by radially sweeping the  $^{55}\text{Fe}$  source.

Due to the difference in size between the PMT and the field cage, there was a radial dependence of the light collection on the location where the scintillation light was produced. An optical model was developed to calculate the light collection efficiency for the PMT as a function of radius from the center axis. The optical model calculates the geometrical collection of the electroluminescence light as the electrons drift through the secondary region. While there are additional variations of light transmission as a function of incident angle, the effect is small compared to

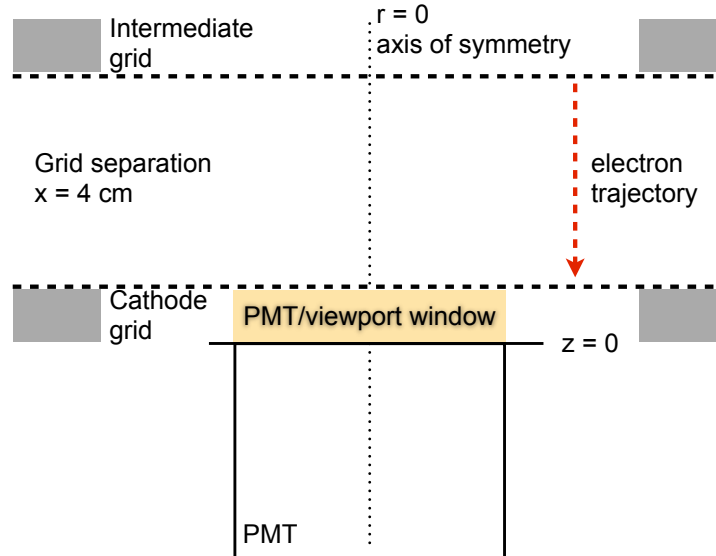


**Figure 3.12.** Schematic of the geometry used for the optical response model. The PMT diameter is 4.6 cm, and the PMT/viewport window thickness is 7.35 mm. The light collection efficiency is calculated as a function of radius and integrated over the electron track ( $z$ ).

the geometric effects and not needed for this model. A schematic of the detector geometry used in calculating the geometric response is shown in Figure 3.12.

The PMT surface is divided into small voxels, and at each point along the electron track the projection of the area of the PMT surface voxel normal to the event position is calculated as:

$$dA = r \partial r \partial \phi \cos \theta, \quad (3.2)$$

where

$$\cos \theta = \frac{t - z}{D}, \quad (3.3)$$

$t$  is the thickness of the PMT/viewport window of 7.35 mm,  $z$  is the position along the electron track, and  $D$  is defined as:

$$D = \sqrt{(t - z)^2 + (R - r \cos \phi)^2 + (r \sin \phi)^2}, \quad (3.4)$$

which is the normal vector that points from the event coordinate  $(R, Z)$  to a point  $(r, \phi)$  on the PMT window. The fraction of light collected at the event radius is then calculated as the average solid angle covered by the PMT:

$$F(R) = \frac{\Omega(R)}{4\pi}, \quad (3.5)$$

where  $\Omega(R)$  is the average solid angle subtended by the PMT during the electron drift through the secondary region at a radius  $R$ .

As the electron cloud radius increases beyond the PMT radius, the light collection efficiency drops dramatically due to solid angle and reflections. To validate the optical model, a collimated  $^{55}\text{Fe}$  source was translated between 0 (chamber axis) and 4.5 cm in 0.5 cm steps and the normalized energy deposition was measured. Figure 3.13 demonstrates a good agreement between the optical model and the experimental results.



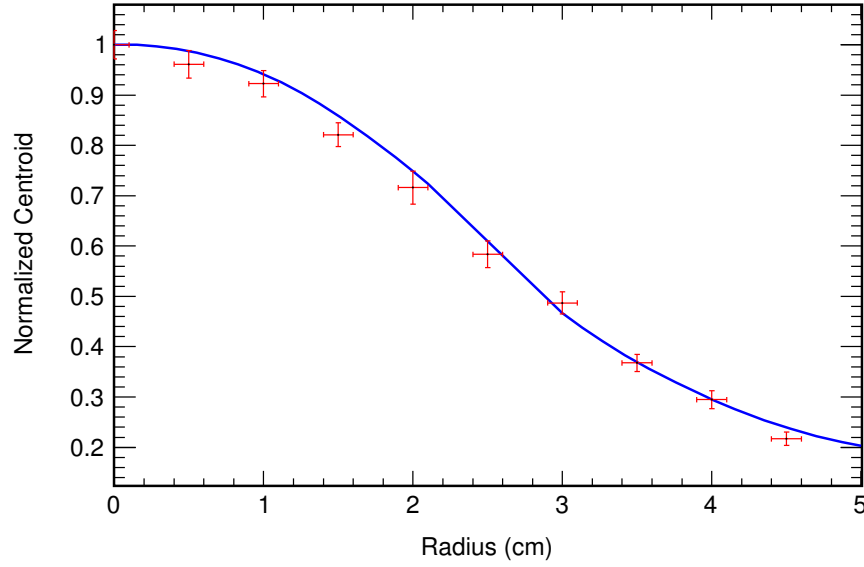


**Figure 3.13.** Normalized  $^{55}\text{Fe}$  centroid as a function of source radius. The theoretical prediction (blue) matches well with the experimental values (red).

### 3.8 Geant4 Simulation

As a systematic check of the detector, a Geant4 simulation [130] of the detector was developed. The model of the detector in Geant4 is shown in Figure 3.14, which can be compared to the photograph of the actual detector field cage in Figure 3.1. A collimated  $^{55}\text{Fe}$  source was simulated within the cathode hemisphere. A histogram is generated of the energy depositions within the active volume, which shows both the primary and escape X-ray peaks, with the same ratio of intensities as the experimental data, Figure 3.15.

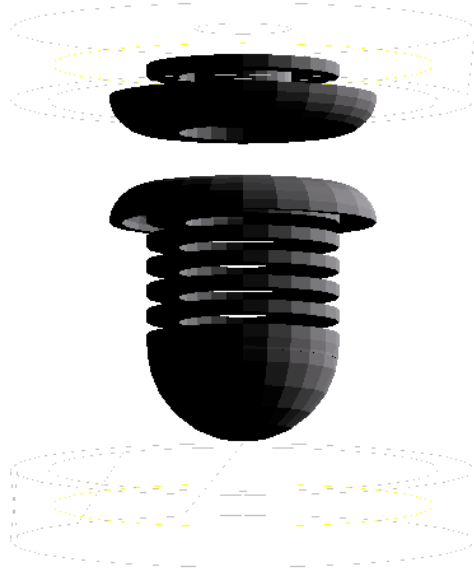


**Figure 3.14.** The modeled detector in Geant4 included the field cage rings, field shaping rings, and the grids which bounded the amplification region. This field cage is then put in the chamber and filled with argon and 1.5% nitrogen gas mixture.

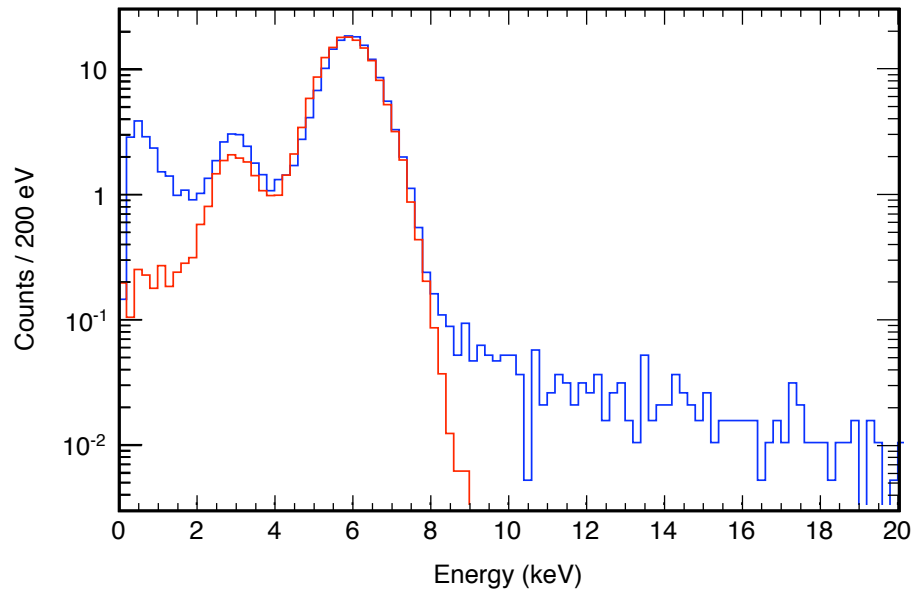


**Figure 3.15.** The simulated  $^{55}\text{Fe}$  spectrum (red) correctly predicts both the primary X-ray peak as well as the X-ray escape peak. The energy resolution is determined from the Poisson statistics and the analytical model determined in Section 3.7. The additional high energy tail in the measured spectrum (blue) is not expected in the simulated data as no backgrounds were modeled.

# Single-Phase Argon Nuclear Ionization Quench Factor Measurement

The single-phase Ar detector did not have single electron sensitivity and thus could not directly measure the ionization yield. An experiment was conducted, however, to measure the nuclear ionization quench factor in gaseous Ar using a 60 keV neutron generator [131] at Lawrence Livermore National Laboratory (LLNL). In order to measure the nuclear ionization quench factor, neutrons are generated in the  ${}^7\text{Li}(p,n){}^7\text{Be}$  reaction and allowed to elastically scatter off the gaseous Ar target. In the experiment, the neutrons deposited up to  $\sim 13$  keVr of recoil energy, with the majority of the scatters depositing  $< 8$  keVr. The measured nuclear ionization quench factor cannot be directly compared to the atomic collision model, Section 2.3. The atomic collision model utilizes the TRIM algorithm [99], which was developed for the transport of ions in amorphous materials, and does not apply to materials of gaseous densities. It may still be an acceptable assumption that the nuclear ionization quench factor is approximately equal in gas and liquid Ar, because the energies and cross sections remain the same. In this Chapter, the experimental setup used for measuring the nuclear ionization quench factor in gaseous Ar is discussed in Section 4.1. A discussion of the details for the neutron generation using the 60 keV neutron generator [131] is provided in Section 4.2. Results obtained from this experiment are discussed in Section 4.3 and compared

with the predictions of the atomic collision model, Section 4.4.

## 4.1 Experimental Setup

Measurement of the nuclear ionization quench factor was made using a portable neutron generator, Section 4.2. The single-phase Ar detector was self-contained and placed on a cart so it could be moved to the experimental location, Figure 4.1. The experiment took place in a classified area of LLNL, so no photographs of the setup can be provided. The experimental schematic generated in MCNP is shown in Figure 4.2. The experiment took place in a large concrete dome, with an inner diameter of  $\sim 22$  m and a wall thickness of  $\sim 2$  m. The detector was placed 2 m from the concrete wall and 1 m from the neutron source. Four configurations were used for data taking: beam off background, beam on with no attenuation, beam on with a 5 cm Pb shield to block gamma rays, and beam on with 12.5 cm poly shield for measuring the gamma ray backgrounds. The pulsed nature of the neutron source allowed for a reduction of backgrounds by a factor of 50 based on a 2% live time. The results obtained from the experiment apply to gaseous argon, and are thus not directly relevant to the atomic collision model, Section 2.3, but they still provide a limited validation of the model.

## 4.2 Neutron Generation

Using the  ${}^7\text{Li}(p,n){}^7\text{Be}$  reaction and an incident 1.93 MeV proton beam, neutrons are generated between 0 and 135 keV [132, 133, 131]. Neutrons are generated with an energy and angular distribution, Figure 4.3, which results in a broad energy spectrum incident on the Ar detector.

The neutrons generated from the  ${}^7\text{Li}(p,n){}^7\text{Be}$  reaction span multiple resonances of  ${}^{40}\text{Ar}$ , which results in broad detected recoil spectra, Figure 4.4. The maximum amount of energy that a neutron can deposit in a single recoil,  $T_{\text{ArMax}}$ , is

$$T_{\text{ArMax}} = \frac{4mM}{(m+M)^2} E_n \approx 0.095 E_n, \quad (4.1)$$

where  $m$  is the mass of the neutron,  $M$  is the mass of the argon, and  $E_n$  is the

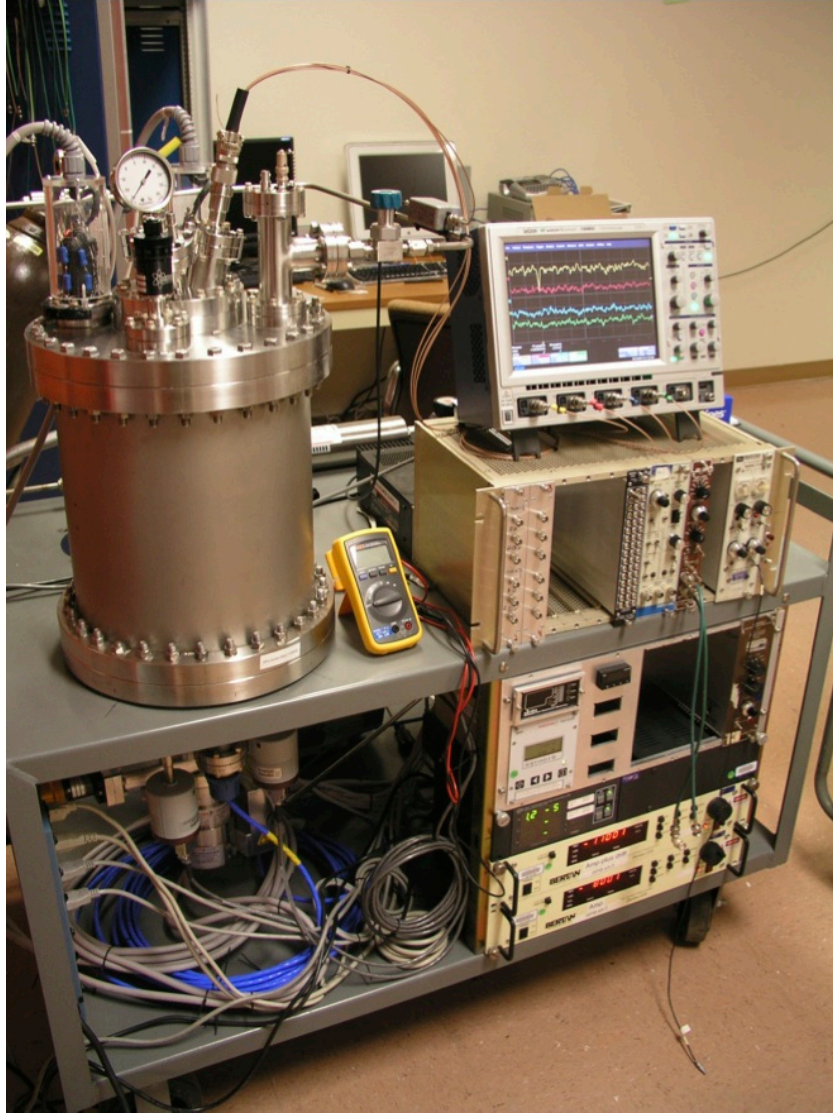


**Figure 4.1.** The single-phase detector was housed on a cart for ease of transportation. The oscilloscope shown in the picture was not used in the experiment. The high voltage feedthroughs entered the chamber from the top, while the pressure gauges and turbo pump were mounted below the detector. The PMT was mounted outside of the chamber, with a Quartz viewport looking into the amplification region.

energy of the incident neutron. For 135 keV neutrons, the maximum recoil energy is calculated to be  $\sim 13$  keVr. With a gaseous Ar detector, multiple scatters do not have to be taken into account as the mean free path of the neutrons is  $\sim 10$  m at an Ar pressure of 400 torr.

The detector is placed 1 m from the neutron source, which provides a neutron

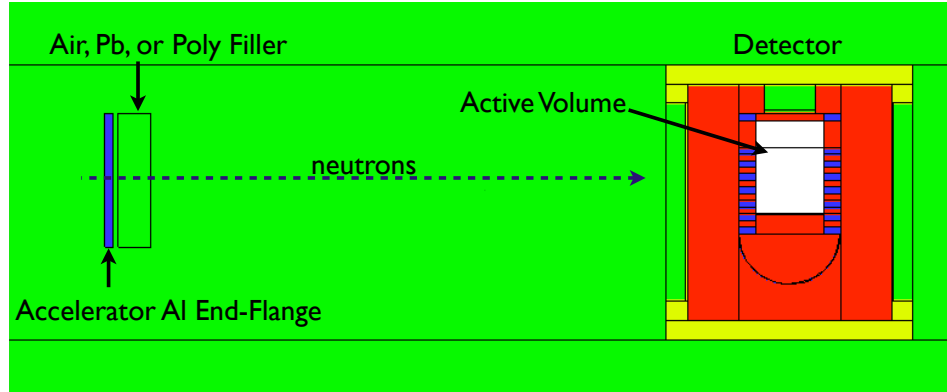


**Figure 4.2.** Schematic for measuring the ionization yield in LAr. The protons are accelerated toward a Li target, where they are generated with an angular and energy distribution. The neutrons were uncollimated and entered the detector with energies up to 135 keV, Section 4.2.

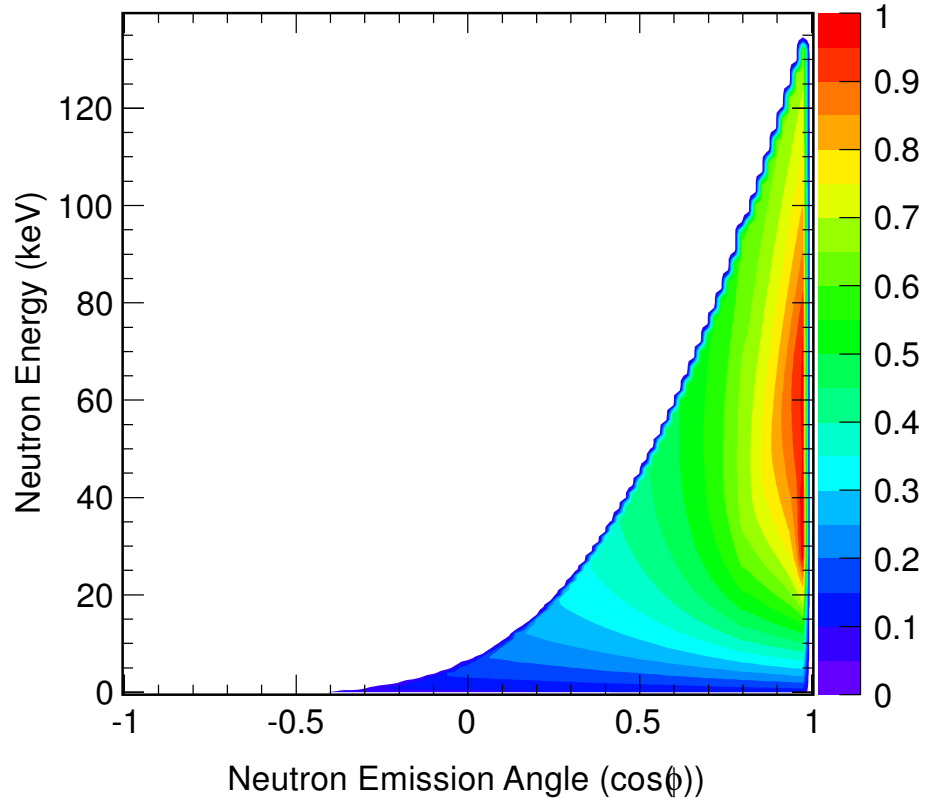


**Figure 4.3.** Neutron distribution calculated for 1.93-MeV incident protons. The sharp energy cut-off at each angle is due to the kinematic limits set on the reaction, limiting the maximum energy transfer to the exiting neutron.

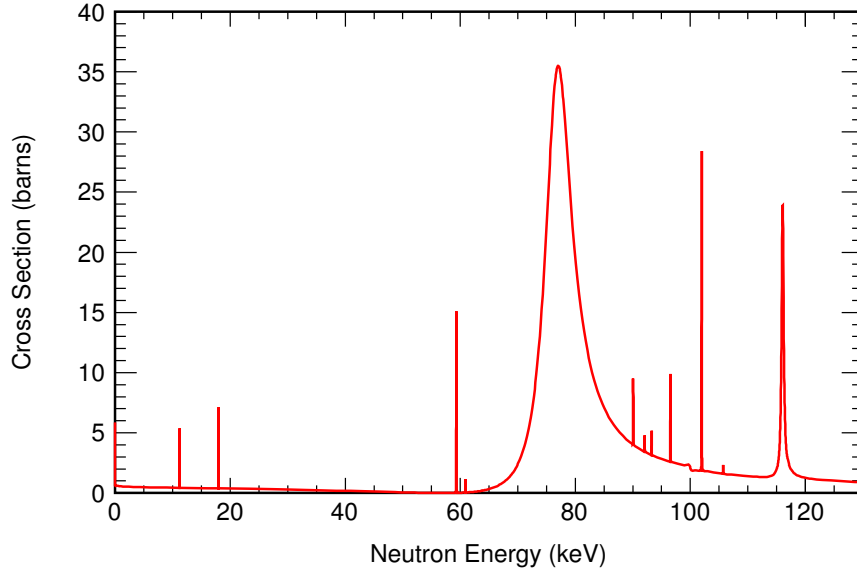


**Figure 4.4.** Cross section for neutron-elastic scatter on  $^{40}\text{Ar}$ . The 80 keV resonance is sufficiently broad such that a neutron incident at the upper energy end of the resonance can deposit the maximum energy possible in elastic scattering and still remain within the resonance. The width of the 80 keV resonance results in a large number of multiple scatters within the detector, which must be limited or accounted for.

spectrum incident on the detector shown in Figure 4.5. While most of the Ar recoils are generated by neutrons within the 80 keV resonance, the higher energy neutrons extend the Ar recoil spectrum up to  $\sim 13$  keVr, Figure 4.6. The portable neutron generator, Figure 4.7, was designed for active detection of shielded special nuclear materials (SNM) and has a neutron yield of  $5 \times 10^6$  neutrons/s at a repetition rate of 100 Hz. More details on the neutron generator performance are provided in Table 4.1. The portable neutron generator produces protons using an electron cyclotron resonance (ECR) source and accelerates them with a compact radiofrequency quadrupole (RFQ). The internals of the portable neutron generator are shown in Figure 4.8.

### 4.3 Nuclear Ionization Quench Factor Results

To determine the nuclear ionization quench factor, three data sets were taken: a background data set, a data set with 12.5 cm of polyethylene shield to measure

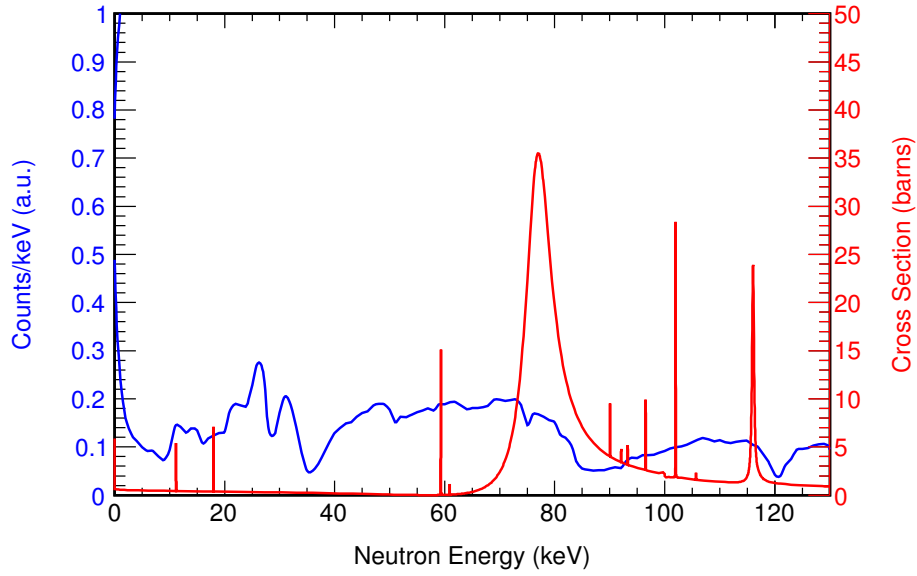


**Figure 4.5.** Predicted neutron spectrum (blue) incident on the single-phase Ar detector for on-axis operation with a 1.93 MeV proton beam. The  $^{40}\text{Ar}(\text{n},\text{el})$  cross section (red) is shown for reference.

**Table 4.1.** Specifications for the portable neutron generator used for the measurement of the nuclear ionization quench factor in gaseous Ar. This Table is reproduced from a previous publication by C. Hagmann [131].

Accelerated Ions	Protons
Reaction	$^7\text{Li}(\text{p},\text{n})^7\text{Be}$
Neutron Yield	$5 \times 10^6/\text{s}$
Output Beam Energy	1.93 MeV
Average Proton Current	1 $\mu\text{A}$
Repetition Rate	100 Hz
Pulse Width	30 $\mu\text{s}$
Wall Plug Power	2 kW
Instrument Weight	230 kg in 2 boxes
Target	Natural Li on a Ag backing, 1 $\text{mg}/\text{cm}^2$
Radiation Dose	$\sim 1 \text{ mRem/hr}$ at 2.5 m



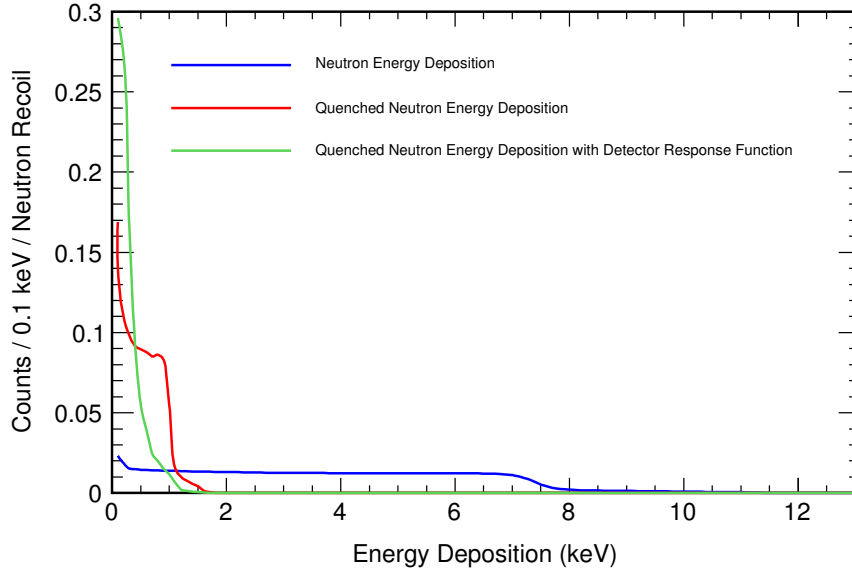


**Figure 4.6.** Predicted energy deposition spectrum (blue) assuming the incident neutron spectrum of Figure 4.5. Isotropic scattering was assumed with a maximum energy deposition calculated from Equation (4.1). The nuclear ionization quench factor, Chapter 2, is applied (red), and the detector response function, Section 3.7, is applied to the predicted quenched data (green).

the gamma backgrounds, and a data set with 5 cm of Pb shielding to measure the neutron recoil spectrum.

The energy scale was calibrated using the primary and escape X-ray peaks from the  $^{55}\text{Fe}$  source. The resulting data was time normalized and the background was subtracted from both the Pb-shield and polyethylene-shield data. The background subtracted data for the Pb and polyethylene are plotted together in Figure 4.9. The difference between the two spectra disappears at energies greater than  $\sim 1.8$  keVee, indicating an end-point of the nuclear recoil spectrum produced by the neutrons. The predicted recoil spectrum, Figure 4.6, puts the end-point at 13 keVr, which would result in a measured nuclear ionization quench factor of 0.138. The error is determined by the movement of the 1.8 keVee end-point based on the statistical fluctuations and the selected energy bin width. For a fluctuation of  $\sim 25$  counts, the end-point would be expected to move  $\pm 0.15$  keVee, resulting in a nuclear ionization quench factor of  $0.138 \pm 0.012$ .



**Figure 4.7.** The portable neutron generator used to irradiate the single-phase Ar detector for measurement of the nuclear ionization quench factor. The internals of the generator are shown in Figure 4.8.



**Figure 4.8.** The internals of the portable neutron generator used to irradiate the single-phase Ar detector. The generator was designed and built by AccSys, Inc., [134]. Protons are produced by an electron cyclotron resonance (ECR) source and accelerated by a compact radiofrequency quadrupole (RFQ).

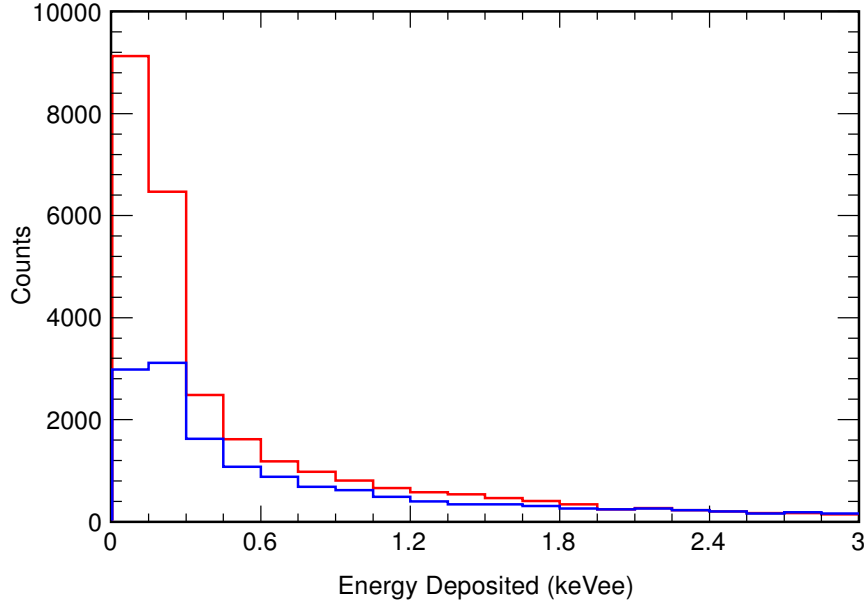


**Figure 4.9.** Background subtracted spectra for the data with the Pb shielding (red) and the polyethylene shielding (blue). The point at which the two spectra become indistinguishable is the end-point of the nuclear recoil spectrum. With the calculated end-point energy of 13 keVr, a nuclear ionization quench factor of  $0.138 \pm 0.012$  is calculated from this measurement.

## 4.4 Comparison with Model

To compare the measured value of the nuclear ionization quench factor with that of the atomic collision model, Section 2.3, corrections need to be made for electron recombination. The predicted nuclear ionization quench factor increases by the ratio of the electron collection efficiency for the nuclear recoil versus that of the  $^{55}\text{Fe}$  in gaseous Ar:

$$q_{ion}^{pred} = q_{ion}^{model} \frac{CE_{nucl}}{CE_{elec}}, \quad (4.2)$$

where  $q_{ion}^{pred}$  is the expected nuclear ionization quench factor,  $q_{ion}^{model}$  is the atomic collision model intrinsic ionization quench factor,  $CE_{nucl}$  is the predicted electron collection efficiency for 10 keVr nuclear recoils, and  $CE_{elec}$  is the predicted electron collection efficiency for  $^{55}\text{Fe}$ . The effect of the electron recombination on the nuclear ionization quench factor is small in gaseous Ar, as the electron collection efficiencies are approximately equal for the nuclear recoil and  $^{55}\text{Fe}$  due to the low

Ar densities and large electron thermalization lengths. Because the end-point energy of the recoil spectrum is beyond the predictions of the atomic collision model, a comparison with the 10 keVr prediction was used. For 10 keVr, the quench factor prediction is  $\sim 0.13$ , with electron recombination excluded. When the electron recombination is included in the calculation, the nuclear ionization quench factor can be determined for a variety of electron energies produced in  $Ar + Ar$  collisions. The corrected ionization yield model subsequently predicts that the nuclear quench factor should fall between  $\sim 0.11$  and  $\sim 0.15$  for electron energies of 1 eV and 10 eV, respectively. These predicted values agree with the measured value of  $0.138 \pm 0.012$ , which suggests that the ionization yield model makes a reasonably accurate prediction of the ionization yield.

Unfortunately, shortly after this experiment was performed, the portable neutron generator malfunctioned and was no longer available for follow-up ionization yield measurements with the dual-phase Ar detector.

# Gamma or Neutron Argon Recoils Resulting in Liquid Ionization (G/NARRLI) Detector

The Gamma or Neutron Argon Recoils Resulting in Liquid Ionization (G/NARRLI) detector, Figure 5.1 is a small dual-phase Ar detector to be used for measuring the nuclear ionization quench factor at low ( $< 10$  keV) energies [135]. A overview of the detector design is presented in Section 5.1, while the electrostatic model of the detector is described in Section 5.2. Techniques and methods used for wavelength shifting the Ar scintillation light are described in Section 5.3. A discussion of the operation of the detector and the slow control system is presented in Section 5.4. The event characteristics and signal analysis are presented in Sections 5.6 and 5.7, respectively. A discussion of the means of measuring and achieving the required purity of the LAr is provided in Section 5.8. Calibration of the detector using single liquid electrons is described in Section 5.9.

## 5.1 Design of the G/NARRLI Detector

The G/NARRLI detector consists of  $\sim 100$  g of LAr within the primary volume, a gaseous secondary volume above the primary volume, and 1 kg of LAr surrounding the primary volume. The primary volume is 3.75 cm high and 5 cm in diameter,

created by applying an electric potential to copper field rings which act as the active volume boundary. The field rings are held in place with ultra-high vacuum (UHV) compatible glass-filled polyether ether ketone (PEEK) support rods. The cathode field ring has a stainless steel mesh with 30  $\mu\text{m}$  thick wires at a mesh density of 50 wires per inch. The anode is a stainless steel field shaping ring, with the same stainless steel mesh as the cathode. The extraction grid is fabricated with 15  $\mu\text{m}$  stainless steel wire on a copper field ring at a 1 mm pitch. The cathode is usually held at a potential of -30 kV, while the extraction grid is held at a potential of  $\sim 20$  kV. The electric field strength in the primary region is  $\sim 2.5$  kV/cm. The secondary liquid/gas region is 2.5 cm tall. Approximately 4 kV/cm is needed for complete electron extraction [136, 137], while  $\sim 9$  kV/cm is needed for efficient electroluminescence [138, 139]. The liquid surface is held  $\sim 0.5 - 1$  cm above the extraction grid, which provides an electron extraction electric field of  $\sim 6$  kV/cm and an amplification electric field of  $\sim 9$  kV/cm in the gas. The detector is held in place using stainless steel support rods and is leveled prior to a detector run using bubble levels. The liquid height is verified using a capacitive liquid level meter, Section 5.4, and the event rise time, Section 5.6. The detector has four internal 1-inch diameter Hamamatsu 8520 PMTs modified for cryogenic operation [140]. The PMTs are placed behind a fused silica glass window which is coated with TPB, Section 5.3. The coating allows the UV Ar scintillation light to be wavelength shifted to longer wavelengths which can be efficiently detected by the PMTs.

The G/NARRLI detector is placed inside a 4.5 inch inner diameter cryogenic dewar produced by Cryofab [141], and the LAr is produced *in-situ* using an acoustic Stirling cycle cryocooler produced by Q-Drive [142]. A vacuum jacket is used to reduce the heat load on the system and increase the rate of LAr production. In order to keep the system clean, a SAES getter [143] and recirculation system are used to evaporate LAr, purify the Ar, and then re-condense the Ar within the cryostat. The experimental setup is placed on a cart, Figure 5.2, so that it can be conveniently moved to various locations for nuclear quenching measurements.

The PMT signal connections are made through Bayonet Neill-Concelman (BNC) feedthroughs, while the PMT high voltage (HV) is passed through and safe high voltage (SHV) feedthrough. In order to provide the high potentials (up

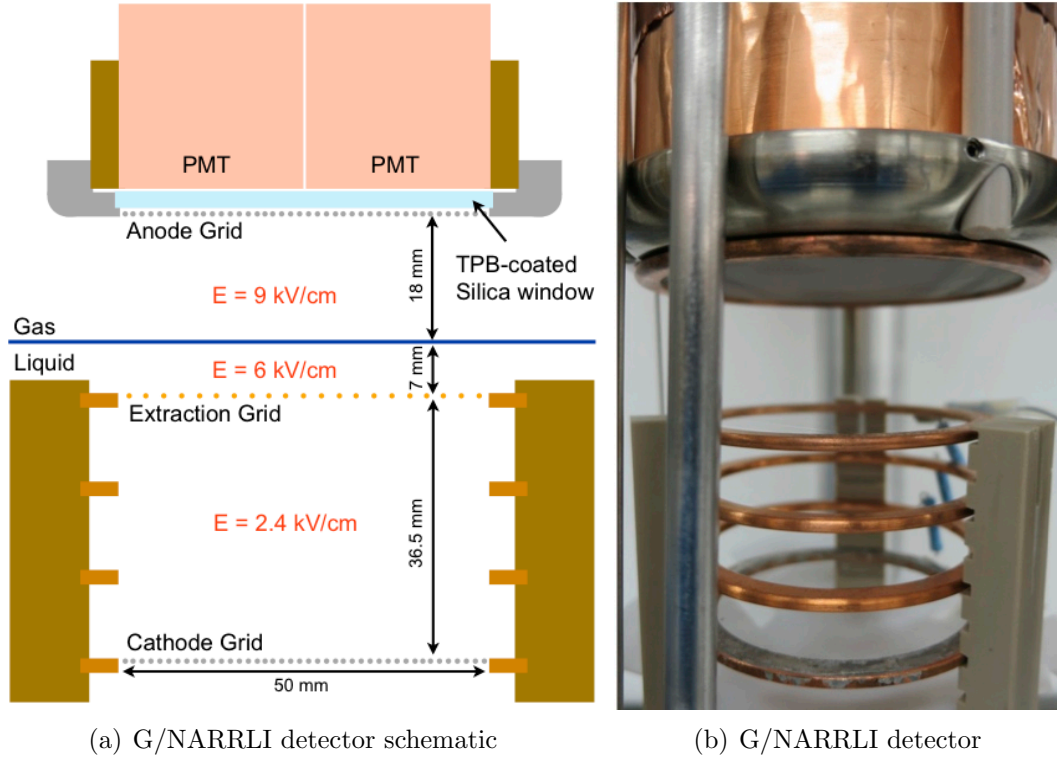


**Figure 5.1.** The G/NARRLI detector consists of a  $\sim 100 \text{ g}$  LAr primary volume in which the interaction occurs. Electroluminescence occurs in the amplification region and the proportional scintillation is detected by a PMT.

to  $-30 \text{ kV}$ ) required for the cathode and extraction grid, custom UHV compatible HV feedthroughs were fabricated. The high voltage wire is fed through a stainless steel tube and connected to the end of an internal ceramic HV feedthrough. The space inside the stainless steel tube is subsequently filled with silicone oil to provide resistance to electrical breakdown. The HV feedthrough is passed through a Swagelok feedthrough, with the internals (wire and oil) completely isolated from the detector.



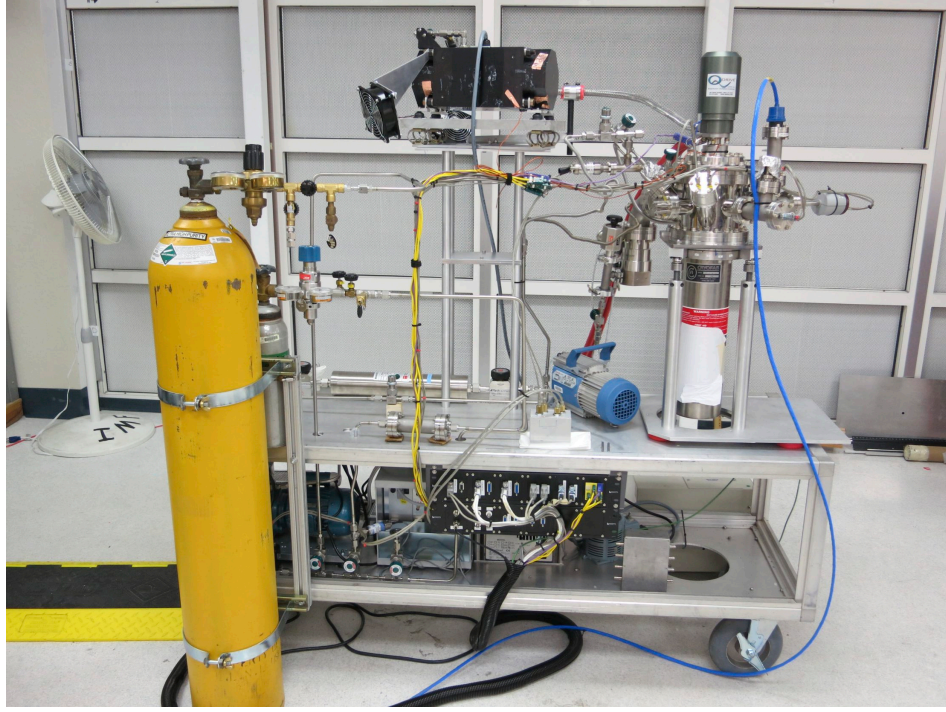


**Figure 5.2.** The G/NARRLI detector is placed on a movable cart for easy transportation to nuclear quenching measurement locations. The recirculation system is used to purify the Ar and keep the electron collection efficiency consistent over an extended period of time.

## 5.2 Electrostatic Model

### 5.2.1 COMSOL Model Setup for the G/NARRLI Detector

Understanding the electric field uniformity within the G/NARRLI detector is important for estimating the reduction of electron collection efficiency by edge effects within the active volume. An electrostatic model of the G/NARRLI detector was created to check the electric field uniformity within the active volume. The electrostatic model was prepared using COMSOL [144], a finite element analysis software package. The geometry was approximated as a 2-dimensional axially symmetric detector, Figure 5.3. The outer boundary defined by the aluminum support rods and the bottom aluminum support plate are set to ground in the simulation. The cross sections of the field rings are assumed to be rectangular, which increases the effect of the electric field near the corners of the field rings. In the experiment, the corners of the field rings are rounded off to decrease the electric field strength near



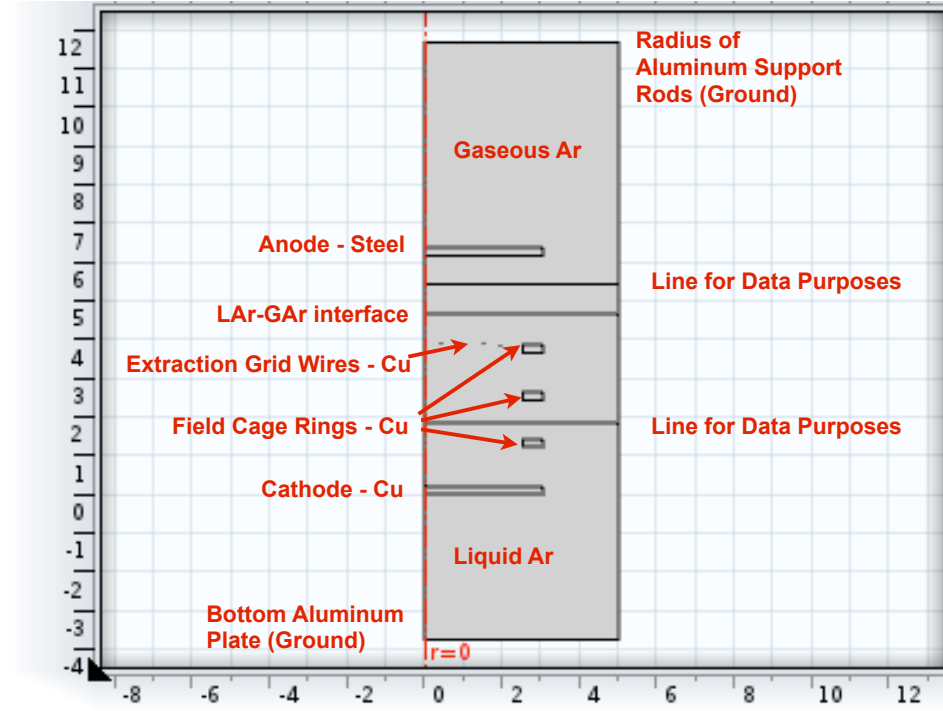


**Figure 5.3.** An example of the simplified geometry of the G/NARRLI detector. In this instance, the cathode and anode are solid and there is an extraction grid, but these components can be altered in different simulations.

the field rings. Because the rounding of edges is not captured by the simulation, an upper limit of the edge effects can be attained. The geometry is meshed, with the bulk of the calculations performed in close proximity to the grids and field cage rings, Figure 5.4.

### 5.2.2 Study of the Current G/NARRLI Design

The current geometry of the G/NARRLI detector is well described by the geometry shown in Figure 5.3, aside from the missing grids at the anode and cathode. The voltages applied to the field cage are as follows: -30 kV on the cathode and -20 kV on the extraction grid HV feedthrough, which produces -22.5 kV on the extraction grid due to the voltage divider between the cathode and extraction grid. The complete voltage potential map can be seen in Figure 5.5.

Electron field emission can be a source of low energy backgrounds within a dual-phase detector, and can also be a contributor to sparking. Electric field

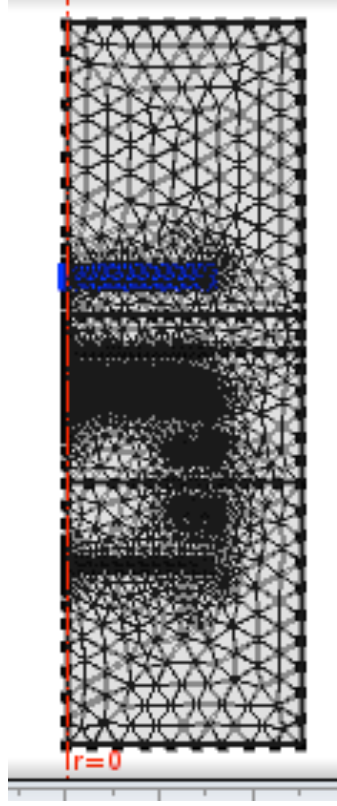


**Figure 5.4.** The mesh density increases around the extraction grid, where the diameter of the wires is  $30\text{ }\mu\text{m}$ .

breakdown and electron field emission can both occur near the small-diameter grid wires. Local electric fields near the cathode, extraction grid, and anode were simulated. The local electric field near the extraction grid is shown in Figure 5.6. The electric field near the extraction grid is much larger than that on the cathode and thus it is of primary concern for electron field emission. The local electric field near the anode wires is larger than that of the extraction grid, but no field emission can occur there since they are held at a ground potential. In order to prevent any electron field emission from the wires, the wires should also have an ultra-smooth finish.

It is important to understand the uniformity of the electric field to estimate the fraction of events in which electrons are lost to edge effects. Figures 5.7 and 5.8 show the radial and axial components of the electric field throughout the detector. The axial ( $z$ ) component of the electric field constitutes the drift field within the active region, the extraction field in the liquid above the extraction grid, and the

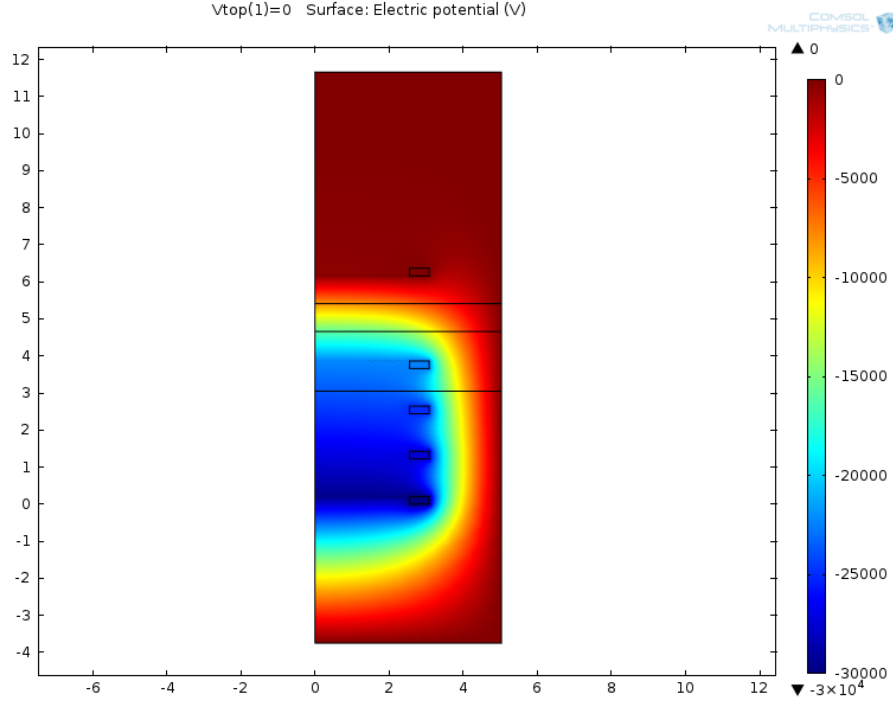


**Figure 5.5.** Voltage potential surface plot for the current G/NARLI detector.

amplification field in the gas below the anode. The radial component of the electric field should be zero within the active region to prevent the radial drift of electrons out of the active region or into the field rings. The increased radial component of the electric field due to the edge effects extends  $\sim 0.75$  cm inward from the field cage rings. For complete collection of the electrons produced in an ionization event, the event needs to occur within the radius of 1.75 cm around the detector axis, which reduces the active region volume by  $\sim 50\%$ .

The COMSOL software can also be used to perform particle tracking within the simulation toolkit. Electrons generated near the cathode can be tracked up to the height of the anode, as shown in Figure 5.9. The paths of the electrons show a slight divergence in the inner ( $< 1.75$  cm radius) region, with occasional large divergence for a radius between 1.75 cm and 2.5 cm, resulting in departure from the active region or collision with the field rings.

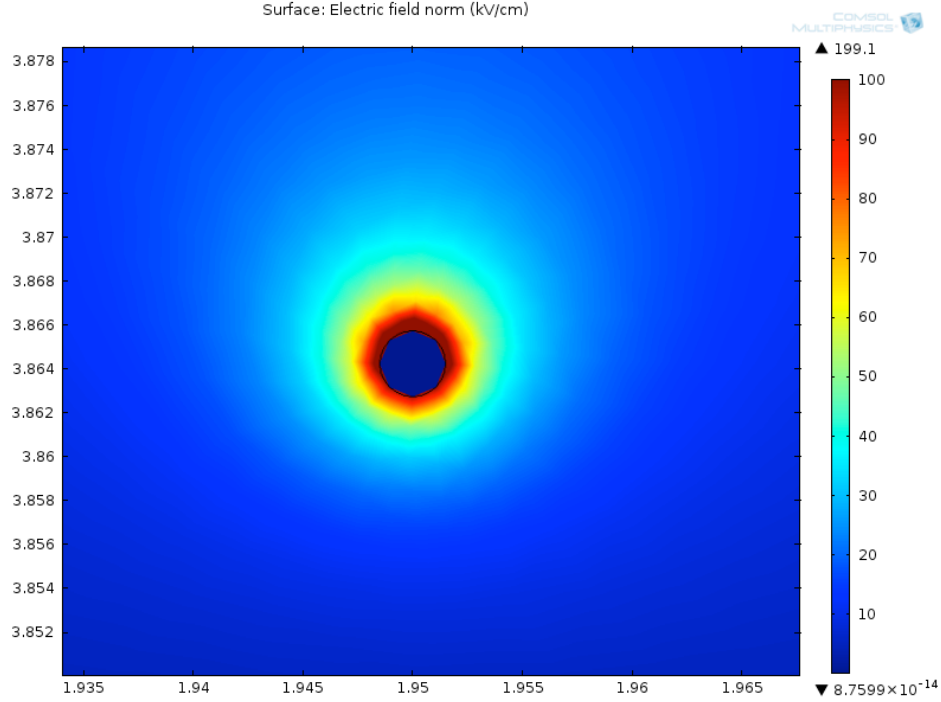


**Figure 5.6.** Local electric field near an extraction grid wire. The circular wire is modeled as an octagon due to the finite size of the mesh elements within the simulation. Due to the high electric fields near the extraction grid wires, ultra-smooth finished wires should be used for the grid to prevent electron field emission or electric breakdown.

### 5.3 Wavelength Shifting

The G/NARRLI detector operates with pure Ar detector medium and a tetraphenyl butadiene (TPB) coated window for wavelength shifting. Two methods used to deposit the TPB on windows and reflectors are (1) vacuum evaporation of TPB and (2) dissolving TPB in toluene and spraying or brushing the mixture on the window or reflector surface [79]. The spraying method can be performed without fabrication of a vacuum evaporator unit, but the TPB coating becomes nonuniform due to the variation in TPB concentrations. Vacuum evaporation requires the fabrication of a vacuum chamber, which is more costly and time intensive. The coatings produced through vacuum evaporation are much more uniform and reproducible when compared to the spray application technique. Figure 5.10 shows a comparison of the TPB layers under microscope through vacuum evaporation and the spraying technique. In the G/NARRLI detector, the window was

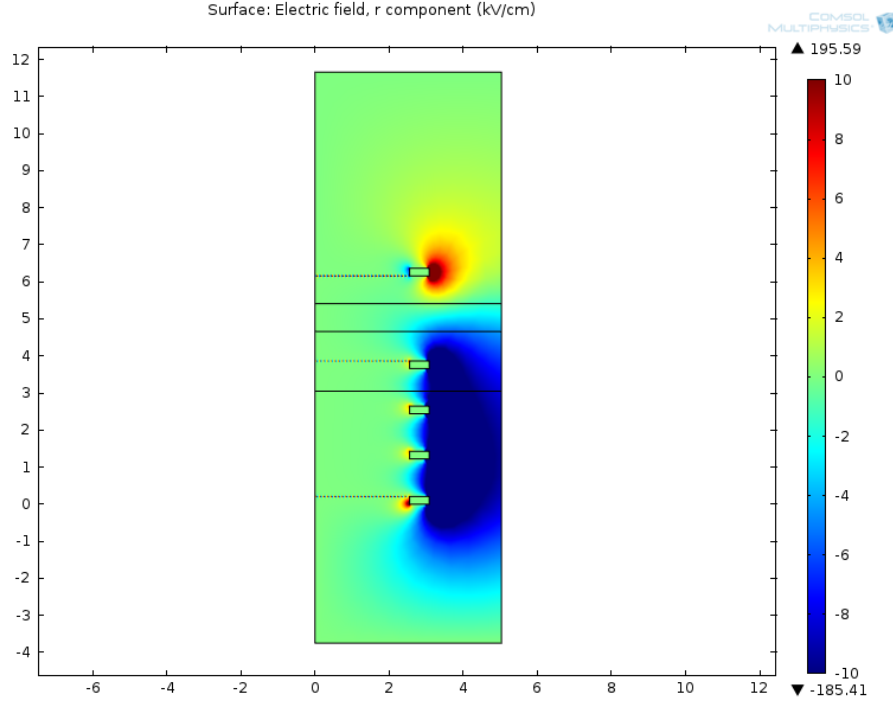


**Figure 5.7.** The radial component of the electric field within the active region is  $\sim$ zero for radii  $< 1.75$  cm. At greater radii it becomes significant and causes edge effects, which reduce the electron collection efficiency.

coated using the vacuum evaporation process, Section 5.3.1. It is also possible to utilize reflectors coated in TPB to wavelength shift the scintillation light, and then reflect it back to the PMTs.

### 5.3.1 Vacuum Evaporation of TPB

A vacuum evaporator has been constructed for coating the windows and reflectors with TPB [145]. The vacuum evaporator, shown in Figure 5.11, has a large central opening at the top along with three ports used for the electrical feedthrough, pumping connections and a viewport. The chamber is pumped down to a base pressure of  $\sim 10^{-3}$  Torr using a scroll pump. The TPB is held in a crucible, Figure 5.12, which is connected through the electrical feedthrough to a variac and transformer for applying current to the crucible.

Prior to filling the crucible, the TPB weight is measured using a Citizen CT603 0.2 mg resolution scale [146]; this measurement determines the subsequent coating

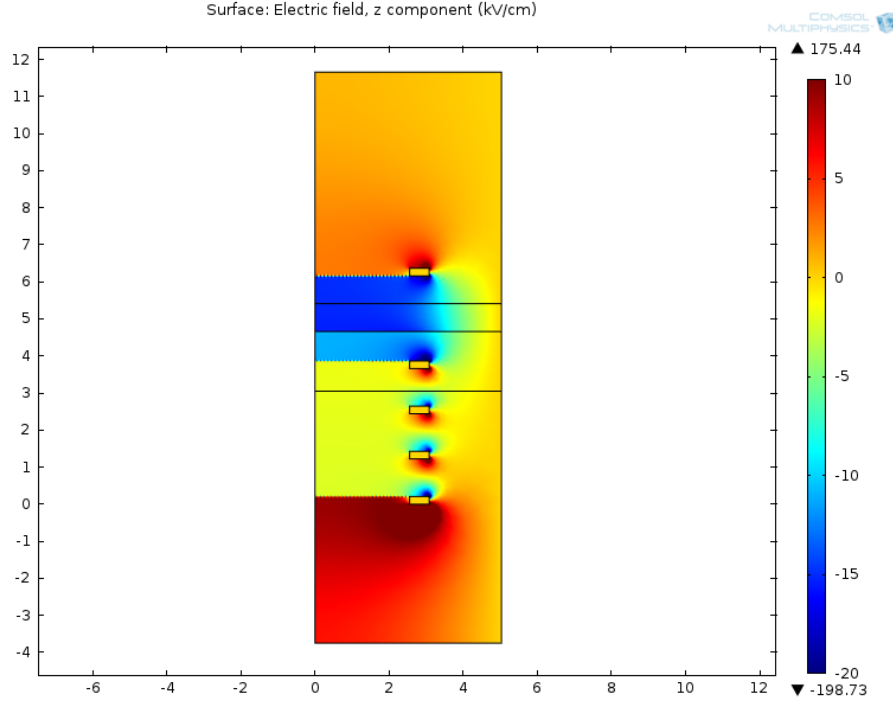


**Figure 5.8.** The axial component of the electric field within the active region shows the expected increase in the transition between the active LAr region and extraction LAr region, and another increase in the transition to the gaseous amplification region.

thickness. The TPB evaporates into the chamber at a temperature of 208°C, into a  $\sim 2\pi$  solid angle. The coating thickness is calculated based on the standoff distance of the part being coated:

$$t_{TPB} = \frac{M_{TPB}}{4\pi d_W^2}, \quad (5.1)$$

where  $t_{TPB}$  is the TPB coating thickness,  $M_{TPB}$  is the mass of TPB in the crucible, and  $d_W$  is the distance from the crucible to the window or reflector. With the chamber at the base pressure of  $\sim 10^{-3}$  Torr and continuously evacuated, the current flowing through the crucible is slowly increased, allowing the temperature of the crucible and TPB to stabilize. The 208°C melting temperature of TPB corresponds to a current of  $\sim 45$  A. As the TPB starts to evaporate, the pressure within the chamber rises slowly until it peaks at a few mTorr, Figure 5.13. When the pressure decreases to the base pressure, all of the TPB has been evaporated and the chamber may be opened. As an additional check, before opening the chamber,

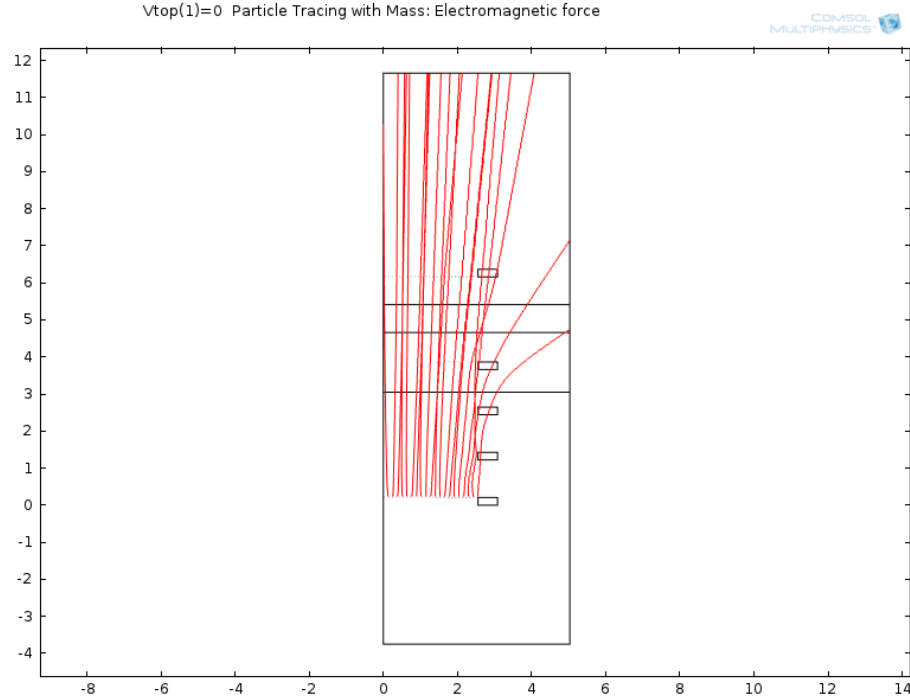


**Figure 5.9.** The paths of the drifting electrons are calculated in the COMSOL simulation. There is minimal divergence for events with a radius  $< 1.75$  cm and a large divergence for events with a radius between  $1.75$  cm and the edge of the active region. For events with a radius  $> 1.75$  cm, the drift paths have the possibility of colliding with the field rings or exiting the active volume, resulting in a decreased electron yield.

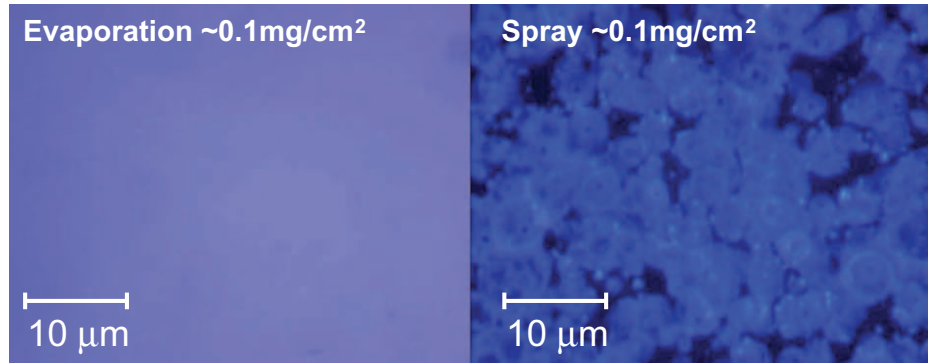


**Figure 5.10.** Surface structure of vacuum evaporated and sprayed TPB on 3M™ foil under the microscope, illuminated by 250 nm light [79].



**Figure 5.11.** The vacuum evaporation system is used for coating both reflectors and windows with TPB to wavelength shift the Ar scintillation light. The chamber is pumped down to a base pressure of  $\sim 10^{-3}$  Torr before the crucible is heated to the melting temperature of the TPB.

the viewport is used to verify complete evaporation of TPB.

### 5.3.2 TPB Window Coating

When coating a viewport or a PMT window, the TPB layer needs to be sufficiently thick for high light conversion, but sufficiently thin to permit high transmission of the wavelength shifted light. Figure 5.14 [88], shows the light collection efficiency as a function of different TPB thicknesses. The optimal thickness for a window was determined to be  $\sim 0.05$  mg/cm<sup>2</sup>, with a 10-50% gain in light collection by using the vacuum evaporation process compared to the spraying technique. For



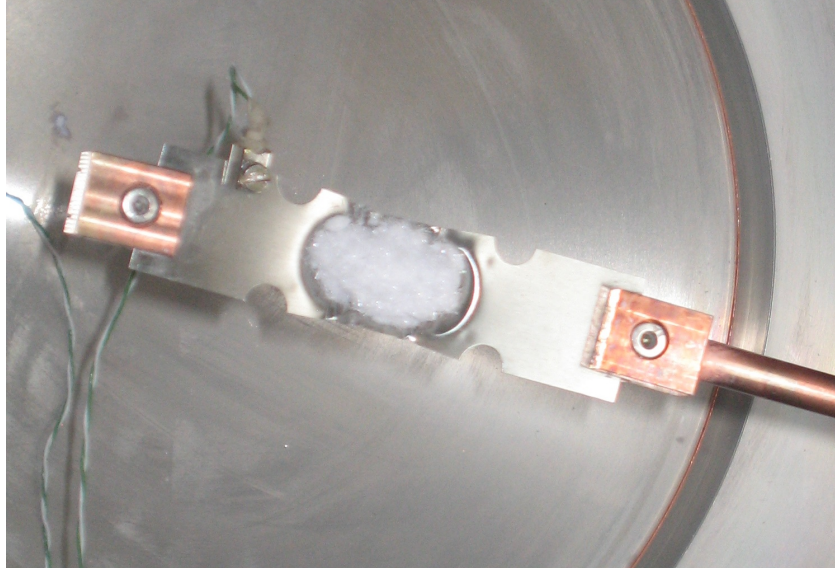


**Figure 5.12.** The TPB is loaded into a crucible heated by the flow of current. Evaporation of the TPB occurs once it reaches its melting point. Prior to filling the crucible, the TPB weight is measured to determine the coating thickness of the window or reflector, as given in Equation (5.1).

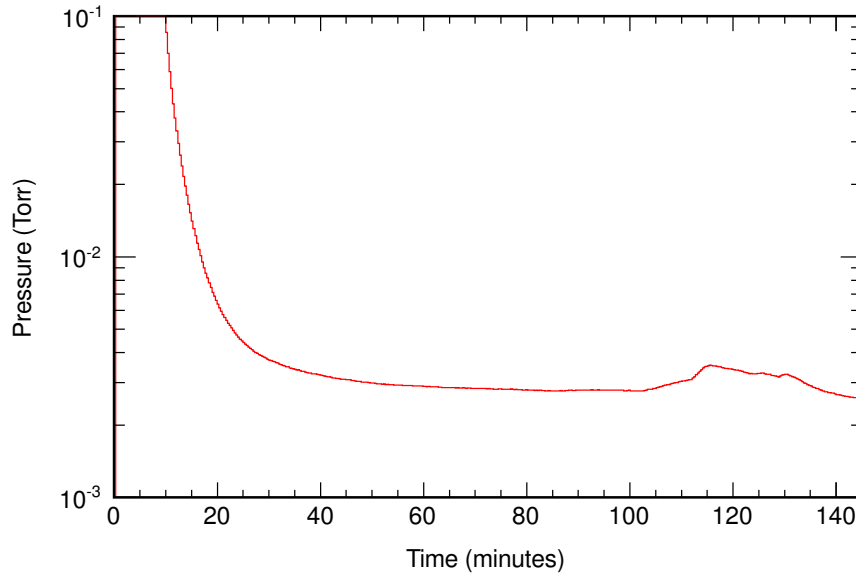


**Figure 5.13.** During the TPB coating process, the pressure remains stable, until the TPB evaporation starts. At this point, the pressure increases. Once all the TPB is evaporated, the pressure drops again. The vacuum pump is continuously operated during the coating process.

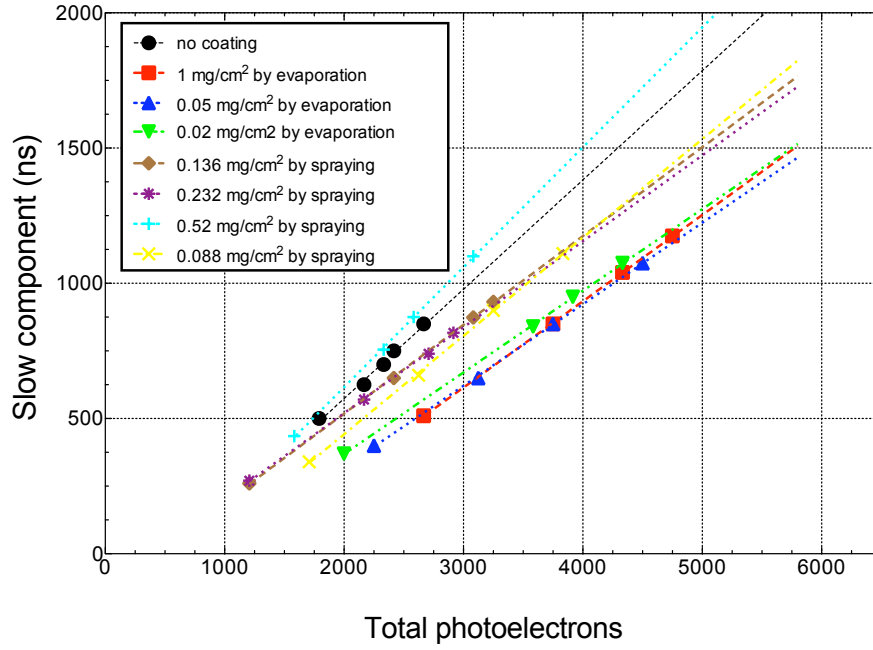


**Figure 5.14.** Number of photoelectrons as a function of time for various TPB thicknesses on a PMT window [88]. Vacuum evaporation produces more uniform TPB coatings, which increases the effectiveness of the wavelength shifting process. An optimal thickness for a window is  $\sim 0.05 \text{ mg/cm}^2$ .

the operation of the G/NARRLI detector, a fused silica window was coated with  $\sim 0.06 \text{ mg/cm}^2$  and placed between the PMTs and the amplification gas region. An example of a window coated with  $\sim 0.06 \text{ mg/cm}^2$  TPB through the vacuum evaporation process is shown in Figure 5.15.

### 5.3.3 TPB Reflector Coating

Two types of reflectors are used in the dual-phase Ar systems: a reflective foil made by 3M [147], and a polytetrafluoroethylene (PTFE) cloth called Tetratex (TTX) [148]. PTFE is a very good reflector of light, and the cloth allows for it to be easily coated and placed within the detector.

TTX is a better reflector of light at wavelengths below 375 nm than the 3M foil, Figure 5.16, but it is more difficult and expensive to obtain. With the membrane structure of the TTX, thin coatings ( $\sim 0.2 \text{ mg/cm}^2$ ) provide the highest light output from the reflectors. 3M foils require a much thicker TPB coating to obtain

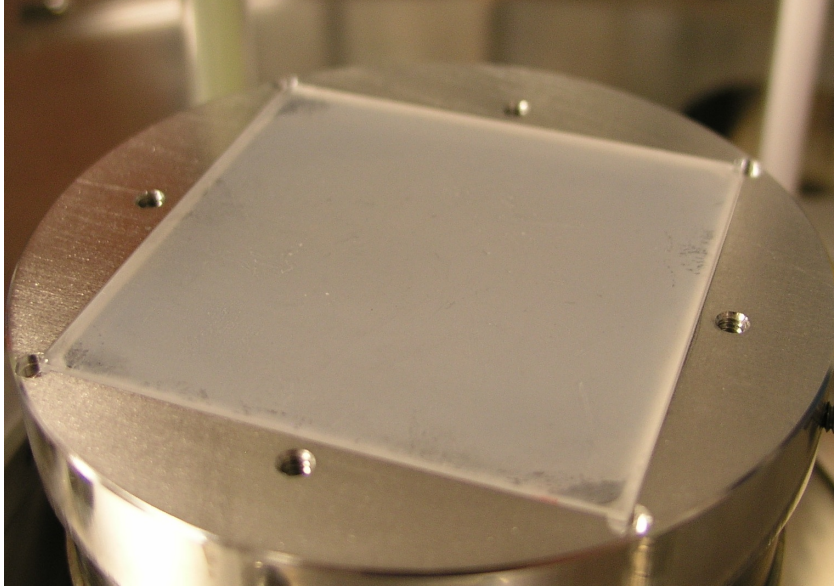


**Figure 5.15.** A window coated with  $\sim 0.06 \text{ mg/cm}^2$  of TPB using the vacuum evaporation system developed at the Pennsylvania State University.

similar results. The optimal coating areal density was previously measured to be  $\sim 4 \text{ mg/cm}^2$ , Figure 5.17 [88]. As the thickness of the TPB coating approaches  $\sim 4 \text{ mg/cm}^2$ , the coating becomes brittle and less maneuverable within the detector; therefore, an optimal thickness is set between  $2 \text{ mg/cm}^2$  and  $3 \text{ mg/cm}^2$ . 3M foil is used for the reflectors inside the G/NARRLI detector due to material availability. Shown in Figure 5.18 is a 3M foil reflector coated with  $\sim 2 \text{ mg/cm}^2$  of TPB, with and without UV lamp illumination to demonstrate the wavelength shifting property.

## 5.4 G/NARRLI Detector Operation

The G/NARRLI detector is first pumped down to a base pressure of  $\sim 10^{-6}$  Torr using a turbo pump backed by a dry diaphragm pump. For standard high purity operation, Section 5.8, the time required for the chamber pressure to increase to  $10^{-3}$  Torr after closing off the turbo pump with a gate valve is  $> 6$  minutes. A helium leak checker is available to detect leaks if modifications are made to the plumbing or the outgassing time is short. The argon flows through a SAES purifier [143] before entering the dewar. An additional small cylinder of  $^{37}\text{Ar}$  is mounted on

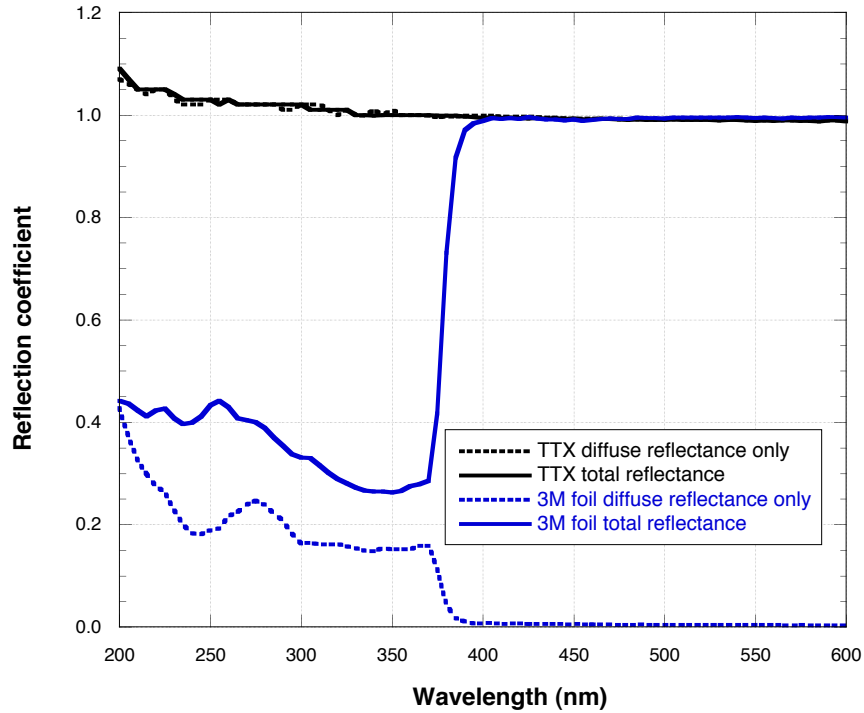


**Figure 5.16.** The two types of reflectors used are 3M foil and Tetratex (TTX) PTFE cloth. TTX cloth is a better overall reflector, especially at shorter wavelengths [88].

the cart for low energy calibration runs, Section 6.2. A schematic of the plumbing system is shown in Figure 5.19.

A Q-Drive 2S132K-FAR acoustic pulse tube cryocooler [142] is used to liquify the argon and fill the detector. The cryocooler is equipped with a 1 m long transfer tube, which allows for the coldhead to be placed at a distance from the compressor, Figure 5.20. The cryocooler generates  $\sim 20$  W of cooling power at 87 K, which is used to liquify the Ar as it flows into the chamber. A flow controller is used to hold the pressure stable as the Ar flows into the chamber and liquifies on the coldhead, Figure 5.21. The coldhead is housed inside a vacuum jacket which has a valve outside the chamber to allow for continuous pumping, if required. After liquifying on the coldhead, Ar flows down into the dewar until a pre-specified height is reached.

The liquid level is monitored using a capacitive liquid level meter, which measures the capacitance change between the outer tube and the inner rod as the liquid fills the level meter. The length of the liquid level meter is 110 mm, the

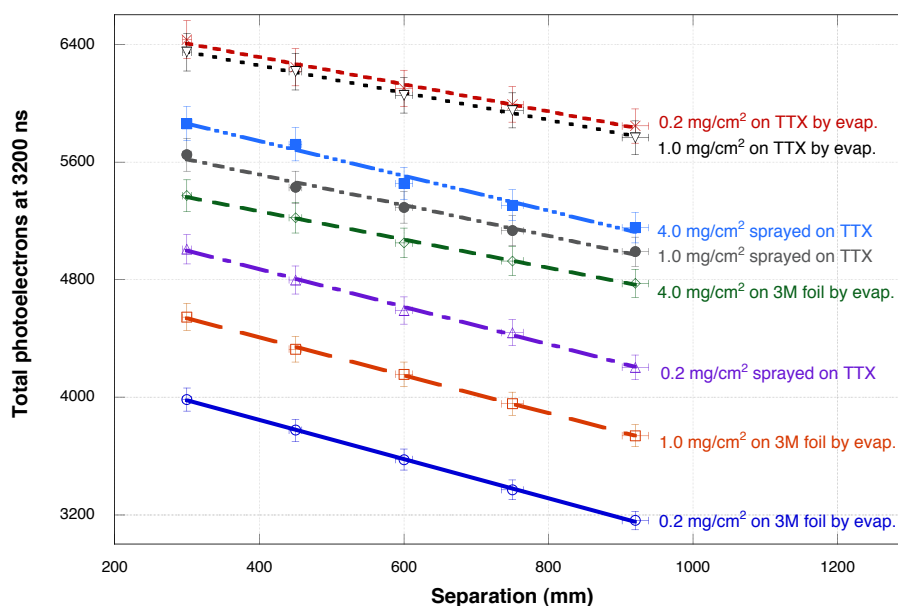


**Figure 5.17.** The TTX cloth is a better overall reflector and requires a thinner TBP coating than the 3M foil. This is primarily due to the membrane features of the cloth [88].

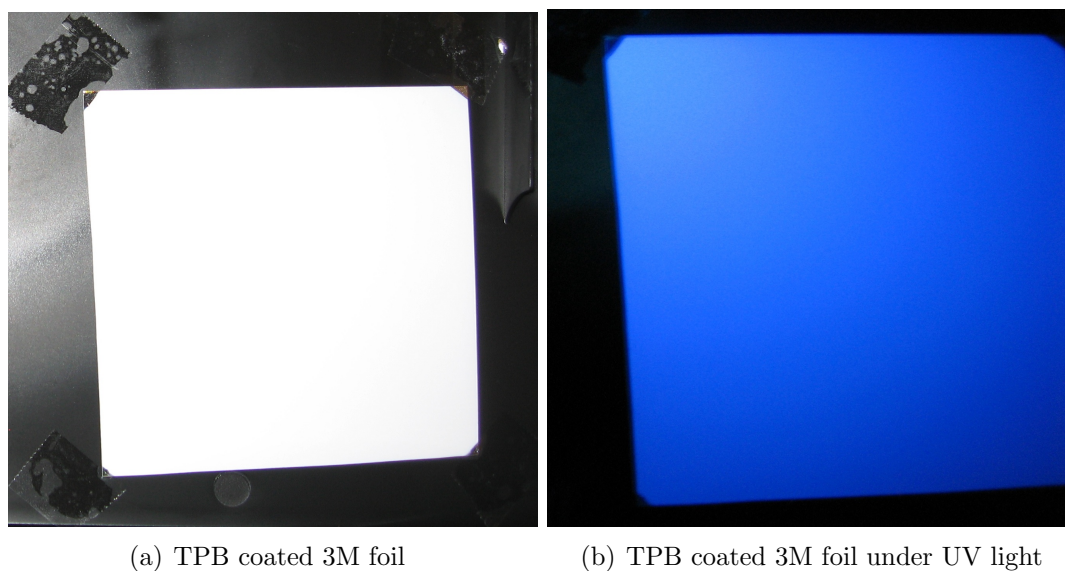


**Figure 5.18.** (a) 3M foil coated with  $\sim 2\text{mg}/\text{cm}^2$  of TPB; the corners of the foil are uncoated where the reflector was held in place inside the vacuum evaporator; (b) the reflector shown in (a) with UV light illumination. The UV light is converted to  $\sim 400\text{nm}$  and reflected from the 3M foil. There is no light visible on the corners of the foil where no TPB was deposited. The variation in light output is due to the non-uniform illumination from the UV lamp.

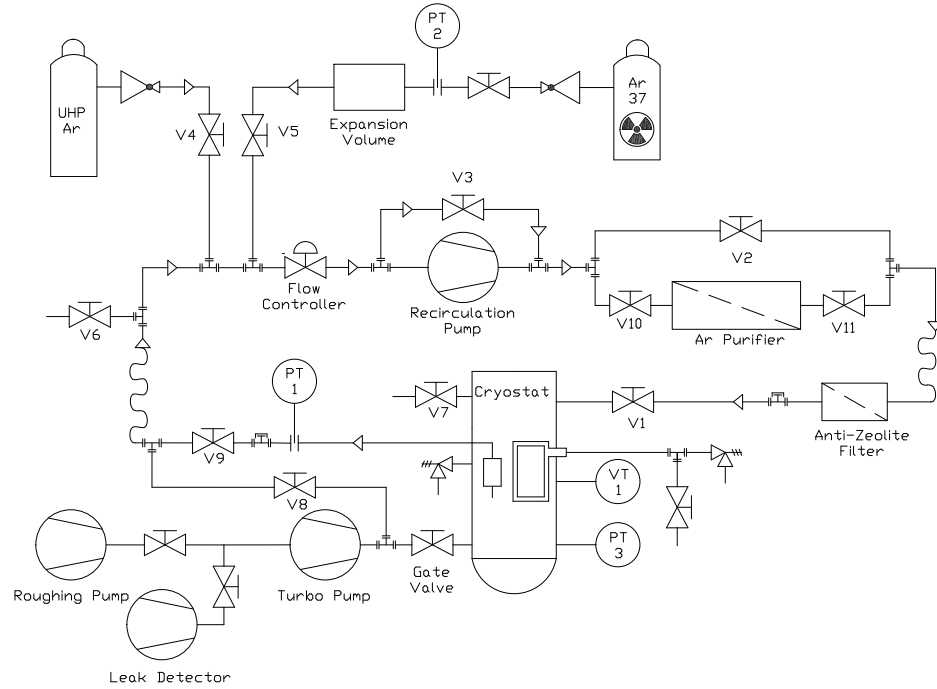


**Figure 5.19.** Plumbing schematic for the G/NARRLI detector. The straight lines represent fixed tubing, while the curved lines represent flexible tubing.

inner sensing rod is 1.5875 mm in diameter, and the inner diameter of the outer tube is 6 mm. The measured capacitance is  $\sim 4.6$  and  $\sim 6.4$  pF in gas and liquid argon, respectively. The base capacitances depend on the wiring connected to the level meter and must be corrected if the type or length of wiring changes. A capillary effect of an 8 mm rise in the liquid level inside the tube is expected, but the effect is calibrated out during operation. The calibration of the liquid level meter is measured to be  $\sim 0.015$  pF/mm with a mm accuracy in determining the height of the liquid. Once the capacitive liquid level meter measures the desired liquid level, the flow control stops the injection and the detector is ready for operation. Typical fill times are  $\sim 15$  hours, which occur overnight with the slow control system. The temperature of the condenser and the liquid level during a cooldown are shown in Figure 5.22.

In addition to monitoring the liquid level within the detector, resistance temperature detectors (RTDs) are placed on the condenser, the copper shield of the PMTs, and at the bottom of the dewar. There are two heaters within the system



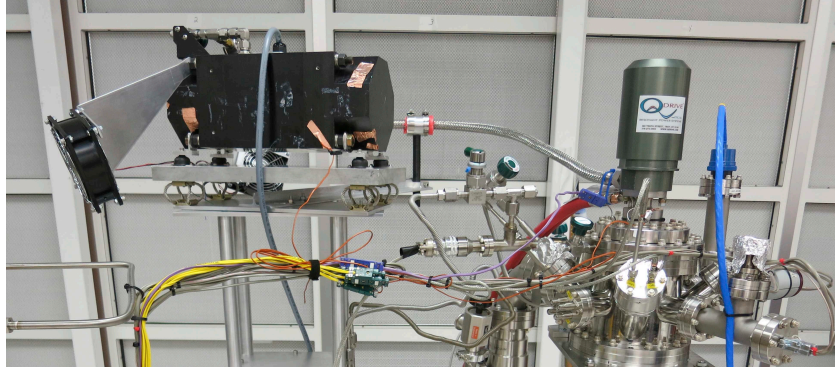


**Figure 5.20.** The cryocooler used with the G/NARRLI detector is an acoustic Stirling cycle cryocooler produced by Q-Drive [142]. The coldhead is connected with a 1 m long tube, which allows for the compressor to have a separate support structure from the detector chamber.

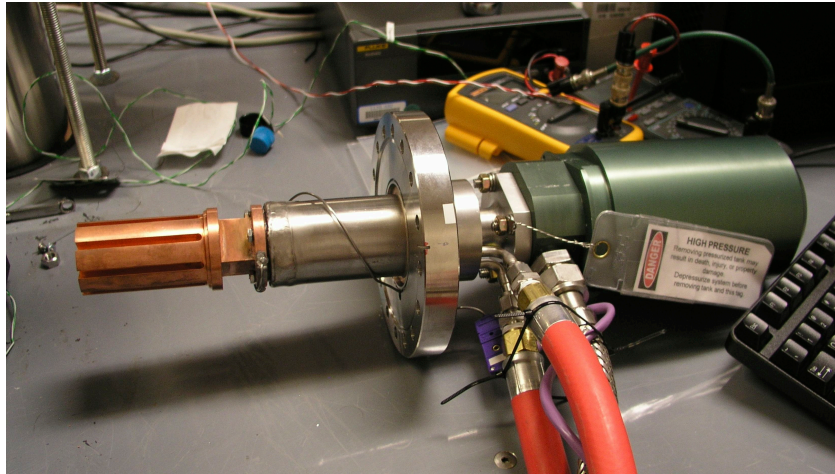


**Figure 5.21.** The cryocooler coldhead has a copper condenser to increase the surface area in contact with the argon for liquefaction. The copper condenser is housed inside a vacuum jacket to reduce the external heat load on the system.

which are used with the proportional-integral-derivative (PID) controller. The first heater is wrapped around the condenser with a copper heat sink to maintain the temperature within the system while the cryocooler is kept at a constant output. The second heater, placed below the detector at the bottom of the dewar is used to rapidly evaporate the liquid argon.

The cryocooler is equipped with a thermocouple within the coldhead, which serves to measure the temperature of the system. Thermocouples are placed on the cryocooler compressor and the coldhead reject water to monitor the performance

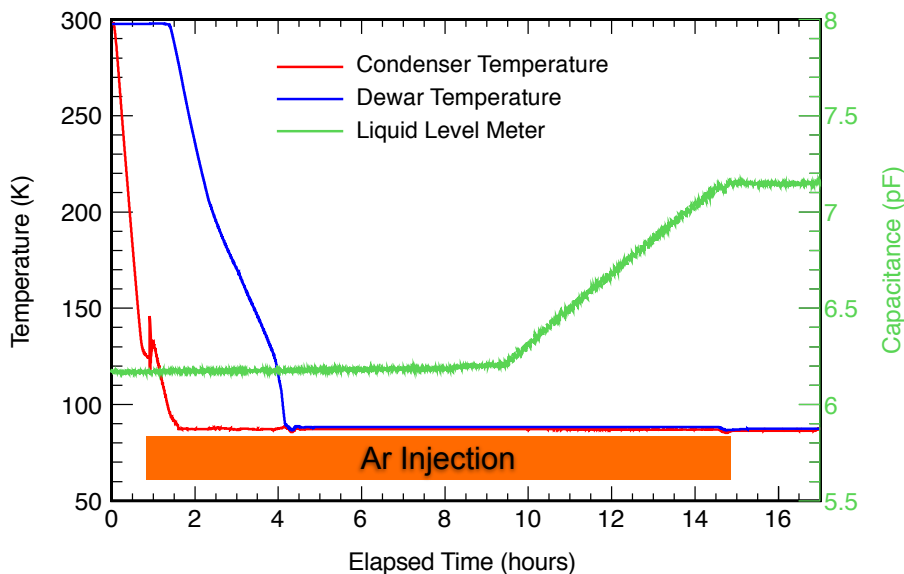


**Figure 5.22.** The liquid level is monitored overnight while the cryocooler liquifies the Ar to fill the detector. After  $\sim 15$  hours of cooling, the detector is filled with LAr to the desired height and the slow control system stops the injection of Ar.

of the cryocooler and shut the cryocooler down if it strays from normal operation and the temperature rise is too high.

A slow control program was written in LabView to monitor and control the detector operation. A PID routine is used to hold the system at constant temperature and pressure. The RTD on the condenser is used in the PID controller, which has a fluctuation in temperature of  $\pm 0.05$  K, and a pressure stability of  $\pm 1$  Torr. In normal operating conditions, the detector is held at 820 Torr and 89.3 K. The complete argon liquid-gas vapor pressure curve, as calculated from Equation (1.21) with the constants given in Table 1.4 is shown in Figure 5.23.

To retain purity within the system, a KNF N143 SN.12E double-diaphragm pump [149] is used to pump the argon through the SAES purifier. The liquid is pumped through a capillary that has been inserted, causing the liquid to turn into gas and flow through the circulation system. With  $\sim 20$  W of cooling power, a recirculation rate of 1.8 slpm is obtained to purify the entire 1 kg of Ar detector volume 2-3 times per day.



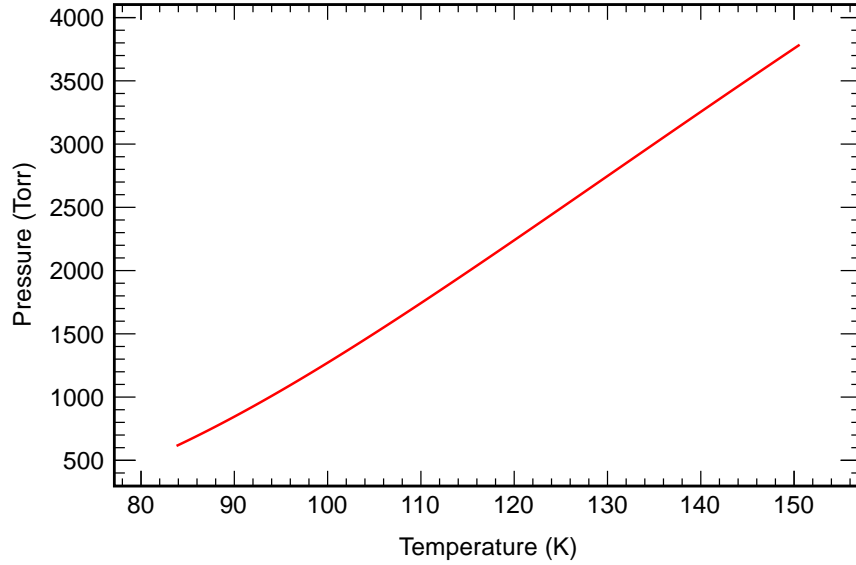


**Figure 5.23.** The argon liquid-gas vapor pressure curve, as calculated from Equation (1.21) with the constants given in Table 1.4. The G/NARRLI detector primarily operated at 820 Torr and 89.3 K.

## 5.5 Photomultiplier Tube Characteristics

Hamamatsu 8520-mod low temperature photomultiplier tubes (PMTs) [140] were used for light collection within the detector. The PMT signals were acquired using a LeCroy Waverunner Xi-A 8-bit oscilloscope [150], operating at 250 MHz bandwidth. The PMT array is held with a PEEK holder to electrically isolate the PMTs from the anode. A grounded copper shield cup is placed around the PMTs to aid in the prevention of high voltage sparks directly to the PMTs. The PMTs are wrapped with teflon tape to allow independent application of bias voltages. Of the four PMTs used, two exhibited high gain, while the other two exhibited low gain. The two PMTs with high gain had a large separation between the noise-wall and the single photoelectron (s.p.e.) peak. One of the low gain PMTs had good energy resolution and separation from the noise-wall, while the other had poor energy resolution and noise-wall separation. The two PMTs with low gain were run at increased bias voltages to make up for a portion of the gain differences. The s.p.e. pulses were approximately 5-10 ns in width, with an amplitude of 10-20 mV. Figure 5.24 shows the histogram of the integral of the s.p.e. peak for

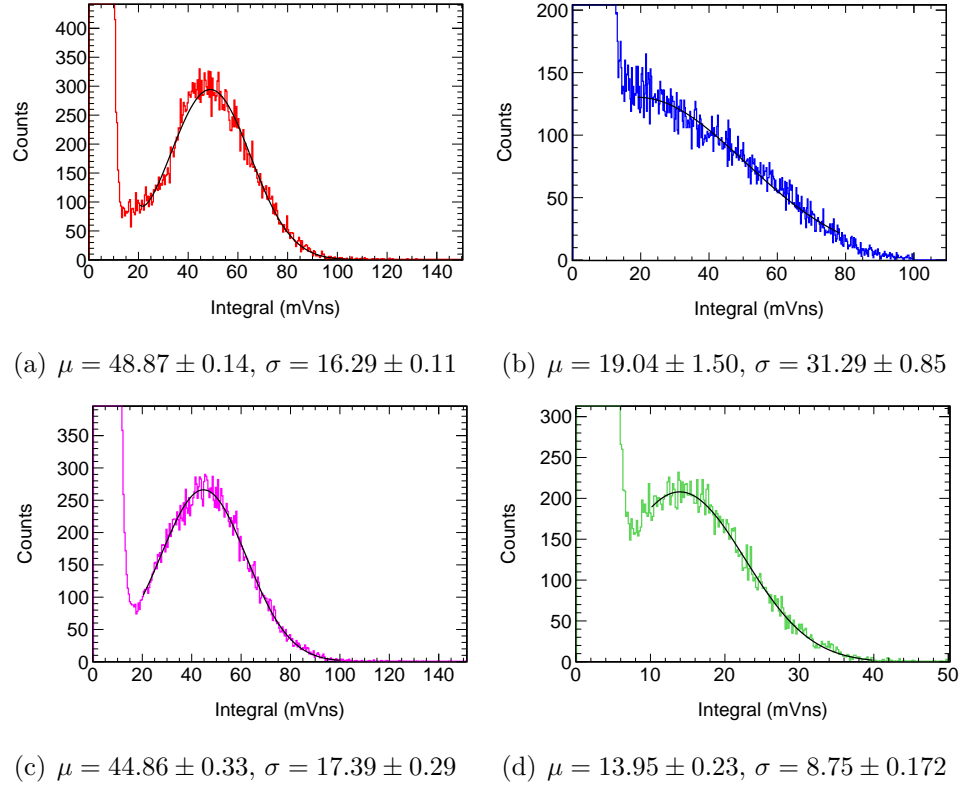


**Figure 5.24.** The s.p.e. peaks from each of the 4 PMTs used in the G/NARRLI detector, (a) PMT1, (b) PMT2, (c) PMT3, (d) PMT4, are used to gain match the PMTs within the analysis of the data. Three of the PMTs have a large separation from the noise wall, while the fourth PMT has poor resolution and no separation from the noise wall. The PMTs are calibrated by taking the median above the noise wall, which are calculated as 50.4, 38.2, 48, and 18 mV·ns for PMT1, PMT2, PM3, and PMT4, respectively.

each of the PMTs. Using the s.p.e. peaks, the data from each channel is further gain matched through the analysis, with the resulting data presented in number of photoelectrons (p.e.).

## 5.6 Event Characteristics

When radiation interacts within the detector, the energy is deposited to liberate photons, electrons, and phonons. The photons are initially detected as the primary (S1) pulse. The electrons are drifted through the active volume via the drift electric field. When the electrons reach the liquid above the extraction grid, the electric

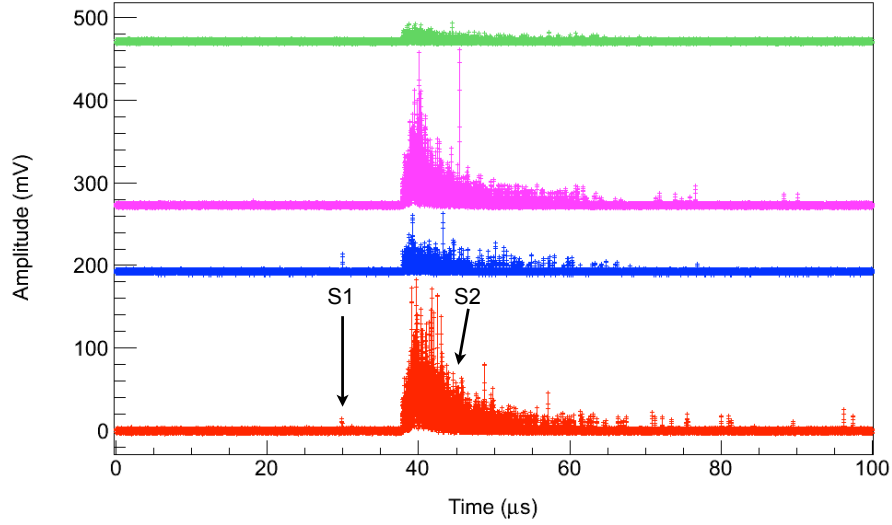


**Figure 5.25.** The primary S1 pulse is created when the  $\gamma$ -ray interacts in the liquid. The primary electrons are then drifted to the gas phase, where amplification occurs during a  $\sim 3\mu\text{s}$  drift. The S2 pulse subsequently decays with a time constant of  $\sim 3.2\mu\text{s}$  since there are no more electrons passing through the gain region. The PMTs collect varying signals which can be utilized for position reconstruction, Section 5.7.

field increases and the electrons are extracted from the liquid surface to the gas phase. With an electric field  $>4\text{ kV/cm}$ , complete electron extraction from the liquid-gas interface is achieved [51]. As the electrons drift through the gas phase, a secondary (S2) pulse is generated by electroluminescence. The S2 pulse has a rise time corresponding to the electron drift time through the gaseous Ar, and a decay time corresponding to the Ar triplet decay time of  $3.2\mu\text{s}$ . The time between the S1 and S2 pulse can be used to determine the axial position of the interaction. The drift speed through the active region depends on the electric field, with typical values of  $2\text{--}3\text{ mm}/\mu\text{s}$  in the G/NARRLI detector. An example trace for an  $^{241}\text{Am}$   $\gamma$ -ray event showing both the S1 and S2 pulses is shown in Figure 5.25. Each PMT collects a different amount of light, which allows for a reconstruction of the event location, Section 5.7.

Several criteria are used for signal analysis, which are similar to those used in signal pathologies analysis of the single-phase Ar detector, Section 3.6. The first cut used when analyzing the data requires that the time of the S2 event corresponds with the trigger position of the DAQ. This helps to eliminate high-energy events

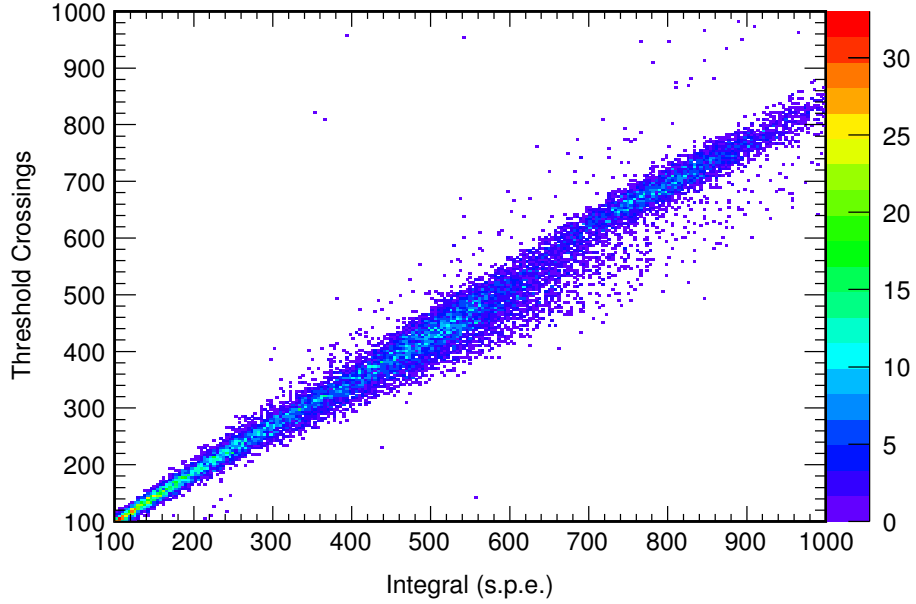


**Figure 5.26.** The number of threshold crossings in the event is plotted against the calculated integral in photoelectrons (p.e.). With calibrated PMT single photoelectron peaks, the number of threshold crossings is equal to the calculated integral in photoelectrons.

which may span multiple traces, such as interactions of muons. By requiring a clean trace before and after the event, the events that are observed as signal *grass*, which contain PMT pulses throughout the entire trace, are also rejected. In order to check that the baselines of the PMTs do not wander throughout the trace, the number of threshold crossings can be compared to the calculated integral. For low energy events ( $< \sim 6$  keVee), PMT pulses are sufficiently separated in time from each other such that one threshold crossing corresponds to nearly a single photoelectron, Figure 5.26.

## 5.7 Event Position Reconstruction

The electrostatic model, Section 5.2, shows that the edge effects can have a large impact on the electron collection efficiency. Additionally, the PMT collection efficiency for the light produced in the amplification region can vary by 30-40% depending on the event transverse position. In order to minimize the variation of

the signals, a fiducialization cut is introduced into the analysis. For a four-PMT setup, the fiducialization relies on taking the ratios of the PMT signals. The two ratios used are:

$$\text{North/South} = (PMT1 + PMT2)/(PMT3 + PMT4) \quad (5.2)$$

and

$$\text{East/West} = (PMT1 + PMT3)/(PMT2 + PMT4), \quad (5.3)$$

where  $PMT1, 2, 3, 4$  represent the light collected by each of the four PMTs. The numerator and denominator of each ratio is set to positive value if the first PMT in the numerator collects more light, or negative if the second PMT in the numerator collects more light. Positions are normalized by either adding or subtracting unity (1) from each of the two ratios to shift the fiducialization value towards zero. The fiducialization plots show the reconstructed location of the events, allowing for a fiducialization cut to eliminate edge events. Figure 5.27 shows a schematic of the PMT and  $^{241}\text{Am}$  source layout used in the purity measurements, Section 5.8. The reconstructed fiducialization plot showing the expected event locations is presented in Figure 5.28.

When taking purity data, the  $^{241}\text{Am}$  is collimated vertically along the drift direction to generate photoelectric events evenly throughout the length of the active volume. When checking the purity, it is important to minimize the radial effect of the signal variation so that the variation in response can be correctly attributed to the drifting of electrons through the active region. The effectiveness of the fiducialization cut is shown in Figure 5.29, with the spectrum shown before and after a standard fiducialization cut. The standard fiducialization cut requires that the absolute value of the North/South and East/West ratios be less than 4, cutting  $\sim 50\%$  of the events within the active region, in agreement with the electrostatic model prediction, Section 5.2.

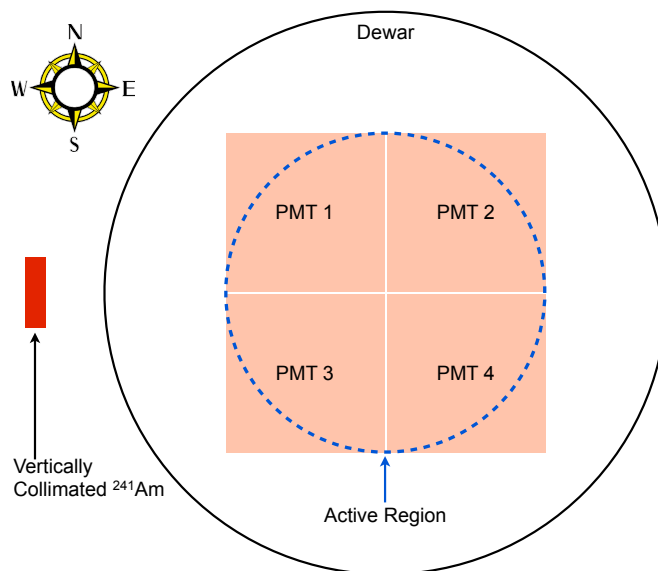


**Figure 5.27.** The four PMTs are placed in a grid pattern which is divided into North, South, East, and West regions, where each PMT resides in two regions. In the purity measurements, the  $^{241}\text{Am}$  source is collimated vertically and placed on the side of the detector.

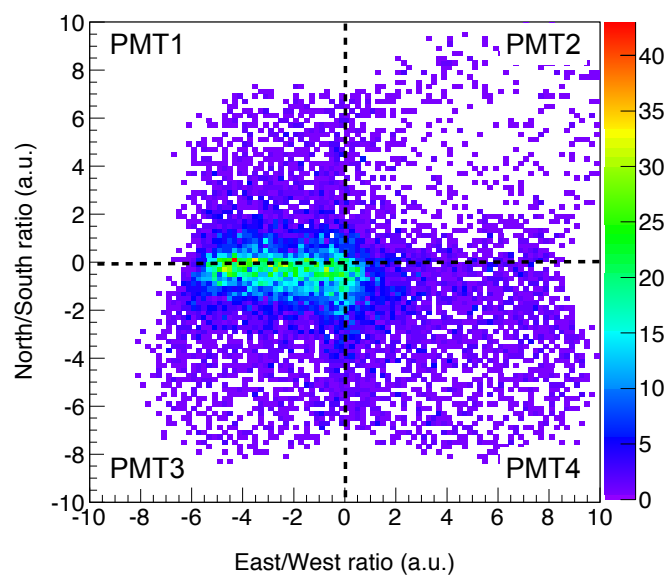


**Figure 5.28.** With the vertically collimated  $^{241}\text{Am}$  source, the gamma rays preferentially interact on the side closest to the source. The reconstructed fiducialization plot correctly shows the increase in the event rate for the detector region closer to the source, with a collimation size consistent with the experiment.

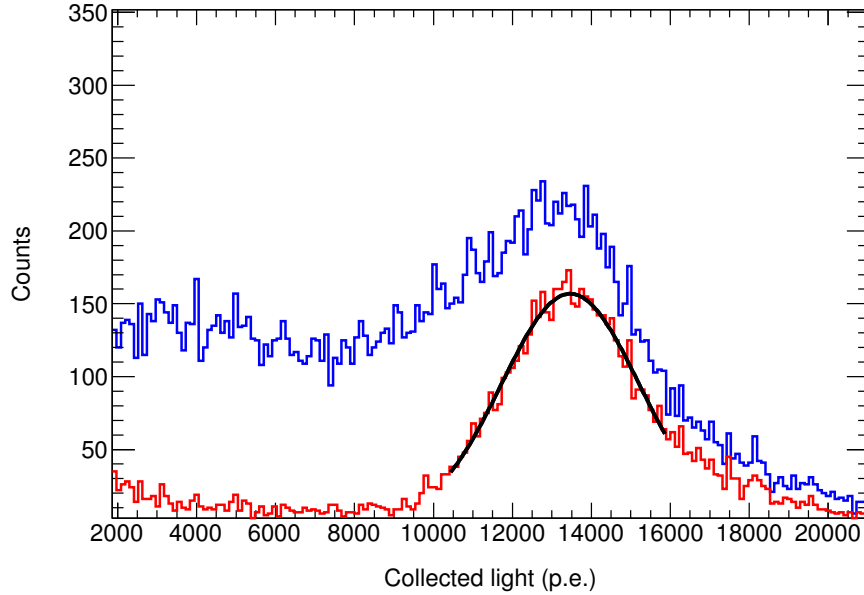


**Figure 5.29.** Since the  $^{241}\text{Am}$  gamma rays interact throughout the entire active volume, the edge effects create a plateau on the low-energy side of the photoelectric peak, visible with no fiducialization cut (blue). When a fiducialization cut of  $|\text{North/South}|$  and  $|\text{East/West}| < 4$  (red) is applied, the edge events are removed, and the gaussian photopeak is fit at  $\sim 13500$  p.e.

## 5.8 Measuring Detector Purity Through the Electron Lifetime

When electronegative impurities such as oxygen are present within the detector, the electrons are lost during the drift through the liquid argon, resulting in a lower observed signal. The electron lifetime during drift through the active volume is calculated using the vertically collimated  $^{241}\text{Am}$  data. The time between the S1 and S2 pulses provides the drift time of the electrons through the LAr. In a scatter plot of the integral of the S2 pulses versus the drift time, the S2 light collected decreases as the drift time increases due to a decrease in electron collection efficiency. Fitting the data with an exponential fit, the slope of the exponential represents the inverse of the electron lifetime. When the electron lifetime is much longer than the electron drift time, there is no decrease in signal, and no correction for the axial position needs to be applied. The data is binned based on the electron drift time, allowing for the exponential fit to be determined. Figure 5.30 shows the scatter plot of

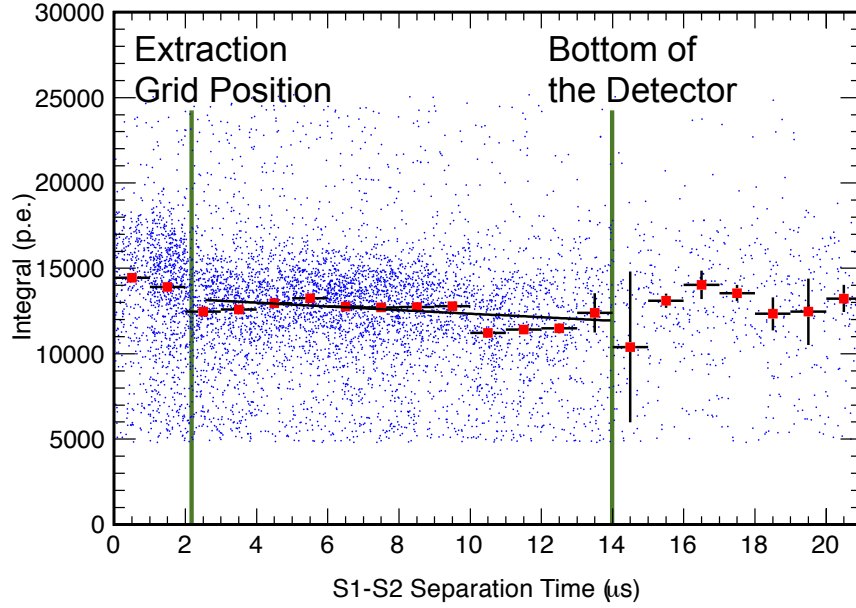


**Figure 5.30.** Vertically collimated  $^{241}\text{Am}$  is used to measure the purity of the G/NARRLI detector. The time between the S1 and S2 pulses provides the electron drift time. The scatter plot of the S2 event integral versus the electron drift time is fit with an exponential function to obtain the electron lifetime. The inverse of the slope of the exponential is the electron lifetime.

S2 event integral versus the drift time of the event. The electron lifetime fit of  $118 \pm 20 \mu\text{s}$  to collect  $\sim 90\%$  of the drifted electrons is obtained.

The desired purity of the detector is retained for  $\sim 5$  days before the electron lifetime becomes detrimental to the detector resolution. In order to recover the desired purity within the detector, recirculation of the LAr using the recirculation system and the SAES purifier is performed, Section 5.4. Figure 5.31 shows the stability of the detector purity along with the recovery of the desired purity with the operation of the recirculation system. Recirculation was primarily performed overnight, not during data taking. Recirculation can also be performed during data taking with no significant loss in energy resolution.



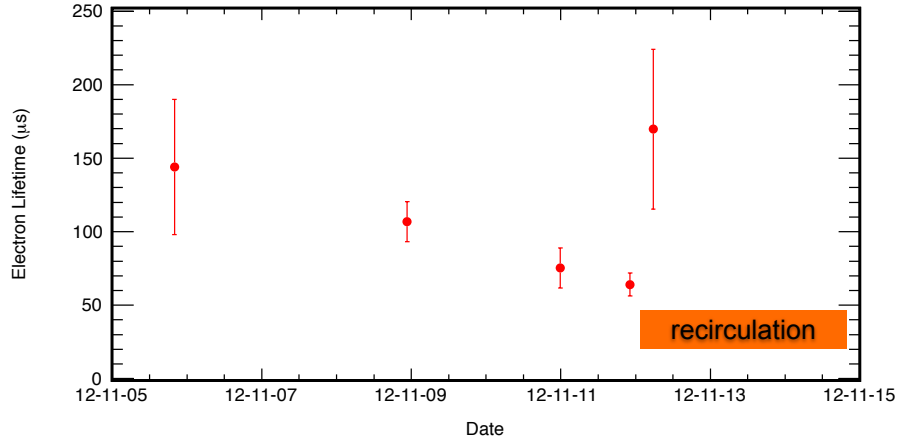


**Figure 5.31.** The measured electron lifetimes are stable for  $\sim 5$  days before the electron lifetime begins to decrease significantly. Recirculation recovers the original purity.

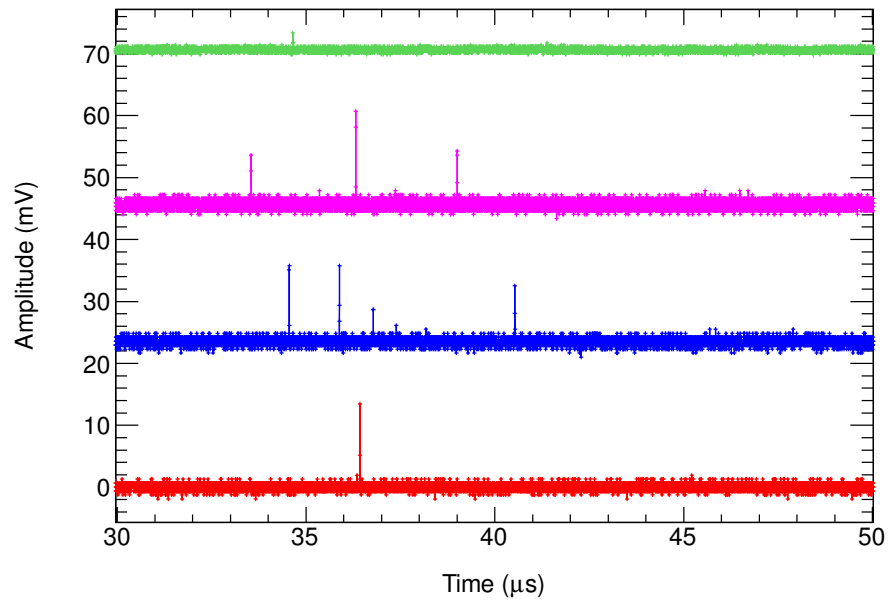


**Figure 5.32.** Single electrons produce  $\sim 10$  p.e. which are sparsely dispersed over the course of  $\sim 6$ - $10$   $\mu$ s. The event shown has a reconstructed event integral of 8.14 p.e., with an event width of 6.98  $\mu$ s.

## 5.9 Single Ionization Electron Detection

Detection of single ionization electrons using an ionization detector reaches the sensitivity limit. With the G/NARRLI detector, single ionization electrons were detected, enabling a direct energy calibration of the detector. Single ionization electrons are seen as short  $\sim 10$  p.e. bursts over the course of  $\sim 10$   $\mu$ s. An example single ionization electron event is shown in Figure 5.32. The trace is clear of photoelectrons aside from the single ionization electron event. The distribution of light is spread evenly over the event width, incompatible with the S1 event structure in LAr (sharp singlet peak followed by a  $\sim 1$   $\mu$ s decay time for the triplet state), confirming the presence of single ionization electron S2 events. In the histogram of the low light collection events, Figure 5.33, the single ionization electron peak is present with a centroid of  $8.2 \pm 0.1$  p.e. per ionization electron (i.e.), and a  $\sigma$  of  $3.4 \pm 0.1$  p.e. The double ionization electron event peak is visible with the centroid of the gaussian constrained to 16.4 p.e. per i.e.

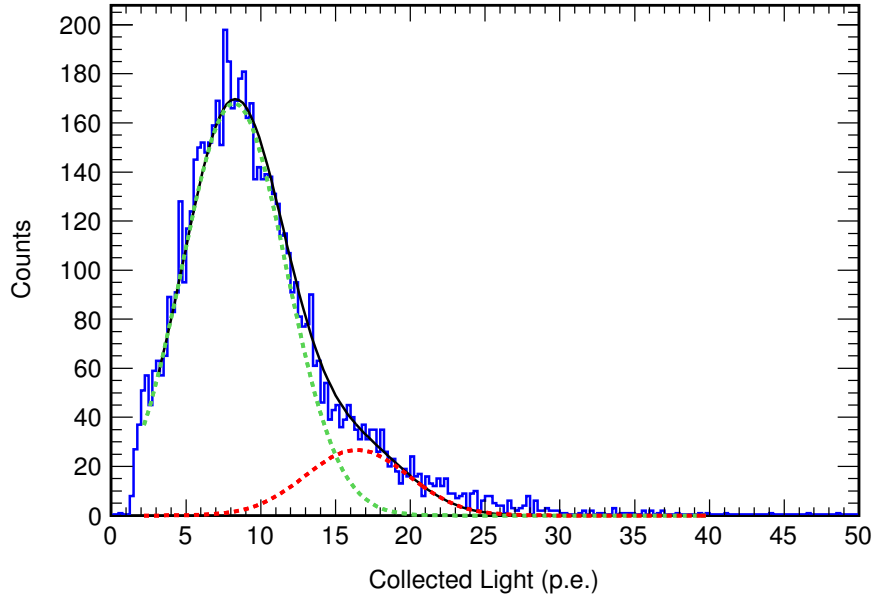


**Figure 5.33.** Measured single ionization electron peak at  $8.22 \pm 0.07$  p.e. per i.e., with a  $\sigma = 3.46 \pm 0.07$  p.e. The double ionization electron peak is constrained to double the light output (16.4 p.e. per i.e.), with the amplitude allowed to float in the fit. The  $\chi^2/\text{d.o.f.} = 173.3/103$ .

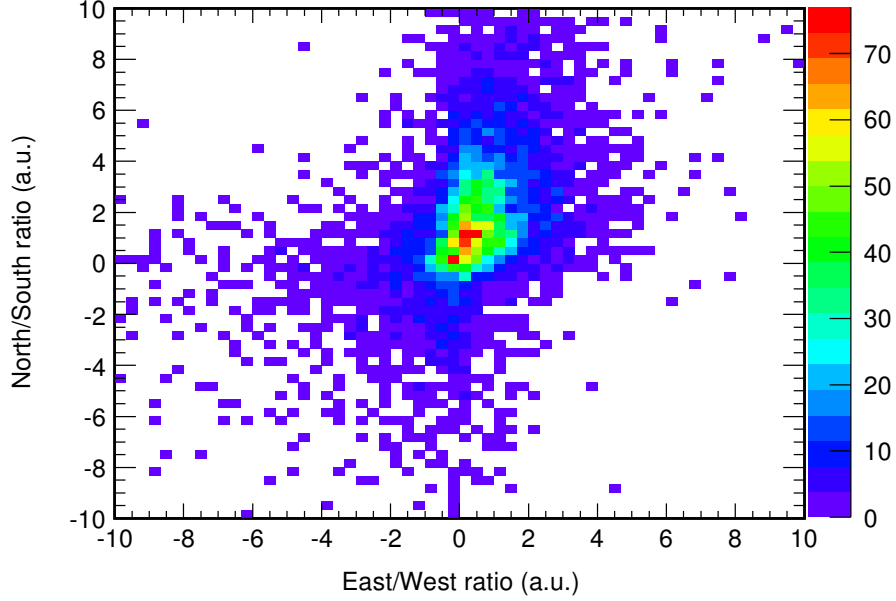


**Figure 5.34.** Reconstructed positions of the i.e. events show a distinct bias in the direction of the  $^{55}\text{Fe}$  and teflon structures.

In liquid xenon detectors, it is well known that single ionization electrons are emitted from the liquid-gas interface. Electrons from previous ionization events are trapped at the liquid-gas interface due to the high work function at the boundary and randomly emitted later in time [51]. Argon has a much lower work function, and with the extraction electric field of  $\sim 6 \text{ kV/cm}$ , nearly 100% of generated electrons are predicted to cross the liquid-gas boundary. In the data in which the single ionization electrons were observed, the teflon and a metallic piece were present within the active volume. The metallic piece was an  $^{55}\text{Fe}$  source used for low energy calibration of the detector, Section 6.1. The  $^{55}\text{Fe}$  source was electrically connected to the field cage, and teflon was used as the  $^{55}\text{Fe}$  source holder. Using the detector fiducialization method, Section 5.7, the locations of the single ionization electrons are biased towards PMT 2, shown in Figure 5.34, which is where the teflon source holder was located. In operation without the  $^{55}\text{Fe}$  source present, single ionization electrons were not visible, which further suggests that the  $^{55}\text{Fe}$  or teflon was the source of the single electrons.

## Electron Transport Model Validation

The ionization yield model discussed in Chapter 2 was validated experimentally. While the atomic collision model, Section 2.3, can only be validated through direct measurement of the nuclear ionization yield, the electron transport model, Section 2.4, can be validated with electron recoils. Validation of the electron transport model was performed using  $^{37}\text{Ar}$  and  $^{55}\text{Fe}$  X-rays at various drift fields. The  $^{37}\text{Ar}$  provides data at 270 eV and 2.8 keV, while the  $^{55}\text{Fe}$  provides data at 5.965 keV. In this Chapter, the methods used to make the electron recombination measurements are presented, followed by the experimental results for  $^{55}\text{Fe}$ ,  $^{37}\text{Ar}$ , and  $^{241}\text{Am}$ . While  $^{241}\text{Am}$  was also used in the experiments, no comparison with the simulation was performed due to the relatively high energy deposited by its 60-keV gamma ray. In Section 6.4 a discussion is presented of the means for determining the ionization profiles that resemble those produced through the decay of  $^{37}\text{Ar}$  and  $^{55}\text{Fe}$ . Lastly, a review is provided of the electron recombination results obtained from the electron transport model, Section 6.5, along with the comparison between the model and experiment, Section 6.6.

### 6.1 Validation Using $^{55}\text{Fe}$

Similar to earlier experiments with the single-phase argon detector, Section 3.3,  $^{55}\text{Fe}$  was used as a low-energy calibration source in the dual-phase argon detector.  $^{55}\text{Fe}$  decays through electron capture followed by X-ray emission to provide a localized source of  $\sim 6$  keV X-rays, Table 3.1.

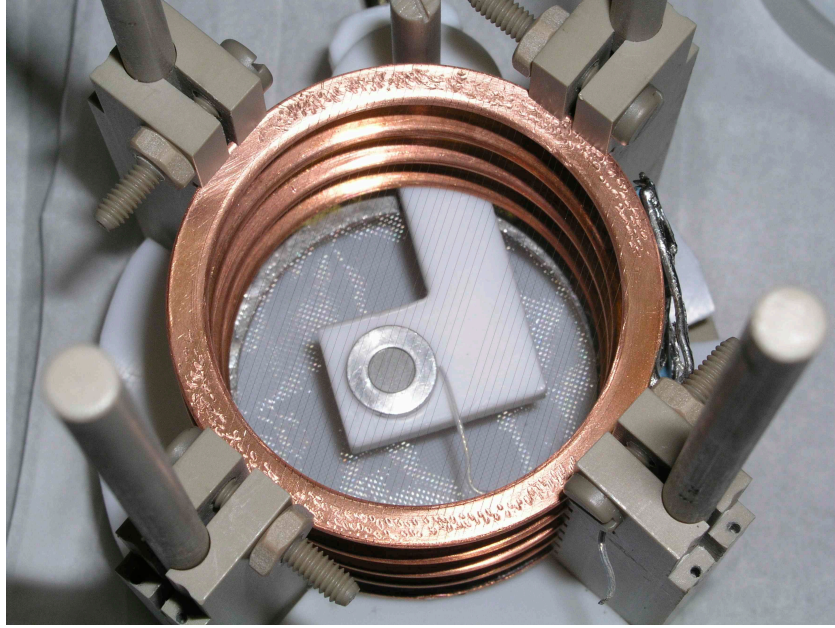


**Figure 6.1.** The  $^{55}\text{Fe}$  is housed in a teflon source holder to prevent breakdown between the holder and the field cage. The source is electrically coupled to the field cage to provide the electric potential required to drift the electrons away from the  $^{55}\text{Fe}$  surface.

### 6.1.1 Experimental Procedure for $^{55}\text{Fe}$ Measurements

The  $^{55}\text{Fe}$  source used was 5 mm in diameter and electroplated on the surface of an aluminum puck, with the exterior  $^{55}\text{Fe}$  surface left bare. The activity of the  $^{55}\text{Fe}$  was  $\sim 1$  kBq at the time of data collection. With an attenuation length or mean free path in LAr of  $28\text{ }\mu\text{m}$  for the  $\sim 6$  keV X-rays [151], the  $^{55}\text{Fe}$  source must not only be located inside the detector, but within the active volume. To mount the  $^{55}\text{Fe}$  source within the active volume, it was held with a dielectric to prevent electric breakdown. The  $^{55}\text{Fe}$  source must also be electrically coupled to the field cage in order to extract the electrons from the interaction sites near the  $^{55}\text{Fe}$  sample surface. The source holder used is shown in Figure 6.1. A magnet was mounted on the outer edge of the teflon source holder to allow for source manipulation via another magnet placed outside the dewar which houses the detector. This method of source manipulation allowed the  $^{55}\text{Fe}$  to be taken in and out of the active volume without opening the detector.

**Table 6.1.**  $^{37}\text{Ar}$  decays 100% via electron capture.[152]

Energy [keV]	Branching Ratio	Decay Mode
2.8224	$0.9017 \pm 0.0024$	K-shell Capture
0.2702	$0.0890 \pm 0.0027$	L-shell Capture
0.0175	$0.0093^{+0.0006}_{-0.0004}$	M-shell Capture

### 6.1.2 $^{55}\text{Fe}$ Spectra and Source Localization

With a mean free path of  $\sim 40 \mu\text{m}$  [151], the 3 keV Ar excitation X-rays do not escape the dual-phase detector active volume, and no X-ray escape peak is observable. Figure 6.2 shows the measured spectrum of the  $^{55}\text{Fe}$ . Only a single analysis cut has been applied when analyzing the event traces to produce this spectrum, requiring the position of the event within the trace to correspond with the DAQ trigger location. Demonstration of radial localization of the  $^{55}\text{Fe}$  source within the active region is shown in Figure 6.3. The reconstructed position of the source location using the light collection ratios for the North/South and East/West PMTs shows localized event generation at the center of the active region. The North/South ratio is the light collected by the upper 2 PMTs divided by the light collected by the lower 2 PMTs. The East/West ratio is the light collected by the right 2 PMTs divided by the light collected by the left 2 PMTs. With these ratios plotted against each other, the (x,y) position of the event within the active volume can be reconstructed.

## 6.2 Validation Using $^{37}\text{Ar}$

$^{37}\text{Ar}$  decays via electron capture followed by an Auger electron emission cascade. The electron usually proceeds by the capture of a K-shell electron ( $\sim 90\%$  of the time), producing a 2.8 keV electron peak. The L-shell electron capture branch occurs in  $\sim 9\%$  of decays, producing a 270 eV peak, Table 6.1 [152].

While it has been shown that  $^{37}\text{Ar}$  can be used as a calibration source in gaseous argon [153], it had not been previously used in a dual-phase argon detector.

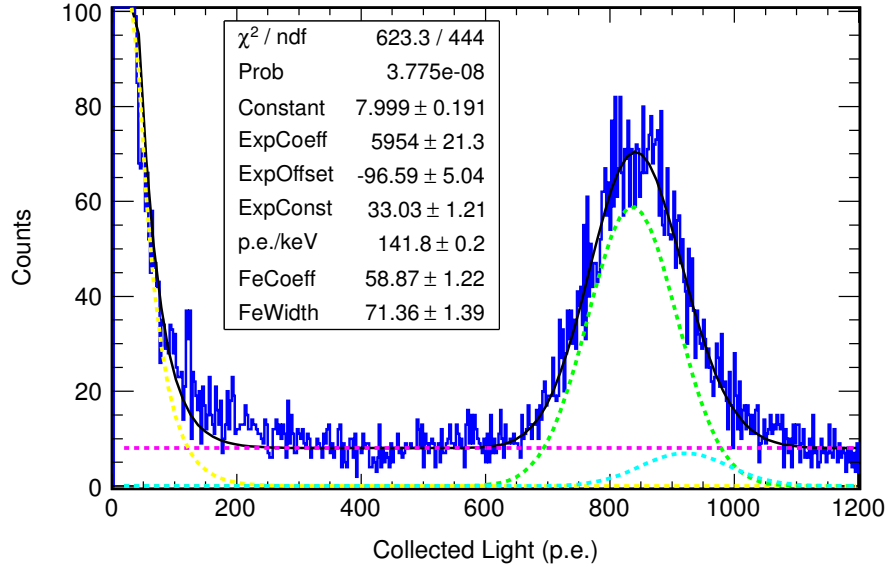


**Figure 6.2.**  $^{55}\text{Fe}$  produces a peak at  $\sim 6$  keV, which is shown in terms of photoelectrons. The spectrum shown was taken with a drift field of 2.4 kV/cm and a gain field of 8.2 kV/cm. A cut requiring that the events are triggered events was used to generate the spectrum which was fit with a double gaussian as the  $^{55}\text{Fe}$  peaks at 5.89 and 6.49 keV (green and cyan), based on the defined X-ray intensities, Table 3.1. The background is represented with an exponential (yellow) and constant (magenta) component.

### 6.2.1 Experimental Procedure for $^{37}\text{Ar}$ Measurements

For the production of the  $^{37}\text{Ar}$ , natural argon was irradiated with neutrons at McClellan Nuclear Research Center. The neutrons were captured primarily on  $^{40}\text{Ar}$  and  $^{36}\text{Ar}$ , producing  $^{41}\text{Ar}$  and a small quantity of  $^{37}\text{Ar}$ . The  $^{41}\text{Ar}$  decayed quickly and the  $^{37}\text{Ar}$  was the dominant remaining radioactive nuclide, Figure 6.4. A summary of isotopic data relevant to the irradiation process is given in Table 6.2.

Approximately 1 liter of  $^{nat}\text{Ar}$  at 160 psi was irradiated next to the reactor core for 4 hours to produce  $\sim 50$   $\mu\text{Ci}$  of  $^{37}\text{Ar}$ . The gas was then cryogenically extracted and transferred to a lecturer's cylinder (2.24 L) and pressurized with  $^{nat}\text{Ar}$  to 1300 psi. The activity was verified by measuring the  $^{41}\text{Ar}$  emission through the lecture bottle shortly after irradiation. The  $^{37}\text{Ar}$  was first injected into a calibration volume of  $\sim 250$   $\text{cm}^3$ , and then pumped through a SAES purifier into the detector using the recirculation pump. A schematic of the plumbing is shown in Figure

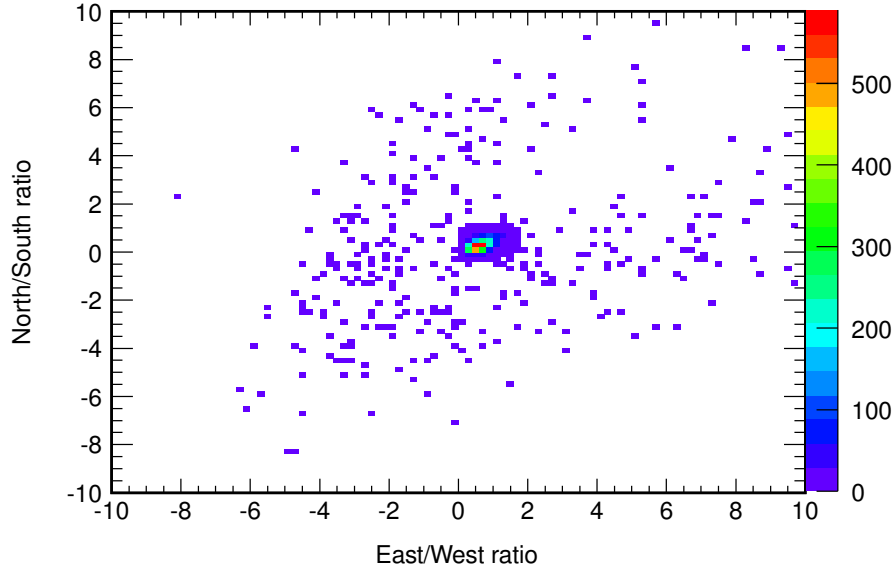


**Figure 6.3.** With an energy cut on the  $^{55}\text{Fe}$  peak, the reconstructed source location was based on the fiducialization ratios, Section 5.7. The North/South ratio is the light collected from the top 2 PMTs divided by the light collected by the bottom 2 PMTs. Similarly, the East/West ratio is the light collected from the right 2 PMTs divided by the light collected by the left 2 PMTs.

5.19, and the entire setup is shown in Figure 6.5.

### 6.2.2 $^{37}\text{Ar}$ Spectra and Localization

Once the  $^{37}\text{Ar}$  was injected into the detector, it mixed throughout the entire liquid/gas volume to create a uniform radiation source. Unlike the experiment involving the  $^{55}\text{Fe}$  source, the fiducialization plot of the  $^{37}\text{Ar}$  K-shell peak shows the expected uniformly distributed source, Figure 6.6. Since the  $^{37}\text{Ar}$  was located uniformly throughout the active region, the variation in detector response as a function of radial position resulted in a low-energy plateau of the  $^{37}\text{Ar}$  K-shell peak. As the event location approached the detector periphery, edge effects such as the loss of electrons (due to non-uniform electric field lines) and lower light collection by the PMTs (due to angle of incidence to the PMTs and the anode grid) became more significant, resulting in a decrease in signal. With the application of a fiducial cut requiring the absolute value of the North/South ratio and East/West



**Table 6.2.** Natural argon consists primarily of  $^{40}\text{Ar}$  with the second most abundant isotope being  $^{36}\text{Ar}$ . After irradiation the  $^{41}\text{Ar}$  decayed away rapidly, leaving primarily the  $^{37}\text{Ar}$ .

Isotope	Isotopic Fraction	$t_{1/2}$
$^{40}\text{Ar}$	0.996	Stable
$^{36}\text{Ar}$	0.00337	Stable
$^{38}\text{Ar}$	0.00063	Stable
$^{41}\text{Ar}$	-	109.34 minutes
$^{37}\text{Ar}$	-	35.04 days
$^{39}\text{Ar}$	-	269 years

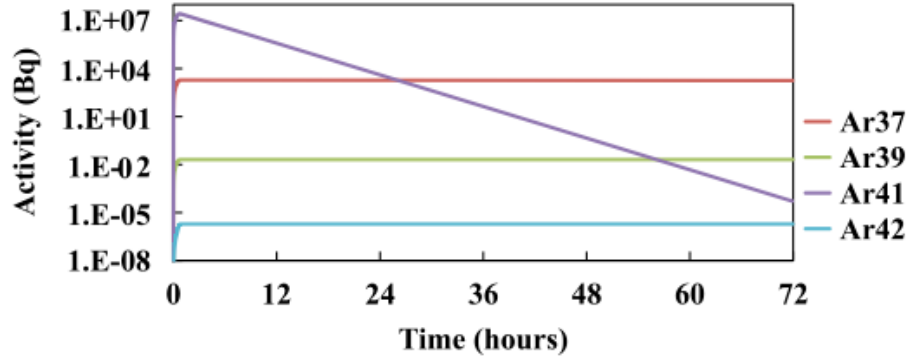


**Figure 6.4.** Isotopic activities after the irradiation of natural Ar, from Aalseth *et al.* [153].  $^{41}\text{Ar}$  decays rapidly, resulting in  $^{37}\text{Ar}$  being the dominant remaining radioactive isotope. While  $^{39}\text{Ar}$  was also produced, the post-irradiation activity of the  $^{37}\text{Ar}$  is  $\sim 10^5 \times$  larger than that of  $^{39}\text{Ar}$ .

ratio to be less than 4, the low-energy tail of the K-shell peak diminishes, preserving the expected K-shell peak. Two additional cuts were used to obtain the final  $^{37}\text{Ar}$  spectra, Figure 6.7. The event was required to occur at the trigger point of the trace, and to have a *clean* pre- and post- event baseline (requiring no more than 3 photoelectrons be present before the event and no more than 5 photoelectrons present after the event). By requiring a clean pre- and post-event baseline, the tail of larger events are not misinterpreted as  $^{37}\text{Ar}$  events.

With an  $^{37}\text{Ar}$  spectrum constructed in this fashion, a low-energy peak is visible in addition to the K-shell peak. The low-energy peak at  $\sim 100$  photoelectrons is well matched to the  $^{37}\text{Ar}$  L-shell decay peak which deposits 270 eV in the detector



**Figure 6.5.**  $^{37}\text{Ar}$  was first injected into a calibration volume of  $\sim 250\text{ cm}^3$ , and then pumped through a SAES getter into the detector using the circulation system. As the  $^{37}\text{Ar}$  decayed, the number of calibration volumes injected increased to maintain a nearly constant activity of  $^{37}\text{Ar}$  inside the detector.

volume. This observation of the  $^{37}\text{Ar}$  L-shell peak is the first demonstration of sub-keV spectroscopy in dual-phase argon detectors, suggesting a considerable potential for measurements involving low-energy ionization yield. A deviation from the expected gaussian shape can be seen on the high-energy side of the K-shell peak. This high-energy shoulder is due to the  $^{37}\text{Ar}$  events which occurred in the liquid region above the extraction grid. Events which occurred above the extraction grid experience a higher electron drift field, reducing the amount of initial electron-ion recombination, Section 6.3. A complete  $^{37}\text{Ar}$  spectrum is shown in Figure 6.7 with both K-shell peaks and the L-shell peak fitted with gaussians. The position, amplitude, and width of each gaussian were the parameters in the numerical fit. Based on the peak areas, the probability of an L-shell event is  $\sim 1/10$ th that of a K-shell event, matching the previously reported branching ratio [152], also given in Table 6.1.

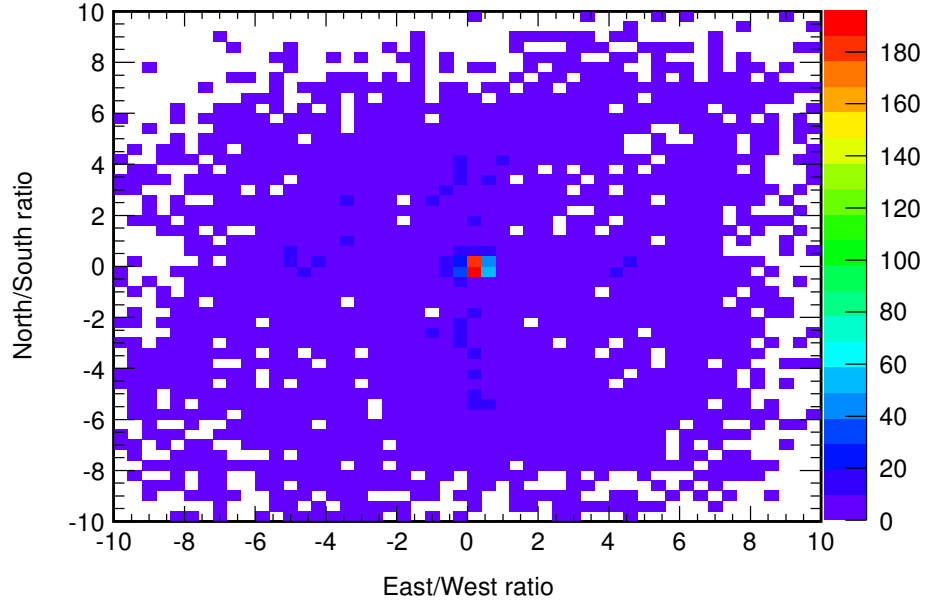


**Figure 6.6.** For the  $^{37}\text{Ar}$  K-shell peak, the events occur uniformly throughout the active region. The small increase in events at (0,0) is associated with the low-energy tail of the  $^{55}\text{Fe}$  peak.

### 6.3 Event Integrals with Varying Drift Field

For the following experiment,  $\sim 500 \text{ cm}^3$  of  $^{37}\text{Ar}$  at a pressure of  $\sim 800$  torr was injected into the dual-phase argon detector. The total  $^{37}\text{Ar}$  decay rate inside the detector was approximately 3 kBq, with an event rate within the active volume of  $\sim 300$  Hz. The data was taken with both  $^{37}\text{Ar}$  and  $^{55}\text{Fe}$  present together in the detector, and with an electron lifetime of  $118 \pm 20 \mu\text{s}$  to collect  $\sim 90\%$  of electrons produced at the bottom of the active region. The loss of  $\sim 10\%$  between the top and the bottom of the active volume both decreases the centroid (number of electrons) and affects the width of the  $^{37}\text{Ar}$  peak (resolution). However, the dominant contribution to the energy resolution was the statistical error in the number of electrons produced. Since the  $^{55}\text{Fe}$  source was localized, the electron lifetime did not have an effect on the resolution, but still decreased the ionization yield by  $\sim 10\%$ . Figure 6.8 shows the  $^{55}\text{Fe}$  peak along with both the  $^{37}\text{Ar}$  K-shell and L-shell peaks.

The observation of a single electron peak, Figure 5.33, allowed for the conversion

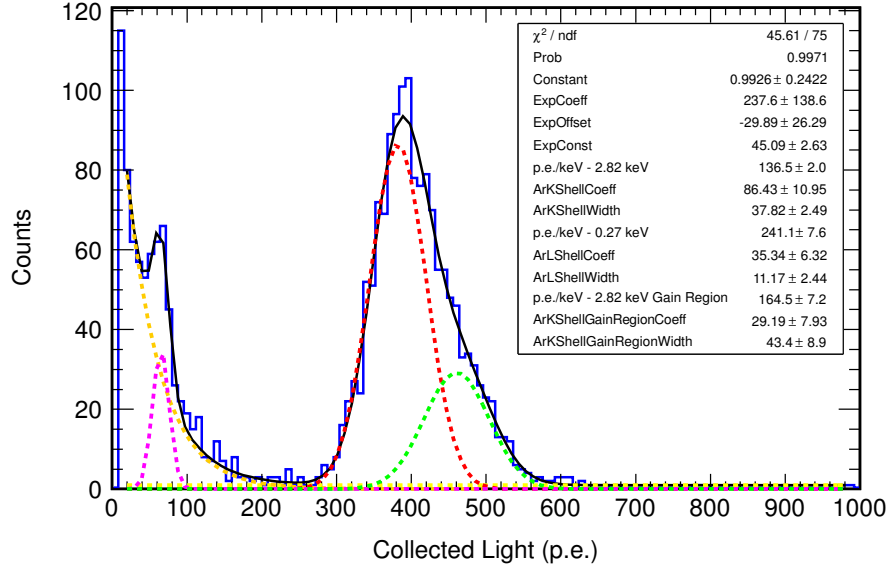


**Figure 6.7.**  $^{37}\text{Ar}$  spectrum (blue) contains a primary K-shell peak at 2.82 keV in red. The green gaussian corresponds to the K-shell events which occur above the extraction grid in a higher electric field. The higher electric field reduces recombination and increases the ionization yield. The L-shell peak at 270 eV was fit with the magenta gaussian. The superposition of each component of the fit is shown in black. The ratio of K-shell to L-shell capture events was a free parameter, determined to be  $\sim 10:1$ , which agrees well with the known branching ratio [152].

of the spectrum from the number of photoelectrons to the number of detected electrons. Figure 6.9 shows the calibration curve for the light yield obtained from the location of the single electron peak at various amplification fields.

$^{37}\text{Ar}$  and  $^{55}\text{Fe}$  data was collected with varying drift fields to measure the electron yield dependence on the electric drift field. The data was also used for a comparison with the electron transport model. Gain fields of 6.5 kV/cm and 8.1 kV/cm in the gas region were used, to allow for a comparison of the electron yields at different light yields. In addition to the experiments with  $^{55}\text{Fe}$  and  $^{37}\text{Ar}$ , an experiment with  $^{241}\text{Am}$  was conducted during a different cooldown period. The  $^{241}\text{Am}$  data was not used in validation of the electron transport model as the 60 keV gamma ray energy is above the energy threshold of the simulation. For  $^{241}\text{Am}$ , Figure 6.10,  $^{55}\text{Fe}$ , Figure 6.11, and the  $^{37}\text{Ar}$  K-shell peak, Figure 6.12, the number of liquid electrons is dependent on the electric field in the active region.

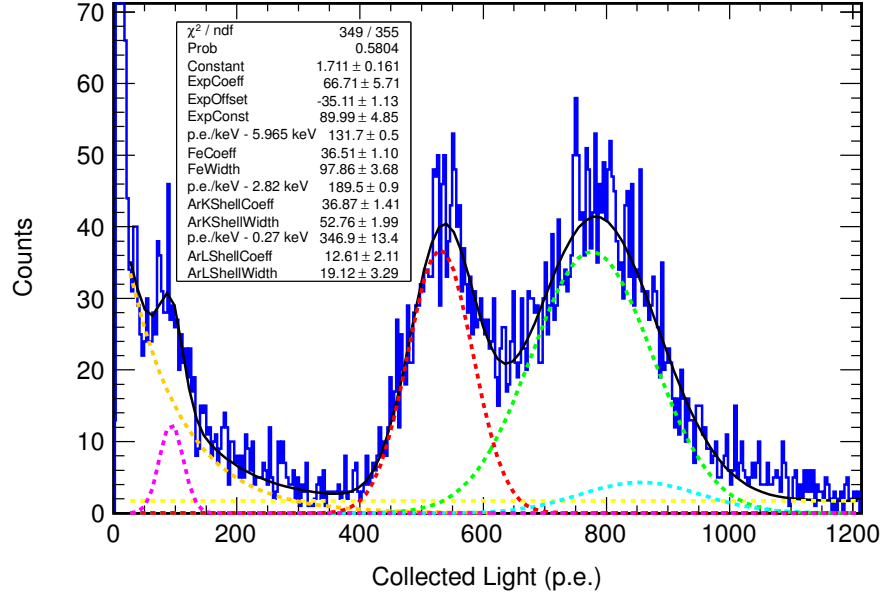


**Figure 6.8.** Event integral spectra for  $^{55}\text{Fe}$  at 5.89 and 6.49 keV (green and cyan), and  $^{37}\text{Ar}$  at 2.82 keV (red) and 270 eV (magenta). For this experiment, the drift field was 2.4 kV/cm and the gain field was 9.0 kV/cm.

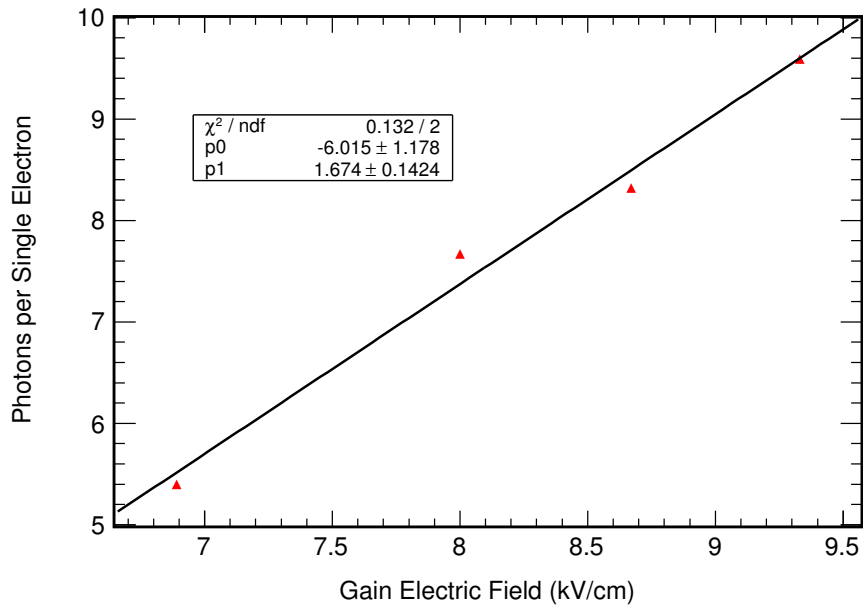


**Figure 6.9.** The number of photoelectrons per liquid electron scales linearly with the electric field in the amplification region.

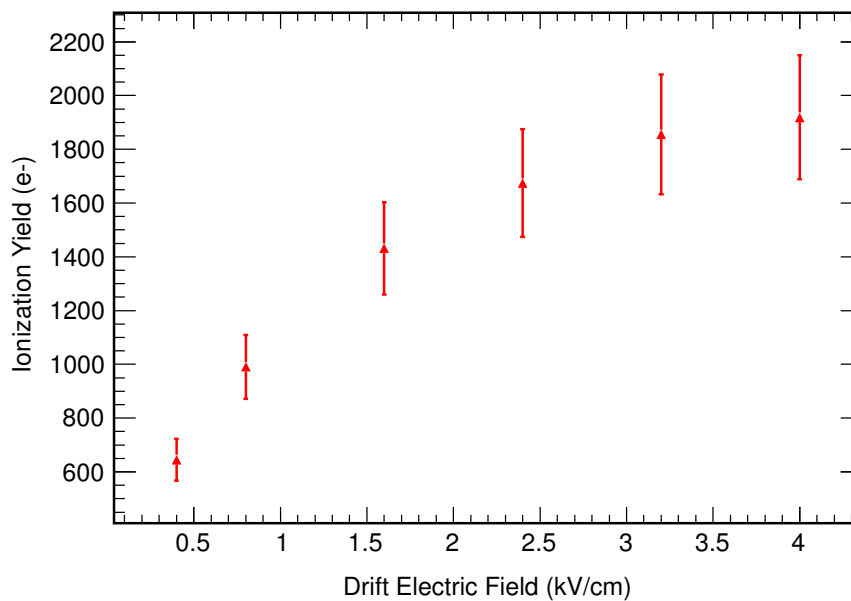


**Figure 6.10.** The number of electrons detected from the  $^{241}\text{Am}$  photo-peak as a function of the applied electric field. The error bars represent the  $1\text{-}\sigma$  on the  $^{241}\text{Am}$  energy peak.

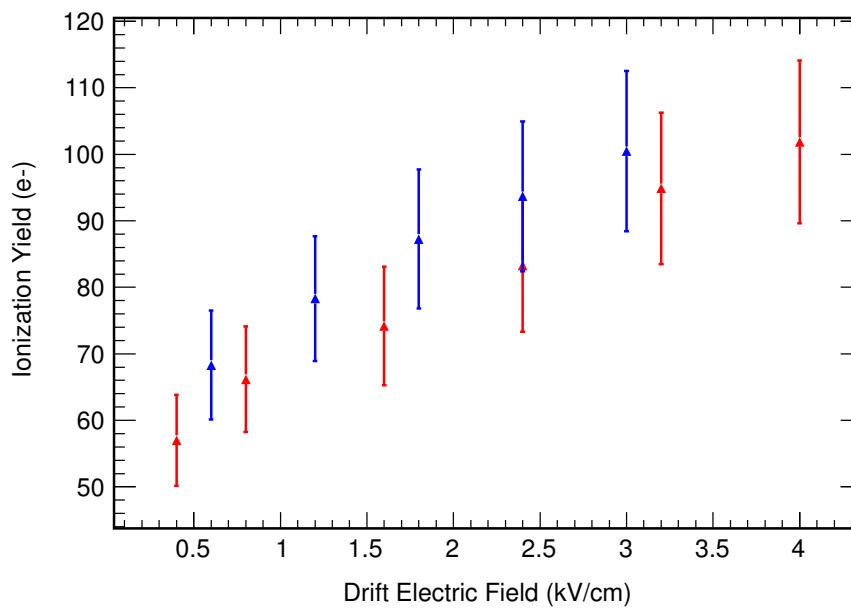


**Figure 6.11.** The number of electrons detected from the  $^{55}\text{Fe}$  source as a function of the applied electric field. For gain fields of 8.05 kV/cm (blue), and 6.44 kV/cm (red). The error bars represent the  $1\text{-}\sigma$  on the  $^{55}\text{Fe}$  energy peak.

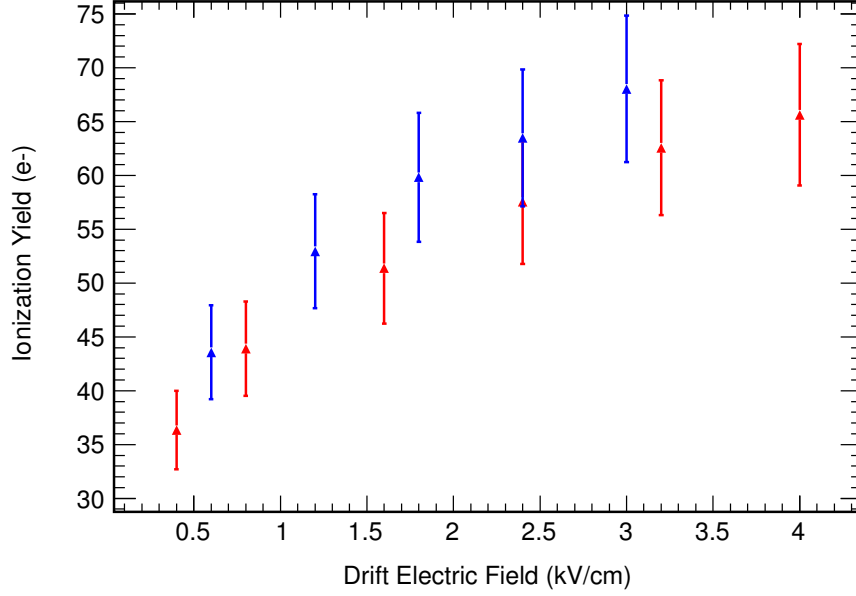


**Figure 6.12.** The number of electrons detected from the  $^{37}\text{Ar}$  K-shell events as a function of the applied electric field. For gain fields of 8.05 kV/cm (blue), and 6.44 kV/cm (red). The error bars represent the 1- $\sigma$  on the  $^{37}\text{Ar}$  K-shell energy peak.

For lower electric fields, the geminate local recombination is greater than at higher electric fields, resulting in a smaller signal detected by the photomultiplier tubes. This is not true in the case of the 270 eV  $^{37}\text{Ar}$  peak. With an energy of  $\sim 270$  eV, the track length of the Auger electrons is of the order nm [154, 129], shorter than the  $\sim 2.6$   $\mu\text{m}$  thermalization length of the secondary electrons [155]. The thermalization length of the secondary electrons allows the electrons to escape the ion cloud during thermalization, which removes the electric field dependence, Figure 6.13.

With the known dependence of the ionization yield on the electric drift field at 0.270, 2.8, 6, and 60 keV, the *infinite field W-values* were calculated by extrapolating the results to high electric field (50 kV/cm). The results are shown in Table 6.3. This extrapolation leads to the reduction of the effect of the electric field on the initial local recombination, making nearly all of the initially produced charge available for detection. The experimental data acquired for the electric field dependence of the  $^{37}\text{Ar}$  and  $^{55}\text{Fe}$  signals produced in the detectors allows the

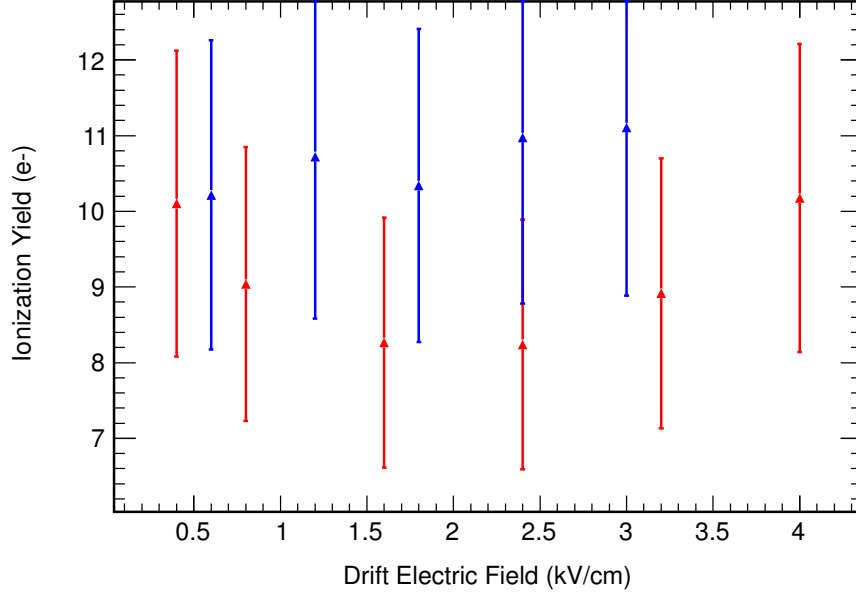


**Figure 6.13.** The number of electrons detected from the  $^{37}\text{Ar}$  L-shell events as a function of the applied electric field. For gain fields of 8.05 kV/cm (blue), and 6.44 kV/cm (red). The error bars represent the  $1\text{-}\sigma$  on the  $^{37}\text{Ar}$  L-shell energy peak.

**Table 6.3.** The infinite field W-values for liquid argon were calculated by extrapolating the measured recombination data to an electric field of 50 kV/cm. The increased W-value for  $^{55}\text{Fe}$  results from the loss of electrons during drift from the source, along with a potential loss of electrons which do not escape the proximity of the source. The W-value errors are determined from the error of the logarithmic fit to the data sets.

Decay Isotope	Event Energy (keV)	W-Value (eV)
$^{37}\text{Ar}$ L-shell	0.27	$28.08 \pm 1.70$
$^{37}\text{Ar}$ K-shell	2.82	$28.00 \pm 2.69$
$^{55}\text{Fe}$	5.9	$41.01 \pm 5.00$
$^{241}\text{Am}$	60	$17.74 \pm 1.70$

validation of the electron transport model. The decreased electron yields for  $^{55}\text{Fe}$  are likely due to two factors. It is possible that not all of the electrons escape from the physical proximity of the source. Approximately  $\sim 10\%$  of the electrons to escape the  $^{55}\text{Fe}$  source are lost during drift due to impurities.



## 6.4 Ionization Profile Source Terms

In order to model the electron recombination of  $^{37}\text{Ar}$  and  $^{55}\text{Fe}$ , both the total number of electrons created and the ionization density need to be calculated. Through the use of the elastic and inelastic cross sections at each electron-atom collision, the electron transport code inherently calculates both the number of electrons and the ionization density for a given event.

The  $^{37}\text{Ar}$  source term was calculated using the Evaluated Atomic Data Library (EADL) tables [126, 127], Tables 6.4 and 6.5. The initial direction was randomly sampled, and the energies of the electrons emitted in the Auger relaxation were sampled from the EADL tables. With a K or L-shell vacancy, the EADL tables were used to sample the Auger relaxation of the resulting  $^{37}\text{Cl}$  atom. In the simulation of  $^{37}\text{Ar}$ , the initial shell vacancy was assumed to be either the K-shell or the L1-shell to correspond with the respective  $^{37}\text{Ar}$  peak being simulated. The vacancy probabilities given in Tables 6.4 and 6.5 were normalized to 1, as the X-ray contribution could be neglected in this model. A random probability was then compared to the EADL tables to determine the appropriate secondary and tertiary shells to fill the vacancies. The new vacancy in the tertiary shell was then filled by repeating this process until the vacancy was in an M-shell. Once the vacancy was in the M-shell, the resulting ion was either an  $^{37}\text{Cl}^{2+}$  or  $^{37}\text{Cl}^{3+}$ , which energetically limits the Auger process from continuing.

The transport of the initial Auger electrons is subsequently modeled using the electron transport code. Due to the high energy of the Auger electrons when an ionization event occurs, the direction of the secondary electron is randomly selected, and the energy of ejection is sampled from the Mueller-Fiedler distributions, Table 6.6 [156]. The Mueller-Fiedler distributions were measured for He, but are assumed to apply in Ar. If the primary electron energy is below 100 eV or above 600 eV, then the respective 100 eV and 600 eV secondary electron distributions are used. If the primary electron energy is between 100 and 600 eV, the distributions are interpolated in accordance with the primary electron energy.

For  $^{55}\text{Fe}$ , the initial X-ray emission energy was randomly selected in accordance with the X-ray emission probabilities, Table 3.1. The X-ray is assumed to undergo photoelectric absorption and produce a high energy electron of the X-ray energy

**Table 6.4.** The EADL transition table for the  $^{37}\text{Cl}$  K-shell [126, 127], which is used to generate the source term of Auger electrons in the decay of  $^{37}\text{Ar}$ . The source term is then used as an input into the electron transport code to determine the fraction of electrons that escape the initial ion cloud as the high energy Auger electrons slow down and are drifted under an electric field. The EADL tables for  $^{37}\text{Cl}$  are used as  $^{37}\text{Ar}$  decays via electron capture to produce  $^{37}\text{Cl}$  with an electron vacancy, which is subsequently filled with higher shell electrons.

Secondary Vacancy	Tertiary Vacancy	Probability	Electron Energy (eV)
K-Shell Vacancy			
L1	L1	6.475e-2	2268.80
L1	L2	7.074e-2	2327.37
L1	L3	1.362e-1	2329.15
L1	M1	1.409e-2	2512.01
L1	M2	5.345e-3	2524.43
L1	M3	1.027e-2	2524.56
L2	L2	1.267e-2	2385.94
L2	L3	3.172e-1	2387.72
L2	M1	6.769e-3	2570.58
L2	M2	1.841e-3	2583.00
L2	M3	2.144e-2	2583.13
L3	L3	1.801e-1	2389.50
L3	M1	1.306e-2	2572.36
L3	M2	2.144e-2	2584.78
L3	M3	2.462e-2	2584.91
M1	M1	7.574e-4	2755.22
M1	M2	5.113e-4	2767.64
M1	M3	9.894e-4	2767.77
M2	M2	6.154e-5	2780.06
M2	M3	1.402e-3	2780.19
M3	M3	8.095e-4	2780.32

minus the ionization potential of the argon target atom. The high energy electron was then transported and tracked in the same way as the Auger electrons of  $^{37}\text{Ar}$ .

## 6.5 Electron Transport Model Results

The electron transport model was run for  $\sim 100$  trials for the electric fields of 0.5, 1.0, 2.0, and 4.0 kV/cm. Each trial was run until each electron had traversed

**Table 6.5.** The EADL transition table for the  $^{37}\text{Cl}$  L-shell [126, 127], which is used to generate the source term of Auger electrons in the decay of  $^{37}\text{Ar}$ . The source term is then used as an input into the electron transport code to determine the fraction of electrons that escape the initial ion cloud as the high energy Auger electrons slow down and are drifted under an electric field. The EADL tables for  $^{37}\text{Cl}$  are used as  $^{37}\text{Ar}$  decays via electron capture to produce  $^{37}\text{Cl}$  with an electron vacancy, which is subsequently filled with higher shell electrons.

Secondary Vacancy	Tertiary Vacancy	Probability	Electron Energy (eV)
L1-Shell Vacancy			
L2	M1	1.774e-1	33.73
L2	M2	7.170e-2	46.15
L2	M3	7.989e-2	46.28
L3	M1	3.484e-1	35.51
L3	M2	7.756e-2	47.93
L3	M3	2.084e-1	48.06
M1	M1	7.217e-3	218.37
M1	M2	9.420e-3	230.79
M1	M3	1.867e-2	230.92
M2	M2	2.037e-4	243.21
M2	M3	3.007e-5	243.34
M3	M3	4.336e-4	243.47
L2-Shell Vacancy			
M1	M1	1.687e-2	159.80
M1	M2	2.611e-1	172.22
M1	M3	1.790e-2	172.35
M2	M2	1.507e-1	184.64
M2	M3	5.378e-1	184.77
M3	M3	1.532e-2	184.90
L3-Shell Vacancy			
M1	M1	1.660e-2	158.02
M1	M2	8.747e-3	170.44
M1	M3	2.700e-1	170.57
M2	M2	2.488e-3	182.86
M2	M3	2.819e-1	182.99
M3	M3	4.200e-1	183.12

**Table 6.6.** Cumulative secondary electron energy distributions for a primary electron emission energy. The distribution functions were measured for He [156], and assumed to apply for Ar. If the primary electron energy is between 100 and 600 eV, the distributions are interpolated; otherwise the closest distribution, either at 100 eV or 600 eV, is used.

Primary Electron Energy	Secondary Electron Energy					
	0 eV	2 eV	4 eV	10 eV	20 eV	40 eV
100 eV	1.0	1.0	0.796	0.508	0.268	0.133
200 eV	1.0	1.0	0.833	0.466	0.262	0.095
300 eV	1.0	1.0	0.919	0.508	0.224	0.087
400 eV	1.0	1.0	0.843	0.500	0.256	0.073
500 eV	1.0	1.0	0.855	0.513	0.239	0.069
600 eV	1.0	1.0	0.861	0.490	0.269	0.078

approximately  $1 \mu\text{m}$ ,  $9\text{E}7$  time steps for  $0.5 \text{ kV/cm}$ ,  $6\text{E}7$  time steps for  $1.0 \text{ kV/cm}$  and  $3\text{E}7$  time steps for  $2.0$  and  $4.0 \text{ kV/cm}$ . The number of electrons that escape from the initial ion cloud are shown in Figures 6.14 - 6.16. Due to the low number of charges generated, and the low ionization density of the  $270 \text{ eV } ^{37}\text{Ar}$  L-shell electrons, there was no dependence on the electric drift fields in the ranges studied. This can also be explained by the electron track lengths, which were on the order of nm's shorter than the  $\sim 2.6 \mu\text{m}$  thermalization length of the secondary electrons generated by the primary L-shell electron[155]. The larger thermalization length of the secondary electrons allows the electrons to escape the ion cloud before they are below the critical recombination energy (Table 2.5), which removes the electric field dependence.

The electron transport code produces three quantities: the number of ionizations, excitations, and the number of electrons that escape from the ion cloud. The total number of ionizations and excitations to occur during the thermalization process are shown in Table 6.7. The ratio of excitation to ionizations is calculated to be  $\sim 0.162 \pm 0.041$  by the simulation, which is within  $1\text{-}\sigma$  of the published measured value,  $0.19 \pm 0.02$  [87]. The prediction should be lower than that of the experiment, as the electrons which undergo recombination add to the excitation signal. The electron transport model was run at  $50 \text{ kV/cm}$  to obtain the *infinite field W-value*, or average energy required to generate an electron which escapes the initial ion cloud. The calculated infinite field W-values for  $^{37}\text{Ar}$  and  $^{55}\text{Fe}$  are

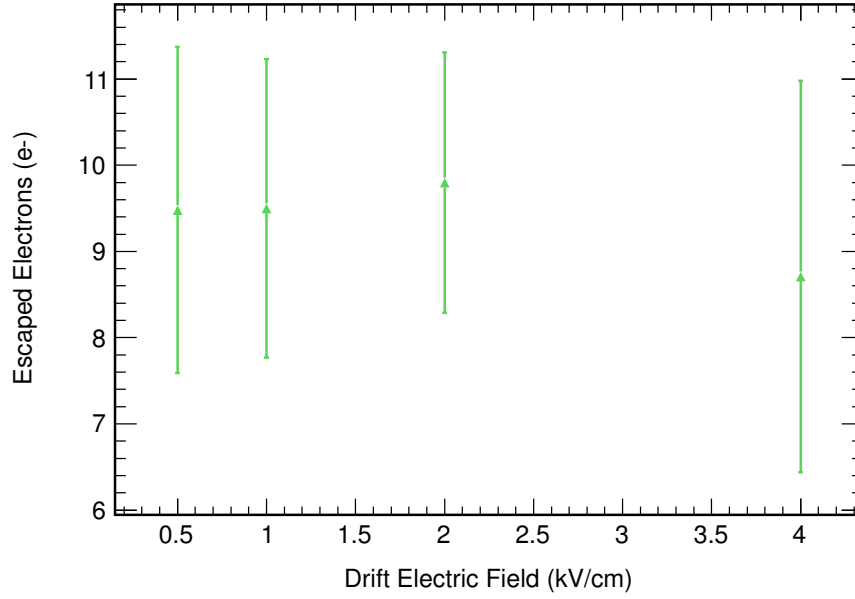


**Figure 6.14.** The predicted number of electrons that escape the ion cloud in the electron recombination model as a function of the electric field for the  $^{37}\text{Ar}$  L-shell peak. The error bars correspond to the  $1\text{-}\sigma$  standard deviation of the predicted electron yield.

**Table 6.7.** The electron transport code calculates the total number of electrons and photons created during the thermalization process of the initial high energy electrons for  $^{37}\text{Ar}$  and  $^{55}\text{Fe}$ . Based on the fraction of excitons generated as the electrons slow down ( $N_{\text{exc}}/N_{\text{ion}}$ ), the predicted values are in  $1\text{-}\sigma$  agreement with previously measured data of 0.2 [94]

Decay Isotope	Energy (keV)	Ionizations	Excitations	$N_{\text{exc}}/N_{\text{ion}}$
$^{37}\text{Ar}$ L-shell	0.27	$8.26 \pm 1.27$	$1.41 \pm 0.19$	$0.171 \pm 0.035$
$^{37}\text{Ar}$ K-shell	2.82	$115.06 \pm 4.79$	$18.68 \pm 4.60$	$0.162 \pm 0.041$
$^{55}\text{Fe}$	5.965	$243.96 \pm 10.18$	$48.76 \pm 5.82$	$0.20 \pm 0.026$

given in Table 6.8.

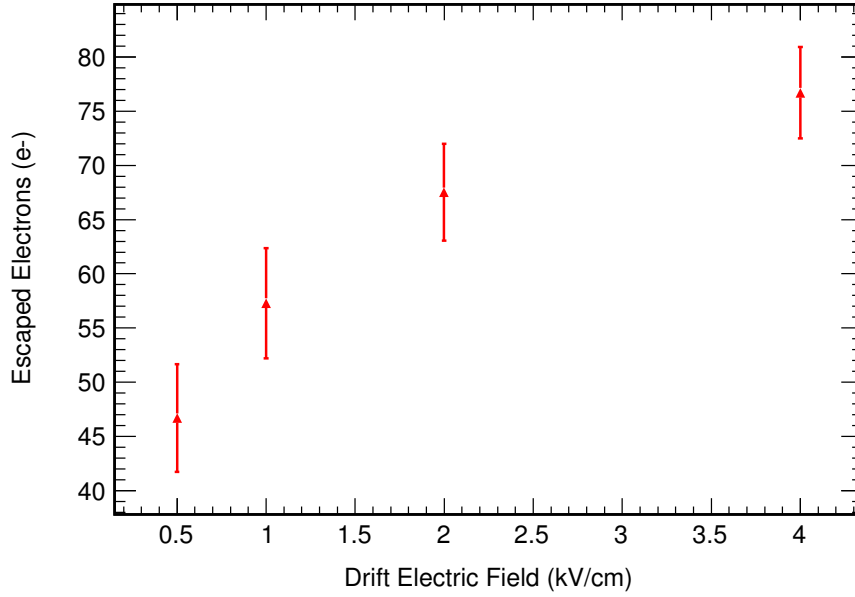


**Figure 6.15.** The predicted number of electrons that escape the ion cloud in the electron recombination model as a function of the electric field for the  $^{37}\text{Ar}$  K-shell peak. The error bars correspond to the  $1\text{-}\sigma$  standard deviation of the predicted electron yield.

**Table 6.8.** The infinite field W-values for liquid argon were calculated by running the electron transport code for an electric field of 50 kV/cm.

Decay Isotope	Energy (keV)	W-Value (eV)
$^{37}\text{Ar}$ L-shell	0.27	$24.3 \pm 1.0$
$^{37}\text{Ar}$ K-shell	2.82	$27.78 \pm 1.40$
$^{55}\text{Fe}$	5.965	$27.07 \pm 1.29$

## 6.6 Comparison between the Measurements and the Electron Transport Model

Validation of the electron transport model was obtained through comparison of the predicted drift field dependent ionization yields for the  $^{37}\text{Ar}$  and  $^{55}\text{Fe}$  with the experimental values. The ratio of predicted to measured yields was determined for  $^{37}\text{Ar}$  L-shell,  $^{37}\text{Ar}$  K-shell and  $^{55}\text{Fe}$  events. The drift field-dependent ratios for each of the peaks are shown in Figure 6.17. The  $^{37}\text{Ar}$  L-shell predictions

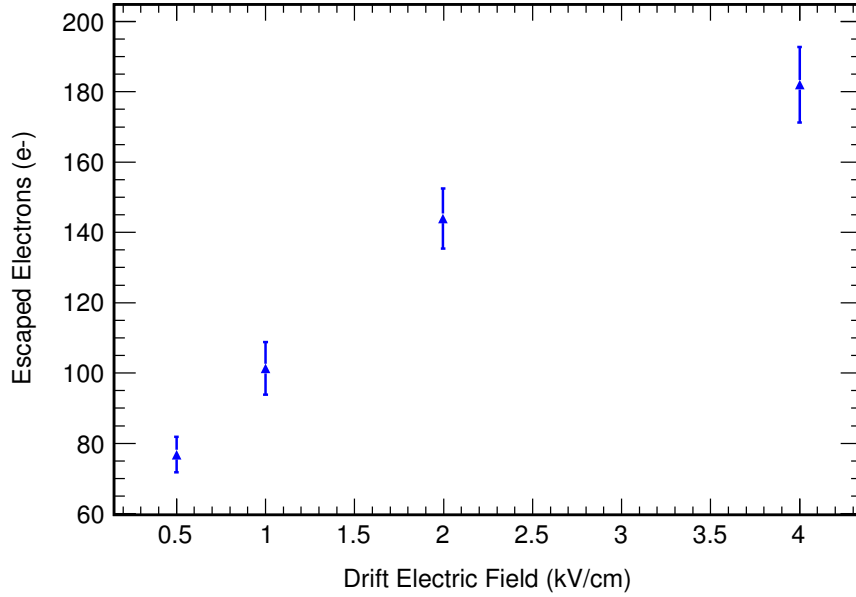


**Figure 6.16.** The predicted number of electrons that escape the ion cloud in the electron recombination model as a function of the electric field for the  $^{55}\text{Fe}$ . The error bars correspond to the  $1\text{-}\sigma$  standard deviation of the predicted electron yield.

match both the electron yields and the lack of electric field dependence seen in the experiment. For the  $^{37}\text{Ar}$  K-shell peak, the measured ionization yield was  $\sim 10\text{-}15\%$  lower than that of the model, which is within  $1\text{-}\sigma$  of both the model and the experiment when the loss of electrons during drift is taken into account. The  $^{55}\text{Fe}$  data had the largest discrepancy up to  $\sim 80\%$  lower than the electron transport model. The over-estimate of the  $^{55}\text{Fe}$  electron yields by the simulation can partially be understood through columnar recombination within the detector, which occurs after the electrons escape from the ion cloud and was not included in this simulation. As was stated in Section 6.3, the electron lifetime resulted in a  $\sim 10\%$  loss of the electrons during drift from the bottom of the active volume. The additional over-estimate by the model along with the measured high W-value, 41.01 eV, compared to the previously measured value of 23.6 eV, Table 6.3, suggest that there were additional effects which led to the loss of electrons produced by the  $^{55}\text{Fe}$  source. One potential location for the loss of electrons could be the electric field irregularities around the source. Electric field irregularities could lead to

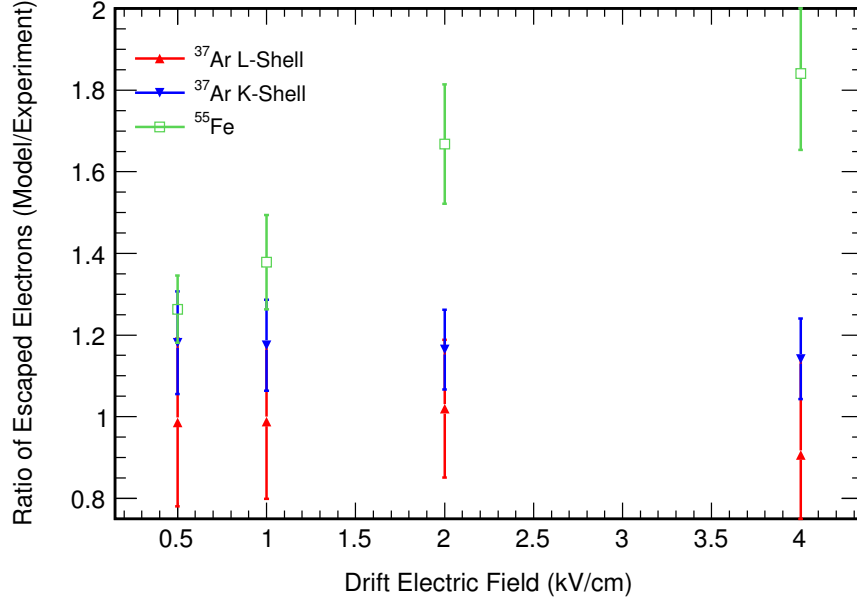


**Figure 6.17.** The ratio of the drift field dependent ionization yields from the simulation to that measured in the dual-phase Ar detector. A logarithmic fit was applied to the combination of the different gain field experimental data sets and compared to the electron transport model predictions.

incomplete electron extraction from the  $^{55}\text{Fe}$  source surface, as the mean free path of the  $^{55}\text{Fe}$  X-rays was  $\sim 28 \mu\text{m}$  [151]. The electric field effects would be amplified as the electric field increased, which explains the decreased agreement between the electron transport model and experiment at higher electric fields. Incomplete electron extraction from the source surface could also explain the localization of the single liquid electrons to the  $^{55}\text{Fe}$  source location, Section 5.9. For these reasons, the discrepancy between the model and experiment for the  $^{55}\text{Fe}$  results does not detract from the usefulness of the electron transport model.

With the successful validation of the electron transport code, the predictions made in Chapter 2 can be utilized with an additional degree of certainty. Additionally, this allows for further predictions of the expected signals from coherent neutrino-nucleus scatter (CNNS), Section 8.1.



# G/NARRLI Detector Nuclear Ionization Quench Factor Measurements

In order to directly validate the predictions of the ionization model described in Chapter 2, the nuclear ionization yield should be experimentally measured at low energies. The ionization yield can be measured at  $\sim 7$  keVr using neutrons generated with the  ${}^7\text{Li}(p,n){}^7\text{Be}$  reaction, by elastically scattering neutrons off argon. In this Chapter, a discussion of the method for production and optimization of the neutrons via the  ${}^7\text{Li}(p,n){}^7\text{Be}$  reaction is presented in Section 7.2. A description is provided of the Center for Accelerator Mass Spectrometry (CAMS), the facility where the experiment took place, including the procedure used to calibrate the energy of the proton beam, Section 7.4. A prediction of the expected signal from the detector produced by the neutron energy deposition is discussed in Section 7.5. Lastly, a description of the method for extraction of the ionization yield from acquired neutron scatter data is provided in Section 7.6.

## 7.1 Detector Transport and Setup

The schematic of the experimental setup in which the neutrons are generated by the  ${}^7\text{Li}(p,n){}^7\text{Be}$  reaction is shown in Figure 7.1. The neutrons pass through the collimator and interact within the dual-phase Ar detector. The dual-phase Ar

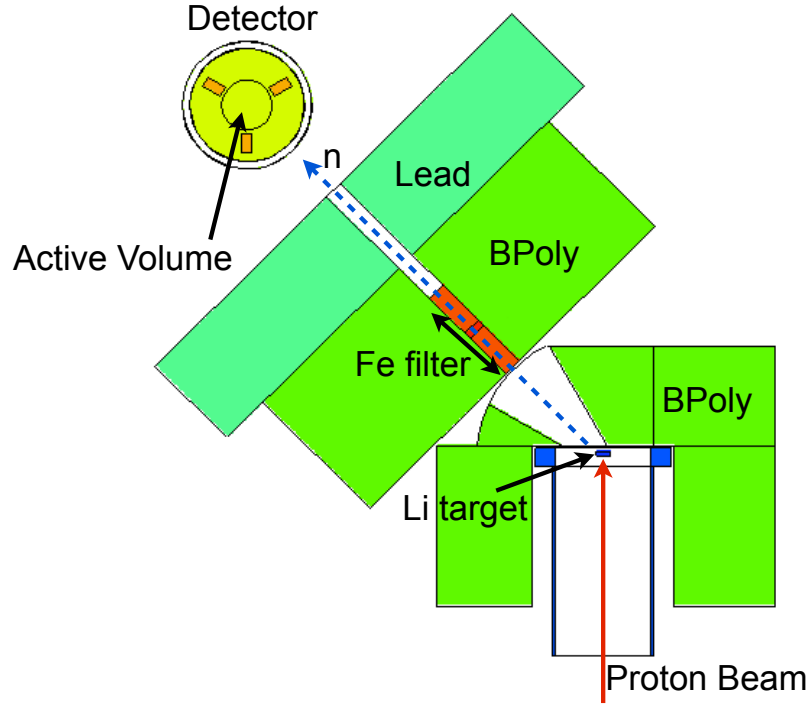


**Figure 7.1.** Schematic of the experimental setup for measuring the ionization yield in LAr. The protons are accelerated toward a Li target, where neutrons are generated with an energy and angular distribution that depends on the incident proton energy. The neutrons are collimated at  $45^\circ$  and subsequently filtered before entering the detector, Section 7.2.

detector was designed to be *portable*, Chapter 5, which allowed the entire detector along with the electronics rack and accompanying components to be loaded on the back of a flat-bed truck and moved to the experimental facility, Figure 7.2. Once the detector has been transported to CAMS, the detector can be made operational and take data continuously within two to three days. In CAMS the detector is placed on a rotatable table, Figure 7.3, so that the energy and angular distribution measurements can be tuned to the desired specifications, Section 7.2.

## 7.2 Neutron Generation and Optimization

Similar to prior experiments with the portable neutron generator, the  ${}^7\text{Li}(p,n){}^7\text{Be}$  reaction was used to produce neutrons of desired energies for the experiment.



**Figure 7.2.** The entire detector, electronics rack, leak checker, and all accompanying parts were loaded in a flat-bed truck and moved to CAMS. The process took approximately an hour. The detector is shown outside the facility awaiting setup.

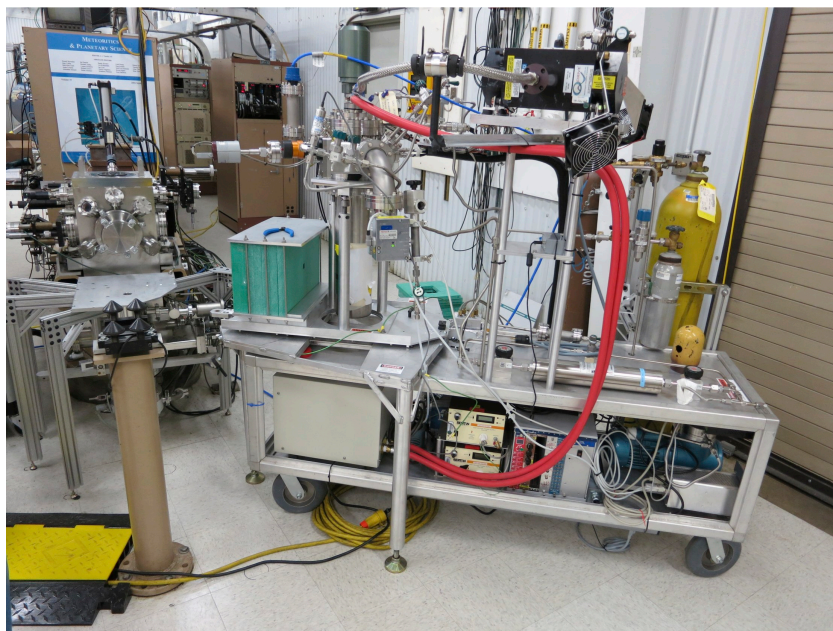


**Figure 7.3.** After moving the detector to CAMS, it was placed on a rotatable table to allow for tuning of the neutron energy and angular distributions, Section 7.2. The detector was plugged in and operational within two to three days after the move.

Neutrons were generated with an energy and angular distribution driven by the reaction kinematics, Figure 4.3. This distribution and the location of the detector could be manipulated to obtain the desired neutron spectrum at the detector.

Using Equation (4.1), the maximum recoil energy can be calculated for an 85 keV neutron, which is at the higher energy end of the 80 keV resonance, Figure 4.4. For an 85 keV neutron scattering within the detector, the maximum energy deposited to the argon nucleus is  $\sim 8.1$  keVr, which will leave the neutron with the energy of 76.9 keV. The 76.9 keV energy is still within the 80 keV resonance, with a cross section of  $\sim 10$  barns, allowing the neutron to scatter again, depositing additional energy within the detector. Multiple scatters result in a smeared end-point energy in the deposition spectra, as the multiple scatters are seen as a single event within the detector.

Placing the detector at  $45^\circ$  decreases the high-energy component of the neutron spectrum, providing a sharp cut-off, Figure 7.4. Neutrons with emission angles not in the vicinity of  $45^\circ$  are blocked using a collimator. The collimator consists of 15 cm of borated polyethylene to block the neutrons and 10 cm of Pb to block the gamma rays produced in the target and by neutron captures on boron. The aperture of the collimator is  $\pm 1.5^\circ$ , providing a neutron beam 3 cm in diameter within the detector. Side rails on the detector table hold the collimator in constant alignment with the center of the active region. The collimator and detector were aligned with respect to the proton beam using a  $45^\circ$  mirror and a laser pointer which was press-fit inside the collimator opening, Figure 7.5. The rotatable table was machined with a slot positioned every  $0.5^\circ$  between  $30^\circ$  and  $60^\circ$ , with a central position of  $45^\circ$ , to allow for alteration of the incident neutron spectrum, if desired.

In practice, the cut-off of the spectrum has a smooth curvature due to the energy spread of the proton beam. The neutron spectrum was predicted with MCNPX [158, 159], assuming a proton FWHM energy spread of 3 keV. With the proton beam energy spread, the neutrons populate higher energies, overlapping with a greater fraction of the 80 keV resonance, resulting in a greater number of multiple scatters. Figure 7.6 shows the spread of neutron energies and includes the additional low-energy component due to the neutrons that scatter within the collimator and exit the aperture. A tail in the spectrum extends up to  $\sim 125$  keV due to high energy neutrons which scatter from low angles to  $45^\circ$  and exit the

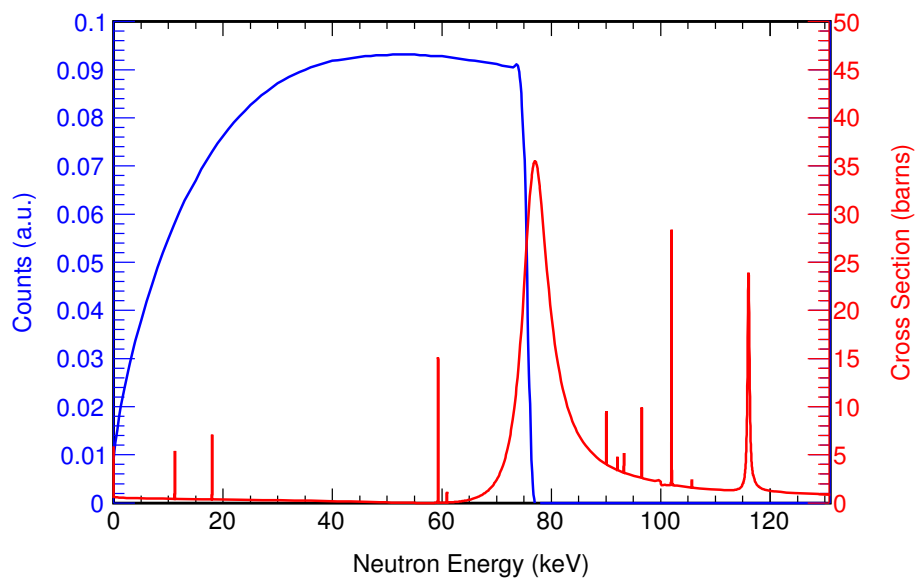


**Figure 7.4.** Neutron spectrum at an angle of  $45^\circ$  (blue) [132, 133] with a sharp drop off at the low-energy side of the 80 keV resonance in the cross section for neutron elastic scatter on Ar (red) [157].

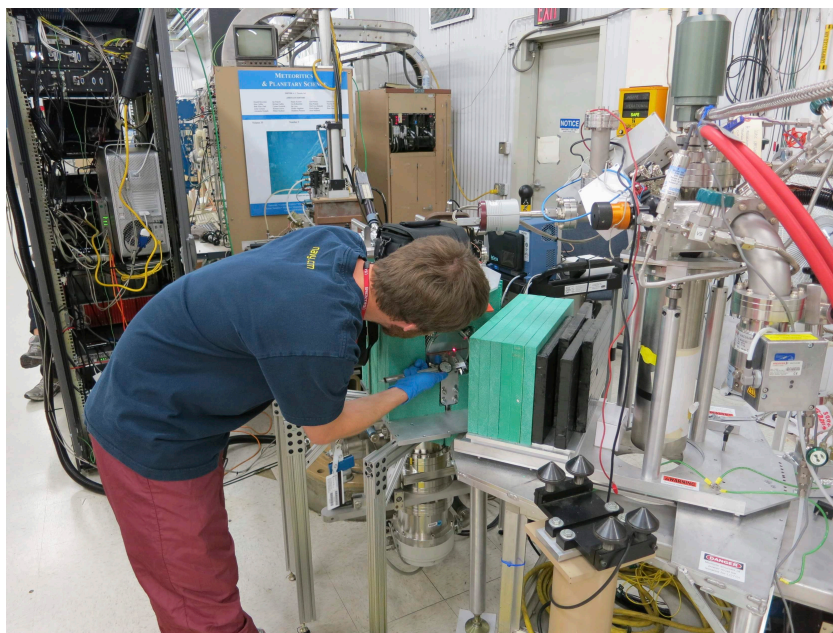


**Figure 7.5.** The collimator and detector were aligned to  $45^\circ$  using a laser pointed through the collimator. When the laser reflected off a  $45^\circ$  mirror back into itself, the collimator and detector were both at  $45^\circ$ .

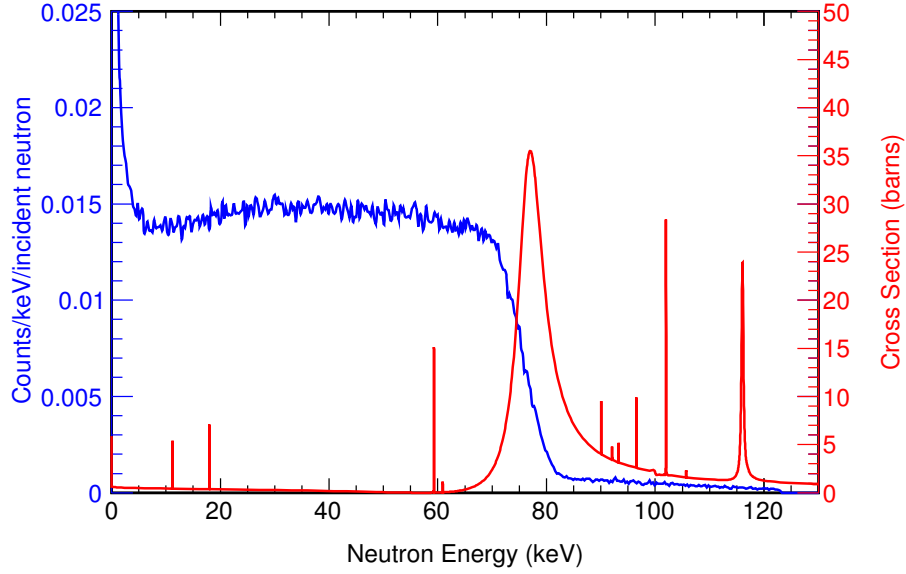


**Figure 7.6.** Predicted neutron spectrum (blue) exiting the collimator at  $45^\circ$  for incident 1.93 MeV protons with a 3 keV FWHM energy spread. The  $^{40}\text{Ar}(n,\text{el})$  cross section (red) is shown for reference.

aperture.

To optimize the neutron spectrum and further reduce the number of multiple scatters, a neutron filter can be used within the collimator [160, 39]. For the ionization yield measurement, the neutron spectrum is further optimized using a filter composed of natural iron and natural titanium.  $^{56}\text{Fe}$  has a resonance dip at 73 keV, which aligns with the low-energy tail of the 80 keV resonance in  $^{40}\text{Ar}$  to reduce the flux of higher energy neutrons which result in multiple scatters. The resonance dip at 82 keV still allows a fraction of higher energy neutrons to pass through the filter and produce a small multiple scatter signal. Additionally,  $^{56}\text{Fe}$  has a low energy resonance dip at 24 keV, which allows the passage of low-energy neutrons which add to low-energy scatter background within the detector.  $^{48}\text{Ti}$  preferentially scatters the low-energy neutrons, by a factor of  $\sim 4\times$  more than the 73 keV neutrons. The (n,el) cross sections for  $^{56}\text{Fe}$  and  $^{48}\text{Ti}$  are overlaid with the (n,el) cross section for  $^{40}\text{Ar}$  in Figure 7.7. The neutron spectrum exiting the filter is comprised primarily of neutrons below 73 keV, a small fraction of neutrons between 73 and 83 keV, and a low intensity tail that extends up to  $\sim 125$  keV,



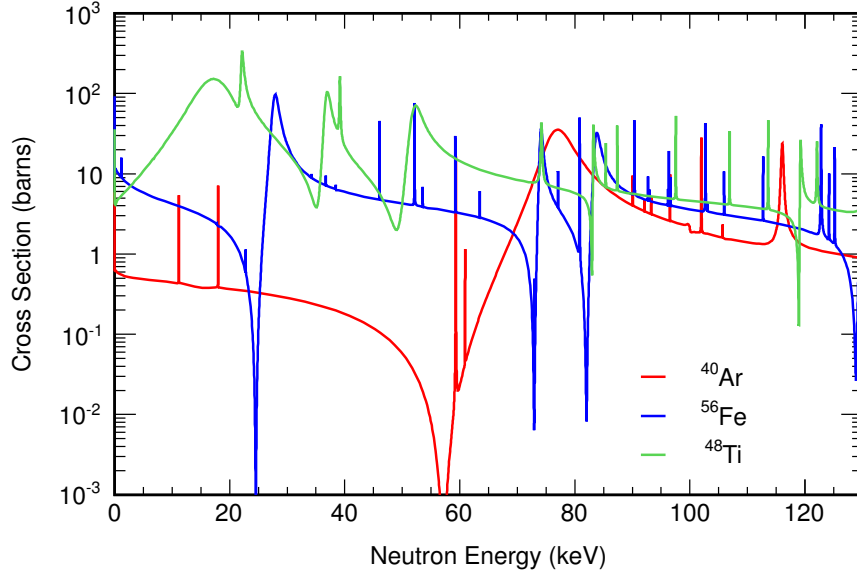


**Figure 7.7.** The (n,el) cross sections for  $^{56}\text{Fe}$  (blue) and  $^{48}\text{Ti}$  (green) show that the neutrons scatter preferentially to leave 73 keV neutrons which scatter within the 80 keV resonance in  $^{40}\text{Ar}$  (red), the primary isotope within the detector volume [157]. The three resonance dips in  $^{56}\text{Fe}$  occur at 24, 73, and 82 keV.  $^{48}\text{Ti}$  preferentially scatters low-energy neutrons to increase the signal-to-background ratio.

Figure 7.8. While the total neutron rate decreases with the filter, the fraction of incident neutrons which interact within the 80 keV resonance increases by a factor of  $\sim 8x$ . The filter was press-fit inside the collimator, but no additional effort was made to prevent the streaming of neutrons or gammas between the filter and the collimator.

### 7.3 LUXSim Simulations

The Geant4 [130] based simulation software package, LUXSim [161] is used to better understand the operation of the G/NARRLI detector. A detailed geometry of the G/NARRLI detector is developed for the simulation, shown in Figure 7.9. The geometry includes the dewar containing the detector, the feedthrough flange above the detector, the external Al and internal PEEK support rods, the field shaping rings, and the PMTs. The neutron spectrum is obtained from an MCNPX [158, 159] simulation which models the transport of the protons through the Li

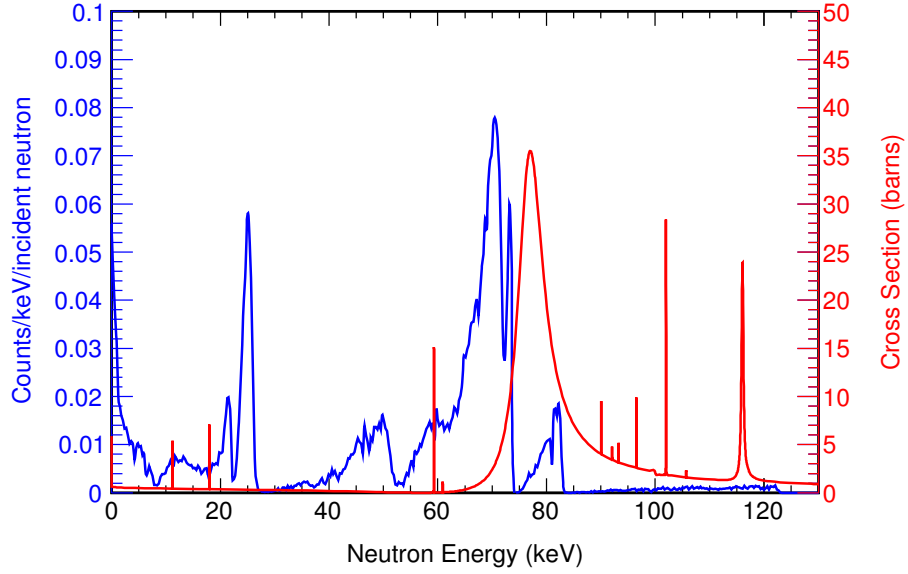


**Figure 7.8.** Predicted neutron spectrum (blue) out of the collimator operating at  $45^\circ$ , for a 1.93 MeV proton beam with a 3 keV FWHM energy spread. The Fe/Ti filter reduces the neutrons above and below the 73 keV  $^{56}\text{Fe}$  resonance. The regions of interest are the areas under both the neutron spectrum and the  $^{40}\text{Ar}$  (n,el) cross section (red).

target. The proton beam is assumed to have a 5 keV FWHM, and generates both  $^7\text{Li}(p,n)^7\text{Be}$  neutrons and  $^7\text{Li}(p,p')^7\text{Li}$  gammas. The neutron spectrum is then transported through the shielding and collimator setup, with the incident beam on the detector being input into the LUXSim simulation.

The energy deposition within the Ar active volume from the  $^7\text{Li}(p,n)^7\text{Be}$  neutrons was simulated. The shoulder at 7 keVr corresponding to a maximum energy of 73 keV that can be deposited by a neutron in a single scatter, Equation (4.1), is less distinct when no filter is in place, as the multiple scatters populate energies above 7 keVr. With the filter in place, the number of multiple scatters decreases, providing a sharp shoulder which can be utilized as the end-point of the spectrum to measure the ionization yield at 7 keVr, Figure 7.10. For the remainder of this analysis, the energy deposition spectrum with the Fe/Ti filter was used.



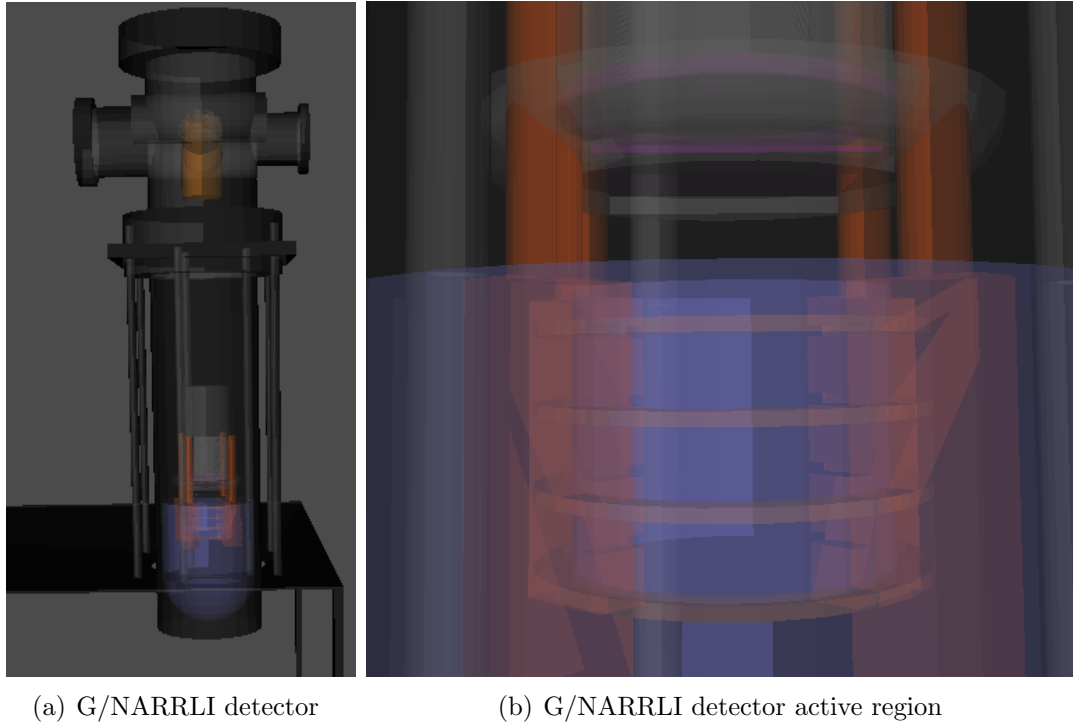


**Figure 7.9.** The G/NARRLI detector coded into Geant4 for the purposes of detector calibration comparison and signal prediction for calculating the ionization yield.

## 7.4 Measurements at the Center for Accelerator Mass Spectrometry (CAMS) Facility

The ionization yield measurements took place at the Lawrence Livermore National Laboratory's Center for Accelerator Mass Spectrometry (CAMS). The  $\mu$ -Probe tandem accelerator, Figure 7.11, was used to accelerate protons to 1.93 MeV and bombard a lithium (Li) target to produce neutrons, Section 7.2. If the proton energy is too low, neutrons are not generated with sufficiently high energies to interact with the 80 keV  $^{40}\text{Ar}$  resonance. If the proton energy is too high, too many high-energy neutrons are generated, leading to an increase in the frequency of multiple scatters. For these reasons, the proton beam energy was calibrated using a silicon detector with a  $^{226}\text{Ra}$  check source. The silicon detector and the  $^{226}\text{Ra}$  source were placed approximately 12 inches from the end of the proton beam. The  $^{226}\text{Ra}$  source was attached to the side of the chamber with a screw, while the silicon detector was placed on a ladder which allowed it to be moved between

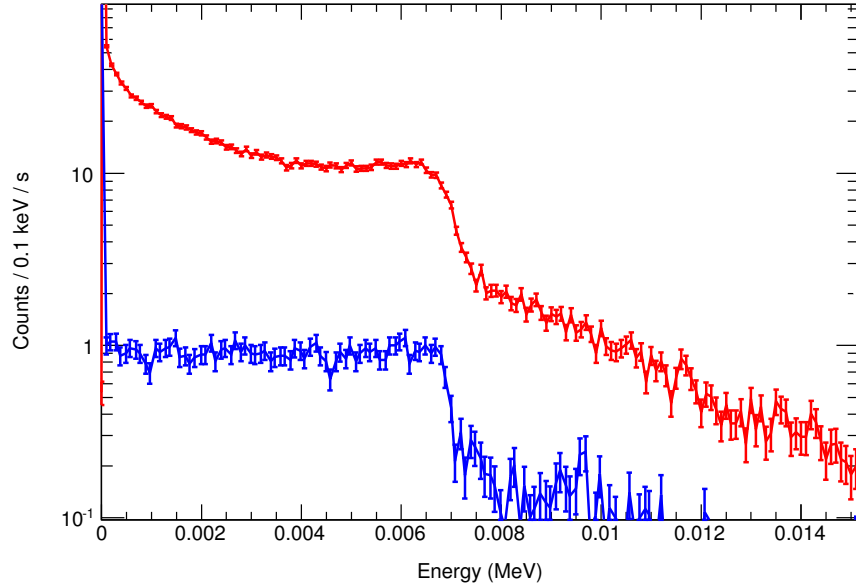


**Figure 7.10.** Prediction of the energy deposited per neutron, which includes multiple scatters, with the Fe/Ti filter (blue) and without the filter (red). The filter reduces the fraction of multiple scatters and the low-energy component due to the neutrons with energies below 40 keV.

the  $\alpha$  check source and the proton beam, Figure 7.12. The Si detector was an Ortec TB-018-150-200, with a 15 mm<sup>2</sup> active area and a sensitive depth of 200  $\mu$ m. Data from the Si detector was acquired using an Ortec pocket multi-channel analyzer(MCA). The Si detector was calibrated with 5 of 6  $\alpha$  peaks of  $^{226}\text{Ra}$  (the highest energy peak was non-linear) to obtain the conversion from MCA channels to energy of

$$E = 8.383 \times 10^{-4} \cdot MCA - 10.33 \times 10^{-2}, \quad (7.1)$$

where  $MCA$  is the MCA channel number, and  $E$  is the energy deposited in the Si detector. With the known calibration, it was determined that the actual proton energy was 15 keV below the energy provided by the accelerator instrumentation.

Produced in 2006 by PolyPlus [162], the Li target was 10  $\mu$ m thick, 8 mm in diameter, and coated onto a 5 mm thick Ag puck with base diameters of 15 mm (front) and 13 mm (back) to act as a beam dump for the protons. The target was held in place on an aluminum ISO flange using an aluminum source holder, which is held down with 4 screws to provide a good thermal contact for removal of the

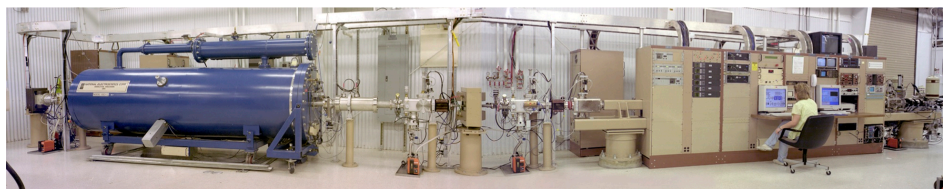


**Figure 7.11.** Proton accelerator was used to bombard a Li target and create a neutron spectrum via the (p,Li) reaction.

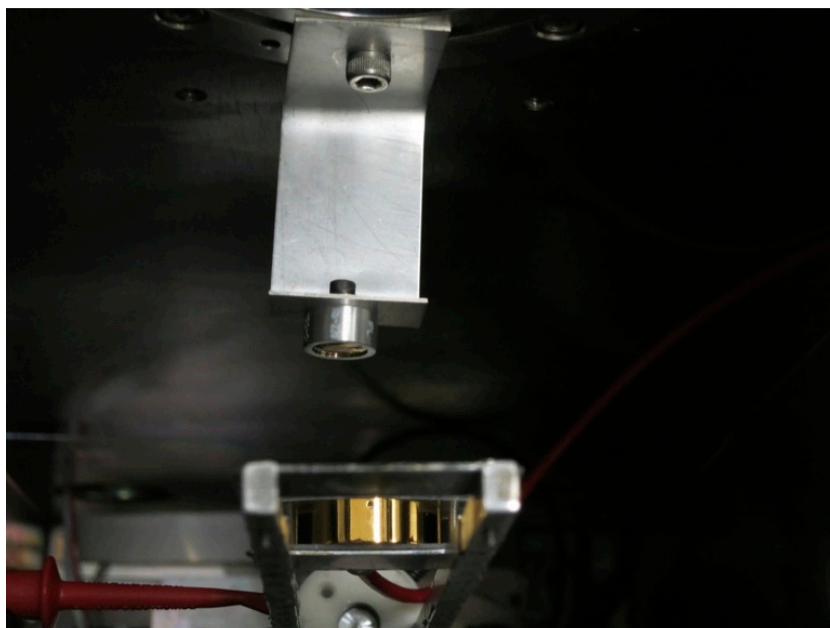


**Figure 7.12.** The  $^{226}\text{Ra}$   $\alpha$  source was held against the side of the vacuum chamber. The Si detector was electrically isolated and attached to a ladder so it could be moved up into the proton beam and down to the  $\alpha$  source for energy calibration.

heat produced by the protons, Figure 7.13. The sealed Li target was placed in a glove bag and filled with Ar to prevent the oxidation of the Li. After  $\sim 20$  minutes of filling the glove bag with Ar and 6 full flushes of the fill gas, the Li target was taken out and attached to the target holder, Figure 7.14. The target was held in electrical contact with the end flange and the nipple which houses the target, so that the beam current could be read directly off of the nipple, eliminating the need to apply a voltage to contain the secondary electrons.

Once the target was installed, it could be viewed through a viewport on the nipple using a mirror placed inside. The Li target holder was coated with an epoxy/phosphor mixture to provide visual beam profile diagnostics, Figure 7.15.

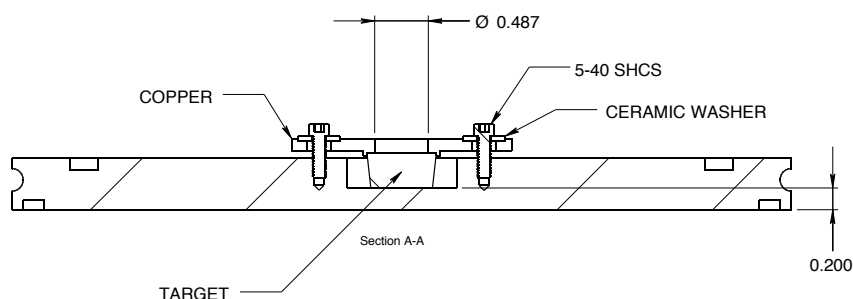


**Figure 7.13.** The Li target was held in place with an Al target holder which pressed the target against the Al end flange. The Li target was held in both thermal and electrical contact with the Al flange. Thermal contact provided a heat sink for the target so that the heat produced as the protons stopped did not vaporize the Li. Electrical contact allowed the proton current to be read directly from the end flange, using the nipple as a charge trap, so that no electrical bias was required to contain the secondary electrons.

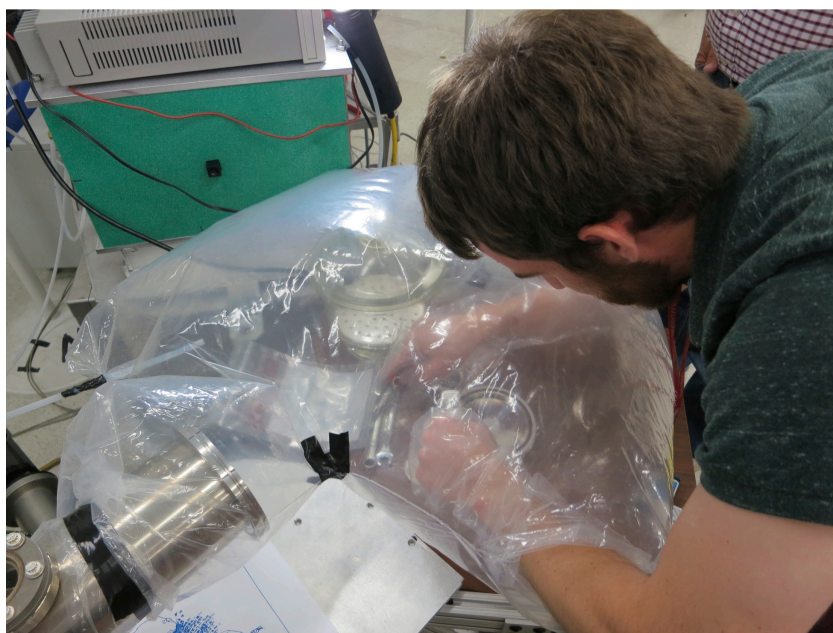


**Figure 7.14.** To install the Li target, the target, target holder, end flange and all tools needed were placed in a glove bag, which was attached to the end nipple. The beam line was back-filled with Ar. The end flange was then removed from the nipple, which filled the glove bag with Ar. The Ar then flowed through the beam line and the glove bag for 20 minutes, including 6 flushes of the glove bag before the Li was removed from its sealed package.

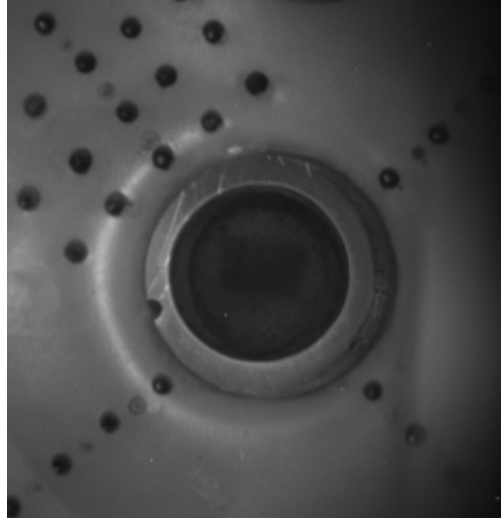


**Figure 7.15.** The Li target is 10  $\mu\text{m}$  thick and 8 mm in diameter, coated on a 5 mm thick Ag beam stop. The target is held in place using an Al target holder which is coated with an epoxy/phosphor mixture. The phosphor allows the proton beam to be seen with the camera and provides visual beam diagnostics.

When the proton beam was directed on target, it could be seen as a 3 mm by 3 mm beam spot on the Li, with a halo extending out about to  $\sim 15$  mm in diameter, Figure 7.16.

To proton energy,  $E_p$ , was additionally checked by measuring the threshold for neutron generation. The threshold measured was not that for neutron generation, but for generating neutrons at an  $45^\circ$  angle. It has been previously shown that the neutron yield,  $Y$ , scales with  $E_p^{3/2}$  [163, 164], which results in a linear relation between  $Y^{2/3}$  and  $E_p$ , Figure 7.17. The measured threshold proton energy of 1.898 MeV agrees with the previously published value for generation of neutrons at  $45^\circ$  of 1.90 MeV, Figure 7.18 [132].

Neutron generation rates were measured to be to 5-10 times lower than those predicted by MCNPX [158, 159]. Since the target was produced in 2006, the Ag backing has diffused into the Li target. The Ag scatters the protons, which reduces the energies of the protons and decreases the thickness of Li which the protons traverse before their energies drop below the threshold for neutron generation. At room temperature, Ag diffuses into Li with a diffusion constant of  $\sim 5 \times 10^{11}$

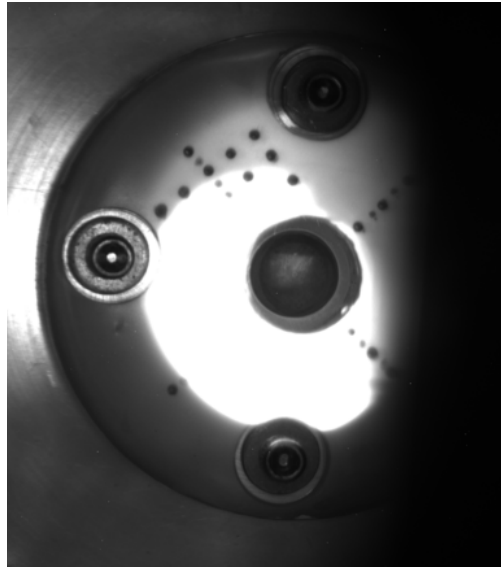


**Figure 7.16.** When the accelerator is on, protons bombard the Li in a 3 mm diameter beam spot, with an additional halo which extends out to a diameter of  $\sim 15$  mm.

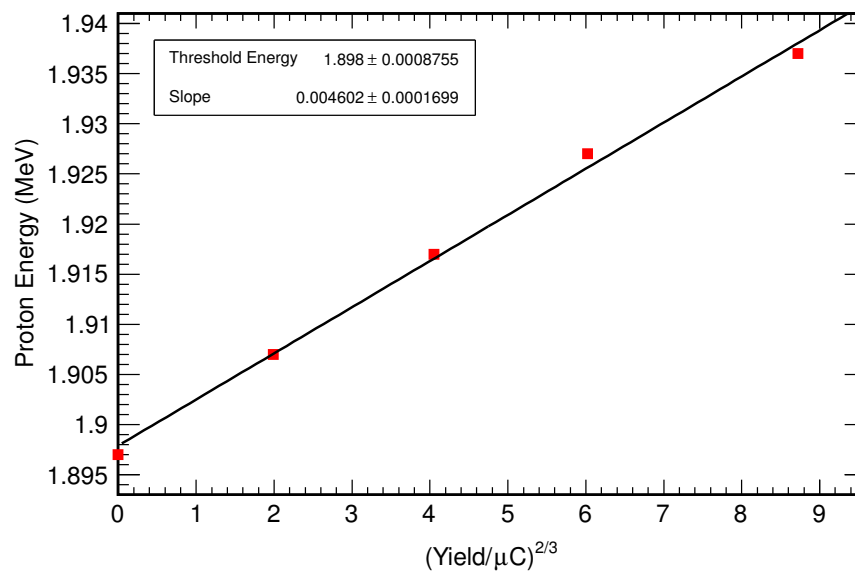


**Figure 7.17.** The neutron yield scales with the proton energy to the power of  $3/2$ . A linear fit produced in this fashion results in a neutron generation threshold of 1.898 MeV.

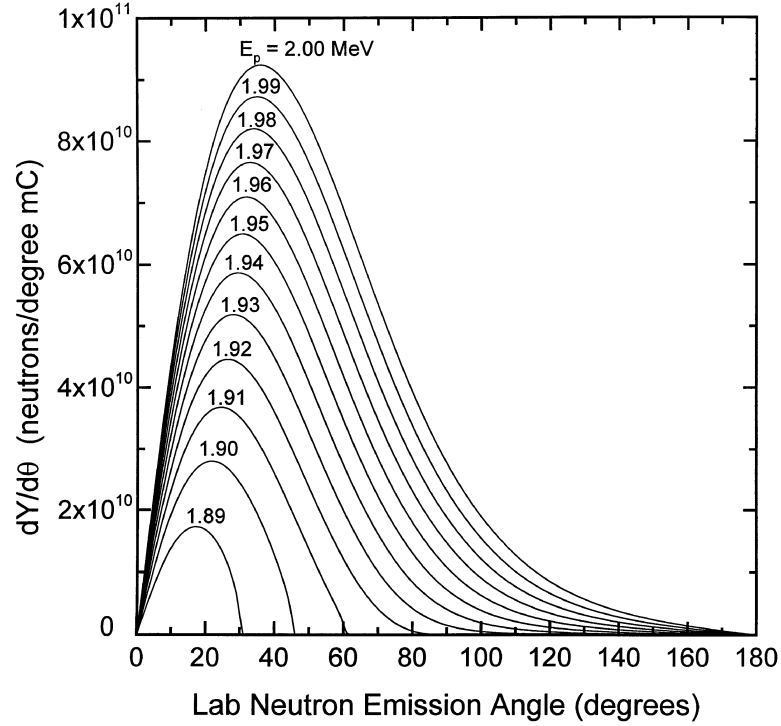


**Figure 7.18.** Neutron yields for proton energy in the vicinity of the reaction threshold, previously published by Lee and Zhou [132]. The threshold for generating neutrons at  $45^\circ$  is  $\sim 1.90$  MeV, which agrees well with the measured value of 1.898 MeV in our experiment.

$\text{cm}^2/\text{s}$ . [165]. With the diffusion length defined as

$$L_{Ag \rightarrow Li} = \sqrt{D_{Ag} \times t}, \quad (7.2)$$

where  $D_{Ag}$  is the diffusion constant for Ag diffusion into Li and  $t$  is time, a diffusion length of  $\approx 4 \mu\text{m}/\text{hour}$  results. Based on the calculated diffusion length, it is reasonable to conjecture that a significant fraction of Ag has diffused into the Li target. The resulting decrease in neutron yield was calculated with the assumptions that the  $\text{AgLi}_x$  target was homogenous, the compound stopping power [166] was constant throughout the target and scaled linearly with the atom fraction per Bragg-Kleeman Rule [132, 167, 168, 169], and that the Li atom number was constant. The calculated neutron yields with respect to that of a pure Li target are shown in Figure 7.19, with the deficit reaching up to a factor of  $\sim 20$  for  $\text{AgLi}_x$ .

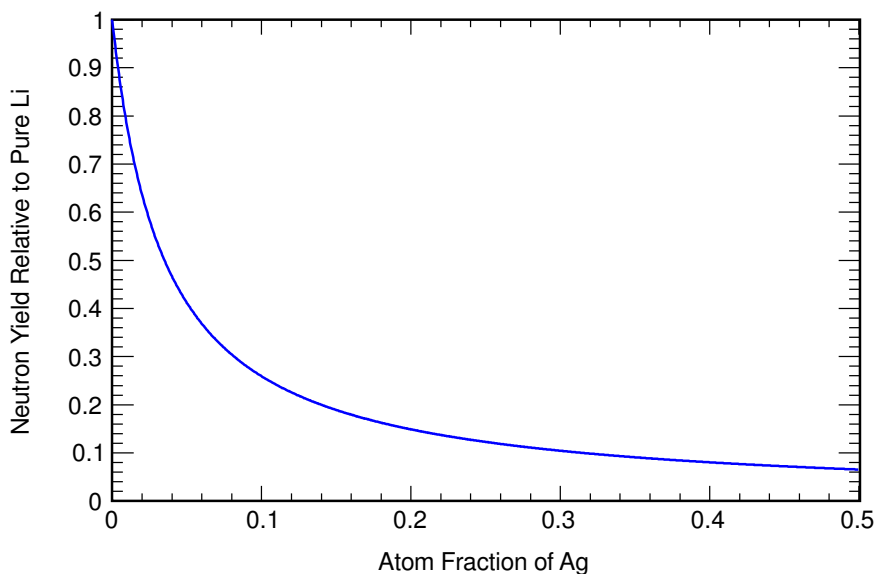


**Figure 7.19.** Ag diffuses into the Li target and acts to scatter the protons, reducing the active target thickness. This in turn reduces the neutron yields compared to the expected yields from pure Li. For a 5–10 $\times$  reduction, the Li target has a stoichiometry between  $\text{Ag}_2\text{Li}_3$  and  $\text{Ag}_3\text{Li}_{10}$ .

While the Li target did not produce a sufficient flux of neutrons to measure the ionization yield, the gamma yields from the target were nearly unaltered since the protons could traverse the entire target thickness prior to their energies dropping below the  ${}^7\text{Li}(\text{p},\text{p}'){}^7\text{Li}$  threshold. Measurements of both the rate and spectrum of gamma background with the dual-phase Ar detector were performed. By tuning the proton beam to just below the threshold for generating neutrons at  $45^\circ$ , the gamma backgrounds from the  ${}^7\text{Li}(\text{p},\text{p}'){}^7\text{Li}$  reaction and the  ${}^{11}\text{B}(\text{n},\alpha){}^7\text{Li}$  gammas from neutron capture in the borated polyethylene shielding were considered. The gammas produced by neutron captures increase with increased neutron yields, but the primary source of background gamma rays is the  ${}^7\text{Li}(\text{p},\text{p}'){}^7\text{Li}$  reaction. The background gamma rates were measured to be 12 Hz, Figure 7.20, within the fiducial volume of the detector and with the same analysis cuts that were used to measure the ionization yield. Additional Pb shielding has been applied, with an MCNPX predicted reduction in gamma rates of 5x, which would result in a background gamma rate of  $\sim 2.5$  Hz, twice the natural background rate measured



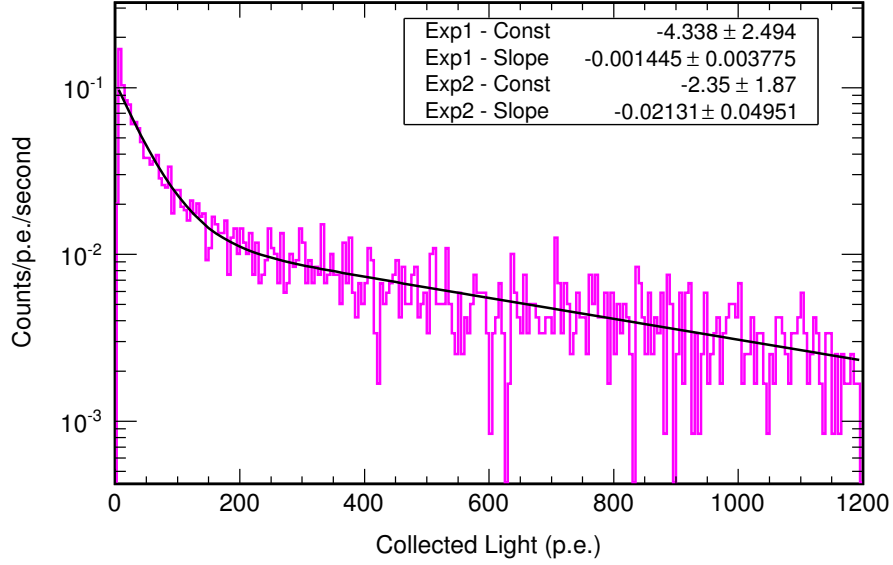


**Figure 7.20.** The proton beam was tuned to produce neutrons below the angle of  $45^\circ$ , providing both  ${}^7\text{Li}(p,p'){}^7\text{Li}$  gammas from the Li target and a fraction of the  ${}^{11}\text{B}(n,\alpha){}^7\text{Li}$  gammas from neutron capture in the shielding. With the implemented analysis cuts that were used when measuring the ionization yield, the background gamma rate was measured to be 12 Hz. The rate is expected to drop to 2.5 Hz with additional Pb shielding, as predicted by MCNPX.

within the detector.

## 7.5 Prediction of the Neutron Signal

Using the ionization yield predicted in Chapter 2, the energy deposition spectrum, Figure 7.10, was converted to an electron signal. The electron signal was then converted to photoelectrons on the assumption of 10 photoelectrons per single electron, which was in agreement with the measured single electron response of the detector, Section 5.9. Finally, a Poisson error was assumed on both the number of electrons generated as well as the number of photoelectrons generated per recoil event. The full progression of the signal can be seen in Figure 7.21.

Given the predicted signal within the detector after Poisson resolution, Figure 7.21(d), and the measured gamma backgrounds, Figure 7.20, the feasibility of the ionization yield measurement with the reduced neutron yields is obtained. Scaling

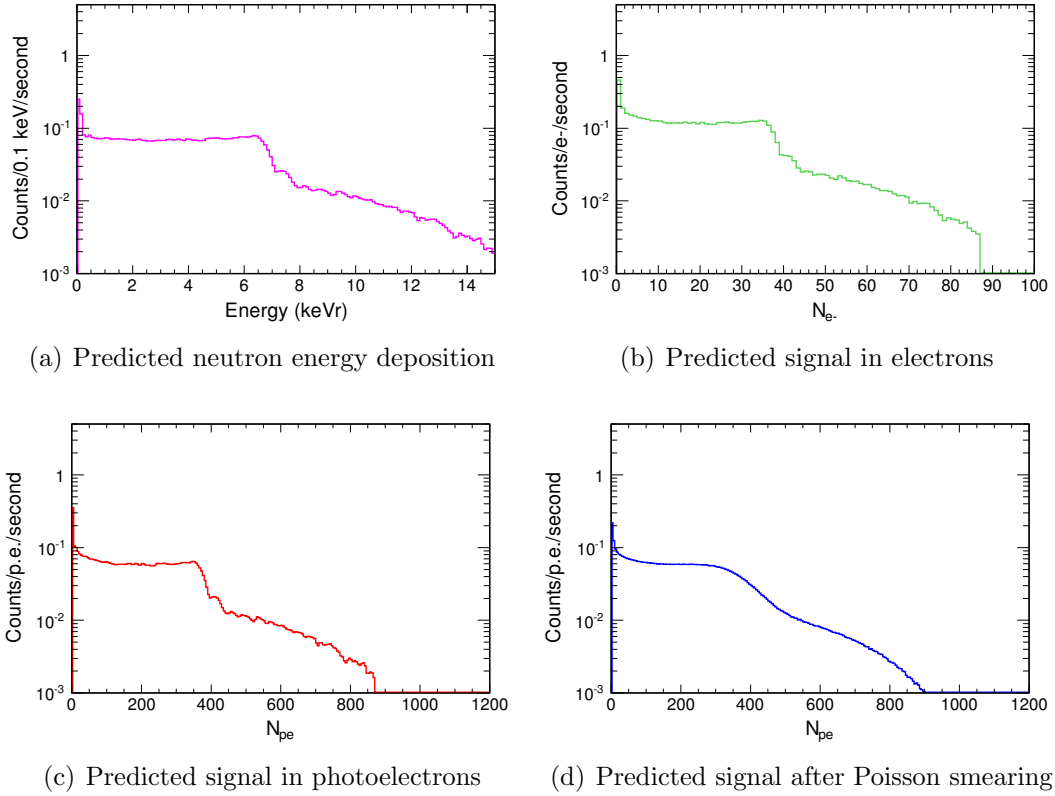


**Figure 7.21.** (a) Neutron energy deposition within the detector assuming an event rate of 6 Hz. The analysis cuts had the acceptance rates as follows: standard analysis cuts: 95%, fiducial cut: 50%, live time fraction: 31%; (b) neutron energy deposition was converted into electron signal, using the ionization yield predicted in Chapter 2; (c) predicted signal in photoelectrons, assuming 10 photoelectrons per single ionization electron, in accordance with the measurements in Section 5.9; (d) Poisson statistics are assumed for both the number of electrons generated per recoil and the total number of photoelectrons generated from the electrons.

down the measured gamma background by a factor of 0.2 for the reduction of 5x predicted by MCNPX for the new shielding, allows for a direct comparison between the neutron signal and expected gamma background, Figure 7.22.

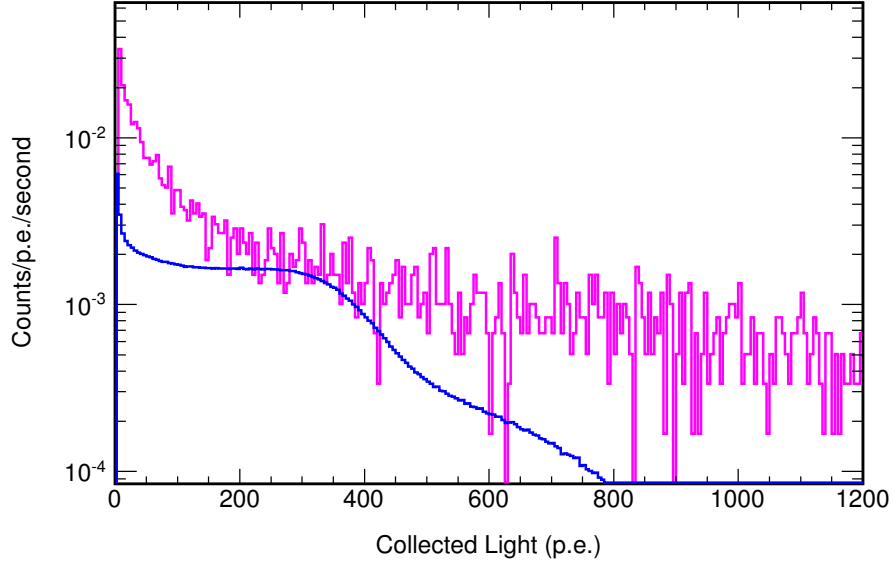


**Figure 7.22.** Predicted signal from neutron scatters (blue), and the measured gamma backgrounds, Figure 7.20, with a rate scaled by a factor of 0.2 (magenta) corresponding to a predicted 5x reduction in rate with increased shielding. This shows approximately equal signal to background rates, which suggest the feasibility of the neutron measurement with the neutron deficit if the gamma rates are reduced.

## 7.6 Extraction of the Ionization Yield

An analysis routine was developed to extract the measured ionization yields from the measured spectrum, in a similar manner as was performed by Sorensen *et al.* in [42]. The background subtracted signal was used as an input in the analysis routine, with a goal of fitting a predicted signal to the measured signal. When the measured signal was not available, a background subtracted signal was generated for 50,000 neutron events, which equates to a predicted run time of 16 hours for the Li target with the neutron deficit. This run time would decrease to 1.6 hours for a target with pure Li, exhibiting a maximum neutron yield. With the increased gamma shielding, the gamma event rate between 50 and 1000 photoelectrons is 1.6 Hz, while the predicted neutron signal rate for the same area is 0.7 Hz. The predicted signal in terms of photoelectrons, Figure 7.21(d) is populated with 50,000 events (0.88 Hz). The measured gamma background is fit with a double exponential, Figure 7.20, and populated with 136,500 gamma events to retain the total background rate of

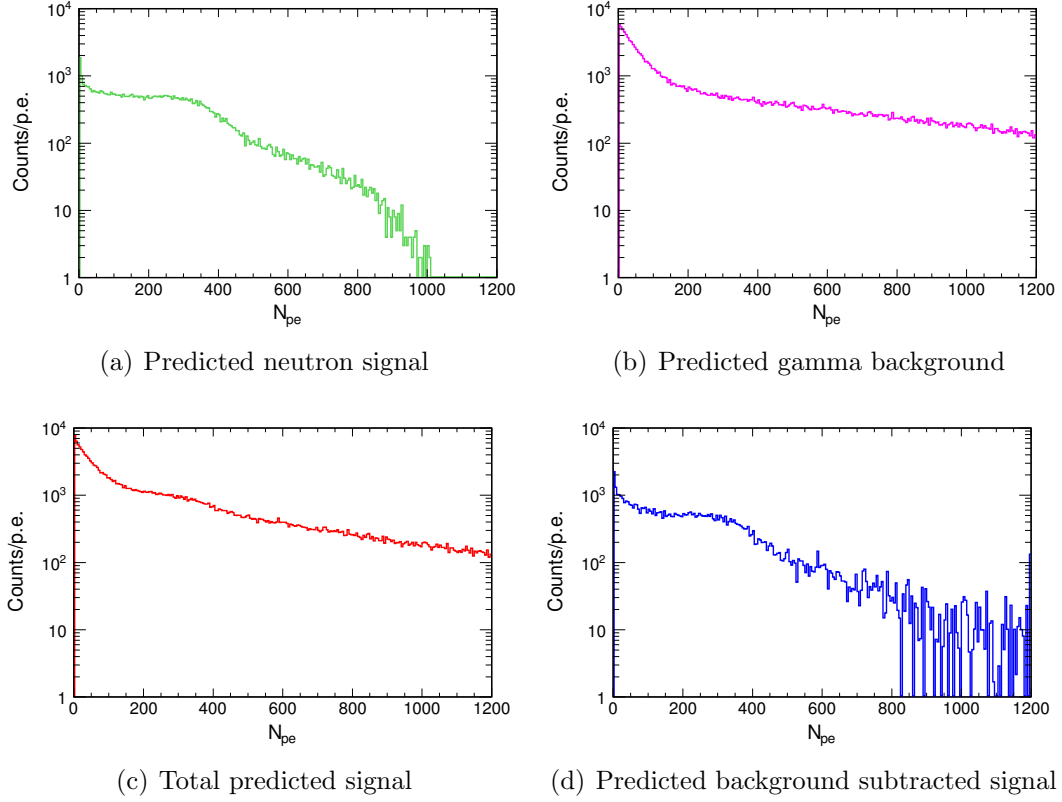


**Figure 7.23.** (a) 50,000 events producing the expected neutron signal, which equates to a run time of 16 hours with the  $AgLi_x$  target. (b) 136,500 events producing the expected gamma background, based on the exponential fit of the measured gamma spectrum. 136,500 background events were used to match the expected signal to background ratio. (c) Addition of plots (a) and (b) to generate the expected total signal. (d) Predicted background subtracted signal generated by subtracting the exponential fit of the measured gamma background, Figure 7.20, from the total signal (c).

2.4 Hz. The two signals are then combined to obtain a total spectrum and the scaled fitted curve is subsequently subtracted to obtain the background subtracted spectrum. The details of the signal calculation are shown in Figure 7.23.

The analysis routine fits the background subtracted signal, Figure 7.23(d), by starting with the neutron energy deposition, Figure 7.10, and using a floating spline of ionization yield points to generate the output signal. It was again assumed that each electron generates 10 photoelectrons. The analysis routine assumed a given ionization yield curve and generated the output signal. The output signal is then compared with the input background subtracted signal using either the maximum likelihood or least-squared ( $\chi^2$ ) methods. For the maximum likelihood binned

method, the predicted ionization yield values were calculated by maximizing

$$L(v_i(\theta)) = \prod f(n_i; v_i(\theta)), \quad (7.3)$$

where  $f(n_i; v_i(\theta))$  is the probability to obtain the expected value  $v_i$ , with the input estimator  $\theta$ , which is the predicted ionization yield. Since the analysis routines utilize binned data, the maximum likelihood ratio  $\lambda(\theta) = f(n_i; v(\theta))/f(n_i; n_i)$  is maximized [91, 170]. Equivalently,

$$-2\ln(\lambda(\theta)) = 2 \sum \left[ v_i(\theta) - n_i + n_i \ln \left( \frac{n_i}{v_i(\theta)} \right) \right] \quad (7.4)$$

is minimized [171]. The  $\chi^2$  method [170] was applied for the minimization of

$$\chi^2(Q_y) = \sum_{i=1}^j \frac{[n_i - v(Q_y)]^2}{\sigma_i^2}, \quad (7.5)$$

where  $n_i$  is the number of events with the photoelectrons in the  $i^{th}$  bin,  $\sigma_i$  accounts for the statistical fluctuation of the  $i^{th}$  bin, and  $j$  is the total number of bins. The ionization yield spline points were allowed to fluctuate with a new prediction of the expected signal at each step. The predicted spectrum was then compared to the simulated background subtraction signal through the maximum likelihood or  $\chi^2$  methods. The final ionization yield,  $Q_y$ , obtained from the analysis was chosen to minimize Equation (7.4) or (7.5). A maximum ionization yield was placed at  $1.5\times$  the yield which would generate the observed end point in the background subtracted signal. It was additionally assumed that  $Q_y \rightarrow 0$  as  $E_r \rightarrow 0$ . Since the analysis fits the entire spectrum, it is possible to accurately predict the ionization yield at  $\sim 7$  keVr, even with a smearing of the shoulder due to detector resolution.

In development of the methodology for extracting the ionization yield from the data, the input ionization yield assumed was that predicted in Chapter 2. A light yield of 10 photoelectrons per single electron was assumed, both for generating the background subtracted signal and in the fit routines. For 50,000 events, the analysis routine was performed 25 times, extracting the input ionization yield with a slight underestimate, specifically at low recoil energies, Figure 7.24. The small error bars on the ionization yield spline demonstrates the reproducibility of the

analysis routine. The analysis output signal matches the background subtracted signal prediction which was input into the analysis, Figure 7.25. It is important to compare the input and output spectra to verify that the analysis routine did not find a local minima of the predicted ionization yields. Based on these results, it should be possible to measure the ionization yield with the deficit of neutrons, since the analysis routines extract the input ionization yield with sufficient robustness.

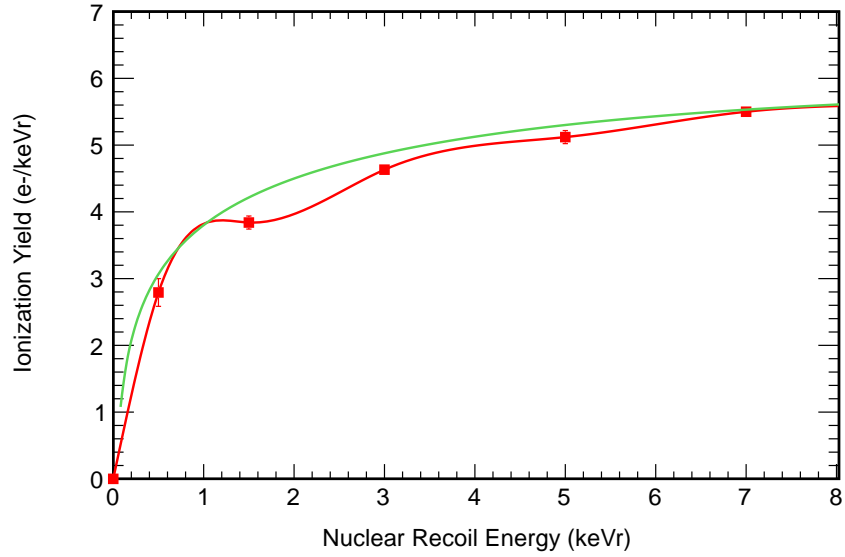


**Figure 7.24.** The ionization yield prediction from Chapter 2 (green) was used as an input ionization yield to generate the background subtracted signal, Figure 7.23(d). The analysis routine predicted the ionization yield at the energies of 0.5, 1.5, 3, 5, and 7 keVr (red squares). The red curve is the spline fit of the predicted ionization yield values, and the error bars which are primarily contained within the markers.

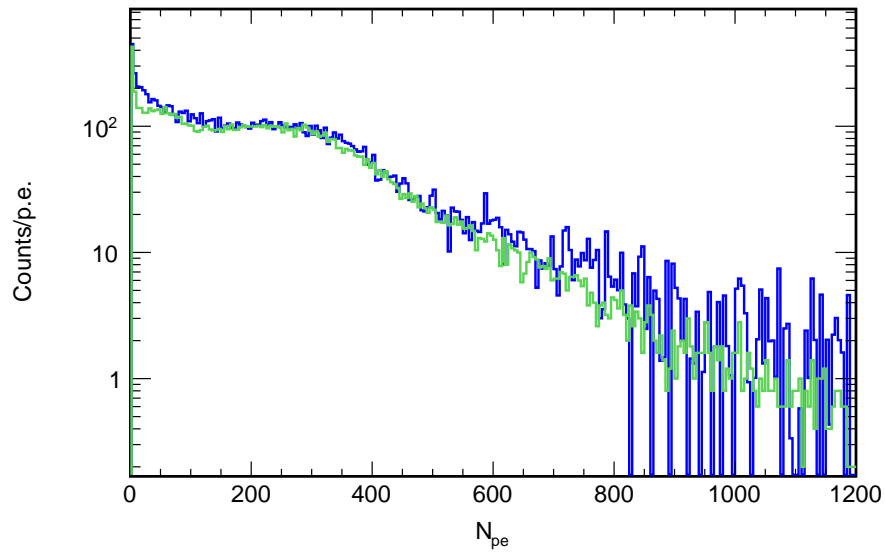


**Figure 7.25.** The background subtracted signal prediction (blue) was input into the analysis routine. The analysis routine generated the predicted signal (green) for the ionization yield spline fit, Figure 7.24.

# Prospects for Detection of CNNS and Conclusions

In this concluding Chapter, an updated prediction of the magnitude of the CNNS signal for an Ar detector is presented in Section 8.1, using the ionization yield model described in Chapter 2. The expected background in an Ar CNNS detector is also discussed in Section 8.1. A discussion is provided for the potential extended applications of a CNNS detector in other areas of neutrino physics in Section 8.3. Lastly, the conclusions of this Dissertation are presented in Section 8.4, with the future work described in Section 8.5.

## 8.1 Detection of Coherent Neutrino-Nucleus Scatter (CNNS)

### 8.1.1 CNNS Signal from Nuclear Reactors

With the detailed first principles model of the low-energy ionization yield, Chapter 2, a more accurate estimate of the CNNS signal in LAr is provided. Through the course of these predictions, a nuclear reactor neutrino spectrum is assumed for the isotopic content of 61.9%  $^{235}\text{U}$ , 27.2%  $^{239}\text{Pu}$ , 6.7%  $^{238}\text{U}$ , and 4.2%  $^{241}\text{Pu}$ , shown in Figure 8.1. A total flux of  $6 \times 10^{12} \text{ } \bar{\nu}\text{cm}^{-2}\text{s}^{-1}$ , with the detector placed 25 m from a 3 GWth core is assumed [34, 25, 29]. The Ar recoil spectrum produced by



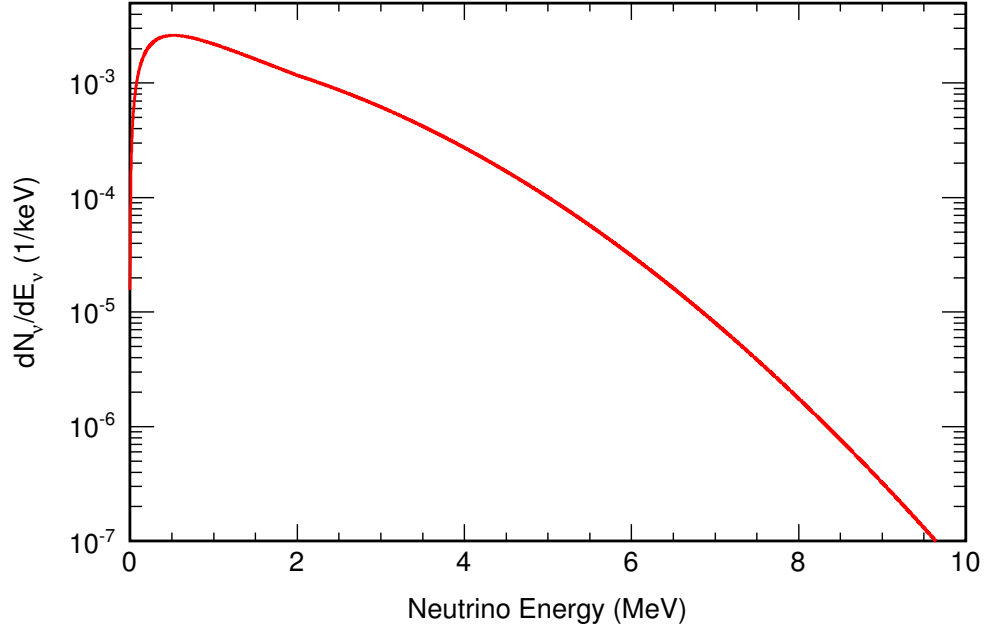


**Figure 8.1.** Reactor antineutrino spectrum for an average isotopic content of 61.9%  $^{235}\text{U}$ , 27.2%  $^{239}\text{Pu}$ , 6.7%  $^{238}\text{U}$ , and 4.2%  $^{241}\text{Pu}$  [34, 25, 29]. There is debate over the shape of the spectrum at energies below 2 MeV, but the low-energy neutrinos will not provide sufficient energy for detection by CNNS.

CNNS, Figure 8.2, is calculated using Equation (1.15), with natural Ar isotopic abundances.

With the known recoil energies, the ionization yields in LAr, Figure 2.16, were used to predict the detectable signal resulting from CNNS in Ar. The scintillation yield is neglected in this analysis, as CNNS is only expected to produce a few photons of S1 scintillation light, which is not detectable and distinguishable from background photoelectrons. To predict the electron yield from CNNS in Ar, the ionization yield calculation described in Chapter 2 was performed at sampled energies in the recoil spectrum, Figure 8.2, for 10,000 events. The electron yield from each event was then histogrammed to obtain the predicted CNNS electron yield spectrum. This process was performed both with and without the effect of electron recombination being accounted for, with the results shown in Figure 8.3. For low electron yields, the electron recombination has a small effect, not affecting the prospect of detecting CNNS using this method significantly. As shown in

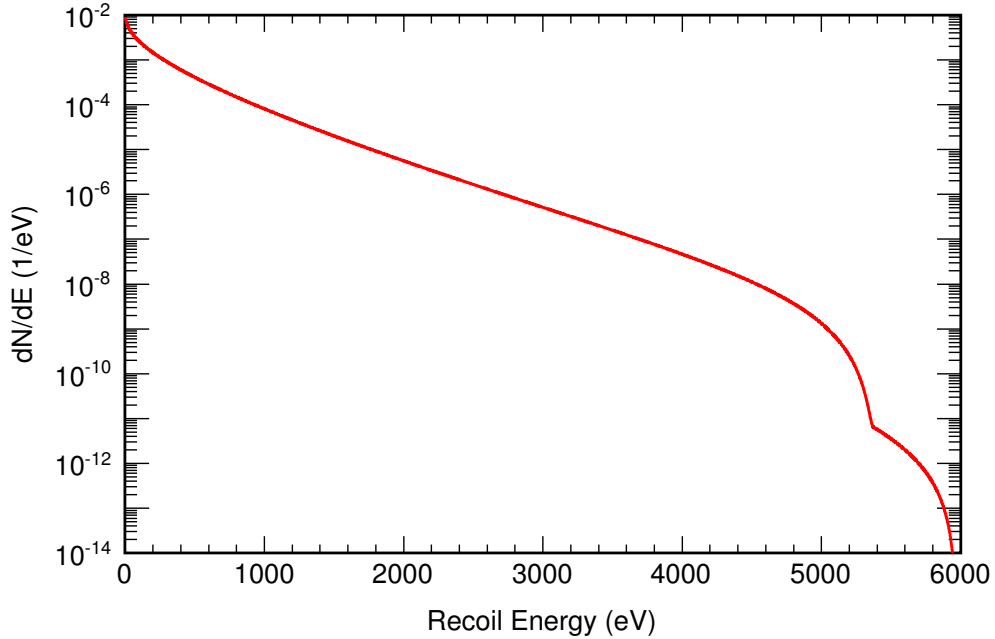


**Figure 8.2.** Expected Ar recoil spectrum from CNNS, with an input reactor neutrino spectrum given in Figure 8.1. The bulk of the spectrum is due to  $^{40}\text{Ar}$  recoils, while the shoulder at 5 keVr is due to the contribution of  $^{36}\text{Ar}$ .

Figure 2.16, it was assumed that the electron emission energy was 10 eV during the Ar collision cascade, and the electron drift electric field was 1 kV/cm.

One method of boosting the electron signal and extracting a signal from the excitation events, which would normally not induce ionization, is to use the Penning mechanism [87], Section 1.5.3. With the addition of 1% Xe, 60% of excited Ar atoms produce an electron by ionizing Xe instead of producing scintillation light. This in effect boosts the detectable signal from CNNS without any detector modifications. For a 10 kg Ar detector, the amount of Xe to be added can be calculated using Rouolt's Law, Equation (1.20) [81], to be 330 g, which remains almost completely in the liquid phase. In the ionization model, the probability of an excited Ar atom producing an electron through the Penning effect is randomly sampled on an event by event basis, with a 60% probability of the ionization to occur. The resulting electron yields after electron recombination with and without 1% Xe are shown in Figure 8.4.

A conservative threshold for detection can be set to two or more electrons, but

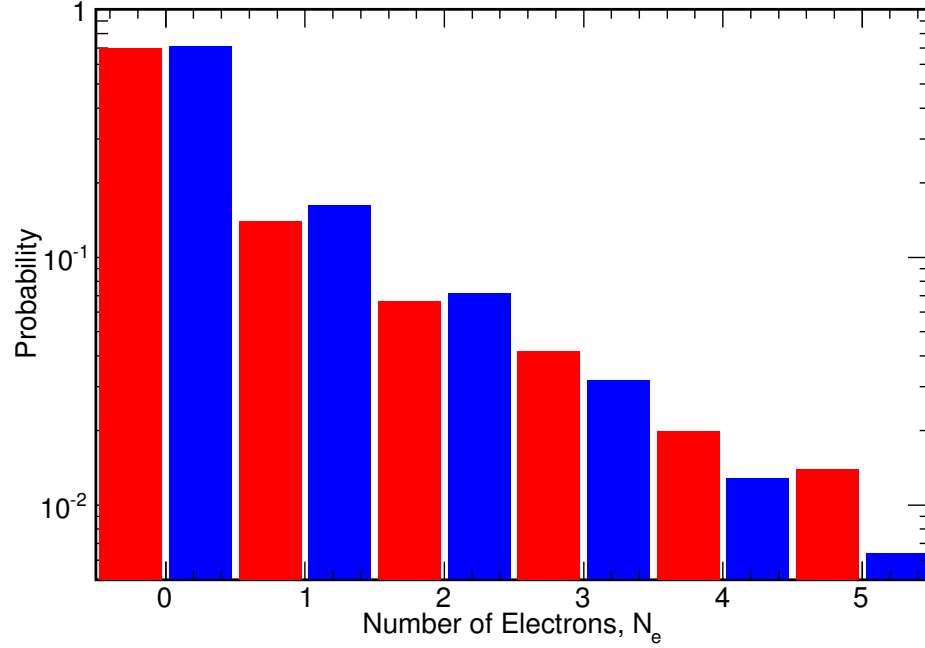


**Figure 8.3.** Predicted electron yields in a pure Ar detector from CNNS recoils, without (red) and with (blue) electron recombination, based on the ionization yield predictions of Chapter 2. 70% of recoils produce 0 electrons, while 14% produce 1 electron and 16% produce 2 or more electrons. A conservative threshold for detection could be set to 2 electrons, resulting in 16% of all CNNS interactions being detectable.

there is also the potential for detecting the single electron CNNS events in LAr. In Ar, the potential well for electrons crossing the liquid-gas barrier is smaller than in Xe, which suggests that the single electron backgrounds could be much lower [51] compared to Xe detectors. This results in a potential for setting the threshold to a single ionization electron. However, in the studies presented here, a conservative threshold of 2 or more electrons was used.

### 8.1.2 CNNS Backgrounds

The backgrounds in a dual-phase Ar CNNS detector can be categorized as emanating from reducible and irreducible sources. The first reducible source of concern is the  $\beta$ -decay of  $^{39}\text{Ar}$ , which is present in the detector medium. The other reducible sources of interest are the gamma ray Compton scatters and fast neutron scatters

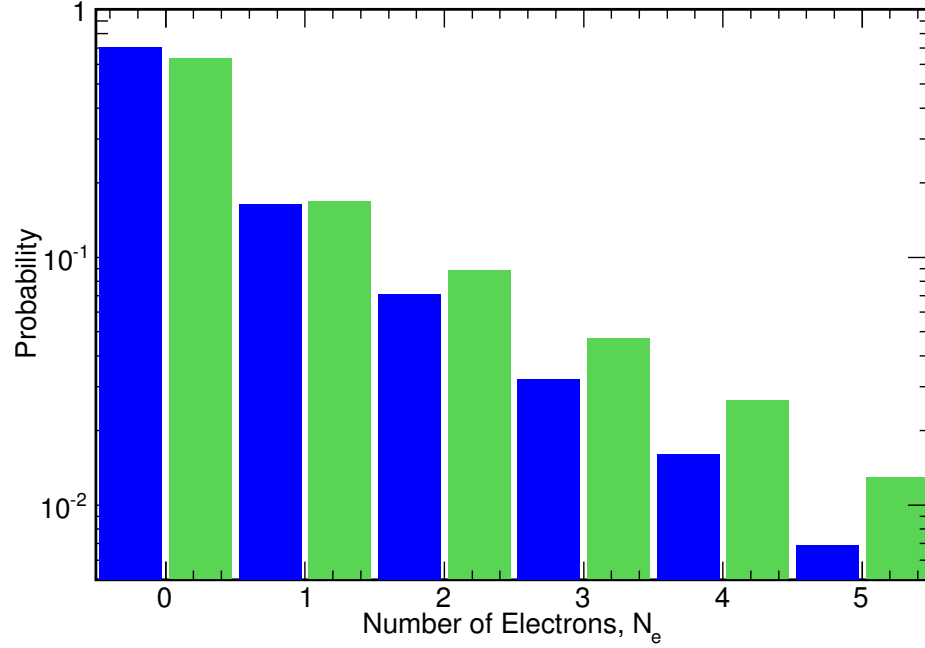


**Figure 8.4.** Predicted electron yields after electron recombination for pure Ar (blue) and with 1% Xe doping (green). For pure Ar, 30% of all recoils produce ionization, with 16% producing 2 or more electrons. With 1% Xe, 37% of all recoils produce ionization, with 20% producing 2 or more electrons.

within the detector. The irreducible source which sets the ultimate limit on the CNNS detection in terms of the minimum distance from an intense neutrino source such as a reactor is the solar neutrino background, Section 8.1.2.2.

#### 8.1.2.1 Close Proximity Reactor Monitoring

$^{39}\text{Ar}$  decays via  $\beta$ -decay with an end-point energy of 565 keV and a half-life of 269 years. It has been measured that the activity of  $^{39}\text{Ar}$  is  $\sim 1$  Bq/kg in  $^{nat}\text{Ar}$  [172, 173, 174]. The Coulomb corrected electron spectrum is approximately constant at low energies, with an activity of  $\sim 5$  mBq $\cdot(e^-)^{-1}\text{kg}^{-1}$  [175]. For the  $W$ -value of 23.6 eV per electron-ion pair, the activity is calculated to be  $\sim 119$   $\mu\text{Bq}\cdot(e^-)^{-1}\text{kg}^{-1}$  or  $\sim 10.3$  events $\cdot(e^-)^{-1}\text{kg}^{-1}\text{day}^{-1}$  for energies below 1 keV. Efforts have been made to collect Ar from exhaust streams of underground mining facilities, which is depleted in  $^{39}\text{Ar}$  by more than  $25\times$  that of  $^{nat}\text{Ar}$  [176]. With an assumed depletion factor

of 25, the background  $^{39}\text{Ar}$  rate drops to just  $0.4 \text{ events} \cdot (e^-)^{-1} \text{ kg}^{-1} \text{ day}^{-1}$ ,  $\sim 10\times$  lower than the predicted CNNS rates.

Gamma backgrounds for CNNS occur due to small angle Compton recoils from both internal and external sources of gamma radioactivity. Neutron backgrounds are nuclear recoils produced by neutron scattering or capture within the detector. Gamma and neutron backgrounds have been previously simulated for the case of a 2 cm Pb internal shield with a 10 cm borated polyethylene outer shield [34]. Cosmic muons may produce neutrons which are factored into the neutron backgrounds, but the direct muon background can be rejected due to the high energy depositions  $\gg 1 \text{ keV}$ . A comparison of the expected CNNS rates and background rates is shown in Figure 8.5, with the gamma and neutron backgrounds taken from [34]. For long-range monitoring with CNNS, the detector sizes need to increase, which decreases the relative gamma and neutron backgrounds. The CNNS signal, however, decreases with distance-squared, which leaves  $^{39}\text{Ar}$  as the primary background, which must be reduced for detection at longer standoff. Measurements have been made, suggesting that the reduction in  $^{39}\text{Ar}$  backgrounds for depleted Ar could be  $> 100\times$  that of natural Ar [177]. Even with a  $100\times$  reduction in  $^{39}\text{Ar}$  activity, the signal to background ratio could still be too low for detection, and must be investigated further.

#### 8.1.2.2 Long Range Detection Limit

Even with the reduction of the  $^{39}\text{Ar}$ , gamma and neutron backgrounds, a solar neutrino background is present and increases in relative importance as the reactor neutrino flux decreases in the long range detection scenario. For long range detection of CNNS from a nuclear reactor, the solar neutrino flux becomes the dominant background. Solar neutrinos are neutrinos emitted during the fusion processes within the sun. Inverse  $\beta$ -decay detectors are only sensitive to electron neutrinos, and thus insensitive to solar neutrinos. Since the CNNS interaction is flavor independent, a LAr CNNS detector is sensitive to both the antineutrinos from the nuclear reactor and the solar neutrinos. Table 8.1 includes the information on the solar neutrino flux which is used to calculate the maximum stand-off for successful CNNS measurement. For neutrinos with an energy below 1 MeV, the CNNS interaction does not produce an observable signal, and are thus ex-

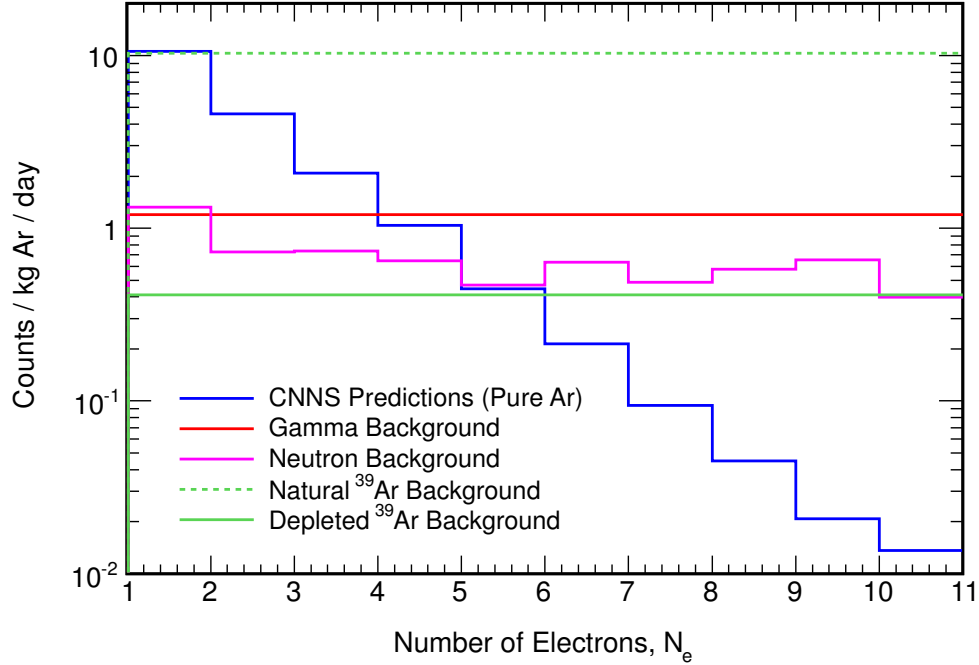


**Figure 8.5.** Predicted CNNS signals for pure LAr (blue), with the backgrounds overlaid. The gamma (red) and neutron (magenta) backgrounds were calculated previously [34], with 2 cm of Pb and 10 cm of borated polyethylene shields. The  $^{39}\text{Ar}$  background for natural Ar (dashed-green) is reduced by  $25\times$  with depleted argon (solid-green). The event rate assumes a neutrino flux of  $6 \times 10^{12} \bar{\nu}\text{cm}^{-2}\text{s}^{-1}$  25 m from a 3 GWth core.

cluded when calculating the background flux. The solar neutrino flux with a maximum emission energy above 1 MeV is calculated to be  $\sim 1.18 \times 10^9 \nu\text{cm}^{-2} \text{s}^{-1}$  [19, 20, 21, 22], which is approximately equal to the antineutrino flux from a nuclear reactor at  $\sim 1.8$  km. Beyond 1.8 km, the solar neutrino background becomes larger than nuclear reactor signal, and a CNNS detector becomes ineffective for detecting clandestine nuclear reactors. For any long range searches for clandestine nuclear reactors, an inverse  $\beta$ -decay detector should be used instead of a CNNS detector.

Atmospheric neutrinos are created during the decay of pions and muons as they travel towards the earth and present a background in many detection scenarios. They do not contribute to the CNNS background, however, since they deposit energies greatly in excess of those typical for the CNNS interactions and

**Table 8.1.** The total flux of solar neutrinos is  $\sim 6 \times 10^{10} \nu \text{cm}^{-2} \text{s}^{-1}$  [19, 20, 21, 22], but the very low energy neutrinos ( $< 1 \text{ MeV}$ ) do not have sufficiently high energy to produce an observable signal.

Source	$\langle E \rangle$ (MeV)	$E_\nu^{max}$ (MeV)	Flux $\Phi$ ( $\text{cm}^{-2} \text{s}^{-1}$ )
<i>pp</i>	0.2668	$0.423 \pm 0.03$	$5.95 \times 10^{10} (1 \pm 0.01)$
<i>pep</i>	1.445	1.445	$1.40 \times 10^8 (1 \pm 0.015)$
<i>hep</i>	9.628	18.778	$9.3 \times 10^3$
$^7\text{Be}$	0.3855 / 0.8631	0.3855 / 0.8631	$4.77 \times 10^9 (1 \pm 0.10)$
$^8\text{B}$	$6.735 \pm 0.036$	$\sim 15$	$5.05 \times 10^6 (1_{-0.16}^{+0.20})$
$^{13}\text{N}$	0.7063	$1.1982 \pm 0.0003$	$5.48 \times 10^8 (1_{-0.17}^{+0.21})$
$^{15}\text{O}$	0.9964	$1.7317 \pm 0.0005$	$4.80 \times 10^8 (1_{-0.19}^{+0.25})$
$^{17}\text{F}$	0.9977	$1.7364 \pm 0.0003$	$5.63 \times 10^6 (1 \pm 0.25)$

can thus be readily rejected, including methods such as muon veto using external detectors.

Geo-neutrinos are generated within the earth, from  $^{238}\text{U}$ ,  $^{232}\text{Th}$ ,  $^{40}\text{K}$ ,  $^{235}\text{U}$ , and  $^{87}\text{Rb}$ , with the main contributions obtained from  $^{238}\text{U}$ ,  $^{232}\text{Th}$ , and  $^{40}\text{K}$ . The decay chains of  $^{238}\text{U}$  and  $^{232}\text{Th}$  generate a total heating power of  $H \approx 20 \text{ TW}$  within the earth [24, 178]. Each decay chain releases approximately 1  $\nu$  per 10 MeV of energy release. The total number of neutrinos emitted,  $L_\nu$ , is calculated as:

$$L_\nu(U + Th) \approx H/\Delta E \approx 1.25 \times 10^{25} \text{ s}^{-1}, \quad (8.1)$$

where  $H$  is the heat released from the earth, and  $\Delta E$  is the energy released per neutrino ( $Q/N$ ). The geo-neutrino flux is then calculated by dividing the neutrino generation rate by the surface area of the earth to obtain

$$\Phi(U + Th) \approx \frac{L_\nu}{4\pi R_\oplus^2} \approx 1.67 \times 10^6 \nu \text{cm}^{-2} \text{s}^{-1}, \quad (8.2)$$

where  $R_\oplus$  is the radius of the earth. It is expected that  $\approx 40\%$  of the neutrinos emitted oscillate to a different flavor prior to reaching the earth's surface [24], but since CNNS is flavor independent, a CNNS detector is sensitive to all of the originally emitted neutrinos. The decay of  $^{40}\text{K}$  within the earth produces a heating power of  $\sim 4 \text{ TW}$ , with 1  $\nu$  released per  $\sim 0.69 \text{ MeV}$  of energy [178, 24]. Using the

same calculation method used for  $^{238}\text{U}$  and  $^{232}\text{Th}$ , a neutron flux from  $^{40}\text{K}$  is calculated to be  $\approx 4.83 \times 10^6 \text{ } \nu\text{cm}^{-2} \text{ s}^{-1}$ . The  $^{40}\text{K}$  neutrinos have a maximum energy of 1.461 MeV. The total geo-neutrino flux at the earth's surface is  $\sim 6.5 \times 10^6 \text{ } \nu\text{cm}^{-2} \text{ s}^{-1}$ , which is approximately  $200\times$  smaller than the observable solar neutrino flux. Due to their low flux, geo-neutrinos do not need to be considered as background in CNNS studies.

## 8.2 Reactor Monitoring

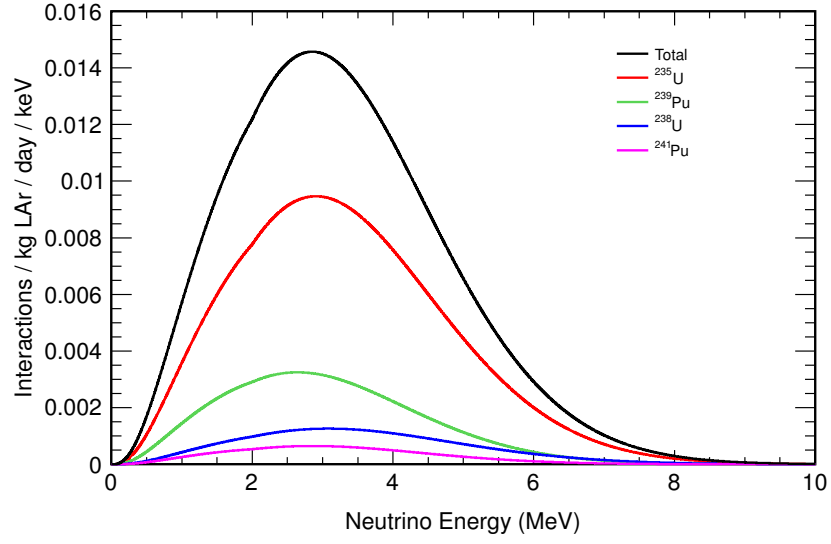
### 8.2.1 Inverse Beta Decay vs CNNS for Neutrino Detection

The capability of inverse  $\beta$ -decay detectors to monitor nuclear power reactors [10, 11], Section 1.3 is now well known. The use of CNNS for detection could considerably decrease the detector size and/or increase the detection rates. Figure 8.6 shows the comparison of interaction rates per kg of detector material for a LAr CNNS detector and a liquid scintillator  $((\text{CH}_2)_n)$  inverse  $\beta$ -decay detector. For LAr doped with 1% Xe, 20% of CNNS interactions on LAr are predicted to be detected at the 2 ionization electron level. For this instance, a LAr CNNS detector produces  $\sim 2\times$  the detectable events per kg of detector material as that of a liquid scintillator inverse  $\beta$ -decay detector. If a 1-electron event threshold can be set in the CNNS detector, the ratio of event rate per kg for CNNS on LAr versus inverse beta decay on  $(\text{CH}_2)_n$  increases to  $\sim 4$ .

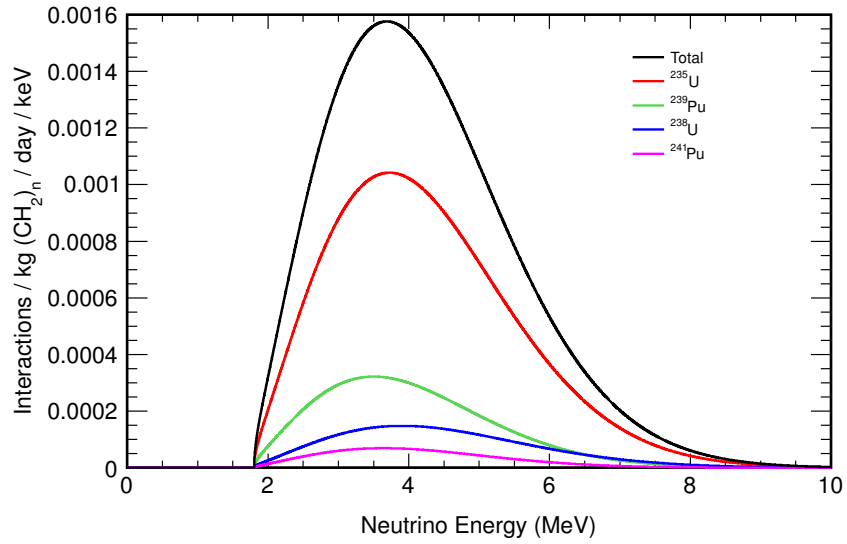
With the isotopic content variation given by Figure 1.3, and assuming that the number of detectable events does not change with the isotopic content, the number of events detected per kg of detector material are shown for inverse beta decay and CNNS, with the conservative assumption of 2 electron detection threshold, Figure 8.7. With this threshold lowered to 1 electron, the detected event rate is predicted to double. For close proximity reactor monitoring, CNNS on LAr benefits from the increased cross section to reduce the detector mass by a factor of  $2\text{-}4\times$ .

With an increased reaction rate, a CNNS detector can also benefit from a decreased fast neutron background. While in inverse  $\beta$ -decay detectors the fast neutrons directly mimic the neutrino signal, in a CNNS detector, due to the mass

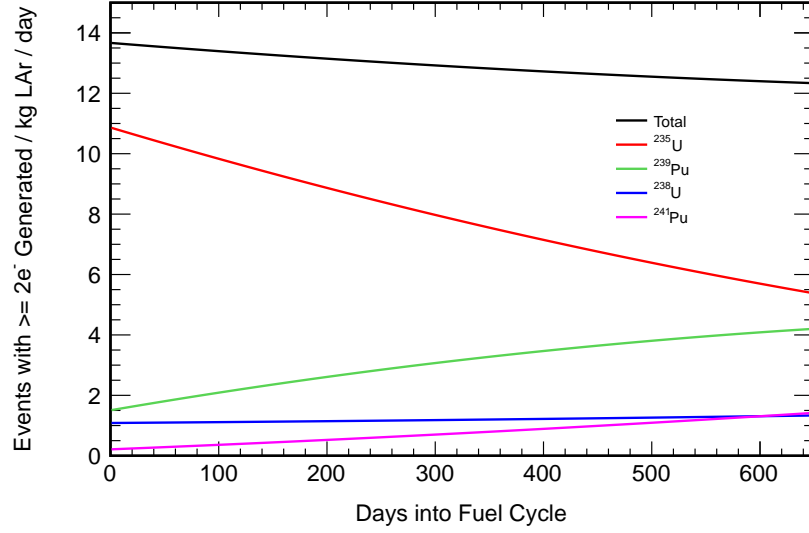




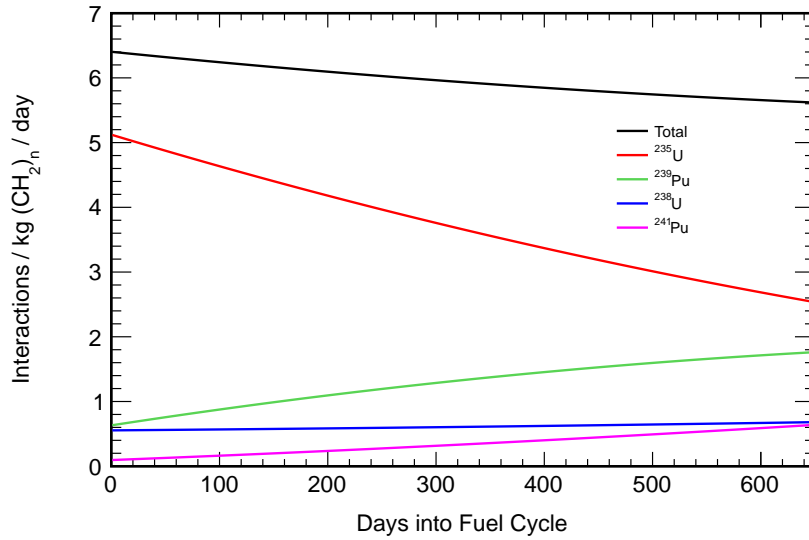
(a) CNNS

(b) Inverse  $\beta$ -decay

**Figure 8.6.** (a) Predicted interaction spectrum for CNNS on LAr. (b) Predicted interaction spectrum for inverse  $\beta$ -decay on  $(\text{CH}_2)_n$ . Note CNNS interaction occurs for the low-energy neutrinos, while inverse  $\beta$ -decay has a 1.804 MeV threshold.



(a) CNNS

(b) Inverse  $\beta$ -decay

**Figure 8.7.** (a) Predicted interaction rate per kg of Ar per day for CNNS on LAr with 1% Xe as a function of days into the fuel cycle. An event detection threshold of 2 or more electrons was assumed. (b) Predicted interaction rate per kg of  $(\text{CH}_2)_n$  per day for inverse  $\beta$ -decay on  $(\text{CH}_2)_n$  as a function of days into the fuel cycle. CNNS produces  $\sim 2\times$  the event rate per kg of detector material compared to inverse  $\beta$ -decay, with an increase to  $\sim 4\times$  for a CNNS detection threshold of 1 electron.

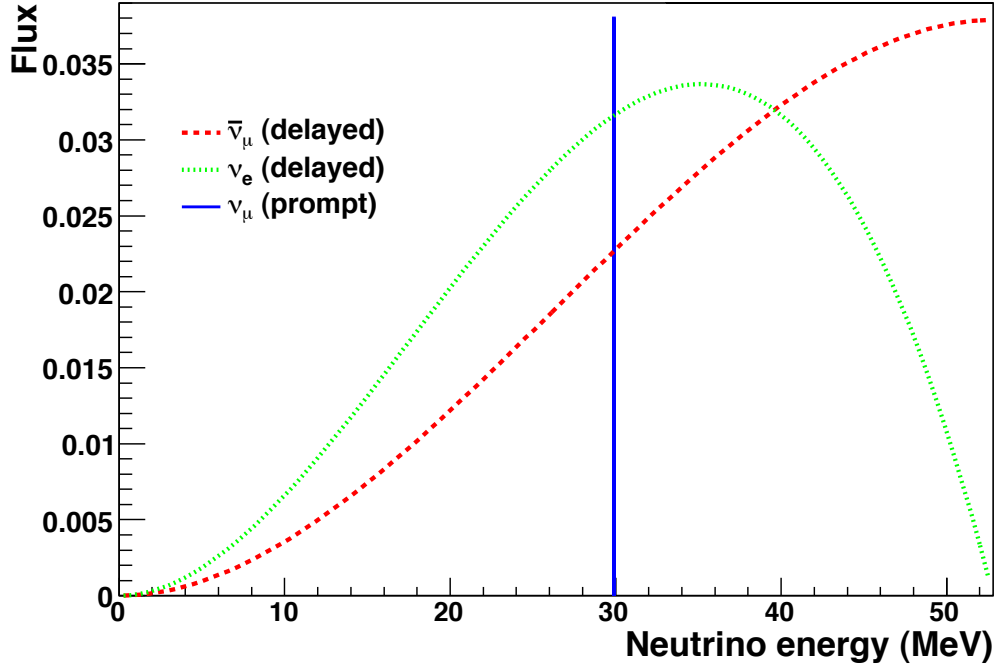


**Figure 8.8.**  $\nu_e$ ,  $\nu_\mu$ , and  $\bar{\nu}_\mu$  are produced through the decay of stopped-pions.  $\nu_\mu$  or produced through the initial decay of the stopped  $\pi^+$ , with  $\nu_e$  and  $\nu_\mu$  produced through the decay of the  $\mu$  produced in the  $\pi^+$  decay. Figure taken from [180].

difference between the neutrino and neutron, only very low angle scatters produce signals comparable to the neutrino signal.

### 8.2.2 Detection of CNNS using Neutrino Beams

Another possibility for detection of CNNS is using a neutrino beam instead of a nuclear reactor. Stopped-pion source neutrino beams such as the Spallation Neutron Source (SNS) produce neutrinos with energies up to  $\sim 50$  MeV, Figure 8.8, through the decay of stopped-pions, Section 1.1.2. Due to space constraints, any detector used would be  $\sim 20$  m away from the neutrino source, for a total neutrino flux of  $3.65 \times 10^7 \text{ cm}^{-2}\text{s}^{-1}$ , composed equally of each of the three generated neutrinos [179]. The full details of the SNS production of neutrinos are given in Table 8.2.

With neutrino energies up to 50 MeV, the average recoil energy is 15 keVr for an assumed neutrino energy of 30 keV. With the ionization yield predictions of

**Table 8.2.** Primary parameters for SNS and the production of neutrinos through stopped-pion decay [179].

Parameter	Value
proton beam power on target	1.4 MW
proton beam kinetic energy	1.0 GeV
average beam current on target	1.4 mA
protons on target per pulse	$1.4 \times 10^{14}$
pulse repetition rate	60 Hz
$\pi^+$ per proton	0.068
$\pi^+$ per second	$6.14 \times 10^{14}$
$\Phi(\nu_e) = \Phi(\nu_\mu) = \Phi(\bar{\nu}_\mu)$	$6.14 \times 10^{14}$

Chapter 2, the predicted average recoil energy is  $\sim 2.25$  keVee, which has been displayed with both gaseous Ar (Chapter 3) and dual-phase Ar detectors (Chapter 6). The challenge in detecting CNNS with a stopped-pion source is the low flux of neutrinos produced. For a detector placed 20 m from SNS, the expected interaction rate within Ar is only  $\sim 1.06$  events  $\text{kg}^{-1} \text{day}^{-1}$ . Due to the higher neutrino energy, it is possible to use a Xe detector, which increases the event rate to  $\sim 1.81$  events  $\text{kg}^{-1} \text{day}^{-1}$ . There is potential to increase these rates if the detector can be moved closer to the neutrino source, but there are often space constraints limiting this opportunity.

Given the low interaction rates, the natural and beam induced backgrounds must be very well shielded and reduced. The primary beam related background is the neutrons produced within the beam-line due to a loss of  $\sim 1$  W/m, which are detected through *sky shine* at the detector. The predicted neutron flux at a stand-off distance of 20 m is  $\sim 8.64$  neutrons  $\text{MeV}^{-1} \text{cm}^{-2} \text{day}^{-1}$  [180, 181]. Natural backgrounds are similar to those assumed for the nuclear reactor experiment, Section 8.1.2, with a beam pulsing reduction factor of  $\sim 4 \times 10^4$ .

### 8.3 CNNS Detection for Neutrino Physics

The lack of neutrino flavor dependence of the CNNS interaction allows for a CNNS detector to expand the current field of neutrino physics. With no dependence on the flavor of the incident neutrino, a CNNS can probe the total neutrino flux

rates without a dependence on the neutrino mixing angles. One such application of this is the utilization of CNNS detectors in neutrino oscillation experiments. In measuring  $\theta_{13}$ , experiments such as Daya Bay [13], Double CHOOZ [12], and RENO [14] detect the disappearance of  $\bar{\nu}_e$  from nuclear reactors. A near detector ( $\sim 500$  m) measures the initial neutrino flux, and far detectors ( $\sim 1500$  m) measure the variation from the expected interaction rate. An important challenge in these experiments is ensuring that the detector efficiencies of the near and far detectors are very well understood as to not introduce a phantom neutrino mixing angle. The implementation of a CNNS detector could allow for a more accurate estimate of the total neutrino flux at the near and far detectors; it could directly measure the fraction of neutrinos that have oscillated out of the  $\bar{\nu}_e$  flavor.

In addition to the neutrino oscillation experiments, CNNS could be applied to the detection of Non-Standard Interactions (NSI) of neutrinos [182]. CNNS could also be used to measure the neutrino magnetic moment ( $\mu_\nu$ ), which the Standard Model predicts to have a value of  $\mu_\nu \leq 10^{-19} \mu_B (m_\nu/1\text{eV})$ , where  $m_\nu$  is the neutrino mass and  $\mu_B$  is the Bohr magneton ( $\mu_B = (e\hbar)/(2m_e)$ ), but is experimentally predicted to have larger values. A non-zero neutrino magnetic moment would be observable in a variation of deviation from the predicted recoil spectrum [25].

## 8.4 Conclusions

Coherent neutrino-nucleus scatter (CNNS) remains an undetected interaction mode of neutrinos with matter. Its detection would thus represent an important contribution to the fundamental science. Due to the flavor independence of CNNS, direct detection of the supernova neutrino flux could be achieved without taking into account the flavor oscillation. Additionally, the increased interaction rate, resulting from the increased cross section of interaction relative to that of inverse beta decay, could make it possible to monitor nuclear reactors with smaller detectors. This dissertation has focused on predicting the magnitude of expected CNNS signals in a dual-phase Ar detector, thus contributing to the understanding of the feasibility of CNNS detection using this detector technology.

With the ionization yield simulation, a framework for predicting the signals from low energy interactions producing both nuclear and electron recoils has been

developed. The ionization yield for nuclear recoils in LAr was predicted to be  $\sim 4e^-/\text{keVr}$  below 10 keVr. The nuclear ionization quench factor was measured to be  $0.138 \pm 0.012$  in gaseous Ar, which is in good agreement with the predicted value from the simulation. Additionally, the electron transport model was validated using electron recoils in liquid argon, with both the number of electrons generated and the electric field dependence being in good agreement with simulation. While the framework currently applies to liquid argon, it has a potential to be extended to other noble element detectors by use of appropriate cross sections. The signal for CNNS in LAr was predicted to produce  $\sim 60$  recoils per kg Ar per day, with 70% producing 0 electrons, 14% producing 1 electron, and 16% of recoils producing 2 or more electrons.

A small dual-phase Ar detector, the G/NARRLI detector, has been designed and commissioned with a goal to demonstrate the required sensitivity. For the first time in an argon ionization counter, the G/NARRLI detector has demonstrated sub-keV spectroscopy through the detection of the 270 eV  $^{37}\text{Ar}$  L-shell electron capture peak. Additionally, with the detection of single ionization electrons, the G/NARRLI detector has shown the sensitivity required to observe the CNNS interaction in LAr. Thus the G/NARRLI detector has displayed the capabilities required for detecting CNNS, albeit on a scale smaller than that required to obtain reasonable event rates.

The scalability of a dual-phase Ar detector in conjunction with low atomic mass results in the potential to obtain much higher event rates than those possible with relatively compact Si, Ge, or Xe detectors. During the operation of a dual-phase Ar detector such as the G/NARRLI detector, special attention must be paid to prevent breakdown of the high voltage being applied to the field cage. If the voltage applied to the detector produces fields sufficiently below the breakdown threshold, it is possible for the detector to operate continuously and reliably. For CNNS detection, the dual-phase Ar detector must be capable of operating in a stable manner over the course of months rather than just days, as demonstrated in the G/NARRLI detector. Due to the small signals from CNNS, an inverse  $\beta$ -decay detector is likely to be better suited for nuclear safeguards applications than a CNNS detector. Future CNNS detectors are unlikely to be capable of accurately reconstructing the direction or energy of nuclear reactor neutrinos due to the small

ionization signals ( $< \sim 5e^-$ ). In order to first detect the CNNS interaction, the two primary backgrounds that are capable of mimicking the signals produced by the CNNS interaction must be suppressed: the natural  $^{39}\text{Ar}$  background and the single electron background. A  $25\times$  reduction of the  $^{39}\text{Ar}$  activity has previously been demonstrated, with the potential for a reduction of  $100\times$  or more. For a reduction of  $25\times$ , the CNNS signal to  $^{39}\text{Ar}$  background ratio should be sufficient for the first ever detection of CNNS. With a lower electron extraction work function in argon than that of xenon, a dual-phase Ar detector has the potential to greatly reduce the single electron background compared to a dual-phase Xe detector.

Prior to building a full-scale detector for detecting CNNS, it is crucial to measure the ionization yield in LAr at energies below 10 keVr to show the sensitivity to low-energy nuclear recoils. The experimental and analytical structure has been put in place to measure the ionization yield at 7 keVr once a new Li target is obtained. The new Li target for neutron production is predicted to provide the required signal-to-noise ratio for this measurement.

## 8.5 Future Work

New Li targets are currently being acquired with a tantalum backing instead of silver to prevent the reduction of the neutron yield. With the new targets, the ionization yield measurement will be replicated with a greater signal-to-noise ratio, allowing for the measurement of the ionization yield at energies below 7 keVr. Additionally, the Li target will be 1  $\mu\text{m}$  thick, reducing the gamma background by  $\sim 10\times$  compared to that measured for the 10  $\mu\text{m}$  target.

After the measurement of the ionization yield in LAr is made, the effort to directly detect CNNS with a dual-phase Ar detector will continue. The first step will be to develop a large, 10 kg active volume detector that needs to demonstrate the same sensitivities shown by the G/NARRLI detector. In order to increase the low-energy signal sensitivity, reflectors will be implemented to obtain  $\sim 4\pi$  light collection. Due to the energy scale of CNNS recoils, it is of utmost importance to reduce the single electron background as much as possible. The 10 kg Ar detector can then be placed in close proximity to a nuclear reactor at a nuclear power generating station. Possible locations that have been suggested for this

measurement include the San Onofre Nuclear Generating Station (SONGS) in San Onofre, California and the Angra Nuclear Power Plant in Rio de Janeiro, Brazil. Positive correlation of CNNS signals with the reactor being shut down for refueling cycles would be the basis for claiming the first ever detection of CNNS, and stimulate further development of CNNS detectors and their applications.



# Bibliography

- [1] PARTICLE DATA GROUP, “Review of Particle Physics,” *Physical Review D*, **86**(1), p. 32 (2012).
- [2] ARS TECHNICA, “NASA’s Great Observatories after Chandras anniversary,” [arstechnica.com/science/2009/08](http://arstechnica.com/science/2009/08).
- [3] ATLAS COLLABORATION, “Observation of a new particle in the search for the Standard Model Higgs boson with the ATLAS detector at the LHC,” *Physics Letters B*, **716**(1), pp. 1–29 (2012).
- [4] CHOOZ COLLABORATION, “Search for neutrino oscillations on a long baseline at the CHOOZ nuclear power station,” *The European Physical Journal C - Particles and Fields*, **27**(3), pp. 331–374 (2003).
- [5] MENTION, G. *et al.*, “Reactor antineutrino anomaly,” *Physical Review D*, **83**(7), p. 073006 (2011).
- [6] BERNSTEIN, A. *et al.*, “Nuclear reactor safeguards and monitoring with antineutrino detectors,” *Journal of Applied Physics*, **91**(7), pp. 4672–4676 (2002).
- [7] BERNSTEIN, A. *et al.*, “Monitoring the thermal power of nuclear reactors with a prototype cubic meter antineutrino detector,” *Journal of Applied Physics*, **103**(7), pp. 074905–074905–10 (2008).
- [8] BOWDEN, N. *et al.*, “Experimental results from an antineutrino detector for cooperative monitoring of nuclear reactors,” *Nuclear Instruments and Methods in Physics Research Section A: Accelerators, Spectrometers, Detectors and Associated Equipment*, **572**(2), pp. 985–998 (2007).
- [9] BOWDEN, N., “Reactor monitoring and safeguards using antineutrino detectors,” in *XXIII Conference on Neutrino Physics and Astrophysics*, vol. 136 of *Journal of Physics Conference Series*, 23rd International Conference on

Neutrino Physics and Astrophysics, Christchurch, New Zealand, MAY 25-31, 2008 (2008).

- [10] SADLER, L. E. *et al.*, “Towards above-ground antineutrino detectors for co-operative monitoring: Background radiation studies,” in *IEEE Nuclear Science Symposium Conference Record, 2008. NSS '08*, pp. 3045–3048 (2008).
- [11] BOWDEN, N. S. *et al.*, “Observation of the isotopic evolution of pressurized water reactor fuel using an antineutrino detector,” *Journal of Applied Physics*, **105**(6), pp. 064902–064902–8 (2009).
- [12] DOUBLE CHOOZ COLLABORATION, “Indication of Reactor  $\nu_e$  Disappearance in the Double Chooz Experiment,” *Physical Review Letters*, **108**(13), p. 131801 (2012).
- [13] DAYA BAY COLLABORATION, “Observation of electron-antineutrino disappearance at Daya Bay,” *arXiv:1203.1669* (2012).
- [14] RENO COLLABORATION, “Observation of Reactor Electron Antineutrino Disappearance in the RENO Experiment,” *arXiv:1204.0626* (2012).
- [15] BARGER, V. *et al.*, “Long-wavelength vacuum neutrino oscillations and the solar-neutrino deficit,” *Physical Review Letters*, **65**(25), pp. 3084–3087 (1990).
- [16] BARGER, V. *et al.*, “Reexamination of neutrino oscillation solutions to the solar-neutrino problem,” *Physical Review D*, **43**(4), pp. 1110–1128 (1991).
- [17] LOBASHEV, V. and SERDYUK, O., “A pion and muon magnetic trap as a source of electron and muon neutrinos,” *Nuclear Instruments and Methods*, **136**(1), pp. 61–71 (1976).
- [18] VERGADOS, J. D. *et al.*, “Coherent neutral current neutrino-nucleus scattering at a spallation source: A valuable experimental probe,” *Physical Review D*, **79**(11), p. 113001 (2009).
- [19] GIUNTI, C. and KIM, C. W., “Standard Solar Models,” in *Fundamentals of Neutrino Physics and Astrophysics*, Oxford University Press, New York, pp. 359–363 (2007).
- [20] BAHCALL, J. N., “ $^7\text{Be}$  solar neutrino line: A reflection of the central temperature distribution of the Sun,” *Physical Review D*, **49**(8), pp. 3923–3945 (1994).
- [21] BAHCALL, J. N. *et al.*, “Standard neutrino spectrum from  $^8\text{B}$  decay,” *Physical Review C*, **54**(1), pp. 411–422 (1996).

- [22] BAHCALL, J. N., “Gallium solar neutrino experiments: Absorption cross sections, neutrino spectra, and predicted event rates,” *Physical Review C*, **56**(6), pp. 3391–3409 (1997).
- [23] GAISSER, T. K. and HONDA, M., “Flux of Atmospheric Neutrinos,” *Annual Review of Nuclear and Particle Science*, **52**(1), pp. 153–199 (2002).
- [24] FIORENTINI, G. *et al.*, “Geo-neutrinos and earth’s interior,” *Physics Reports*, **453**(56), pp. 117–172 (2007).
- [25] VOGEL, P. and ENGEL, J., “Neutrino electromagnetic form factors,” *Physical Review D*, **39**(11), pp. 3378–3383 (1989).
- [26] HUBER, P. and SCHWETZ, T., “Precision spectroscopy with reactor antineutrinos,” *Physical Review D*, **70**(5), p. 053011 (2004).
- [27] BERNSTEIN, A. *et al.*, “Nuclear Security Applications of Antineutrino Detectors: Current Capabilities and Future Prospects,” *Science & Global Security*, **18**(3), pp. 127–192 (2010).
- [28] LAWRENCE LIVERMORE NATIONAL LABORATORY - SCIENCE AND TECHNOLOGY REVIEW, “Identifying the Source of Stolen Nuclear Materials,” <https://www.llnl.gov/str/JanFeb07/Smith.html>.
- [29] ZACEK, G. *et al.*, “Neutrino-oscillation experiments at the Gsgen nuclear power reactor,” *Physical Review D*, **34**(9), pp. 2621–2636 (1986).
- [30] FREEDMAN, D. Z., “Coherent effects of a weak neutral current,” *Physical Review D*, **9**(5), pp. 1389–1392 (1974).
- [31] PASCHOS, E. A. and KARTAVTSEV, A. V., “Coherent Neutrino-Nucleus Scattering,” *arXiv:hep-ph/0309148* (2003).
- [32] DRUKIER, A. and STODOLSKY, L., “Principles and applications of a neutral-current detector for neutrino physics and astronomy,” *Physical Review D*, **30**(11), pp. 2295–2309 (1984).
- [33] BARBEAU, P. *et al.*, “Toward coherent neutrino detection using low-background micropattern gas detectors,” *Nuclear Science, IEEE Transactions on*, **50**(5), pp. 1285 – 1289 (2003).
- [34] HAGMANN, C. and BERNSTEIN, A., “Two-phase emission detector for measuring coherent neutrino-nucleus scattering,” *Nuclear Science, IEEE Transactions on*, **51**(5), pp. 2151 – 2155 (2004).

- [35] AKIMOV, D. *et al.*, “Detection of reactor antineutrino coherent scattering off nuclei with a two-phase noble gas detector,” *Journal of Instrumentation*, **4**(06), pp. P06010–P06010 (2009).
- [36] LINDHARD, J. *et al.*, “Integral equations governing radiation effects (Notes on atomic collisions, III),” (1963).
- [37] ZIEGLER, J. F., “Stopping of energetic light ions in elemental matter,” *Journal of Applied Physics*, **85**(3), pp. 1249–1272 (1999).
- [38] JONES, K. W. and KRANER, H. W., “Energy lost to ionization by 254-eV  $^{73}\text{Ge}$  atoms stopping in Ge,” *Physical Review A*, **11**(4), pp. 1347–1353 (1975).
- [39] BARBEAU, P. S. *et al.*, “Large-mass ultralow noise germanium detectors: performance and applications in neutrino and astroparticle physics,” *Journal of Cosmology and Astroparticle Physics*, **2007**(09), pp. 009–009 (2007).
- [40] SORENSEN, P. *et al.*, “The scintillation and ionization yield of liquid xenon for nuclear recoils,” *Nuclear Instruments and Methods in Physics Research Section A: Accelerators, Spectrometers, Detectors and Associated Equipment*, **601**(3), pp. 339–346 (2009).
- [41] MANZUR, A. *et al.*, “Scintillation efficiency and ionization yield of liquid xenon for monoenergetic nuclear recoils down to 4 keV,” *Physical Review C*, **81**(2), p. 025808 (2010).
- [42] SORENSEN, P. *et al.*, “Lowering the low-energy threshold of xenon detectors,” *arXiv:1011.6439* (2010).
- [43] CABRERA, B., “Very Low Threshold Scattering - an Experimentalist’s Perspective,” in *Low Threshold Detectors for Detection of Coherent Neutrino Scattering*, Livermore Valley Open Campus, Livermore, CA (2012).
- [44] SADOULET, B., “CDMS Technology and Coherent Neutrino Scattering,” in *Low Threshold Detectors for Detection of Coherent Neutrino Scattering*, Livermore Valley Open Campus, Livermore, CA (2012).
- [45] CABRERA-PALMER, B., “Coherent Neutrino-Nuclear Scattering with Germanium,” in *Low Threshold Detectors for Detection of Coherent Neutrino Scattering*, Livermore Valley Open Campus, Livermore, CA (2012).
- [46] BARTON, P., “Low Noise Threshold in Ge PPC Detectors,” in *Low Threshold Detectors for Detection of Coherent Neutrino Scattering*, Livermore Valley Open Campus, Livermore, CA (2012).

- [47] TIFFENBERG, J., “CONNIE experiment overview,” in *Low Threshold Detectors for Detection of Coherent Neutrino Scattering*, Livermore Valley Open Campus, Livermore, CA (2012).
- [48] BOLOZDYNIA, A., “Russian Emission Detector,” in *Low Threshold Detectors for Detection of Coherent Neutrino Scattering*, Livermore Valley Open Campus, Livermore, CA (2012).
- [49] AKIMOV, D., “Detection of Small Ionization Signals in a Two-Phase LXe Detector: Successes and Obstacles,” in *Low Threshold Detectors for Detection of Coherent Neutrino Scattering*, Livermore Valley Open Campus, Livermore, CA (2012).
- [50] MADLAND, D., “Total prompt energy release in the neutron-induced fission of  $^{235}\text{U}$ ,  $^{238}\text{U}$ , and  $^{239}\text{Pu}$ ,” *Nuclear Physics A*, **772**(34), pp. 113–137 (2006).
- [51] APRILE, E. *et al.*, “Hot Electron Emission,” in *Noble Gas Detectors*, WILEY-VCH Verlag GmbH & Co. KGaA, Weinheim, pp. 62–64 (2006).
- [52] XENON10 COLLABORATION, “Design and performance of the XENON10 dark matter experiment,” *Astroparticle Physics*, **34**(9), pp. 679–698 (2011).
- [53] XENON100 COLLABORATION, “First Dark Matter Results from the XENON100 Experiment,” *Physical Review Letters*, **105**(13), p. 131302 (2010).
- [54] ZEPLIN-II COLLABORATION, “First limits on WIMP nuclear recoil signals in ZEPLIN-II: A two-phase xenon detector for dark matter detection,” *Astroparticle Physics*, **28**(3), pp. 287–302 (2007).
- [55] ZEPLIN COLLABORATION, “The ZEPLIN III dark matter project,” *New Astronomy Reviews*, **49**(26), pp. 277–281 (2005).
- [56] ARDM COLLABORATION, “The Argon Dark Matter Experiment (ArDM),” (2008).
- [57] BRUNETTI, R. *et al.*, “WARP liquid argon detector for dark matter survey,” *New Astronomy Reviews*, **49**(26), pp. 265–269 (2005).
- [58] TAKAHASHI, T. *et al.*, “The average energies,  $W$ , required to form an ion pair in liquefied rare gases,” *Journal of Physics C: Solid State Physics*, **7**, p. 230 (1974).
- [59] DOKE, T. *et al.*, “Estimation of Fano factors in liquid argon, krypton, xenon and xenon-doped liquid argon,” *Nuclear Instruments and Methods*, **134**(2), pp. 353–357 (1976).

- [60] WALKOWIAK, W., “Drift velocity of free electrons in liquid argon,” *Nuclear Instruments and Methods in Physics Research Section A: Accelerators, Spectrometers, Detectors and Associated Equipment*, **449**(12), pp. 288–294 (2000).
- [61] YOSHINO, K. *et al.*, “Effect of molecular solutes on the electron drift velocity in liquid Ar, Kr, and Xe,” *Physical Review A*, **14**(1), pp. 438–444 (1976).
- [62] SUZUKI, M. and KUBOTA, S., “Mechanism of proportional scintillation in argon, krypton and xenon,” *Nuclear Instruments and Methods*, **164**(1), pp. 197–199 (1979).
- [63] KUBOTA, S. *et al.*, “Liquid and solid argon, krypton and xenon scintillators,” *Nuclear Instruments and Methods in Physics Research*, **196**(1), pp. 101–105 (1982).
- [64] HITACHI, A. *et al.*, “Effect of ionization density on the time dependence of luminescence from liquid argon and xenon,” *Physical Review B*, **27**(9), pp. 5279–5285 (1983).
- [65] TAKAHASHI, T. *et al.*, “Emission spectra from Ar-Xe, Ar-Kr, Ar-N<sub>2</sub>, Ar-CH<sub>4</sub>, Ar-CO<sub>2</sub> and Xe-N<sub>2</sub>, gas scintillation proportional counters,” *Nuclear Instruments and Methods in Physics Research*, **205**(3), pp. 591–596 (1983).
- [66] HIMI, S. *et al.*, “Liquid and solid argon, and nitrogen-doped liquid and solid argon scintillators,” *Nuclear Instruments and Methods in Physics Research*, **203**(13), pp. 153–157 (1982).
- [67] KUBOTA, S. *et al.*, “Dynamical behavior of free electrons in the recombination process in liquid argon, krypton, and xenon,” *Physical Review B*, **20**(8), pp. 3486–3496 (1979).
- [68] KETO, J. W. *et al.*, “Production Mechanisms and Radiative Lifetimes of Argon and Xenon Molecules Emitting in the Ultraviolet,” *Physical Review Letters*, **33**(23), pp. 1365–1368 (1974).
- [69] DORENBOS, P. *et al.*, “Quantum efficiencies of several VUV-sensitive photomultiplier tubes,” *Nuclear Instruments and Methods in Physics Research Section A: Accelerators, Spectrometers, Detectors and Associated Equipment*, **325**(12), pp. 367–369 (1993).
- [70] NAKAMURA, K. *et al.*, “Latest bialkali photocathode with ultra high sensitivity,” *Nuclear Instruments and Methods in Physics Research Section A: Accelerators, Spectrometers, Detectors and Associated Equipment*, **623**(1), pp. 276–278 (2010).

- [71] FRANKE, S. *et al.*, “Temperature dependence of VUV transmission of synthetic fused silica,” *Journal of Physics D: Applied Physics*, **39**(14), pp. 3042–3046 (2006).
- [72] KRYLOV, B. *et al.*, “Channels of energy transfer to atomic nitrogen in excited argonnitrogen mixtures,” *Journal of Physics B: Atomic, Molecular and Optical Physics*, **35**(20), pp. 4257–4270 (2002).
- [73] CHESHNOVSKY, O. *et al.*, “Emission spectra of xenon impurity states in solid and liquid krypton,” *The Journal of Chemical Physics*, **59**(10), pp. 5554–5561 (1973).
- [74] LALLY, C. *et al.*, “UV quantum efficiencies of organic fluors,” *Nuclear Instruments and Methods in Physics Research Section B: Beam Interactions with Materials and Atoms*, **117**(4), pp. 421–427 (1996).
- [75] MCKINSEY, D. *et al.*, “Fluorescence efficiencies of thin scintillating films in the extreme ultraviolet spectral region,” *Nuclear Instruments and Methods in Physics Research Section B: Beam Interactions with Materials and Atoms*, **132**(3), pp. 351–358 (1997).
- [76] MUTTERER, M. *et al.*, “Noble-Gas Scintillation Counters for the Detection of Energetic Heavy Ions,” *Nuclear Science, IEEE Transactions on*, **26**(1), pp. 382–387 (1979).
- [77] BURTON, W. M. and POWELL, B. A., “Fluorescence of Tetraphenyl-Butadiene in the Vacuum Ultraviolet,” *Applied Optics*, **12**(1), pp. 87–89 (1973).
- [78] MCKINSEY, D. *et al.*, “Detecting ionizing radiation in liquid helium using wavelength shifting light collection,” *Nuclear Instruments and Methods in Physics Research Section A: Accelerators, Spectrometers, Detectors and Associated Equipment*, **516**(2-3), pp. 475–485 (2004).
- [79] ARDM COLLABORATION, “Development of wavelength shifter coated reflectors for the ArDM argon dark matter detector,” *Journal of Instrumentation*, **4**(06), pp. P06001–P06001 (2009).
- [80] BUGEL, L. *et al.*, “Demonstration of a lightguide detector for liquid argon TPCs,” *Nuclear Instruments and Methods in Physics Research Section A: Accelerators, Spectrometers, Detectors and Associated Equipment*, **640**(1), pp. 69–75 (2011).
- [81] LUPIS, C., “On the definitions of Raoult’s and Henry’s Laws,” *Scripta Metallurgica*, **2**(8), pp. 429–433 (1968).

- [82] NATIONAL INSTITUTE OF STANDARDS AND TECHNOLOGY, “NIST Chemistry WebBook,” [webbook.nist.gov/chemistry/](http://webbook.nist.gov/chemistry/).
- [83] DRII, L. I. and RABINOVICH, V. A., “Dependence of vapor pressure of argon,” *Zh. Fiz. Khim.*, **40**, pp. 709–711 (1966).
- [84] EDEJER, M. P. and THODOS, G., “Vapor pressures of liquid nitrogen between the triple and critical points,” *Journal of Chemical Engineering Data*, **12**(2), pp. 206–209 (1967).
- [85] MICHELS, A. and WASSENAAR, T., “Vapour pressure of liquid xenon,” *Physica*, **16**(3), pp. 253–256 (1950).
- [86] DOKE, T., “Fundamental properties of liquid Ar, Kr, and Xe and their new application to calorimeters,” *6TH World Multiconference on Systemics, Cybernetics, and Informatics, Vol. XVII, Proceedings: Industrial Systems and Engineering III*, pp. 30–37 (2002).
- [87] KUBOTA, S. *et al.*, “Evidence of the existence of exciton states in liquid argon and exciton-enhanced ionization from xenon doping,” *Physical Review B*, **13**(4), pp. 1649–1653 (1976).
- [88] MAVROKORIDIS, K., *Characterisation of Liquid Xenon and Argon as Targets for Direct Dark Matter Detection*, Doctor of philosophy, University of Sheffield (2009).
- [89] GRANDI, L., *WARP An argon double phase technique for dark matter search*, Doctor of philosophy, University of Pavia (2005).
- [90] NI, K., *Development of a Liquid Xenon Time Projection Chamber for the XENON Dark Matter Search*, Doctor of philosophy, Columbia University (2006).
- [91] SORENSEN, P., *A Position-Sensitive Liquid Xenon Time-Projection Chamber for Direct Detection of Dark Matter: The XENON10 Experiment*, Doctor of philosophy, Brown University (2008).
- [92] PHIPPS, J. A. *et al.*, “Total Ionization in Argon by Heavy Ions of Energies 8 to 100 keV,” *Physical Review*, **135**(1A), pp. A36–A39 (1964).
- [93] SORENSEN, P. and DAHL, C. E., “Nuclear recoil energy scale in liquid xenon with application to the direct detection of dark matter,” *Physical Review D*, **83**(6), p. 063501 (2011).
- [94] DOKE, T. *et al.*, “Absolute Scintillation Yields in Liquid Argon and Xenon for Various Particles,” *Japanese Journal of Applied Physics*, **41**(Part 1, No. 3A), pp. 1538–1545 (2002).



- [95] THOMAS, J. and IMEL, D. A., "Recombination of electron-ion pairs in liquid argon and liquid xenon," *Physical Review A*, **36**(2), pp. 614–616 (1987).
- [96] ONSAGER, L., "Initial Recombination of Ions," *Physical Review*, **54**(8), pp. 554–557 (1938).
- [97] GERBER, G. *et al.*, "Ionization Processes in Slow Collisions of Heavy Particles, 1: He and He<sup>+</sup> on Ne, Ar, Kr, Xe," *Journal of Physics B: Atomic and Molecular Physics*, **5**(7), pp. 1396–1411 (1972).
- [98] GERBER, G. *et al.*, "Ionization processes in slow collisions of heavy particles II. Symmetrical systems of the rare gases He, Ne, Ar, Kr," *Journal of Physics B: Atomic and Molecular Physics*, **6**(3), pp. 493–510 (1973).
- [99] BIRSACK, J. and HAGGMARK, L., "A Monte Carlo computer program for the transport of energetic ions in amorphous targets," *Nuclear Instruments and Methods*, **174**(12), pp. 257–269 (1980).
- [100] PHELPS, A. V., "Cross Sections and Swarm Coefficients for Nitrogen Ions and Neutrals in N<sub>2</sub> and Argon Ions and Neutrals in Ar for Energies from 0.1 eV to 10 keV," *Journal of Physical and Chemical Reference Data*, **20**(3), pp. 557–573 (1991).
- [101] MOLIERE, G., "Theorie der Streuung Schneller Geldener Teilchen," *Zeitschrift Fur Naturforschung Section A: Journal of Physical Sciences*, **2**(3), pp. 133–145 (1947).
- [102] WILSON, W. D. *et al.*, "Calculations of nuclear stopping, ranges, and straggling in the low-energy region," *Physical Review B*, **15**(5), pp. 2458–2468 (1977).
- [103] FIRSOV, O. B., "Calculation of the interaction potential of atoms," *Soviet Physics JETP-USSR*, **6**(3), pp. 534–537 (1958).
- [104] YAMAMURA, Y. *et al.*, "Shell correction of screening length in interatomic potential," *Nuclear Instruments and Methods in Physics Research Section B: Beam Interactions with Materials and Atoms*, **153**(14), pp. 71–76 (1999).
- [105] ROBINSON, M. T., *Report ORNL-4556, Tech. rep.*, Oak Ridge National Laboratory, (unpublished) (1970).
- [106] COHEN, M. H. and LEKNER, J., "Theory of Hot Electrons in Gases, Liquids, and Solids," *Physical Review*, **158**(2), pp. 305–309 (1967).
- [107] WOJCIK, M. and TACHIYA, M., "Electron transport and electronion recombination in liquid argon: simulation based on the CohenLekner theory," *Chemical Physics Letters*, **363**(34), pp. 381–388 (2002).

- [108] SWOPE, W. C. *et al.*, “A computer simulation method for the calculation of equilibrium constants for the formation of physical clusters of molecules: Application to small water clusters,” *The Journal of Chemical Physics*, **76**(1), pp. 637–649 (1982).
- [109] JASKOLSKI, M. and WOJCIK, M., “Electron Recombination in Ionized Liquid Argon: A Computational Approach Based on Realistic Models of Electron Transport and Reactions,” *J. Phys. Chem. A*, **115**(17), pp. 4317–4325 (2011).
- [110] WOJCIK, M. and TACHIYA, M., “Electron-ion recombination in dense gaseous and liquid argon: effects due to argon cation clusters allow to explain the experimental data,” *Chemical Physics Letters*, **390**(46), pp. 475–480 (2004).
- [111] JASKOLSKI, M. and WOJCIK, M., “Electron-ion recombination in radiation tracks in liquid argon: a computer simulation study,” *Research on Chemical Intermediates*, **35**(4), pp. 453–463 (2009).
- [112] BIAGI-V8.9 DATABASE, [www.lxcat.laplace.univ-tlse.fr/](http://www.lxcat.laplace.univ-tlse.fr/), retrieved Oct 8, 2012.
- [113] BIAGI, S., “Monte Carlo simulation of electron drift and diffusion in counting gases under the influence of electric and magnetic fields,” *Nuclear Instruments and Methods in Physics Research Section A: Accelerators, Spectrometers, Detectors and Associated Equipment*, **421**(12), pp. 234–240 (1999).
- [114] ZATSARINNY, O. and BARTSCHAT, K., “B-spline BreitPauli R-matrix calculations for electron collisions with argon atoms,” *Journal of Physics B: Atomic, Molecular and Optical Physics*, **37**(23), pp. 4693–4706 (2004).
- [115] ALLAN, M. *et al.*, “Near-threshold absolute angle-differential cross sections for electron-impact excitation of argon and xenon,” *Physical Review A*, **74**(3), p. 030701 (2006).
- [116] RILEY, M. E. *et al.*, “Theoretical electron-atom elastic scattering cross sections: Selected elements, 1 keV to 256 keV,” *Atomic Data and Nuclear Data Tables*, **15**(5), pp. 443–476 (1975).
- [117] PHELPS DATABASE, [www.lxcat.laplace.univ-tlse.fr/](http://www.lxcat.laplace.univ-tlse.fr/), retrieved Oct 8, 2012.
- [118] YAMABE, C. *et al.*, “Measurement of free-free emission from low-energy-electron collisions with Ar,” *Physical Review A*, **27**(3), pp. 1345–1352 (1983).
- [119] LXCAT, “Electron Scattering Database,” [www.lxcat.laplace.univ-tlse.fr/](http://www.lxcat.laplace.univ-tlse.fr/).

- [120] HUANG, S. S.-S. and FREEMAN, G. R., “Electron transport in gaseous and liquid argon: Effects of density and temperature,” *Physical Review A*, **24**(2), pp. 714–724 (1981).
- [121] SHINAKA, K. *et al.*, “Electron recombination rate constants in gaseous, liquid, and solid argon,” *The Journal of Chemical Physics*, **88**(12), pp. 7529–7536 (1988).
- [122] WINANT, C. *et al.*, “Dual-phase argon ionization detector for measurement of coherent elastic neutrino scattering and medium-energy nuclear recoils,” in *Nuclear Science Symposium Conference Record, 2007. NSS '07. IEEE*, vol. 3, pp. 2110–2114 (2007).
- [123] KAZKAZ, K. *et al.*, “Operation of a 1-liter-volume gaseous argon proportional scintillation counter,” *Nuclear Instruments and Methods in Physics Research Section A: Accelerators, Spectrometers, Detectors and Associated Equipment*, **621**(13), pp. 267–277 (2010).
- [124] HAMAMATSU, “Ultra Bialkali, Super Bialkali Photomultiplier Tube Series,” [sales.hamamatsu.com](http://sales.hamamatsu.com).
- [125] LBNL ISOTOPES PROJECT, “Table of Radioactive Isotopes,” [ie.lbl.gov/toi/perchart.htm](http://ie.lbl.gov/toi/perchart.htm).
- [126] PERKINS, S. *et al.*, *Tables and graphs of atomic subshell and relaxation data derived from the LLNL Evaluated Atomic Data Library (EADL), Z = 1–100, Technical Report UCRL-50400-Vol.30*, Lawrence Livermore National Laboratory, Livermore, CA (1991).
- [127] NUCLEAR DATA SERVICES, “Photon Interaction Data,” [www-nds.iaea.org/epdl97/](http://www-nds.iaea.org/epdl97/).
- [128] POLICARPO, A. *et al.*, “The argon-nitrogen proportional scintillation counter,” *Nuclear Instruments and Methods*, **55**(0), pp. 105 – 119 (1967).
- [129] BERGER, M. J. *et al.*, “National Institute of Standards and Technology ESTAR Database,” <http://www.nist.gov/pml/data/star/index.cfm>.
- [130] ALLISON, J. *et al.*, “Geant4 developments and applications,” *IEEE Transactions on Nuclear Science*, **53**(1), pp. 270–278 (2006).
- [131] HAGMANN, C. *et al.*, “Active Detection of Shielded SNM With 60-keV Neutrons,” *IEEE Transactions on Nuclear Science*, **56**(3), pp. 1215–1217 (2009).

- [132] LEE, C. and ZHOU, X.-L., “Thick target neutron yields for the  ${}^7\text{Li}(p,n){}^7\text{Be}$  reaction near threshold,” *Nuclear Instruments and Methods in Physics Research Section B: Beam Interactions with Materials and Atoms*, **152**(1), pp. 1–11 (1999).
- [133] NUCLEAR DATA SERVICES, “DROSG-2000: Neutron Source Reactions,” [www-nds.iaea.org/drosg2000.html](http://www-nds.iaea.org/drosg2000.html).
- [134] ACCSYS TECHNOLOGY INC., 1177 A Quarry Lane, Pleasanton, CA 94566 USA.
- [135] FOXE, M. *et al.*, “Measurement of the nuclear ionization quench factor in a dual-phase argon detector,” in *Nuclear Science Symposium Conference Record (NSS/MIC), 2010 IEEE*, pp. 105 –109 (2010).
- [136] BORGHESANI, A. *et al.*, “Electron transmission through the Ar liquid-vapor interface,” *Physics Letters A*, **149**(9), pp. 481–484 (1990).
- [137] BONDAR, A. *et al.*, “Two-phase argon and xenon avalanche detectors based on Gas Electron Multipliers,” *Nuclear Instruments and Methods in Physics Research Section A: Accelerators, Spectrometers, Detectors and Associated Equipment*, **556**(1), pp. 273–280 (2006).
- [138] MONTEIRO, C. *et al.*, “Secondary scintillation yield in pure argon,” *Physics Letters B*, **668**(3), pp. 167–170 (2008).
- [139] MONTEIRO, C. M. B., *Determination of Argon and Xenon Absolute Electroluminescence Yields in Gas Proportional Scintillation Counters*, Doctor of philosophy, University of Coimbra (2010).
- [140] HAMAMATSU, “Ultra Bialkali, Super Bialkali Photomultiplier Tube Series,” [sales.hamamatsu.com](http://sales.hamamatsu.com).
- [141] CRYOFAB, “CF4515 Dewar Flask,” [www.cryofab.com](http://www.cryofab.com).
- [142] QDRIVE, “2S132K-FAR Cryocooler,” [www.qdrive.com](http://www.qdrive.com).
- [143] SAES, “MicroTorr purifiers, MC1500-902F,” [www.saespuregas.com/](http://www.saespuregas.com/).
- [144] COMSOL Multiphysics 4.2a, [www.comsol.com](http://www.comsol.com).
- [145] SIGMA-ALDRICH, “1,1,4,4-Tetraphenyl-1,3-butadiene - suitable for scintillation, 99%,” [www.sigmaaldrich.com/](http://www.sigmaaldrich.com/).
- [146] OLD WILL KNOTT SCALES, “Citizen CT-603 Table Top High Precision Balance,” [www.oldwillknottscales.com/citizen-ct603.html](http://www.oldwillknottscales.com/citizen-ct603.html).

- [147] 3M, “Vikuiti™ Enhanced Specular Reflector foil,” [www.3m.com/](http://www.3m.com/).
- [148] DONALDSON FILTRATION SOLUTIONS, “Tetratex™ (TTX) ePTFE membrane,” [www2.donaldson.com/tetratex](http://www2.donaldson.com/tetratex).
- [149] KNF PUMPS AND SYSTEMS FOR GASES AND LIQUIDS, “Double-Diaphragm Vacuum Pump - N143 SN.12E,” [www.knf.com/usa.htm](http://www.knf.com/usa.htm).
- [150] LECROY, “Waverunner Xi-A 8-bit,” [www.lecroy.com/oscilloscope/](http://www.lecroy.com/oscilloscope/).
- [151] BERGER, M. J. *et al.*, “National Institute of Standards and Technology XCOM Database,” <http://www.nist.gov/pml/data/xcom/index.cfm>.
- [152] BARSANOV, V. *et al.*, “Artificial neutrino source based on the  $^{37}\text{Ar}$  isotope,” *Physics of Atomic Nuclei*, **70**(2), pp. 300–310 (2007).
- [153] AALSETH, C. *et al.*, “Measurement of  $^{37}\text{Ar}$  to support technology for On-Site Inspection under the Comprehensive Nuclear-Test-Ban Treaty,” *Nuclear Instruments and Methods in Physics Research Section A: Accelerators, Spectrometers, Detectors and Associated Equipment*, **652**(1), pp. 58–61 (2011).
- [154] MESYATS, G. A. *et al.*, “Principal Characteristics of the Energetic Electron - Gas Interaction,” in *Pulsed Gas Lasers*, SPIE Publications, p. 70 (1995).
- [155] WOJCIK, M. and TACHIYA, M., “Electron thermalization and electronion recombination in liquid argon,” *Chemical Physics Letters*, **379**(12), pp. 20–27 (2003).
- [156] MULLER-FIEDLER, R. *et al.*, “Double differential cross sections for electron impact ionisation of helium,” *Journal of Physics B: Atomic and Molecular Physics*, **19**(8), pp. 1211–1229 (1986).
- [157] NUCLEAR DATA SERVICES, “Evaluated Nuclear Data File (ENDF),” [www-nds.iaea.org/exfor/endl.htm](http://www-nds.iaea.org/exfor/endl.htm).
- [158] MCKINNEY, G. W. *et al.*, “MCNPX Overview,” in *Proceedings of the 2006 HSSW*, FNAL, IL (2006).
- [159] PELOWITZ, D. B. *et al.*, *MCNPX 2.7.0 Extensions*, Technical Report LA-UR-11-02295, Los Alamos National Laboratory (2011).
- [160] BARBEAU, P. *et al.*, “Design and characterization of a neutron calibration facility for the study of sub-keV nuclear recoils,” *Nuclear Instruments and Methods in Physics Research Section A: Accelerators, Spectrometers, Detectors and Associated Equipment*, **574**(2), pp. 385–391 (2007).

- [161] AKERIB, D. *et al.*, “LUXSim: A component-centric approach to low-background simulations,” *Nuclear Instruments and Methods in Physics Research Section A: Accelerators, Spectrometers, Detectors and Associated Equipment*, **675**(0), pp. 63–77 (2012).
- [162] POLYPLUS BATTERY COMPANY, 2431 5th Street, Suite B, Berkeley, CA 94710 USA.
- [163] OVERLEY, J. *et al.*, “The energy calibration of tandem accelerators,” *Nuclear Instruments and Methods*, **68**(1), pp. 61–69 (1969).
- [164] MARION, J. B., “Accelerator Calibration Energies,” *Reviews of Modern Physics*, **38**(4), pp. 660–668 (1966).
- [165] OTT, A. *et al.*, “Slowly Diffusing Impurities in Lithium Metal,” *Physical Review*, **188**(3), pp. 1088–1092 (1969).
- [166] BERGER, M. J. *et al.*, “National Institute of Standards and Technology PSTAR Database,” <http://www.nist.gov/pml/data/star/index.cfm>.
- [167] POTETYUNKO, G. N., “Verifying the addition rule for the proton-retarding power of multicomponent materials,” *Soviet Atomic Energy*, **52**(2), pp. 137–140 (1982).
- [168] THWAITES, D. I., “Current status of physical state effects on stopping power,” *Nuclear Instruments and Methods in Physics Research Section B: Beam Interactions with Materials and Atoms*, **12**(1), pp. 84–89 (1985).
- [169] ZIEGLER, J. and MANOYAN, J., “The stopping of ions in compounds,” *Nuclear Instruments and Methods in Physics Research Section B: Beam Interactions with Materials and Atoms*, **35**(34), pp. 215–228 (1988).
- [170] PARTICLE DATA GROUP, “Review of Particle Physics,” *Physical Review D*, **86**(1), pp. 391–392 (2012).
- [171] BAKER, S. and COUSINS, R. D., “Clarification of the use of CHI-square and likelihood functions in fits to histograms,” *Nuclear Instruments and Methods in Physics Research*, **221**(2), pp. 437–442 (1984).
- [172] LOOSLI, H., “A dating method with  $^{39}\text{Ar}$ ,” *Earth and Planetary Science Letters*, **63**(1), pp. 51–62 (1983).
- [173] KUTSCHERA, W. *et al.*, “Long-lived noble gas radionuclides,” *Nuclear Instruments and Methods in Physics Research Section B: Beam Interactions with Materials and Atoms*, **92**(14), pp. 241–248 (1994).

- [174] BENETTI, P. *et al.*, “Measurement of the specific activity of  $^{39}\text{Ar}$  in natural argon,” *Nuclear Instruments and Methods in Physics Research Section A: Accelerators, Spectrometers, Detectors and Associated Equipment*, **574**(1), pp. 83–88 (2007).
- [175] WU, C.-s. and MOSZKOWSKI, S. A., *Beta Decay*, 1 ed., Interscience Publishers (1966).
- [176] LOER, B. M., *Towards a Depleted Argon Time Projection Chamber WIMP Search : DarkSide Prototype Analysis and Predicted Sensitivity*, Doctor of philosophy, Princeton University (2011).
- [177] XU, J. *et al.*, “A Study of the Residual  $^{39}\text{Ar}$  Content in Argon from Underground Sources,” *arXiv:1204.6011* (2012).
- [178] KAMLAND COLLABORATION, “Partial radiogenic heat model for Earth revealed by geoneutrino measurements,” *Nature Geoscience*, **4**(9), pp. 647–651 (2011).
- [179] VERGADOS, J. D. *et al.*, “Coherent neutral current neutrino-nucleus scattering at a spallation source: A valuable experimental probe,” *Physical Review D*, **79**(11), p. 113001 (2009).
- [180] SCHOLBERG, K., “Prospects for measuring coherent neutrino-nucleus elastic scattering at a stopped-pion neutrino source,” *Physical Review D*, **73**(3), p. 033005 (2006).
- [181] SCHOLBERG, K. *et al.*, “The CLEAR Experiment,” *arXiv:0910.1989* (2009).
- [182] DAVIDSON, S. *et al.*, “Present and future bounds on non-standard neutrino interactions,” *Journal of High Energy Physics*, **2003**(03), pp. 011–011 (2003).

## Vita

Michael P. Foxe

### Education

***The Pennsylvania State University*** State College, Pennsylvania 2010–2013  
Ph.D. in Nuclear Engineering, May 2013  
Area of Specialization: Radiation Detection

***Purdue University*** West Lafayette, Indiana 2008–2010  
M.S. in Nuclear Engineering, Dec. 2010

***University of California: Berkeley*** Berkeley, California 2004–2008  
B.S. in Chemical Engineering and Nuclear Engineering, May 2008

### Awards and Honors

2nd place Innovations in Fuel Cycle Research Competition - Nuclear Material Accountability and Control Instrumentation 2012

2nd National Conference on Advances in Tools and Solutions for Nuclear Material Detection Session Chair, Detector Materials and Nuclear Material Detection 2011

DHS Nuclear Forensics Graduate Fellowship 2009–2012

ANS Student Conference, Best Paper in Radiation Detection 2009

Robert C. Byrd Scholarship 2004–2008

Boy Scouts of America Eagle Scout Rank 2004

### Research Experience

***Doctoral Research*** The Pennsylvania State University 2010–2013  
Thesis Advisor: Prof. Igor Jovanovic

***Doctoral Research*** Lawrence Livermore National Laboratory 2007–2013  
Research Advisor: Dr. Adam Bernstein  
Measurement of ionization yield in a dual-phase noble gas detector.

***Graduate Research*** Purdue University 2008–2010  
Research Advisors: Prof. Igor Jovanovic and Prof. Yong P. Chen  
Development of a radiation detector based on the utilization of graphene.

***Undergraduate Research*** University of California, Berkeley 2005–2006  
Research Advisor: Prof. Gabor Somorjai  
Synthesis of platinum nano-particles catalysts in a polymer environment.

### Teaching Experience

***Guest Lecturer*** Purdue University 2010  
I gave lectures on nuclear reactor monitoring via antineutrinos and on nuclear engineering principles.

***Teaching Assistant*** Purdue University 2009  
Guest lecturer and teaching assistant for Introduction to Fusion Technologies